

530  
DEK

CENTRAL LIBRARY  
TEZPUR UNIVERSITY  
Accession No. T228  
Date 2/3/13

**SYNTHESIS, SWIFT HEAVY ION IRRADIATION AND  
CHARACTERIZATION OF NANOFIBER REINFORCED  
AND LAYERED SILICATE NANOCOMPOSITE GEL  
POLYMER ELECTROLYTES**

**A thesis submitted in partial fulfillment of the  
requirements for the degree of  
Doctor of Philosophy**

**Madhuryya Deka**

**Registration No. 047 of 2011**



**Department of Physics, School of Science and Technology**

**Tezpur University, Tezpur-784028**

**Assam, India**

**March, 2012**

# **Synthesis, swift heavy ion irradiation and characterization of nanofiber reinforced and layered silicate nanocomposite gel polymer electrolytes**

## **Abstract**

The path breaking studies of Wright and Armand on ionically conducting polymers, called “polymer electrolytes” in the late 1970s have opened an innovative area of materials research with potential applications in the power industry. The main applications of these polymer electrolytes were in rechargeable lithium batteries as an alternative to liquid solution electrolytes. The advantages such as no leakage of electrolyte, higher energy density, flexible geometry and improved safety hazards have drawn the attention of many researchers on the development of lithium polymer batteries and other electrochemical devices such as supercapacitors, electrochromic windows, and sensors. In the present work emphasis has been placed on composite gel polymer electrolytes because of the higher ionic conductivity and better electrochemical, interfacial and thermal stability.

The present thesis is a description of a number of experiments in the active research field of nanocomposites gel polymer electrolytes with polyaniline (PAni) nanofibers and montmorillonite (MMT) as fillers. The nanocomposites electrolytes have been characterized by X-ray diffraction (XRD), Transmission electron microscopy (TEM), Scanning electron microscopy (SEM), Fourier transform infrared spectroscopy (FTIR). The ionic conductivity of the nanocomposites polymer electrolyte films was determined by ac impedance measurements using a Hioki 3532-50 LCR HiTester in the frequency range from 42 Hz to 5MHz. The temperature dependence of ionic conductivity was also measured by heating the samples from room temperature to higher temperature. The interfacial stability of nanocomposites polymer electrolytes was studied by fabricating Li/polymer electrolyte/Li cells at room temperature and was monitored for 15-20 days. The anodic decomposition voltage was determined by linear sweep voltammetry using electrochemical workstation. SHI irradiation of the nanocomposites with 90 MeV oxygen ions ( $O^{7+}$ ) with fluence  $5 \times 10^{10}$ ,  $1 \times 10^{11}$ ,  $5 \times 10^{11}$  and  $1 \times 10^{12}$  and  $5 \times 10^{12}$  ions/cm<sup>2</sup>, has been carried out to study the ion irradiation effects on the nanocomposites.

The thesis contains eight chapters, each of which again has several sub-sections. **Chapter I** reviews the literature of different types of polymer electrolytes viz. solid polymer electrolytes (SPEs), gel polymer electrolytes (GPEs) and composite polymer electrolytes (CPEs). A brief description of ion transport models has also been included in this chapter. In the end, statement of the problem and objectives of the present work have been spelt out.

**Chapter II** focuses on the theoretical aspects of complex impedance spectroscopy and ion transport kinetics in solid, gel and composite polymer electrolytes.

**Chapter III** describes the properties of materials used in the present work viz. polymer, plasticizer, MMT and synthesis of PANi nanofibers by interfacial polymerization method. Synthesis techniques for the preparation of nanocomposites gel polymer electrolytes have been elaborately explained in this chapter. Principles of various characterizations tools and instruments such as ionic conductivity measurement set up, XRD, SEM, TEM, FTIR employed to characterize the nanocomposites polymer electrolytes in the present work have been briefly explained.

In **Chapter IV** complex impedance spectroscopy, XRD, SEM and FTIR of PMMA-(PC+DEC)-LiClO<sub>4</sub> and P(VdF-HFP)-(PC+DEC)-LiClO<sub>4</sub> based nanocomposites gel electrolytes dispersed with dedoped PANi nanofibers have been analyzed to gain an insight into the different characteristic properties such as ionic conductivity, crystallinity, surface morphology and interactions among the various constituents of polymer electrolytes. The electrochemical and interfacial properties have also been studied.

**Chapter V** emphasizes on the two blend based polymer electrolyte systems viz. PEO/P(VdF-HFP)-(PC+DEC)-LiClO<sub>4</sub> synthesized by phase inversion technique and PEO/P(VdF-HFP)-LiClO<sub>4</sub>-dedoped PANi nanofibers synthesized by solution casting technique. In the first system the ionic conductivity has been correlated with the variation of pore size, porosity and electrolyte uptake. In the second system the effect of PANi nanofibers on the ionic transport and electrochemical properties of PEO/P(VdF-HFP) blend complexed with LiClO<sub>4</sub> has been discussed.

**Chapter VI** deals with the electrical and electrochemical properties of solution intercalated nanocomposites based on PMMA-MMT and PVdF-MMT. Both the nanocomposites exhibit mixed intercalated and exfoliated nanostructures as observed in TEM. Properties such as ionic conductivity, surface morphology, electrochemical and

interfacial stability and interaction among different groups in the polymer electrolytes have been analyzed to throw new light on the ionic conduction mechanism in these types of nanocomposite polymer electrolytes.

**Chapter VII** highlights the effect of 90 MeV  $O^{7+}$  ion irradiation on P(VdF-HFP)-(PC+DEC)-LiClO<sub>4</sub>-dedoped PANi nanofibers and PEO-MMT based single ion conductor. Ion irradiation leads to the enhancement of ionic conductivity up to  $10^{11}$  ions/cm<sup>2</sup>. Above that fluence a decreasing trend of ionic conductivity is observed. This has been explained on the basis of chain scission and cross-linking of polymer chains at different ion fluences. On the other hand SHI irradiation on PEO-MMT nanocomposites results in the increase of polymer intercalation inside the galleries of MMT. Ion beam modification of polymer electrolytes is a new research area and in this chapter effort has been made to understand the conduction mechanism of swift heavy ion irradiated nanocomposite polymer electrolytes.

**Chapter VIII** outlines the summary of the major conclusions drawn from the work contained in the present thesis. At the end of this chapter, the future scope of the related field is briefly mentioned.

## **Declaration**

I hereby declare that the thesis entitled “**Synthesis, swift heavy ion irradiation and characterization of nanofiber reinforced and layered silicate nanocomposite gel polymer electrolytes**”, submitted to the School of Science and Technology, Tezpur University in partial fulfillment of the requirements for the award of Doctor of Philosophy in Physics, is a record of original research work carried out by me. Any texts, figures, theories, results or designs that are not of my own devising are appropriately referenced in order to give due credit to the original author(s). All sources of assistance have been assigned due acknowledgement. I also declare that neither this work as a whole nor a part of it has been submitted to any other university or institute for any degree, diploma, associateship, fellowship or any other similar title or recognition.

Date: 30.03.2012  
Place: Tezpur

*Madhuryya Deka*

(Madhuryya Deka)  
Department of Physics  
School of Science and Technology  
Tezpur University  
Tezpur-784028, Assam, India



**Tezpur University**


## **Certificate**

This is to certify that the thesis entitled “**Synthesis, swift heavy ion irradiation and characterization of nanofiber reinforced and layered silicate nanocomposite gel polymer electrolytes**”, submitted to the School of Science and Technology, Tezpur University in partial fulfillment of the requirements for the award of Doctor of Philosophy in Physics, is a record of original research work carried out by Mr. Madhuryya Deka under my supervision and guidance.

All helps received by him from various sources have been duly acknowledged.

No part of the thesis has been submitted elsewhere for award of any other diploma or degree.

Signature of Supervisor:  
Designation: Professor  
School: Science and Technology  
Department: Physics  
Date: 30.3.2012  
Place: Tezpur-784028, Assam, India

  
(Prof. Ashok Kumar)

*Dedicated To*  
*My*  
*Beloved Parents*  
*And*  
*Nankali*



## Acknowledgements

*Any doctoral thesis is not possible without the help and support of many people and to thank or even to acknowledge all of them is not possible within few pages. But I would like to mention as many as I can.*

*First of all, I wish to express my deepest appreciation and thanks to my supervisor, Professor Ashok Kumar, for his intellectually stimulating guidance and invaluable encouragement throughout my candidature as a Ph.D. student. Professor Kumar's comprehensive knowledge and incisive insight on electrolyte materials not to mention his uncompromising and prudent attitude towards research and insistence on quality works have deeply influenced me. Needless to say, I shall be highly obliged to him for all the time.*

*I extend my sincere and hearty gratitude to Dr. D.K. Avasthi, senior Scientist, Inter University Accelerator Center (IUAC), New Delhi, for his keen interest and inspiring suggestions for swift heavy ion irradiation of polymer electrolytes. His constructive comments and assistance at every stage of my work shall remain noteworthy. I also thank P.K. Kulriya, Rahul Singhal and S.A. Khan for their extended help during the irradiation experiment at IUAC, New Delhi.*

*I would like to thank SAIF, Shillong, NEIST, Jorhat, Department of Physics, IIT Guwahati, Department of Chemical Sciences, Tezpur University.*

*I am highly grateful to Prof. A. Choudhury, Prof. J. K. Sarma, Dr. N.S. Bhattacharyya, Dr. N. Das, Dr. G.A. Ahmed, Dr. D. Mahanta, Dr. P. Deb, Dr. K. Barua, Dr. P.K. Karmakar, Dr. M.K. Das, Dr. P. Nath, R. Biswas and Dr. R. Gogoi of Department of Physics and Prof. S.K. Duloi and Dr P. Bharali of Department of Chemical Sciences for their personal involvement, timely help, stimulating discussion to carry out research. I would also extend my gratitude to Prof. N. Karak, Department of Chemical Sciences for his encouragement, inspirational and fruitful discussion in carrying out some of the works related to polymer/clay nanocomposites. I acknowledge the help received from the technical staff of Department of Physics.*

*I would like to thank Mr. Nipu Dutta Department of Chemical Sciences for his help in doing FTIR. Special thanks are due to Dr. Jatindranath Maiti and Dr. Surajit Konwar for their help in electrochemical characterization, Dr. Harekrishna Deka for helping me in*

*synthesizing some of my samples, Rattan Barua for helping in SEM measurements and Prakash Kurmi for helping in XRD measurements.*

*I would like to extend my sincere appreciation to the community of Materials Research Laboratory, Department of Physics, Tezpur University; Dr. Abu Mohd. Pharhad Hussain, Dr. Smritimala Sarmah, Chandrani Nath, Anup Kumar Nath, Jnanendra Upadhyay, Paragjyoti Chutia, Jayanta Hazarika, Sauravjyoti Saikia, Anjalu Ramchiary and Dimpul Konwar.*

*I would like to thank the Center for Industrial and Scientific Research (CSIR), New Delhi, for financial assistance and Inter University Accelerator Center (IUAC), New Delhi, for providing ion beam facility to carry out my research work.*

*I sincerely acknowledge the help received from my lab-mate Somik Banerjee with whom I had plenty of fruitful discussions at various stages. Thank you Nandita for those great moments. I would like to specially thank Rajni Sarmah, IIT Roorkee, for her help and encouraging words. Thank you Sanjibda, Prakashda and Jyoti (Jojo) for being there always. A special mention for Dr. Sanjeev Kr. Bhattacharya for being wonderful brother and friend. I sincerely thank Jagat Dwipendra Ray, Riku Gogoi and Raja Chetia for being wonderful friends. Special acknowledgement goes to Navanath, Rahul, Debashishda, Subasitda, Ankurda, Kunal, Sovonda, Sanchitaba Nabanitaba, Swatiba, Upamanyuda, Durgada, Sikha, Madhulekha, Bandita, Mayuri, Sayan, Runjun, Jadabendra, Rajesh, Bhaskar, Dushanta, Amar, Subhra, Tanuj, Subha, Sabir, Samrat, Nantu and Rabha.*

*No words can repay for the continuous encouragement, moral support, blessings and everything else that I received from my parents, Suren Deka and Era Deka. I am proud of my grandfather Tarun Das and grandmother Sabitri Das for their untiring cooperation and suggestions throughout my research work. A big thank you to my brother Prachuryya Deka and sister Ajanta Deka for their help and support. Last but not least to all my sweet cousins Manashi, Maina, Kaku, Sunu, Jun, Jeeneey, Janmoni and Luki for their welcome distractions that kept me sane throughout.*

## CONTENTS

<b>Abstract</b>	<b>i</b>
<b>Declaration</b>	<b>iv</b>
<b>Certificate</b>	<b>v</b>
<b>Acknowledgements</b>	<b>vii</b>
<b>Content</b>	<b>ix</b>
<b>List of tables</b>	<b>xiii</b>
<b>List of figures</b>	<b>xiv</b>
<b>List of abbreviations</b>	<b>xxiii</b>
<b>CHAPTER I: INTRODUCTION</b>	<b>1</b>
1.1 Types of Polymer Electrolytes and Their Historical Developments	2
1.1.1 Solid Polymer Electrolytes (SPEs)	3
1.1.2 Gel Polymer Electrolytes (GPEs)	5
1.1.3 Composite Polymer Electrolytes (CPEs)	13
1.1.4 Nanocomposite Polymer Electrolytes (NCPEs)	15
1.1.4.1 Inorgani- in-Organic Nanocomposite Electrolytes	15
1.1.4.2 Organi- in-Inorganic Nanocomposite Electrolytes	18
1.2 From Nanocomposite to Nanocomposite Gel Polymer Electrolytes	22
1.3 Ion Transport in Polymers: Mechanisms and Models	26
1.3.1 Arrhenius Model	28
1.3.2 Vogel-Tamman-Fulcher (VTF) Model	28
1.3.3 William-Landel-Ferry (WLF) model	29
1.3.4 Dynamic Bond Percolation (DBP) Model	29
1.3.5 Free Volume Model	30
1.4 Swift Heavy Ion Irradiation of Polymer Electrolytes	33
1.4.1 Nuclear Energy Loss	33
1.4.2 Electronic Energy Loss	34
1.5 Scope of the Thesis and Statement of Thesis Problem	35

<b>CHAPTER II: THEORETICAL ASPECTS</b>	<b>38</b>
2.1 Electrical Conductivity and Impedance Spectroscopy	38
2.1.1 Direct Current Method (D.C. Method)	38
2.1.2. Alternating Current Method (A.C. Method)	40
2.1.2.1 Blocking Electrodes	43
2.1.2.2 Non-Blocking Electrodes (Reversible Electrodes)	44
2.2 Dielectric Relaxation in Amorphous Materials	46
2.2.1 Formalism of Dielectric Data	48
2.3 Kinetics of Ion Transport in Solid Polymer Electrolytes	50
2.4 Kinetics of Ion Transport in Gel Polymer Electrolytes	54
2.5 Kinetics of Ion Transport in Composite Polymer Electrolytes	56
2.6 Kinetics of Intercalation and Ion Transport in Polymer/Clay Nanocomposite Electrolytes	60
 <b>CHAPTER III: EXPERIMENTAL DETAILS</b>	 <b>67</b>
3.1 Parent Materials	67
3.2 Sample Preparation	69
3.3 Furnace and Temperature Controller	72
3.4 Sample Holder	72
3.5 Conductivity Measurements	73
3.6 Transport Number Measurements	74
3.7 X-ray Diffraction	75
3.7.1 Degree of Crystallinity	76
3.7.2 Calculation of d-spacing, Domain length (L) and Strain ( $\epsilon$ )	77
3.8 Fourier Transform Infrared Spectroscopy (FTIR)	80
3.9 Transmission Electron Microscopy (TEM)	82
3.10 Scanning Electron Microscopy (SEM)	83
3.11 Swift Heavy Ion (SHI) Irradiation	85
3.11.1 Parameters Related to Ion Irradiation	88

<b>CHAPTER IV: [PMMA/ P(VdF-HFP)] BASED NANOCOMPOSITE GEL</b>		
<b>POLYMER ELECTROLYTES DISPERSED</b>		
<b>WITH DEDOPED (INSULATING) PANI NANOFIBERS</b>		<b>90</b>
4.1	TEM Studies	91
4.2	Ionic Conductivity Measurements	91
4.3	X-Ray Diffraction (XRD) Analysis	95
4.4	Morphological Studies	96
4.5	FTIR Analysis	98
4.6	Electrochemical Analysis	100
4.7	Summary	103
 <b>CHAPTER V: PEO/P(VDF-HFP) BLEND BASED MICROPOROUS GEL</b>		
<b>AND NANOCOMPOSITE POLYMER ELECTROLYTES</b>		<b>105</b>
5.1	PEO-P(VdF-HFP) based Microporous Electrolytes	107
5.1.1	Morphology, Porosity and Electrolyte Uptake of the Microporous Membranes	107
5.1.2	Ionic Conductivity Measurements	110
5.1.3	XRD Analysis	112
5.1.4	FTIR Analysis	113
5.2	PEO-P(VdF-HFP)-(PC+DEC)-LiClO <sub>4</sub> -dedoped PAni Nanofibers Composite Polymer Electrolytes	115
5.2.1	XRD Analysis	115
5.2.2	Ionic Conductivity Measurements	116
5.2.3	Morphological Studies	120
5.2.4	FTIR Analysis	121
5.2.5	Electrochemical Analysis	122
5.3	Summary	124
 <b>CHAPTER VI: [PMMA/ P(VDF-HFP)]-MMT BASED NANOCOMPOSITE</b>		
<b>GEL POLYMER ELECTROLYTES</b>		<b>126</b>
6.1	TEM Studies	128
6.2	XRD Analysis	129

6.3	Swelling Behavior of Nanocomposites	132
6.4	Ionic Conductivity Measurements	133
6.5	FTIR Analysis	138
6.6	Morphological Studies	139
6.7.	Electrochemical Analysis	140
6.8	Summary	143

**CHAPTER VII: SWIFT HEAVY ION IRRADIATION EFFECTS ON  
NANOFIBER REINFORCED AND LAYERED SILICATE  
NANOCOMPOSITE ELECTROLYTES**

		144
7.1	$O^{7+}$ Ion Irradiated P(VdF-HFP)-(PC+DEC)-LiClO <sub>4</sub> - 6 wt. % dedoped PANi Nanofibers System	146
	7.1.1 Ionic Conductivity Measurements	146
	7.1.2 XRD Analysis	150
	7.1.3 Dielectric Loss Spectra and DSC Analysis	152
	7.1.4 FTIR Analysis	153
	7.1.5 Morphological Studies	155
7.2	$O^{7+}$ Ion Irradiated PEO-20 wt. % MMT System	157
	7.2.1 XRD Analysis	157
	7.2.2 Ionic Conductivity Measurements	159
	7.2.3 Morphological Studies	161
	7.2.4 Complex Dielectric Function	162
	7.2.5 Electric Modulus Studies	164
	7.2.6 FTIR Analysis	166
7.3	Summary	167

**CHAPTER VIII: CONCLUSIONS AND FUTURE PROSPECTS**

8.1	Conclusions	169
8.2	Future Prospects	174
	<b>REFERENCES</b>	176
	<b>LIST OF PUBLICATIONS</b>	205

## List of tables

<b>Table</b>	<b>Captions</b>	<b>Page No.</b>
<b>Table 3.1</b>	Some physical properties of polymers used to synthesize polymer electrolytes.	68
<b>Table 3.2</b>	Some physical properties of organic plasticizers used to synthesize polymer electrolytes.	68
<b>Table 5.1</b>	Degree of crystallinity of PEO-P(VdF-HFP)-LiClO <sub>4</sub> -x% dedoped PANi nanofibers polymer electrolytes at different concentration of PANi nanofibers.	116
<b>Table 6.1</b>	<i>d</i> -spacing and microstrain ( $\epsilon$ ) value of different samples calculated from (001) reflection of MMT.	130
<b>Table 7.1</b>	Volume occupation ( $V_p$ ) of P(VdF-HFP)-(PC+DEC)-LiClO <sub>4</sub> -6 wt. % dedoped PANi nanofibers composite gel polymer electrolytes with different fluence.	149
<b>Table 7.2</b>	Comparison of the values of <i>d</i> -spacing, crystallite size ( $l_c$ ) and strain ( $\epsilon$ ) for (020) reflection of P(VdF-HFP) with ionic conductivity ( $\sigma$ ) at different fluence.	151

## List of figures

<b>Figure</b>	<b>Captions</b>	<b>Page No.</b>
<b>Figure 1.1</b>	Structure of Na-MMT.	19
<b>Figure 1.2</b>	Schematic illustration of different polymer-clay composites.	20
<b>Figure 1.3</b>	Cation motion in polymer electrolytes.	27
<b>Figure 2.1</b>	Experimental set-up for four probes method.	39
<b>Figure 2.2</b>	Equivalent circuit model of a typical electrolyte.	41
<b>Figure 2.3</b>	Equivalent circuit representation of an electrochemical cell.	42
<b>Figure 2.4</b>	Impedance plots of some simple RC circuits.	43
<b>Figure 2.5</b>	Schematic representation of (a) an electrochemical cell with blocking electrodes, (b) impedance plot. The equivalent circuit is shown in inset.	44
<b>Figure 2.6</b>	Schematic representation of impedance plots for the cells with non-blocking electrodes consisting of (a) single ion conducting electrolyte, and (b) both the cation and anion conducting electrolyte (e.g. liquid/polymer gel electrolyte). The equivalent circuits are shown in their corresponding insets.	45
<b>Figure 2.7</b>	(a) Equivalent circuit and impedance spectrum (bold line = spectrum for ideal equivalent circuit. Dotted line = Experimental impedance spectrum for gel electrolytes), (b) Depression of semicircle and tilting of spike caused by replacing capacitors by constant phase elements.	46
<b>Figure 2.8</b>	Schematic drawing of morphology of composite polymer–nonconductive filler electrolytes. Numbers are attributed to (1) highly conductive interface layers coating the surfaces of grains, (2) dispersed insulating grains, (3) matrix polymer ionic conductor.	57



<b>Figure 2.9</b>	Sketch of the polymer–clay system. Here, Ag. denotes the agglomerated (immiscible) state, and Int. denotes the intercalated state; $U_0$ is the plate separation in this state. $T$ is the external longitudinal force applied to the upper plate.	61
<b>Figure 2.10</b>	Sketch of the plate–plate interaction potential $V(U)$ .	61
<b>Figure 2.11</b>	Idealized clay-polymer membrane structure of intercalated PEO in the synthetic lithium hectorite (SHL). Circle dots are represented by the lithium ions, and the PEO chain is shown between the Li ions.	64
<b>Figure 2.12</b>	One-dimensional model of lithium clay-polymer membrane battery cell.	64
<b>Figure 3.1</b>	Chemical structure of different polymers used in the present work.	67
<b>Figure 3.2</b>	Chemical structure of plasticizers used in the present work.	68
<b>Figure 3.3</b>	Block diagram of solution casting technique for sample preparation.	70
<b>Figure 3.4</b>	Block diagram of solution intercalation technique of sample preparation.	71
<b>Figure 3.5</b>	Sample holder used in the present work.	73
<b>Figure 3.6</b>	Conductivity measurement set-up.	74
<b>Figure 3.7</b>	Rigaku Miniflex X-ray diffractometer installed at the Department of Physics, Tezpur University.	76
<b>Figure 3.8</b>	(a) Typical X-ray diffractogram of a semi-crystalline polymer and (b) XRD patterns showing the superposition of crystalline peaks and an amorphous hump.	77
<b>Figure 3.9</b>	Layout of a typical FTIR spectrometer.	81
<b>Figure 3.10</b>	(a) Transmission electron microscope (JEOL JEM 100 CXII) at SAIF, NEHU, Shillong and (b) Scanning electron microscope (JEOL JSM 6390 LV) installed at Tezpur University used for acquiring electron micrographs in the present work.	83

<b>Figure 3.11</b>	Schematic diagram showing the principle of acceleration of ions in a Pelletron.	86
<b>Figure 3.12</b>	Photographs of (a) the high vacuum irradiation chamber in the Materials Science (MS) beam line at IUAC and (b) sample loaded in the ladder used for irradiating the samples.	87
<b>Figure 4.1</b>	TEM image of dedoped PANi nanofibers.	91
<b>Figure 4.2</b>	Complex impedance spectra of (a) PMMA-(PC+DEC)-LiClO <sub>4</sub> -x% dedoped PANi nanofibers (x = 2, 4, 6 and 8 ) and (b) P(VdF-HFP)-(PC+DEC)-LiClO <sub>4</sub> -x% dedoped PANi nanofibers (x = 2, 4, 6, 8 and 10 ). Insets show the Nyquist plots for x=0.	92
<b>Figure 4.3</b>	Variation of ionic conductivity with nanofiber concentration (a) PMMA-(PC+DEC)-LiClO <sub>4</sub> -x% dedoped PANi nanofibers (x = 0, 2, 4, 6 and 8) and (b) P(VdF-HFP)-(PC+DEC)-LiClO <sub>4</sub> -x% dedoped PANi nanofibers (x = 0, 2, 4, 6, 8 and 10).	93
<b>Figure 4.4</b>	logσ vs. temperature inverse curves of (a) PMMA-(PC+DEC)-LiClO <sub>4</sub> -x% dedoped PANi nanofibers (x = 0, 2, 4, 6 and 8) and (b) P(VdF-HFP)-(PC+DEC)-LiClO <sub>4</sub> -x% dedoped PANi nanofibers (x = 0, 2, 4, 6, 8 and 10).	94
<b>Figure 4.5</b>	XRD patterns of (a) pure PMMA, (b) pure P(VdF-HFP) and (b) pure dedoped PANi nanofibers.	95
<b>Figure 4.6</b>	XRD patterns of (i) PMMA-(PC+DEC)-LiClO <sub>4</sub> -x% dedoped PANi nanofibers: (a) x=2, (b) x=4, (c) x=6 and (d) x=8 and (ii) P(VdF-HFP)-(PC+DEC)-LiClO <sub>4</sub> -x% dedoped PANi nanofibers: (a) x=2, (b) x=4, (c) x=6, (d) x=8 and (e) x=10.	96
<b>Figure 4.7</b>	SEM image of (a) pure PMMA, PMMA-(PC+DEC)-LiClO <sub>4</sub> -x% dedoped PANi nanofibers: (b) x=4, (c) x=8, (d) pure P(VdF-HFP) , P(VdF-HFP)-(PC+DEC)-LiClO <sub>4</sub> -x% dedoped PANi nanofibers: (e) x=6 and (f) x=10.	97

<b>Figure 4.8</b>	FTIR spectra of (a) pure PMMA and PMMA-(PC+DEC)-LiClO <sub>4</sub> -x% dedoped PANi nanofibers: (b) x=2, (c) x=4, (d) x=6 and (e) x= 8.	99
<b>Figure 4.9</b>	FTIR spectra of (a) pure P(VdF-HFP) and P(VdF-HFP)-(PC+DEC)-LiClO <sub>4</sub> -x% dedoped PANi nanofibers: (b) x=2, (c) x=4, (d) x=6, (e) x= 8 and (f) x=10.	100
<b>Figure 4.10</b>	Linear sweep voltammetry (LSV) of (a) PMMA-(PC+DEC)-LiClO <sub>4</sub> -x% dedoped PANi nanofibers (x = 0, 2 and 4) and (b) P(VdF-HFP)-(PC+DEC)-LiClO <sub>4</sub> -x% dedoped PANi nanofibers (x = 0, 2,4 and 6).	101
<b>Figure 4.11</b>	Interfacial stability of (a) PMMA-(PC+DEC)-LiClO <sub>4</sub> -x% dedoped PANi nanofibers (x = 0 and 4) and (b) P(VdF-HFP)-(PC+DEC)-LiClO <sub>4</sub> -x% dedoped PANi nanofibers (x = 0 and 6).	102
<b>Figure 4.12</b>	Schematic representation of electrode/polymer electrolyte interfacial passivation (a) without and (b) with dedoped PANi nanofibers.	102
<b>Figure 5.1</b>	Surface SEM micrographs of P(VdF-HFP)-x% PEO porous membranes: (a) x =10, (b) x =20, (c) x =30, (d) x =40, (e) x =50 and (f) x =60.	108
<b>Figure 5.2</b>	Porosity of P(VdF-HFP)-x% PEO microporous membranes as a function of PEO weight ratio.	109
<b>Figure 5.3</b>	Liquid electrolyte uptake of P(VdF-HFP)-x% PEO microporous membranes as a function of PEO weight ratio.	109
<b>Figure 5.4</b>	Room temperature impedance plots of P(VdF-HFP)-x% PEO microporous membranes: (a) x =10, (b) x=20, (c) x =30, (d) x =40, (e) x =50 and (f) x =60.	110
<b>Figure 5.5</b>	Ionic conductivity of P(VdF-HFP)-x% PEO microporous membranes as a function of PEO weight ratio.	112
<b>Figure 5.6</b>	Temperature dependence of ionic conductivity of P(VdF-HFP)-x% PEO Microporous polymer electrolytes: (a) x =10, (b) x =20, (c) x =30, (d) x =40, (e) x =50 and (f) x =60.	112

<b>Figure 5.7</b>	XRD patterns of (a) PEO and (b) P(VdF-HFP).	113
<b>Figure 5.8</b>	XRD patterns of P(VdF-HFP)- $x\%$ PEO microporous membranes: (a) $x = 10$ , (b) $x = 20$ , (c) $x = 30$ , (d) $x = 40$ , (e) $x = 50$ and (f) $x = 60$ .	113
<b>Figure 5.9</b>	FTIR spectra of (a) LiClO <sub>4</sub> , (b) Pure PEO, (c) Pure P(VdF-HFP), (d) P(VdF-HFP)-30 wt. % PEO and (e) P(VdF-HFP)-50 wt. % PEO.	114
<b>Figure 5.10</b>	XRD patterns of (a) PEO, (b) P(VdF-HFP) and (c) dedoped PANi nanofibers.	115
<b>Figure 5.11</b>	XRD patterns of PEO-P(VdF-HFP)-LiClO <sub>4</sub> - $x\%$ dedoped PANi nanofibers: (a) $x = 0$ , (b) $x = 2$ , (c) $x = 4$ , (d) $x = 6$ , (e) $x = 8$ and (f) $x = 10$ .	115
<b>Figure 5.12</b>	Complex impedance spectra of PEO-P(VdF-HFP)-LiClO <sub>4</sub> - $x\%$ dedoped PANi nanofibers: (a) $x = 0$ (b) $x = 2$ , (c) $x = 4$ , (d) $x = 6$ , (e) $x = 8$ and (f) $x = 10$ .	118
<b>Figure 5.13</b>	Variation of ionic conductivity with different weight fraction of dedoped PANi nanofibers.	118
<b>Figure 5.14</b>	$\log \sigma$ vs. temperature inverse curve PEO-P(VdF-HFP)-LiClO <sub>4</sub> - $x\%$ dedoped PANi nanofibers: (a) $x = 0$ , (b) $x = 2$ , (c) $x = 4$ , (d) $x = 6$ , (e) $x = 8$ and (f) $x = 10$ .	119
<b>Figure 5.15</b>	SEM micrographs of PEO-P(VdF-HFP)-LiClO <sub>4</sub> - $x\%$ dedoped PANi nanofibers: (a) $x = 0$ , (b) $x = 2$ , (c) $x = 4$ , (d) $x = 6$ , (e) $x = 8$ and (f) $x = 10$ .	120
<b>Figure 5.16</b>	FTIR spectra of (a) LiClO <sub>4</sub> , (b) dedoped PANi nanofibers: (c) P(VdF-HFP), (d) PEO and PEO-P(VdF-HFP)-LiClO <sub>4</sub> - $x\%$ dedoped PANi nanofibers (e) $x = 2$ , (f) $x = 6$ and (g) $x = 8$ .	122
<b>Figure 5.17</b>	Linear sweep voltammetry plots of (a) PEO-LiClO <sub>4</sub> , (b) PEO-P(VdF-HFP)-LiClO <sub>4</sub> and (c) PEO-P(VdF-HFP)-LiClO <sub>4</sub> -6 wt. % dedoped PANi nanofibers.	123

<b>Figure 5.18</b>	Interfacial stability of (a) PEO-LiClO <sub>4</sub> , (b) PEO-P(VdF-HFP)-LiClO <sub>4</sub> and (c) PEO-P(VdF-HFP)-LiClO <sub>4</sub> -6 wt. % dedoped PA <sub>n</sub> i nanofibers.	123
<b>Figure 6.1</b>	TEM image of (a) PMMA1, (b) PVdF1 and (c) PVdF4.	128
<b>Figure 6.2</b>	XRD patterns in the range $2\theta = 2-10^0$ of (i) :(a) pure MMT, (b) pure PMMA, (c) PMMA1, (d) PMMA2.5 and (e) and PMMA5 and (ii): (a) pure MMT, (b) pure PVdF, (c) PVdF2.5 and (d) PVdF4.	130
<b>Figure 6.3</b>	XRD patterns (a) pure organophilic MMT, (b) pure PVdF, (c) PVdF1, (d) PVdF2.5 and (e) PVdF4. Inset shows reflection of (001) in the range $2\theta = 2-10^0$ .	131
<b>Figure 6.4</b>	Molecular conformation of PVdF (a) TGTG' and (b) TT where the white cyanine balls denote the hydrogen and fluoride atoms and the gray balls represent carbon atoms.	132
<b>Figure 6.5</b>	Swelling behavior of (a) PMMA-clay nanocomposites and (b) PVdF-clay nanocomposites at different clay loading.	133
<b>Figure 6.6</b>	Nyquist plots of (a) gel PMMA and PMMA/MMT nanocomposite gel polymer electrolytes at different clay loading and (b) PVdF and PVdF/MMT nanocomposite gel polymer electrolytes at different clay loading.	134
<b>Figure 6.7</b>	Lithium ion (red balls) motion inside the gallery of MMT in $\beta$ phase of PVdF.	136
<b>Figure 6.8</b>	Temperature dependence of ionic conductivity of (a) gel PMMA and PMMA/MMT nanocomposite gel polymer electrolytes at different clay loading and (b) gel PVdF and PVdF/MMT nanocomposite gel polymer electrolytes at different clay loading.	137

<b>Figure 6.9</b>	FTIR spectra of (i) (a) pure PMMA, (b) gel PMMA, (c) gel PMMA1, (d) gel PMMA2.5 and (e) gel PMMA5 and (ii) (a) pure PVdF, (b) gel PVdF, (c) gel PVdF1, (d) gel PVdF2.5 and (e) gel PVdF4.	139
<b>Figure 6.10</b>	SEM images of (a) pure PMMA, (b) gel PMMA5, (c) pure PVdF and (d) gel PVdF4.	140
<b>Figure 6.11</b>	Linear sweep voltammetry plots of (a) gel PMMA and PMMA/MMT nanocomposite gel polymer electrolytes at different clay loading (b) gel PVdF and PVdF/MMT nanocomposite gel polymer electrolytes at different clay loading.	141
<b>Figure 6.12</b>	Interfacial stability of (a) gel PMMA and PMMA/MMT nanocomposite gel polymer electrolyte with 5 wt. % clay loading and (b) gel PMMA and PMMA/MMT nanocomposite gel polymer electrolyte with 5 wt. % clay loading.	142
<b>Figure 7.1</b>	Nyquist plots of P(VdF-HFP)-(PC+DEC)-LiClO <sub>4</sub> -6 wt. % dedoped PANi nanofibers irradiated with fluence (a) 0, (b) $5 \times 10^{10}$ , (c) $10^{11}$ , (d) $5 \times 10^{11}$ and (e) $10^{12}$ ions/cm <sup>2</sup> .	147
<b>Figure 7.2</b>	Variation of ionic conductivity of P(VdF-HFP)-(PC+DEC)-LiClO <sub>4</sub> -6 wt. % dedoped PANi nanofibers with different fluence.	147
<b>Figure 7.3</b>	Temperature dependence of ionic conductivity of P(VdF-HFP)-(PC+DEC)-LiClO <sub>4</sub> -6 wt. % dedoped PANi nanofibers irradiated with fluence (a) 0, (b) $5 \times 10^{10}$ , (c) $10^{11}$ , (d) $5 \times 10^{11}$ and (e) $10^{12}$ ions/cm <sup>2</sup> .	148
<b>Figure 7.4</b>	XRD patterns of P(VdF-HFP)-(PC+DEC)-LiClO <sub>4</sub> -6 wt. % dedoped PANi nanofibers irradiated with fluence (a) 0, (b) $5 \times 10^{10}$ , (c) $10^{11}$ , (d) $5 \times 10^{11}$ and (e) $10^{12}$ ions/cm <sup>2</sup> .	151

<b>Figure 7.5</b>	Dielectric loss spectra of P(VdF-HFP)-(PC+DEC)-LiClO <sub>4</sub> -6 wt. % dedoped PANi nanofibers irradiated with fluence (a) 0, (b) $5 \times 10^{10}$ , (c) $10^{11}$ , (d) $5 \times 10^{11}$ and (e) $10^{12}$ ions/cm <sup>2</sup> .	153
<b>Figure 7.6</b>	DSC thermograms of (a) pure P(VdF-HFP), (b) pure dedoped PANi nanofibers and P(VdF-HFP)-(PC+DEC)-LiClO <sub>4</sub> -6 wt % PANi nanofibers irradiated with fluence (c) 0, (d) $10^{11}$ and (e) $10^{12}$ ions/cm <sup>2</sup> .	153
<b>Figure 7.7</b>	FTIR spectra of (a) pure PANi nanofibers, (b) pure P(VdF-HFP) and P(VdF-HFP)-(PC+DEC)-LiClO <sub>4</sub> -6 wt. % dedoped PANi nanofibers irradiated with fluence (c) 0, (d) $10^{11}$ and (e) $10^{12}$ ions/cm <sup>2</sup> .	155
<b>Figure 7.8</b>	SEM micrographs of (a) pure P(VdF-HFP) and P(VdF-HFP)-(PC+DEC)-LiClO <sub>4</sub> -6 wt. % dedoped PANi nanofibers irradiated with fluence (b) 0, (c) $10^{11}$ and (d) $10^{12}$ ions/cm <sup>2</sup> .	156
<b>Figure 7.9</b>	XRD patterns of (a) pure MMT, (b) pure PEO and PEO-20 wt. % MMT composite irradiated with fluence (c) 0, (d) $5 \times 10^{10}$ (e) $10^{11}$ , (f) $5 \times 10^{11}$ , (g) $10^{12}$ and (h) $5 \times 10^{12}$ ions/cm <sup>2</sup> .	158
<b>Figure 7.10</b>	Impedance spectra of PEO-20 wt. % MMT nanocomposites irradiated at different fluence.	160
<b>Figure 7.11</b>	Variation of ionic conductivity as a function of ion fluence.	160
<b>Figure 7.12</b>	Temperature dependent ionic conductivity of PEO-20 wt. % MMT at different fluence.	161
<b>Figure 7.13</b>	SEM image of PEO- 20 wt.% MMT nanocomposites irradiated with fluence (a) 0, (b) $5 \times 10^{10}$ , (c) $5 \times 10^{11}$ and (d) $5 \times 10^{12}$ ions/cm <sup>2</sup> .	162
<b>Figure 7.14</b>	Real (a) and imaginary (b) part of complex permittivity of PEO-20 wt. % MMT at different irradiation fluence.	163
<b>Figure 7.15</b>	Tangent loss as a function of frequency for PEO-20 wt. % MMT at different irradiation fluence.	164
<b>Figure 7.16</b>	Real (a) and imaginary (b) part of electrical modulus of PEO-20 wt. % MMT irradiated with different ion fluence.	165

**Figure 7.17** FTIR spectra of (a) pure MMT, (b) pure PEO and PEO-20 wt.% MMT films irradiated with fluence (c) 0, (d)  $1 \times 10^{11}$  and (e)  $5 \times 10^{12}$  ions/cm<sup>2</sup>.

167



## **List of abbreviations**

<b>Abbreviation</b>	<b>Meanings</b>
AC	Alternating Current
AFM	Atomic force microscopy
Al <sub>2</sub> O <sub>3</sub>	Aluminium oxide
BaTiO <sub>3</sub>	Barium titanate
CeO <sub>2</sub>	Cerium oxide
cm	Centimeter
CPE	Composite Polymer Electrolyte
D.C.	Direct current
DBP	Dibutyl phthalate
DEC	Diethyl carbonate
DIEPIG	Diepoxy polyethylene glycol
DMC	Dimethyl carbonate
DME	Dimethoxyethane
DME	Dimethoxyethane
DSC	Differential scanning calorimetry
EC	Ethylene carbonate
FTIR	Fourier transform infrared Spectroscopy
FWHM	Full width at half maxima
GPE	Gel polymer electrolyte
HCl	Hydrochloric acid
LiAlO <sub>2</sub>	Lithium aluminate
LiAsF <sub>6</sub>	Lithium hexafluoro arsenide
LiCF <sub>3</sub> SO <sub>3</sub>	Lithium trifluoromethane sulfonate
LiClO <sub>4</sub>	Lithium perchlorate
LiN(CF <sub>3</sub> SO <sub>2</sub> ) <sub>2</sub>	Lithium bis(trifluoromethanesulfonimide)
LiNBO <sub>3</sub>	Lithium Niobate
LiPF <sub>6</sub>	Lithium hexafluorophosphate
MMT	Montmorillonite

NaClO <sub>4</sub>	Sodium perchlorate
NaOH	Sodium hydroxide
NaSCN	Sodium thiocyanate
NCPE	Nanocomposite polymer electrolyte
NH <sub>4</sub> SCN	Ammonium thiocyanate
NMR	Nuclear magnetic resonance
P(VdF-HFP)	poly(vinylidene fluoride-hexafluoropropylene)
PAN	Poly(acrylonitrile)
PAni	Polyaniline
PbTiO <sub>2</sub>	Lead titanate
PC	Propylene Carbonate
PEG	Poly(ethylene glycol)
PEO	Poly(ethylene oxide)
PMMA	Poly(methyl methacrylate)
POEM	poly(oxyethylene) methacrylate]
PPO	Poly(propylene oxide)
PVA	Poly(vynile alcohol)
PVB	Polyvinyl butyral
PVC	Poly(vynile chloride)
PVdF	Poly(vinylidene fluoride)
SAP	Silca aerogel powder
SAXS	Small-angle X-ray scattering
SEM	Scanning electron microscopy
SHI	Swift heavy ion
SiO <sub>2</sub>	Silicon dioxide
SPE	Solid polymer electrolyte
SS	Stainless Steel
TCNQ	Tetracyanoquinodimethane
TEM	Transmission electron microscopy
TEP	Tryethyl phosphate

TiO <sub>2</sub>	Titanium dioxide
TMP	Trimethyl phosphate
VTF	Vogel-Tamman-Fulcher
WLF	William-Landel-Ferry
XRD	X-ray diffraction
ZrO <sub>2</sub>	Zirconium dioxide
CCl <sub>4</sub>	Carbon tetrachloride

# CHAPTER I

## Introduction

---

---

*This chapter describes the definitions of various types of polymer electrolytes viz. solid polymer electrolytes (SPEs), gel polymer electrolytes (GPEs) and composite polymer electrolytes (CPEs and their historical developments. A brief description of ion conduction mechanisms and models is also included in this chapter. Different aspects of swift heavy ion (SHI) irradiation and energy loss processes due the passage of energetic ions through matters are also discussed here. At the end definition of the problem and scope of the present work is spelt out.*

---

---

Since the discovery of ionic conduction in nonmetallic solids  $\text{Ag}_2\text{S}$  and  $\text{PbF}_2$  by Faraday in 1930 [1], lot of efforts have been devoted by the researchers worldwide to develop newer ion conducting materials for electrochemical devices such as high energy density batteries, supercapacitors, electrochromic windows, sensors etc. Till now several of ion conducting materials like ionic salts, glasses, ceramics etc. have been tried for electrochemical device applications. But in the world leading towards miniaturization, the polymeric ionic conductors called 'polymer electrolytes' are receiving major attention [2-4]. The main reason for using polymeric electrolytes over other liquid and solid electrolytes lies in the free standing consistency, which allows easy handling and cell design, modularity and reliability combined with flexibility and conformability to the electrodes. Ionically conducting phases, free from low molecular weight solvents, based on the dissolution of salts in suitable ion-coordinating polymers are key components in new types of batteries for portable electronic devices and electric cars. Batteries for such applications require polymer electrolytes meeting the following requirements

- (i) A high ionic conductivity,
- (ii) High cationic transport number and
- (iii) Improved chemical, thermal and electrochemical stability.

The need for high ionic conductivity arises from the fact that at what rate or how fast energy from a battery can be drained, which mainly depends on the extent of ionic mobility, hence ionic conductivity of the electrolyte. Requirement of high cationic transport number rather than anionic is also important in view of the battery performance because

concentration gradients caused by the mobility of both cations and anions in the electrolyte arise during discharging, which may result in premature battery failure. For battery applications, along with high ionic conductivity the electrolyte material must be dimensionally stable since the polymer electrolyte will also function as separator in the battery, which will provide electrical insulation between the cathode and the anode. This implies that it must be possible to process polymer electrolyte into free-standing film with adequate mechanical strength. Since the electrolyte membrane is inserted between the cathode and the anode, in order to avoid undesired chemical reactions proceeding at the electrode/electrolyte interfaces, the polymer electrolytes should possess a high chemical stability. In addition, polymer electrolytes must have an electrochemical stability domain ranging from 0 V to as high as 4-5 V [5].

The first ion conducting polymer: poly(ethylene oxide) (PEO) complexed/dissolved with alkali metal salt, was discovered by P.V. Wright et al. [6] in 1973. The initial realization that these materials could be used as electrolytes in battery applications was, however, proposed by Armand [7, 8]. After that, a large number of polymer electrolyte materials involving different kinds of transporting ions, namely,  $H^+$ ,  $Li^+$ ,  $Na^+$ ,  $K^+$ ,  $Ag^+$ ,  $Mg^{2+}$  etc., have been reported since then. Various theoretical approaches have been adopted to understand the ion transport mechanism in the polymer electrolyte materials as well as the physical/chemical processes occurring at the polymer electrolyte/electrode interfaces [9-14]. A number of books/monographs/research papers have been published, which deal with materials designing aspects as well as a variety of techniques usually employed during material/structure/thermal/ion transport characterization studies in the polymer electrolyte systems [9-12].

### **1.1 Types of Polymer Electrolytes and Their Historical Developments**

The development of polymer electrolytes has gone through three stages: 'dry solid polymer electrolytes', 'gel polymer electrolytes' and 'composite polymer electrolytes'. The 'dry systems' use the polymer host as the solid solvent along with lithium salts and do not include any organic liquids. The very first example of "dry solid" polymer electrolyte is the poly(ethylene oxide) (PEO) based systems that showed very low conductivities on the order of  $10^{-8} \text{ S cm}^{-1}$  at ambient temperature [6, 8]. The second category of polymer electrolyte is

called “gel polymer electrolyte” or “plasticized polymer electrolyte” which is neither liquid nor solid or conversely both liquid and solid [5]. Gels possess cohesive properties of solids and the diffusive property of liquids, which makes the gel finding various important applications including polymer electrolytes. On the other hand ‘composite polymer electrolytes’ include high surface area inorganic solids in proportion with a ‘dry solid polymer’ or ‘polymer gel’ system. Generally, high surface area particulate fillers such as  $ZrO_2$ ,  $TiO_2$ ,  $Al_2O_3$  and hydrophobic fumed silica were incorporated in to the polymer matrices and are called “composite polymer electrolytes” [15, 16]. The advantages of composite polymer electrolytes lay in the fact that addition of inorganic filler particles in to the polymer matrix not only increases the ionic conductivity but also improves the mechanical as well as electrode-electrolyte interface stability [17]. A detailed discussion on the above three types of polymer electrolytes and their materials designing is given below.

### ***1.1.1 Solid Polymer Electrolytes (SPEs)***

As already pointed out, after the discovery of the first SPE material: a poly(ethylene oxide) (PEO): alkali metal salt complex, in 1973, followed by an experimental demonstration of the first all-solid-state battery based on the PEO:  $Li^+$ -ion polymer electrolyte in 1979, the activity in this area was enhanced tremendously. The majority of good dry solid polymeric electrolytes reported so far are based on high molecular weight polymers, namely, poly(ethylene oxide) (PEO) and/or poly (propylene oxide) (PPO) complexed/dissolved with different  $Li^+$ -ion salts. The reason for the preference of PEO/PPO as the polymer host has been mainly due to the fact that they usually form stable dry complexes exhibiting a relatively higher ionic conductivity than other solvating polymers. The sequential oxyethylene group:  $-CH_2-CH_2-O-$ , and the polar groups:  $-O-$ ,  $-H-$ ,  $-C-H-$ , in the polymer chains have the ability to dissolve/complex the ionic salts. At Sheffield, in late 1970’s, Wright and his coworkers [18, 19] embarked upon an investigation of morphology of polymer complexes and its relation with ionic conductivity. They found that fully saturated crystalline region of PEO complexes gave poor conductivity and amorphous region gave higher conductivity. At about the same time Killis, Le Nest and Cheradame [20] had independently reached similar conclusions regarding the amorphous PEO by preparing with urethane based PEO networks.

With the confirmation that ionic conductivity in polymer electrolytes is a property of amorphous elastomeric phases [21], number of strategies was employed to suppress the crystallinity of poly(ethoxy) systems in 1980. The branched or comb polyphosphazenes developed by Shriver, Allcock and coworkers at Pennsylvania [22] and Ward's group at Leeds [23] and methoxy copolymer developed by Booth's group at Manchester [24] were among the most successful of these. At about the same time various theories and mechanisms of ion transport in these materials were also developed, which include the dynamic percolation model [25]. Angell at Arizona State University [26] and Torrel at Chalmers [27] discussed the relation between conductivity and relaxation times. The correlation between ionic conductivity, glass transition temperature and the mechanical relaxation was investigated by Cheradame [28] and Watanabe [29].

After the realization that ionic conductivity in dry polymer electrolytes could be increased by (i) suppressing the crystalline part of the host polymer to enhance polymer chain mobility hence the fast cation movement and (ii) increasing the number of charge carriers, much research efforts have been directed to find the optimal combination of host polymer and dopant salt for faster ionic transport. To suppress the crystallization of polymer to enhance polymer chain mobility various efforts have been made, which include cross-linking, co-polymerization, comb formation (side chain and dendritic polymers), polymer alloy (including interpenetrating network) and inorganic filler blend [30]. Killis et al. [31] in combination with cross-linking and co-polymerization were able to achieve ionic conductivity of about  $5 \times 10^{-5} \text{ Scm}^{-1}$  at 25 °C by cross-linking co-polymers of EO and PO. In the comb formation, Hall et al. [32] added PEO side chain to polysiloxane chains and obtained an ionic conductivity value of  $2 \times 10^{-4} \text{ Scm}^{-1}$  at 25 °C. Watanabe et al. [33] extended this method by synthesizing a dendritic polymer by attaching PEO chains to glycidyl ether acid chains.

Increase of charge carriers can be realized by use of highly dissociable salts or by increasing salt concentration etc. Nature of salt, i.e. size of cation and anion, salt's lattice energy, organic/inorganic salt etc., plays very important role in polymer electrolyte's behavior determination. It has been found that larger anion results in amorphous matrix and provides path for cation movement, hence a large ionic conductivity. Vallee et al. [34] obtained ionic conductivity value of  $4 \times 10^{-5} \text{ Scm}^{-1}$  at 25 °C by dissolving lithium

trifluorosulfonyl imide in PEO, which is over two-order magnitude higher than that of NaI-PEO system. Benrabah et al. [35] obtained conductivity value of  $6 \times 10^{-7} \text{ Scm}^{-1}$  at 25 °C with sulfonate system and Fujinami et al. [36] achieved conductivity value of  $2 \times 10^{-5} \text{ Scm}^{-1}$  at 25 °C with siloxy aluminate system. A new type of ‘polymer-in-salt’ material was proposed by Angell et al. [37], where lithium salts are mixed with small proportions of polymer PPO and PEO and found ionic conductivity value in the order of  $10^{-3} \text{ Scm}^{-1}$ .

### ***1.1.2 Gel Polymer Electrolytes (GPEs)***

Gel electrolytes are currently of another great interest, particularly with regard to achieving higher ionic conductivities. Gel polymer electrolytes are formed by incorporation of substantial amount of plasticizers such as ethylene carbonate (EC), propylene carbonate (PC), diethyl carbonate (DEC) etc. to the polymer matrix. The ion conduction in these electrolytes takes place through the liquid electrolytes where the host polymer mostly provides the structural support. In case of SPEs incorporation of plasticizer results in greater ion dissociation, which allows greater number of charge carriers for ion transport in addition to reducing the crystalline content and increasing the polymer segmental mobility [5].

The increase of ionic conductivity due to the addition of low molecular weight plasticizer in SPEs was first observed by Ito et al. [38]. They were able to increase the ionic conductivity of PEO-LiCF<sub>3</sub>SO<sub>3</sub> plasticized with PEG up to  $10^{-3} \text{ Scm}^{-1}$  at 25 °C. The increase of ionic conductivity at room temperature was attributed to the increase in amorphous region of PEO. On the contrary, the increase in ionic conductivity is adversely accompanied by poor interfacial properties due to the presence of hydroxyl end-groups [38]. In order to avoid this problem few researchers have eliminated hydroxyl end groups of PEG by methoxy one [39]. Nagasubramaniam and Stefano [40] used crown ether as plasticizer and were able to obtain ionic conductivity value of  $7 \times 10^{-4} \text{ Scm}^{-1}$  for the PEO-LiBF<sub>4</sub> system. Shodai et al. [41] studied the thermal stability of PEO-LiCF<sub>3</sub>SO<sub>3</sub> plasticized with ethylene carbonate (EC) and propylene (PC) in air as well as argon atmosphere. They found that oxygen in the air lowers the decomposition temperature of PEO and accelerates its decomposition rate. Benedict et al. [42] explored the possibility of using dibutyl phthalate (DBP) as plasticizer in PEO-LiAsF<sub>6</sub> complexes. The activation energy of the system was considerably reduced upon the addition of 0.09 mol of DBP in the system. A series of plasticized polymer electrolytes were



synthesized based on polyethylene oxide (PEO),  $\text{LiN}(\text{CF}_3\text{SO}_2)_2$  (LiTFSI) as the salt and tetraethylene glycol dimethyl ether (tetraglyme) and (EC + PC) as plasticizers. The showed that the complex of PDMAEMA/PEO/LiTFSI/tetraglyme exhibits conductivity value of  $4.74 \times 10^{-4} \text{ Scm}^{-1}$  at 25 °C, which is higher than the PDMAEMA/PEO/LiTFSI/EC + PC system. Kovac et al. [43] carried out microstructural and electrochemical characterization of  $(\text{PEO})_n\text{LiAl}(\text{SO}_3\text{Cl})_4$  ( $n = 2-12$ ) polymer electrolytes containing a mixture of plasticizers, i.e. propylene carbonate (PC) and 1, 2-dimethoxyethane (DME). Using X-ray powder diffractometer analysis, size exclusion chromatography, Raman and FTIR spectroscopy, it was shown that a substantial amount of PC and DME plasticizers remain incorporated in final dry polymer electrolyte and reduces the crystallinity of PEO by more than 50%. The PEO/PC/DME polymer electrolyte exhibited better ionic conductivity at lower temperatures (20-60 °C), while at higher temperatures ( $T > 60$  °C) the polymer without plasticizer showed better conductivity. With respect to salt concentration the conductivity exhibited a maximum value at  $n = 3$ . Itoh et al. [44] prepared two kinds of PEO based comblike polymer electrolytes with poly-4 of 3,5-bis[poly(ethylene glycol) methyl ether (350,  $n = 7.2$ )] styrene and poly-4/TCNQ of 7,7,8,8-tetracyanoquinodimethane (TCNQ) as plasticizer and  $\text{LiN}(\text{CF}_3\text{SO}_2)_2$  as salt and investigated their ionic conductivity, electrochemical, thermal, and mechanical properties. They showed that the polymer electrolytes containing an alternating copolymer poly-4/TCNQ exhibited higher ionic conductivity, better thermal and mechanical stabilities than that of containing a homopolymer poly-4, due to the presence of an aromatic ring and a polar cyano group of the TCNQ unit. Hariharan and Bhide [45] successfully synthesized PEO- $\text{NaPO}_3$  plasticized with PEG<sub>400</sub> by solution casting technique. A combination of X-ray diffraction (XRD), optical microscopy and differential scanning calorimetry (DSC) studies indicated enhancement in the amorphous phase of polymer due to the addition of plasticizer. An enhancement in the cationic transport number was observed from a value of 0.23 for the host polymer electrolyte to the values in the range 0.39–0.42 for the plasticized electrolytes with different concentration of PEG<sub>400</sub>. A gel electrolyte consisting of poly(ethylene oxide) crosslinked with poly(propylene oxide) as a host, propylene carbonate (PC) as a plasticizer, and  $\text{LiClO}_4$  as an electrolytic salt was synthesized by Tien et al. [46] for double layer capacitors. Diglycidyl ether of bisphenol-A was blended with the polymer precursors to enhance the mechanical properties and increase the internal

free volume. This gel electrolyte showed an ionic conductivity as high as  $2 \times 10^{-3} \text{ S cm}^{-1}$  at  $25 \text{ }^\circ\text{C}$  and was electrochemically stable over a wide potential range of  $\sim 5\text{V}$ . PVB/LiClO<sub>4</sub> polymer electrolyte films with PEG<sub>200</sub>, PEG<sub>400</sub> and PEG<sub>600</sub> as plasticizers were prepared by solution-casting method by Li et al. [47]. The bulk conductivity of the electrolyte films increased from  $10^{-10}$  to  $10^{-6} \text{ Scm}^{-1}$  with the addition of plasticizers. PEG<sub>400</sub> exhibited plasticizing function superior to PEG<sub>200</sub> and PEG<sub>600</sub>, and the conductivity of the SPEs could reach  $10^{-6} \text{ Scm}^{-1}$  at room temperature by controlling the ratio of  $[\text{O}]:[\text{Li}^+] = 8$  and adding 30 wt.% PEG<sub>400</sub> with PVB.

Among the gel polymer electrolytes reported till date, poly(acrylonitrile) (PAN)-based gel electrolytes have been extensively studied. In 1981 Watanabe et al. [48, 49] reported the use of plasticizer EC and PC in PAN-LiClO<sub>4</sub> complex. By increasing the plasticizer/LiClO<sub>4</sub> ratio they were able to increase the ionic conductivity up to  $10^{-4}$  to  $10^{-5} \text{ Scm}^{-1}$  at  $25 \text{ }^\circ\text{C}$ . Since the conductivity did not correlate well with PAN content they concluded that PAN host did not play any role in the ion transport mechanism but acted as a matrix for structural stability. Later Abraham and Alamgir [50, 51] found conductivity value of  $1.7 \times 10^{-3} \text{ Scm}^{-1}$  at  $20 \text{ }^\circ\text{C}$  and  $1.1 \times 10^{-5} \text{ Scm}^{-1}$  at  $-10 \text{ }^\circ\text{C}$  for PAN based electrolytes comprising 38 m/o EC, 33 m/o PC with 8 m/o LiClO<sub>4</sub> and 21 m/o of PAN. Peraninage et al. [52] reported that low temperature ionic conductivity of PAN based electrolytes could be greatly enhanced using ternary solvent mixtures consisting of EC, PC and 3-methyl-2-oxazolodionon (MEOX). The electrochemical stability of PAN based electrolytes using LiN(CF<sub>3</sub>SO<sub>2</sub>)<sub>2</sub>, LiAsF<sub>6</sub>, LiCF<sub>3</sub>SO<sub>3</sub> and LiPF<sub>6</sub> salts and plasticizer EC and PC was studied by Choe et al. [53]. They observed oxidation stability window more than 5 V vs Li<sup>+</sup>/Li as revealed by cyclic voltammetry studies. A comparative infrared spectroscopic study for PAN-PC-lithium triflate system was reported by Starkey and Frech [54]. They observed that lithium triflate was highly associated and the lithium ion interaction was stronger with PC than with PAN. According to Appetecchi et al. [55] a fully amorphous gel of PAN-LiClO<sub>4</sub> (1:02) in EC exhibits ion transference numbers more than 0.5 because of the absence of oxygen atoms in the PAN matrix. The transference number enhances to 0.7 by using salts like LiTFSI and LiTFSM. A typical polymer electrolyte comprising of PAN (12%), EC (40%), PC (40%) and LiClO<sub>4</sub> (8%) was prepared by Sun and Jin [56]. The conductivity of the polymer electrolyte was found as high as  $2 \times 10^{-3} \text{ Scm}^{-1}$  at room temperature. A PAN

based gel electrolyte was prepared by incorporating a mixture of  $\text{Pr}_4\text{N}^+\text{I}^-$ , iodine, EC and PC in PAN by Dissanayake et al. [57]. They found a maximum ionic conductivity of  $2.95 \times 10^{-3} \text{ Scm}^{-1}$  at room temperature for the sample with composition PAN (13%): EC (31%): PC (45%):  $\text{Pr}_4\text{N}^+\text{I}^-$  (7%):  $\text{I}_2$  (4%) (by weight). The same group by analyzing the DSC results on PAN/EC/PC/LiTFSI system showed that EC/PC existed in two different environments within the gel network: free EC/PC molecules and EC/PC molecules subjected to pairing interactions by the CN group in PAN. The highest conductivity of the gel electrolyte is obtained for the composition, PAN(15.4%)/EC(41.0%)/PC(41.0%)/LiTFSI(2.6%) (by weight) [58]. Carol et al. [59] used electrospinning technique to prepare fibrous membrane of PAN having a high molecular weight of  $4 \times 10^5$ . The membrane with good mechanical strength and porosity exhibited high uptake when activated with the liquid electrolyte of 1 M  $\text{LiPF}_6$  in a mixture of organic solvents and the gel polymer electrolyte showed ionic conductivity of  $1.7 \times 10^{-5} \text{ Scm}^{-1}$  at 20 °C. The gelled membrane also exhibited stable charge-discharge characteristics when evaluated as a separator in Li-ion cells. Despite the several advantages of PAN-based electrolytes, like high ionic conductivity of the order of  $10^{-3} \text{ Scm}^{-1}$  at 20 °C, good electrochemical stability of 4.5 V and a lithium-transfer number around 0.6, its poor compatibility with lithium metal anode offsets from practical applications. Other studies clearly reveal that the lithium electrode undergoes serious passivation when in contact with PAN-based electrodes and affects cyclability and eventually leads to safety hazards [5].

In 1985, Iijima and Toyoguchi [60] found that poly(methyl methacrylate) (PMMA) could be used as gelating agent. After that the material has attracted a lot of interest as gel polymer electrolytes. The research performed by Bohnke's group [61, 62] showed that atactic PMMA formed ionically conductive gels with  $\text{LiClO}_4$  in propylene carbonate (PC), or mixtures of PC and ethylene carbonate (EC). The addition of PMMA in various proportions to  $\text{LiClO}_4$ -PC electrolyte considerably increased the viscosity to reach a solid rubber-like material. On the other hand, the conductivities at room temperature of these gels decreased very slightly and remained very close to that of the liquid electrolyte. At about 20 wt. % polymer concentrations, these gels possessed room temperature conductivities on the order of  $10^{-3} \text{ Scm}^{-1}$ . This high ion mobility could be explained by the existence of a continuous conduction path available through the solvent. Different characterization techniques showed that PMMA just acted as a matrix and no lithium solvation with PMMA was found.

Stallworth et al. [63] synthesized gel electrolytes based on PMMA with various lithium salts ( $\text{LiClO}_4$ ,  $\text{LiAsF}_6$ ,  $\text{LiN}(\text{CF}_3\text{SO}_2)_2$ ) using plasticizers PC and EC and characterized them by DSC and NMR. They concluded that the gel electrolytes exhibited single glass transition temperature and by dramatic changes in NMR line width, which occurred in the vicinity of glass transition. Vondrak et al. [64] prepared PMMA gel electrolytes with propylene carbonate as plasticizer and complexed with salts of various perchlorates of different cation sizes including lithium. The gel electrolyte, which possesses lithium as cation exhibited maximum conductivity and was attributed to smaller ionic radii. Though PMMA based gel electrolytes exhibit high ionic conductivity, they show poor mechanical property at high plasticizer content [17]. Rajendran et al. [65, 66] reported the improvement in the mechanical property of PMMA by blending with poly(vinyl alcohol) (PVA). However, a decrease in ionic conductivity was observed at higher PVA content due to increased viscosity. The increase in viscosity at higher PVA content was ascribed to the polymer-solution interaction, which decreased the ionic mobility resulting in decreased ionic conductivity [66]. Kim and Oh [67] modified (PMMA)-based polymer gel electrolytes with interpenetrating networks of poly(ethylene glycol dimethacrylate) (PEGDMA) polymers with different numbers of repeating ethylene oxide units. The addition of PEGDMA resulted in the increase of the dimensional stability of PMMA-based gel electrolytes, which is due to a cross-linking effect exerted by the network former. Ionic conductivity can also be enhanced with PEGDMA modification owing to the high donor number and high chain flexibility of the ethylene oxide units. Hashmi et al. [68] carried out a study on gel polymer electrolytes comprising poly methyl methacrylate (PMMA)-ethylene carbonate (EC)-propylene carbonate (PC)-salts,  $\text{LiClO}_4$ ,  $\text{NaClO}_4$  and  $(\text{C}_2\text{H}_5)_4\text{NClO}_4$  ( $\text{TEAClO}_4$ ) with a view to using them as electrolytes in electrical double layer capacitors (EDLCs) based on activated charcoal powder electrodes. The optimum composition of gel electrolytes, PMMA (20 wt%)-EC:PC (1 : 1 v/v)-1 M salt exhibited high ionic conductivity of the order of  $\sim 10^{-3} \text{ Scm}^{-1}$  at room temperature with good mechanical/dimensional stability suitable for their application in EDLCs. The ionic conductivity and transport behavior of gel polymer electrolytes containing PMMA, EC, PC and  $\text{LiBF}_4$  were studied by Osman et al. [69]. The highest room temperature conductivity of  $2.24 \times 10^{-3} \text{ Scm}^{-1}$  was obtained for the sample containing 20 wt. % of  $\text{LiBF}_4$ . The increase in the conductivity with increasing salt concentration was attributed to the increase in the

number and mobility of the charge carriers. The decrease in the conductivity at still higher concentration was due to the saturation of the salt resulting in the reduced number of charged carriers.

Gel polymer electrolyte based on poly(vinylidene fluoride) (PVdF) host has been investigated since the early 1980s as another potential system [70]. PVdF based polymer electrolytes are highly anodically stable due to the presence of strong electron-withdrawing functional group ( $-C-F$ ) and the polymer itself has a dielectric constant of 8.4, which helps in greater dissolution of lithium salts and subsequently supports high concentration of charge carriers. Tsuchida and his coworkers [71, 72] in 1983 showed that the physically cross-linked gelled PVdF had a conductivity of  $1 \times 10^{-3} \text{ Scm}^{-1}$  at 25 °C. Choe et al. [73] reported PVdF-based electrolytes plasticized with a solution of  $\text{LiN}(\text{CF}_3\text{SO}_2)_2$  in PC that offered conductivity of  $1.74 \times 10^{-3} \text{ Scm}^{-1}$  at 30 °C and oxidation potential limits between 3.9 and 4.3 V vs  $\text{Li}^+/\text{Li}$ . Jiang et al. [74] synthesized a novel PVdF-based gel polymer electrolyte using (EC+PC) plasticizer and lithium salts ( $\text{LiCF}_3\text{SO}_3$ ,  $\text{LiPF}_6$  or  $\text{LiN}(\text{SO}_2\text{CF}_3)_2$ ) by thermal extrusion method. They reported that the viscosity of the medium and concentration of the charge carriers, which are directly related to the weight ratio of PVdF-EC-PC and the kind of lithium salt studied, mainly influenced the conductivity of the electrolyte. They also observed that the PVdF-based electrolytes offered excellent electrochemical properties; but this fluorinated polymer was not stable towards lithium leading to poor interfacial properties between lithium and fluorine. Shiao et al. [75] reported that addition of PVdF as host matrix into the ternary and quaternary solvent reduced the ionic conductivity significantly. The electrochemical and dielectric properties of PVdF polymer hosts have also been reported [76]. Choi et al. [77] prepared porous PVdF fiber-based membranes with a three-dimensional network structure, high porosity, large electrolyte solution uptake and adequate mechanical properties by an electrospinning technique using various mixed-solvent compositions with poly(vinylidene fluoride) (PVdF) for use as the matrix in polymer electrolytes with excellent electrochemical properties and adequate mechanical properties. Electrospun PVdF fiber based polymer electrolytes were prepared by immersion of the electrospun membrane in electrolyte solutions. FT-Raman spectroscopic data showed that the lithium ions predominately associated with the EC molecules indicating that  $\text{Li}^+$ -solvated EC is a major mobile ionic species in these polymer electrolytes. In addition, the PVdF chain showed good

interaction with all but one of the linear alkyl carbonate molecules studied, namely diethyl carbonate. This interaction influenced the swelling of PVdF to form a gel phase and is responsible for enhancement of the electrochemical properties. Rajendran and Sivkumar [78] investigated the physical and thermal properties of blend based PVdF-PVC gel polymer electrolytes. The highest ionic conductivity was found to be  $3.86 \times 10^{-3} \text{ Scm}^{-1}$  at room temperature in PVdF (20)–PVC (5)–(60:40) weight ratio of EC/PC (67)–LiClO<sub>4</sub> (8) complex.

Recently, the poly(vinylidene fluoride-hexa fluoropropylene) (PVdF-HFP) (88:12) has drawn the attention of many researchers. This copolymer comprising an amorphous phase of HFP, which helps in entrapping large amount of liquid electrolytes, and the PVdF crystalline phase acts as a mechanical support for the polymer matrix. Capiglia et al. [79] reported a gel polymer electrolyte system comprising of P(VdF-HFP) and a solution of ethylene carbonate (EC), diethyl carbonate (DEC) and LiN(CF<sub>3</sub>SO<sub>2</sub>)<sub>2</sub> as salt. They were able to increase the ionic conductivity up to  $10^{-2} \text{ Scm}^{-1}$  when the weight ratio of P(VdF-HFP) and (EC/DEC/ LiN(CF<sub>3</sub>SO<sub>2</sub>)<sub>2</sub>) was reduced to 20:80. Stephan et al. [80] synthesized a series of P(VdF-HFP)-based gel polymer electrolytes using EC and PC plasticizer and lithium salt LiCF<sub>3</sub>SO<sub>3</sub>, LiBF<sub>4</sub> and LiClO<sub>4</sub>. They observed that the sample containing LiBF<sub>4</sub> as salt exhibited the maximum ionic conductivity, which was attributed to the low lattice energy of the salt. On the other hand the same sample exhibited poor compatibility with lithium metal anode due to the formation of LiF in the layer. A systematic study was made by Saikia and Kumar [81] on PVdF and P(VdF-HFP)-based gel electrolytes using PC+DEC as plasticizer and LiClO<sub>4</sub> as salt separately. They found that P(VdF-HFP)-based gel electrolytes exhibited higher ionic conductivity than PVdF-based gel electrolytes. They concluded that the higher conductivity in case of P(VdF-HFP) than PVdF is a result of higher amorphicity as there are two randomly mixed monomers providing the mobile Li<sup>+</sup> ion more free volume for transport. Ren et al. [82] successfully prepared semi-interpenetrating polymer networks of P(VdF-HFP) based electrolytes with crosslinked diepoxy polyethylene glycol (DIEPEG). The results showed that the blend polymer electrolyte with P(VdF-HFP)/PEI+DIEPEG (60:40 w/w) had an ionic conductivity of  $2.3 \text{ mScm}^{-1}$  at room temperature in the presence of 1 M LiPF<sub>6</sub> in EC and DMC (1:1 w/w). All the blend electrolytes were electrochemically stable up to 4.8 V versus Li/Li<sup>+</sup>. Nonflammable polymeric gel electrolyte has been prepared by Lalia et al. [83] by immobilizing 1M LiBF<sub>4</sub>/EC (ethylene carbonate) + DEC (diethyl carbonate) + TEP

(triethylphosphate) (55:25:20, v/v/v) solution in poly(vinylidene fluoride-co-hexafluoro propylene) (PVdF-HFP) where TEP acts as a fire-retardant solvent in the gel electrolyte. Electrochemical tests on the nonflammable polymeric gel electrolyte based on 1M LiBF<sub>4</sub>/EC + DEC + TEP (55:25:20) indicated the better performance of electrolyte for both cathode (LiMn<sub>2</sub>O<sub>4</sub>) and anode (graphite) materials as compared to other gel electrolytes containing TMP (trimethyl phosphate) as fire-retardant solvent. Good rate capability of the gel electrolyte with the positive electrode was observed.

It is worth mentioning here that the polymer electrolyte films are usually synthesized by adding low-molecular-weight plasticizers like ethylene carbonate, propylene carbonate, dimethyl carbonate, diethyl carbonate, etc. into the host polymer matrix along with the Li salts. This synthesis route results in tacky and mechanically weak films. As a result the gain in ionic conductivity is offset by a loss of mechanical strength and also leads to poor compatibility with the lithium electrodes, which results in serious problems in terms of battery cyclability and eventually safety [17]. In order to retain the mechanical properties of polymer gel electrolytes, the gel films have to be hardened either by chemical or physical curing (high energy radiation), which result in high processing costs. Besides, the main disadvantage of the above process lies in the fact that it has to be carried out in completely moisture free environment because the moisture sensitive lithium salt is present at the initial stage. On the other hand, Bellcore group [84] proposed a different technique to synthesize GPEs wherein polymer membrane is soaked in electrolyte solution. This system can be more specifically described as a heterogeneous phase separated polymer electrolyte membrane. Advantages of this process lie in the fact that the critical moisture control in this process is required only at the time of assembling the cell and mechanical strength is retained as compared to that of solvent cast membranes. The same group successfully launched a reliable and practical rechargeable Li-ion battery using P(VdF-HFP) [85]. Very recently several reports are available on the development of polymer membranes using phase inversion technique [86, 87, 88, 89, 90]. Unfortunately the polymer electrolyte membranes prepared by this technique exhibit poor rate-capability [17].

### 1.1.3 Composite Polymer Electrolytes (CPEs)

Composite polymer electrolytes (CPEs) are prepared simply by dispersing a small fraction of micron size/ inorganic (ceramic)/organic filler particles into the conventional SPE or GPE host [91]. Recent study reveals that in addition to the improvement in the ionic conductivity, mechanical strength and interfacial properties are also enhanced in the composites. The idea of using inert fillers to increase the mechanical properties of polymer electrolytes in their conductive amorphous phase was initially demonstrated by Weston and Steele [92] by showing that the addition of  $\alpha$ -Al<sub>2</sub>O<sub>3</sub> to PEO-LiClO<sub>4</sub> complexes produced a significant improvement in the mechanical stability of the material at temperatures in excess of 100 °C. The characteristics of these composite ceramic polymer materials were further explored by Lique [93]. He reported that the addition of fine powder  $\alpha$ -Al<sub>2</sub>O<sub>3</sub> to PEO-NaSCN complex not only improved the mechanical properties of the amorphous phase of the polymer electrolyte but also increased its conductivity. He suggested that the extent of the latter phenomenon depends critically on the filler particle size. Improvements of the conductivity in the Al<sub>2</sub>O<sub>3</sub> (and SiO<sub>2</sub>)-(PEO)-NaI composite system were also found by Wieczorek [94]. Later Scrosati and co-workers [95, 96] showed that the dispersion of  $\gamma$ -LiAlO<sub>2</sub> ceramic powders having grain size diameter of the order of 1  $\mu$ m to the (PEO)-LiClO<sub>4</sub> complex led to the formation of homogeneous composite membranes with a largely improved mechanical stability at temperatures above the crystalline-to-amorphous transition (i.e., around 60 °C) while still maintaining a conductivity comparable to or higher (depending on composition) than that of the pure (PEO)-LiClO<sub>4</sub> electrolyte complex. In particular, the composite electrolytes containing 10 wt. %  $\gamma$ -LiAlO<sub>2</sub> showed a maximum ionic conductivity [95] beyond which the dilution effect became predominant and the conductivity decreased. As a possible explanation for the observed enhancement in ionic conductivity due to the addition of micron size ceramic fillers, they stated that ceramic filler, when highly dispersed in the polymer matrix, might affect the crystallization rate by preventing the agglomeration of the polymer chains. Fast ionic transport in PEO-based polymer electrolytes is an inherent property of the amorphous phase [10] and thus the addition of a component, which prevents polymer recrystallization, is expected to reasonably produce a positive effect on the overall conductivity. It has also been demonstrated by Scrosati and co-workers [97] that the addition of  $\gamma$ -LiAlO<sub>2</sub> into PEO based electrolyte improves electrochemical property of the electrolyte



and have an exceptionally high lithium metal electrode interfacial stability, which allows obtaining a cycling efficiency approaching 99%. People also studied composite polymer electrolytes for other systems like NaClO<sub>4</sub> [98], PEO-NaH<sub>4</sub>I-Al<sub>2</sub>O<sub>3</sub> [99], LiClO<sub>4</sub> in pyridene matrix [100], and NH<sub>4</sub>SCN [101].

Despite a common agreement on the decrease of polyether crystallinity and changes in the polyether flexibility and hence ionic conductivity caused by the addition of organic or inorganic fillers, little was known about the mechanisms responsible for these changes. Wieczorek et al. [102, 103] proposed a new theory based on Lewis acid-base interaction to analyze the structure and the ionic conductivity of a number of CPEs complexed with alkali metal salts. They incorporated filler particles of three different characters, namely, Lewis acid centres (AlCl<sub>3</sub>), Lewis base centres poly(N,N dimethylacrylamide) and amphoteric Lewis acid-base ( $\alpha$ -Al<sub>2</sub>O<sub>3</sub>) in the PEO–LiClO<sub>4</sub> system. Since PEO has a Lewis base and Li<sup>+</sup> cation has a Lewis acid character, the phenomena occurring in the composite electrolyte could be explained in terms of equilibrium between various Lewis acid–base reactions. Lewis acid–base interactions eventually result in the reduction of ion coupling (resulting in increased salt dissociation) and the formation of lithium ion conducting pathways at the filler surface leading to an increase in ionic conductivity and cation transport number. Croce et al. [104, 105] reported significant enhancements in room temperature ionic conductivity and mechanical property of PEO–LiClO<sub>4</sub> incorporated with inert sub-micrometre SiO<sub>2</sub> and TiO<sub>2</sub> particles. According to them the filler particles behave like solid plasticizer, which kinetically inhibit the crystallization of PEO chains and, hence, supplement the increase in amorphicity in PEO when annealed at 70 °C. This, in turn, lowers the temperature of stabilization of the amorphous phase in the CPEs and, hence, increases the practical applicable range of conductivity of the electrolytes. Enhancement in the room temperature conductivity and electrochemical properties have also been reported for the other polymer electrolyte systems based on PEO: lithium salts (LiClO<sub>4</sub>, LiBF<sub>4</sub>, LiPF<sub>6</sub>, LiCF<sub>3</sub>SO<sub>3</sub>) dispersed with sub-micrometre size particles of ferroelectric materials, namely, BaTiO<sub>3</sub>, PbTiO<sub>3</sub>, LiNBO<sub>3</sub> [106, 107]. Liu et al. [108] prepared an amorphous PEO-SiO<sub>2</sub> composite by in-situ reactions using LiBF<sub>4</sub> salt and were able to increase the lithium transference number up to 0.56. Panero et al. [109] found that addition of up to 30 wt. %  $\gamma$ -LiAlO<sub>2</sub> into PEG complexed with lithium salt could significantly enhance the mechanical properties while conductivity remained almost

same with filler free electrolyte. On the other hand along with the mechanical strength, ionic conductivity was also found to increase in a SiO<sub>2</sub> added systems of PEG-MME and PEG-DME complexed with LiClO<sub>4</sub> [110].

The room temperature ionic conductivity of PEO-LiClO<sub>4</sub> increased by more than two times when a functionalized SiO<sub>2</sub> possessing two surface silanol (Si-OH) groups and an octyl (Si-C<sub>8</sub>H<sub>17</sub>) group was used as filler after thermal treatment. Interestingly, thermal-induced segregation of silica particles was not observed and this could be responsible for the enhancement of conductivity [111]. In another paper, the addition of commercially available mesoporous SBA-15 as fillers into a PEO-LiClO<sub>4</sub>-based SPE improved the mechanical, electrochemical, and physicochemical properties of the electrolyte [112].

#### *1.1.4 Nanocomposite Polymer Electrolytes (NCPEs)*

It has been observed, in general, that the particle size and the physical nature of the dispersoids play a significant role. Generally, smaller the particle size, larger the conductivity enhancement. In part, because of this idea nanocomposite polymer electrolytes (NCPEs) wherein nano-sized inert solid particles are added to the polymer electrolytes are currently the focus of many experimental and theoretical studies [113]. Depending upon the nature of association, two kinds of nanocomposite electrolytes can be found

- (i) Inorganic-in-organic, where inorganic nanoparticles are embedded in polymer matrix and
- (ii) Organic-in-inorganic, where organic polymers are confined in inorganic templates such as layered silicates.

##### *1.1.4.1 Inorgani- in-Organic Nanocomposite Electrolytes*

In 1994 Kumar and Scanlon [114] reviewed the state of the art of CPE based on ionic conductivity, transport number and electrode-electrolyte interfacial reactions. They also substantiated that the ceramic fillers such as nitrides (AlN, BN) have better interfacial properties than SiO<sub>2</sub> or Al<sub>2</sub>O<sub>3</sub> because the passivation of lithium metal will result in the formation of Li<sub>3</sub>N that facilitates for high ionic conductivity. They also proved that nano-sized ceramic fillers had better compatibility with lithium metal than micron sized fillers. Kumar and Coworker [115, 116] also carried out similar DSC studies on the PEO: LiBF<sub>4</sub>

dispersed with nano-sized ceramic filler particles of materials with a high dielectric constant, namely,  $\text{TiO}_2$ ,  $\text{ZrO}_2$ , and identified that interactions between polymer chain and high dielectric constant inorganic fillers were influenced by the size and mass of the particles, which led to a better enhancement in the ionic conductivity. The nature of the interaction was believed to be dipole–dipole type driven by a dielectric constant gradient. Enhancement of ionic conductivity as well as ionic mobility was observed by Morita et al. [117] in a NCPE system containing PEO-grafted-(polymethacrylate) complexed with lithium salt when  $\text{LiN}_2\text{O}_3$  was added as inorganic filler. Bloise and co-workers [118, 119] probed the NMR properties of both nuclei  $^1\text{H}$  and  $^7\text{Li}$  and studied the effects of ceramics and carbon black filler particles on the mobility of PEO chains. Results suggested that the Li-F interaction was found to be weaker in the composite electrolytes prepared with  $\alpha\text{-Al}_2\text{O}_3$  as compared to other electrolytes prepared with  $\gamma\text{-Al}_2\text{O}_3$ . Similar observation was made by Chung et al. [120] using NMR characterization observed that the enhancement in ionic conductivity due to the addition of nano-sized  $\text{TiO}_2/\text{Al}_2\text{O}_3$  in PEO- $\text{LiClO}_4$  system was not due to the corresponding increase in the segmental motion of polymer chains but mainly due to the weakening of polymer–cation association induced by the nanoparticles. Using a PEO- $\text{LiBF}_4$ -sulfated- $\text{ZrO}_2$  electrolyte system, Croce et al. [121, 122] achieved a surprisingly high  $\text{Li}^+$  transference number of 0.8, which was about two times higher than that obtained with ceramic-free electrolyte. Dey et al. [123] demonstrated that addition of  $\text{CeO}_2$  nanoparticles to PEO:  $\text{NH}_4\text{ClO}_4$  could significantly improve the thermal and ionic conductivity of PEO:  $\text{NH}_4\text{ClO}_4$  complex. A maximum conductivity value of  $3.6 \times 10^{-4} \text{ Scm}^{-1}$  was obtained for 25 wt. % of  $\text{CeO}_2$  content. Fullerton and Maranas [124] studied the thermal properties, ionic conductivity, extent of aggregation and polymer mobility of nanoparticle-filled solid polymer electrolytes containing PEO,  $\text{LiClO}_4$  and nanoparticles of  $\text{Al}_2\text{O}_3$  keeping O/Li ratio from 14:1 to 8:1 and  $\text{Al}_2\text{O}_3$  nanoparticle concentration ranging from 5 wt.% to 25 wt.%. They demonstrated that nanoparticle filled polymer electrolyte exhibited better conductivity only at the eutectic composition of 10:1. Hot press technique was employed to synthesize PEO- $\text{KNO}_3$ - $\text{SiO}_2$  nanocomposite solid polymer electrolytes by Agarwal and Mahipal [125]. Fractional dispersal of nano- $\text{SiO}_2$  into the SPE host: (70 PEO: 30  $\text{KNO}_3$ ) enhanced the room temperature conductivity by more than three fold. XRD, DSC and FTIR studies confirmed the complexation of the salt in the polymer. The maximum cationic transport number was

found to be 0.36 as measured by combined ac/dc technique. Using the same synthesis technique Stephan et al. [126] prepared a nanocomposites polymer electrolyte based on PEO, LiClO<sub>4</sub> and nanochitin as filler. The ionic conductivity of the composite polymer electrolytes was enhanced by one order upon addition of nanochitin. The lithium transference number was also increased from 0.24 to 0.51 upon chitin addition. Chen-Yang and co-workers [127] prepared a series of NCPEs based on high molecular weight PEO, LiClO<sub>4</sub> and home made silica aerogel powder (SAP), which had higher surface area and pore volume than that of the conventional silica particle. The ionic conductivity of the CPE was significantly improved by the addition of the as-prepared SAP. The maximum ambient ionic conductivity obtained from the CPE with EO/Li = 6 and 2 wt. % of SAP was about threefold higher than that of the corresponding polymer electrolyte without SAP. In addition, the lithium ion transference number (*t*<sup>+</sup>) of the CPE with EO/Li = 6 and 2 wt.% of SAP at 70 °C was found to be 0.67, which was also three times higher than that of the filler free SPE. Surface modified polyphosphazene nanotubes (PZS) was used as filler in PEO-LiClO<sub>4</sub> solid polymer electrolytes by Zhang et al. [128]. They demonstrated that PZS nanotubes acted as better fillers to polymer electrolytes for its inorganic-organic hybrid structure as compared to those traditional ceramic fillers such as SiO<sub>2</sub>. Maximum ionic conductivity values of  $4.95 \times 10^{-5} \text{ Scm}^{-1}$  at ambient temperature and  $1.64 \times 10^{-3} \text{ Scm}^{-1}$  at 80 °C with 10 wt % content of surface modified PZS nanotubes were obtained and the lithium ion transference number was 0.41.

Molecular sieves, microporous materials with high BET surface areas and two-dimensional intersection channels, especially aluminosilicate molecular sieves (zeolites), have been used as fillers for CPEs [129-131]. Compared to the traditional nanofillers, certain types of molecular sieves were shown to possess much stronger Lewis acid centers in their frameworks and inside the channels, which might contribute to the prevention of the crystallization tendency of the polymer host more effectively, thus resulting in a higher degree of conductivity and Li<sup>+</sup> transference number enhancement. The addition of a molecular sieves was found to decrease the crystallinity of PEO as well as increase the amount of PEO spherulites resulting in a significantly enhanced ionic conductivity and electrochemical stability up to 4.5 V. Xi et al. [132] by adding mesoporous silica fillers into PEO complexed with LiClO<sub>4</sub> were able to significantly improve the conductivity, Li<sup>+</sup> transference number and electrochemical stability of the NCPEs. Kim and Park [133]

prepared a series of NCPEs based on PEO, LiClO<sub>4</sub> and mesoporous silicate mobile crystalline material-41 (MCM-41) by varying the concentration of MCM-41. Their results revealed that maximum ionic conductivity of  $2 \times 10^{-4} \text{ Scm}^{-1}$  could be achieved for 8 wt. % MCM-41. The lithium transference number was also enhanced up to 0.5 at the same concentration of MCM-41.

#### *1.1.4.2 Organic- in-Inorganic Nanocomposite Electrolytes*

Another effective way of producing nanocomposite polymer electrolytes is through the fabrication of polymer layered silicate nanocomposites. Polymer nanocomposite films formed via the intercalation of polymers in the nanometric channels of inorganic clay (e.g., montmorillonite, hectorite, seponite etc.) have drawn considerable attention in recent years. They are known as “intercalation nanocomposites”. Nanocomposites based on polymer/clay systems are also important in view of developing new materials with structural and functional advantages over the conventionally reinforced polymers [134]. Among the widely studied layered silicates or clays montmorillonite (MMT) is a favored choice, the structure of which is shown in figure 1. Montmorillonite (MMT) clays contain stacked silicate sheets measuring  $\sim 10 \text{ \AA}$  in thickness and  $\sim 2800 \text{ \AA}$  in length. The layer thickness is around 1 nm, and the lateral dimensions of these layers can vary from 100 nm to several microns. Stacking of the layers leads to a regular van der Waals gap between the layers called interlayer or gallery. The isomorphous substitution within the layers (i.e. Al<sup>3+</sup> in the aluminate sheet with Mg<sup>2+</sup>) generates negatively charged layers, which are then balanced by alkali and alkaline earth cations (Na<sup>+</sup>, K<sup>+</sup>, Ca<sup>2+</sup>) to maintain charge neutrality [135]. These cations are arranged in between the parallel-superimposed layers. One particular characteristic of these silicate layers is a moderate surface charge known as cation exchange capacity (CEC), generally expressed as mEq/100 g. This charge is not locally constant; it varies from layer to layer, and must be considered as an average value over the whole crystal [136]. Nevertheless organo-modification of the clay is an essential prerequisite to make it organophilic in order to achieve the desirable features in the material system [136]. Depending on the strength of interfacial interactions between the polymer matrix and layered silicate, two different types of polymer-layered silicate nanocomposites are thermodynamically achievable (Figure 1.2):

- (i) *Intercalated Nanocomposites*: In intercalated nanocomposites, the insertion of a polymer matrix into the layered silicate structure occurs in a crystallographically regular fashion, regardless of the clay to polymer ratio resulting into a well ordered multiplayer with repeat distance of a few nanometers.
- (ii) *Exfoliated Nanocomposites*: These nanocomposites are formed when the silicate monolayers are individually dispersed in polymer matrix, the average distance between the segregated layers being dependent on clay loading. The separation between the exfoliated nanolayers may be uniform (regular) or variable (disordered) and the stacks of the original clay structure are lost.

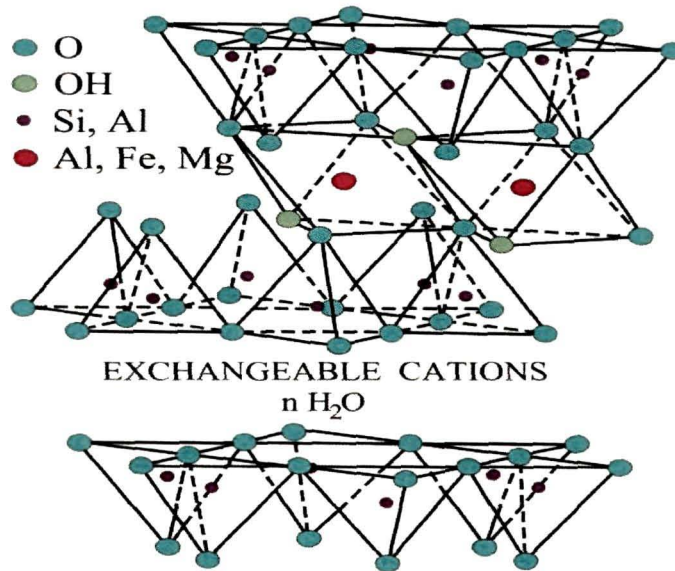


**Figure 1.1:** Structure of Na-MMT.

Aranda and Hitzky [137] first attempted nanocomposite formation by direct intercalation of an insulating polymer, polyethylene oxide (PEO), into montmorillonite (MMT) clay. They succeeded in intercalation without any significant achievement of the desirable properties (e.g., conductivity) of the nanocomposite for applications in devices under ambient conditions. Subsequently, Giannelis and co-workers [138-142] explored the possibility of intercalation on the basis of thermodynamical free energy considerations and simulation studies to investigate the conformational and structural arrangement of polymer

chains between successive clay layers. They observed that the intercalation of a cation-coordinated polymer chain via an ion-exchange reaction is easier than intercalating pure PEO. Fan et al. [143] studied the composite formation with combination of organo-modified Li-MMT/Na-MMT and  $\text{PEO}_{16}\text{LiClO}_4$ . They reported 30 times enhancement in conductivity at room temperature for the composite polymer film ( $3.5 \times 10^{-6} \text{ Scm}^{-1}$ ) in comparison to that of the pure  $\text{PEO}_{16}\text{LiClO}_4$  ( $1.2 \times 10^{-7} \text{ Scm}^{-1}$ ).

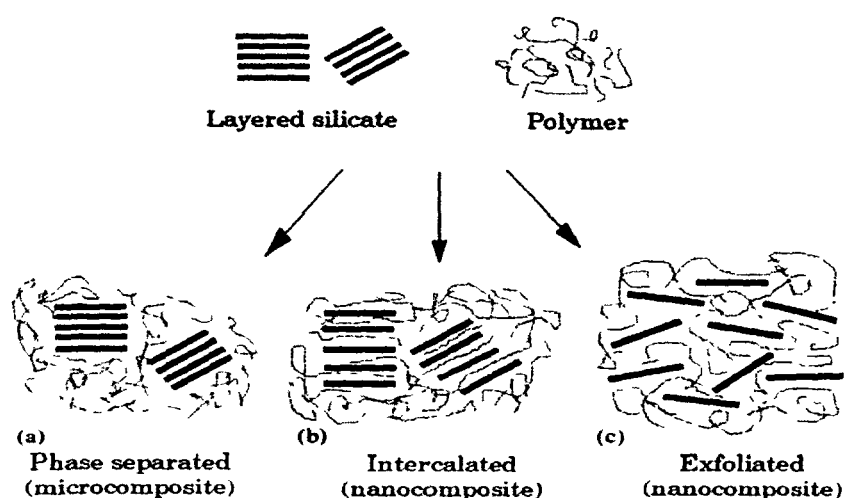


**Figure 1.2:** Schematic illustration of different polymer-clay composites.

A salt free single ion conducting material based on an amorphous polymer poly[(oxyethylene)<sub>8</sub> methacrylate], POEM, and lithium montmorillonite clay were synthesized by Mary Kurian et al. [144]. At low clay content silicate layers were homogeneously distributed in the poly [(oxyethylene)<sub>8</sub> methacrylate] POEM matrix in comparison to higher clay content as revealed by TEM. They reported that at low clay contents, silicate incorporation enhanced the mechanical properties of POEM, while impedance spectroscopy showed an improvement in electrical properties. With clay content  $\geq 15$  wt. %, mechanical properties are further improved but the formation of an apparent superlattice structure correlates with a loss in the electrical properties of the nanocomposite. A nanocomposite electrolyte comprising a polymer-salt complex ( $\text{PEO}_{25}\text{-NaClO}_4$ ) and an organically modified sodium montmorillonite (Na-MMT) was prepared using tape casting technique by varying clay loading [145]. A change in the surface morphology and

topography with different clay concentration was observed by AFM, which was found consistent with the changes in the electrical properties with clay concentration. The observed electrical conductivity was higher at 5 wt. % clay loading at room temperature with a maximum value  $\sim 2.20 \times 10^{-7} \text{ Scm}^{-1}$  at 40 °C. Zhang et al. [146] investigated the FT-IR and X-ray diffraction measurements of PEO/Na-MMT and PEO/NaSCN/Na-MMT at room temperature. Based on experimental results they showed that MMT surface possessed Lewis acid centers, and the interactions of MMT with PEO and PEO-NaSCN could occur several ways, including PEO intercalation, the solvation of PEO toward the interlayer cations, the grain boundary effect, Lewis acid-base interactions, and the epitaxial effect. The Lewis acid-base interactions between PEO and Na-MMT were the main interactions in the electrolytes with high Na-MMT content. The grain boundary effect and the intercalation of PEO in MMT galleries became the dominant interactions in the electrolytes in which Na-MMT content was less than 5 wt. %.

Recently D.K. Pradhan et al. [147] investigated the structural, thermal and electrical behavior of polymer-clay nanocomposite electrolytes consisting of polymer (polyethylene oxide (PEO)) and NaI as salt with different concentrations of organically modified Na<sup>+</sup> montmorillonite (DMMT) filler. They found maximum ionic conductivity to be  $1.8 \times 10^{-8} \text{ Scm}^{-1}$  at room temperature for 5 wt. % DMMT concentration. The same group [148] reported that addition of DMMT into PEO complexed with LiClO<sub>4</sub> show substantial enhancement in ambient temperature conductivity, reasonable improvements in stability properties (thermal/voltage), drastic increase in cation transport, and excellent correlation of electrical properties with the composite nanostructure. Kitajima and Tominaga [149] prepared Poly-[ethylene oxide-co-2-(2-methoxyethoxy)ethyl glycidyl ether], P(EO/EM)/laponite nanocomposites as novel SPE using supercritical processing technique. They showed that supercritically treated CO<sub>2</sub> sample exhibited approximately 25 times higher conductivity value than that of nttreated P(EO/EM)/laponite nanocomposites. This was explained on the basis of dissociation effect of CO<sub>2</sub> molecules on the local structure, where P(EO/EM)-cation interactions occur in the dispersed saponites. Moreno et al. [150] prepared NCPEs based on two different poly(ethylene oxide), having molecular weight 600,000 and 4,000,000 and lithiated bentonite as filler. Comparative analysis of ionic conductivity and mechanical properties of the films showed that the conductivity increased with the inclusion of fillers,



especially for the polymer with low molecular weight. Shukla and Thakur [151] studied the electrical and electrochemical properties of nanocomposite films based on PMMA-LiClO<sub>4</sub> using DMMT as filler. An increase in the fraction of free anion with addition of clay was evident from FTIR. Substantial electrical conductivity enhancement by 4 orders of magnitude at 30 °C and by 6 orders of magnitude at 100 °C occurred on clay addition when compared with room temperature conductivity of the DMMT free film. The highest achieved conductivity value was  $2.3 \times 10^{-5} \text{ Scm}^{-1}$  at room temperature for 2 wt. % DMMT. An improvement in the voltage stability up to  $\sim 4 \text{ V}$  has also been noticed on addition of clay (DMMT).

## 1.2 From Nanocomposite to Nanocomposite Gel Polymer Electrolytes

From the above discussion it is clear that GPEs exhibit high ambient temperature ionic conductivity while losing their mechanical property at high plasticizer content. In addition, interfacial stability of GPEs with lithium metal electrode is very poor, which results in short circuiting of the cell and eventually leads to premature battery failure. In contrast CPEs or NCPEs exhibit very good interfacial stability with lithium electrode along with enhanced mechanical strength. However their ionic conductivity value is far from practical applications. Nanocomposite gel polymer electrolytes, on the other hand combine the high ambient conductivity of conventional gel electrolytes with the excellent stability toward the metal electrode and the good mechanical properties of nanocomposite electrolytes [152].

In 2003 Nan et al. [113] reported a new PEO-LiClO<sub>4</sub> based composite polymer electrolyte containing active nanocomposite particles with EC/PC embedded in mesoporous SiO<sub>2</sub>. A large conductivity value over  $10^{-3} \text{ Scm}^{-1}$  at ambient temperature and  $10^{-2} \text{ Scm}^{-1}$  at 50 °C was achieved by the introduction of EC/PC-SiO<sub>2</sub> in PEO-LiClO<sub>4</sub> complex without deterioration of mechanical property. The enhancement in conductivity was mainly attributed to the conducting EC/PC nanochannels in the active nanocomposite particles. Pradhan et al. [153] investigated the effect of PEG<sub>200</sub> plasticizer on the change in the electrical and the stability properties of PEO-NaClO<sub>4</sub> dispersed with SiO<sub>2</sub> ceramic fillers. A substantial enhancement in the electrical conductivity by two orders of magnitude at room temperature was noticed when compared with that for composite polymer electrolyte films without any

plasticizer. A similar kind of study was carried out by Kuila et al. [154] where they used  $\text{LiMnO}_3$  as nanofiller. A substantial enhancement in the electrical conductivity (about two orders of magnitude at room temperature) had been found on plasticization. A maximum electrical conductivity of  $2.6 \times 10^{-4} \text{ Scm}^{-1}$  at 300K was observed for 30 wt.% of PEG as plasticizer compared to that for the pure PEO– $\text{NaClO}_4$  system of  $1.05 \times 10^{-6} \text{ Scm}^{-1}$ . This was explained on the basis of enhancement of the amorphous phase with concomitant reduction in the energy barrier leading to the maximum segmental motion of lithium ions. Nanocomposites gel polymer electrolytes based on PEO– $\text{LiCF}_3\text{SO}_3$ –EC– $\text{Al}_2\text{O}_3$  complexes were synthesized successfully by Johan et al. [155]. At room temperature, the highest conductivity was obtained for the composition PEO– $\text{LiCF}_3\text{SO}_3$ –EC–15%  $\text{Al}_2\text{O}_3$  with a value of  $5.07 \times 10^{-4} \text{ Scm}^{-1}$ .

Nanocomposite gel polymer electrolytes based on PMMA, PC as plasticizer,  $\text{LiClO}_4$  and  $\text{NaClO}_4$  as salt with varying weight ratio of  $\text{Al}_2\text{O}_3$  were prepared by Kreja et al. [156]. The ionic conductivity of polymer-based electrolytes was enhanced almost by one half orders of magnitude at room temperature due to the addition of nanosized  $\text{Al}_2\text{O}_3$  while the conductivity of liquid electrolytes was decreased by the addition of alumina in the blend. A slight enhancement of mechanical properties was also observed. Kumar and Hashmi [157] carried out a study on the effect of  $\text{SiO}_2$  nanoparticles on PMMA-(EC+PC)- $\text{NaClO}_4$  based gel electrolytes. A maximum ionic conductivity of  $3.4 \times 10^{-3} \text{ Scm}^{-1}$  was found for 4 wt. % of  $\text{SiO}_2$  content. Based on FTIR studies they showed that addition of  $\text{SiO}_2$  nanoparticles (4–5 wt. %) led to the dissociation of undissociated salt/ion aggregates into free ions (anions) in the gel polymer matrix, which eventually resulted in higher ionic conductivity. A slight enhancement in the sodium ion transport number was also observed due to the dispersion of  $\text{SiO}_2$  nanoparticles in the gel system. There are also recent reports on the enhancement of ionic conductivity and electrochemical property of PMMA and PAN based nanocomposite gel electrolytes due to the addition of nano  $\text{Al}_2\text{O}_3$  [158, 159].

Wu et al. [160] carried out a comparative study with metal oxides and mesoporous zeolites as fillers, which were dispersed in the porous polymer matrix of P(VdF-HFP)-based electrolyte comprising EC:PC (1:1 v/v) mixture as the liquid plasticizer. The addition of these solid fillers into the filler-free electrolytes increased the ionic conductivity from  $1.2 \times 10^{-3} \text{ Scm}^{-1}$  to  $2.1 \times 10^{-3} \text{ Scm}^{-1}$ , possibly because of the increased porosity and liquid

electrolyte uptake. More advantageously, these electrolyte systems showed the electrochemical stability up to 5.5 V (versus Li/Li<sup>+</sup>). Nano SiO<sub>2</sub>-P(VdF-HFP) composite porous membranes were prepared as the matrix of porous polymer electrolytes through in-situ composite method based on hydrolysis of tetraethoxysilane and phase inversion. It is found that in-situ prepared nano silica, homogeneously dispersed in the polymeric matrix, enhanced conductivity and electrochemical stability of porous polymer electrolytes, and improved the stability of the electrolytes against lithium metal electrodes [161]. Nanocomposite gel polymer electrolyte (CPE) membranes, comprising P(VdF-HFP), aluminum oxyhydroxide (AlO(OH)<sub>n</sub>) of two different sizes 7 μm/14 nm and LiN(C<sub>2</sub>F<sub>5</sub>SO<sub>2</sub>)<sub>2</sub> as the lithium salt were prepared using a solution casting technique. The incorporation of nanofillers greatly enhanced the ionic conductivity and the compatibility of the composite polymer electrolyte [162]. Nanocomposite gel polymer electrolyte (NCPE) membranes of P(VdF-HFP) matrix with ethylene carbonate and diethyl carbonate mixtures as plasticizing agents, SiO<sub>2</sub> nanoparticles as filler and complexed with LiPF<sub>3</sub>(CF<sub>3</sub>CF<sub>2</sub>)<sub>3</sub> were prepared by solvent casting technique. The membranes containing 2.5 wt. % of SiO<sub>2</sub> exhibited enhanced conductivity of 1.1 mS cm<sup>-1</sup> at ambient temperature [163]. Kumar et al. [164] analyzed the comparison between the performances and morphologies of the PMMA based nanocomposite gel polymer electrolyte membrane with nanosized MgO particles. They achieved good interfacial stability at the electrode/electrolyte interface and ionic conductivity of 8.14 × 10<sup>-3</sup> S cm<sup>-1</sup> as a result of ion-covalent or Lewis acid-base bonds to the ions and ether oxygen based groups. There are also recent reports on the enhancement of ionic conductivity due to the addition of MgO nanoparticles to P(VdF-HFP) based gel electrolytes [165, 166]. Gentili et al. [167] demonstrated that dispersion of surface functionalized fumed nano-silica and alumina to PVdF-carbonate solvent-lithium salt systems enhanced the mechanical stability and, particularly the lithium interfacial properties. Nanowires of SiO<sub>2</sub> were successfully used as filler to enhance the ionic conductivity and voltage stability factor of P(VdF-HFP) based gel electrolytes [168]. Li et al. [169] prepared microporous nanocomposites electrolytes based on P(VdF-HFP) by in-situ hydrolysis of Ti(OC<sub>4</sub>H<sub>9</sub>)<sub>4</sub> using a non-solvent-induced phase separation technique. Compared with the pure polymer membranes, the nanocomposite membranes could uptake larger non-aqueous electrolyte up to 125%. The nanocomposite films exhibited flexible structure with an elongation ratio of

74.4%. The ionic conductivity of the resulting nanocomposite film was  $0.98 \times 10^{-3} \text{ Scm}^{-1}$  at 20 °C. Raghavan et al. [170] prepared a series of porous nanocomposite gel polymer electrolytes of P(VdF-HFP) comprising nanoparticles of BaTiO<sub>3</sub>, Al<sub>2</sub>O<sub>3</sub> or SiO<sub>2</sub> by electrospinning technique. The inclusion of fillers created amorphous regions by the way of the interactions between the filler surfaces and the polymer chains, which resulted in the reduced crystallinity of the polymer. Among the fillers, BaTiO<sub>3</sub> had been observed to exhibit the highest electrolyte uptake, ionic conductivity, electrochemical stability and compatibility with lithium metal. Nanocomposite gel polymer electrolytes based on the blend of PVdF-HFP/PVAc with plasticizer ethylene carbonate and salt LiClO<sub>4</sub> was prepared for various concentrations of BaTiO<sub>3</sub> by Rajendran et al. [171]. The maximum ionic conductivity was found to be  $2.56 \times 10^{-3} \text{ Scm}^{-1}$  at 8 wt. % of BaTiO<sub>3</sub> content at room temperature. The same composition was thermally stable up to 385 °C.

Nanocomposite gel polymer electrolytes based on intercalation of an ion conducting polymer into the nanometric channels of layered silicates followed by addition of low molecular weight plasticizers have attracted great attention in recent years. Hwang et al. [172] synthesized PAN-based nanocomposite gel polymer electrolyte using MMT clay modified by quaternary alkylammonium salts, PC/EC co-solvent and salt LiClO<sub>4</sub>. The PAN/clay nanocomposite electrolyte showed a maximum ionic conductivity of  $1.4 \times 10^{-2} \text{ Scm}^{-1}$  and exhibited superior film formation ability, plasticizer absorption and dimensional stabilities in addition to enhanced electrochemical stability as revealed by cyclic voltammetry study. In a similar study, Meneghetti et al. [173] showed that addition of MMT clay in PMMA resulted in the formation of partially intercalated and partially exfoliated morphology. The ionic conductivity was enhanced to  $8 \times 10^{-4} \text{ Scm}^{-1}$  for 1.5 wt. % clay loading. The PMMA nanocomposite gel electrolyte showed a stable lithium interfacial resistance over a 3-week storage time. Recently, Kim et al. [174] reported composite formation of a plasticized polymer electrolyte (PEO<sub>16</sub>LiClO<sub>4</sub> + 50 wt. % EC) with organically modified Na-MMT. They observed an optimum value of room temperature conductivity of  $10^{-5} \text{ Scm}^{-1}$  for the plasticized electrolyte and  $10^{-4} \text{ Scm}^{-1}$  for the composite (10 wt. % modified MMT). Wang and Dong [175] were able to synthesize exfoliated nanocomposites using P(VdF-HFP) polymer and MMT clay. After gelling with liquid electrolyte solution (1M LiPF<sub>6</sub> in EC: DMC), the obtained GPEs exhibited high ionic

conductivity ( $1\text{--}2.5\text{ mScm}^{-1}$ ) with high cationic transfer number at room temperature, which was attributed to the distinctive characteristic of the well-dispersed silicate layers. The effect of 12-aminododecanoic acid [ $\text{NH}_2(\text{CH}_2)_{11}\text{COOH}$ ] modified MMT clay (ALA–MMT) addition on electrochemical property of PAN/ $\text{LiClO}_4$  polymer electrolytes was recently studied by Chen-Yang et al. [176]. They reported that with the addition of ALA–MMT, the interaction of  $\text{Li}^+$  and  $\text{C}\equiv\text{N}$  was reduced and the  $\text{Li}^+$  cations were less constrained in the polymer matrix and moved more freely in the polymer electrolytes. Besides, the ALA–MMT clay allowed the lithium salt to dissolve in the PAN matrix, resulting in the increase of the concentration of the solvated  $\text{Li}^+$  leading to the increased ionic conductivity and lithium transference number.

### 1.3 Ion Transport in Polymers: Mechanisms and Models

For solvent free polymer electrolytes, such as heteropolymers PEO, salts dissolve because of the lone pair of electrons on the polymer chain oxygen atoms coordinate with the cations. The cation transport process in polymer electrolytes can be envisaged as a ‘roll-on’ mechanism in which a cation is initially coordinated to several oxygen atoms [177]. The linkage to one or more of the polymer segments that lie behind the direction of motion of the cation break and new linkages are formed in the forward direction. The cation motion is clearly facilitated by the flexing of the polymer chain segments, which allow old linkage to be broken and new attachment to be made. For high molecular weight polymer hosts chain diffusion is small and makes little contribution to mechanism for ion transport. Low barriers to bond rotation allow segmental motion of the polymer chain, thus providing a mechanism for ion transport as conductivity is largely determined by local mobility of polymer segments. Figure 1.3 shows the schematic representation of cation hopping of polymer electrolyte in different ways.

For gel polymer electrolytes, polymer is an important constituent along with salt and solvent. The salt provides ions for conduction and the solvent helps dissolution of salt and also provides the medium for ion conduction. The conductivity of gel polymer electrolytes can be explained by ‘Breathing polymeric chain model’ proposed by Chandra et al. [178]. According to this model polymer gel electrolytes generally consist of free ions, ion aggregates and polymer chain dispersed in the gel matrix. The breathing of polymer by

folding/unfolding up of its chains results in density/pressure fluctuations at microscopic level, which assist the motion of ions along with the dissociation of ion aggregates leading to increase of ionic conductivity. The polymer chains act on ion pairs to effect dissociation and the dissociated ions in the solvent are further solvated by the polymer chains, which results in a change in carrier concentration and mobility.

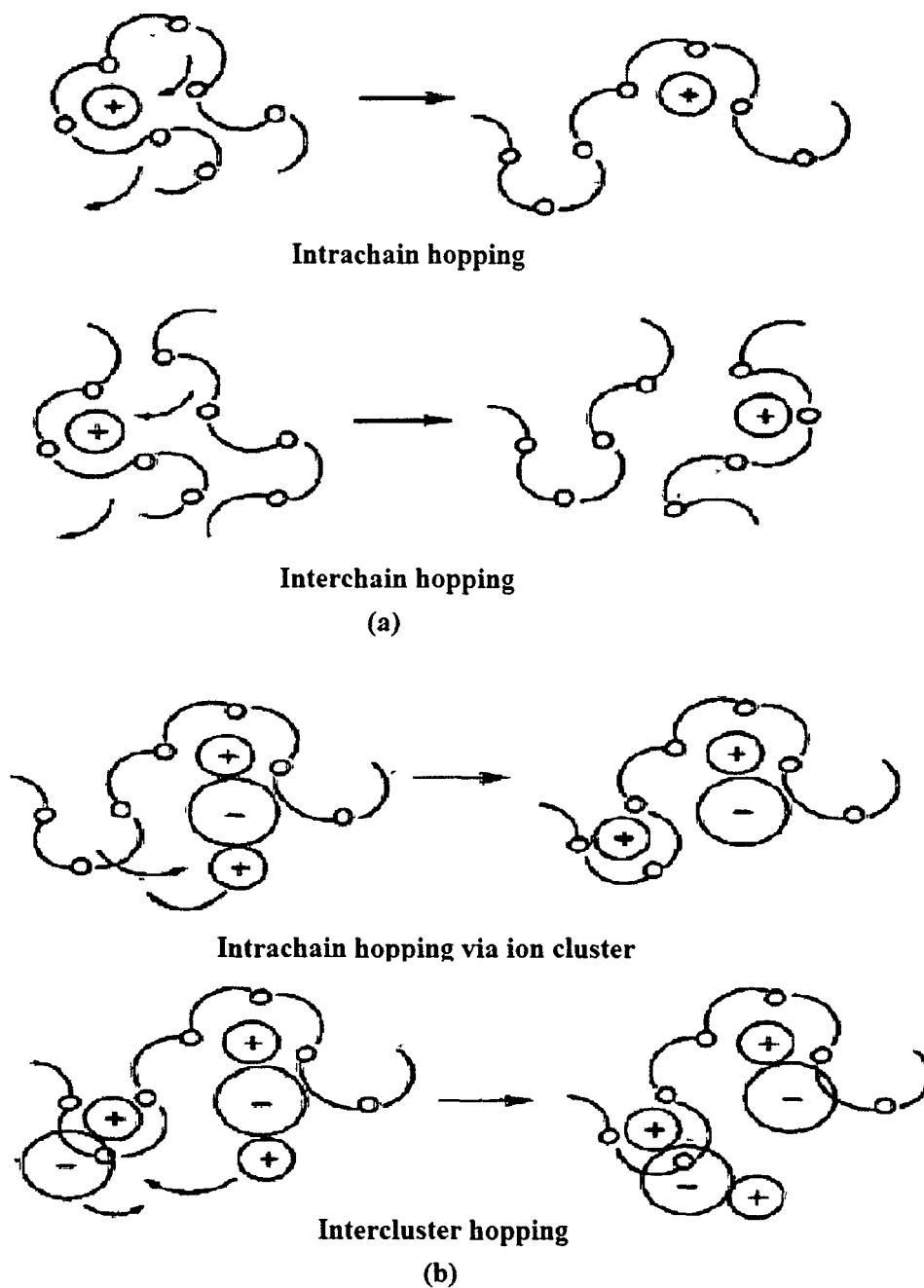


Figure 1.3: Cation motion in polymer electrolytes.

### 1.3.1 Arrhenius Model

Polymer gel electrolyte is a semi-solid hybrid system wherein ionic conduction essentially occurs through the liquid organic phase trapped in constantly flexing polymeric molecular chains above the glass transition temperature of polymer. Therefore, for polymer gel electrolyte systems the Arrhenius for the conductivity

$$\sigma = \sigma_0 \exp\left(-\frac{E_a}{kT}\right) \quad (1.1)$$

where  $\sigma_0$  is the pre-exponential factor,  $E_a$  is the activation energy and  $k$  is the Boltzmann's constant, often provide a good representation of the conductivity-temperature relationship. Linear graph of  $\log \sigma$  vs  $1/T$  is often called as Arrhenius plot, as for an Arrhenius process the logarithm of the relevant performance parameter depends linearly on the reciprocal of temperature. The slope of the curve gives the activation energy of the process. In fact, diffusion is the relevant activated transport process rather than conductivity and the appropriate performance parameter is the diffusion coefficient. The Nernst-Einstein equation provides the link between diffusion and conductivity, but it reveals that  $D$  is proportional to  $(\sigma T)$  rather than  $\sigma$ , and it would be more appropriate to plot  $\log(\sigma T)$  instead of  $\log \sigma$ . For polymer gel electrolytes the temperature range covered is often short and the variation in  $1/T$  is substantially greater than the change in  $\log T$  so that latter can be considered as approximately constant and  $(\sigma T)$  can be replaced by  $\log \sigma$  [179].

### 1.3.2 Vogel-Tamman-Fulcher (VTF) Model

For solid electrolytes, which involve ion hopping between fixed sites, graph of  $\log(\sigma)$  versus  $1/T$  are straight lines, but for the polymer electrolytes the  $\log(\sigma)$  versus  $1/T$  plots are often curved. Such behavior would be for materials such as polymer electrolytes in which conduction occurs in the amorphous region and the conduction process is better describe by the Vogel-Tamman-Fulcher (VTF) equation [180-182].

$$\sigma = AT^{1/2} \exp\left[\frac{-E'_a}{k(T-T_0)}\right]$$

Or,

$$\sigma = \sigma_0 \exp\left[\frac{-B}{k(T-T_0)}\right] \quad (1.2)$$

where  $B$  is a constant, whose dimensions are that of energy, but which is not simply interpreted as an activation term. In configurational entropy terms,  $T_0$  is the temperature at which the probability of configurational transition tends to zero, and it is generally regarded as having a value between 20 to 50 K below glass transition temperature ( $T_g$ ). The value of conductivity becoming vanishingly small as  $T_0$  approaches to  $T$ .

If the conductivity versus temperature dependence curve is linear in large temperature range then it is said to be Arrhenius. VTF (curved) behavior can be modeled as Arrhenius (linear) behavior of dividing the entire temperature range into smaller temperature regions. The interconnection between Arrhenius and VTF behavior of  $\sigma(T)$  are widely reported and discussed in literature [183]. This behavior is rationalized by arguing that since VTF dependence is governed by energy interval  $k(T-T_0)$  and the Arrhenius dependence by the energy  $kT$  (where  $k$  is Boltzmann constant), for  $T \gg T_0$  i.e. when  $T_0$  is quite smaller than  $T$ , the curvature of conductivity versus temperature plot becomes small and VTF equation approaches Arrhenius equation [184].

### 1.3.3 William-Landel-Ferry (WLF) model

In an amorphous polymer above its glass transition temperature, a single empirical function can describe the temperature dependence of all mechanical and electrical relaxation processes. The temperature dependence at a number of relaxation and transport processes can be describe by William-Landel-Ferry (WLF) equation [185].

$$\log \left[ \frac{\eta(T)}{\eta(T_s)} \right] = \log a_T = - \frac{C_1(T - T_s)}{C_2 + T - T_s} \quad (1.3)$$

where  $a_T$  is the mechanical shift factor (express the fluidity or inverse relaxation time or relaxation rate),  $\eta$  is the viscosity,  $T_s$  is reference temperature (usually  $T_s = T_g + 50 \text{ K}$ ) and  $C_1$  and  $C_2$  are constants.

### 1.3.4 Dynamic Bond Percolation (DBP) Model

Kohlrausch summation and Nernst-Einstine relation do not fit well in polymer ionics and the deviation become more significant as the salt concentration increases. In the former case ions move by a local liquid like process rather than by hopping from site to site in an ordered



polymer host. To describe conduction mechanism in polymers adequately, it is important to model it microscopically. Dynamic bond percolation (DBP) theory [186] is a microscopic model for diffusion in dynamical disordered systems. The model assumed that mobile ions move from site to site within the polymer host and the sites lie on a regular lattice.

Assuming simple first-order hopping chemical kinetics for the ion motion, the probability of finding an ion at site  $j$  can be written as

$$\frac{dP_j}{dT} = \sum_j (P_j W_{ji} - P_i W_{ij}) \quad (1.4)$$

where  $W_{ji}$  is hopping rate from site  $j$  to site  $i$ .

The difference between dynamic disordered hopping and ordinary hopping is that the hopping rates  $W_{ij}$  are themselves time dependent, and evolve on the time scale of relaxation of the polymer host. The model of equation (1.4) becomes specific to a percolation situation when it is assumed that  $W_{ij}$  have only two values: each  $W_{ij}$  can be either 0 (probability of  $1-f$ ) or a constant value  $w$  (probability  $f$ ). The assignment of any given bond between cells  $i$  and  $j$  as available (value  $w$ ) or unavailable (value 0) itself evolve in time. The simplest assumption is that the value of the bonds as available or unavailable is reassigned randomly after a renewal time  $\tau_{\text{ren}}$ . This model is then characterized by the two-time scales  $\tau_{\text{ren}}$  and the hopping time,  $1/w$ . The renewal time is determined by the local microviscosity of the solvent. The rate of renewal is the inverse local relaxation time that determines bond breakage near the mobile ions.

### 1.3.5 Free Volume Model

Cohen and Turnbull [187] first proposed the “free volume theory” of transport phenomena in glass forming materials. They derive the equation for diffusion coefficient,  $D$ ,

$$D = ga^* u \exp\left[-\frac{\gamma V^*}{V_f}\right] \quad (1.5)$$

where  $g$  is the geometrical factor,  $a^*$  is approximately equal to the molecular diameter,  $u$  is the average speed of the molecules,  $\gamma$  is numerical factor introduced to correct for overlap of free volume and  $V^*$  is the critical volume just large enough to permit another molecules to jump in after the displacement. Cohen and Turnbull define the free volume as [187]

$$V_f = V - V_0 \quad (1.6)$$

where  $V$  is the average volume per molecule in the liquid and  $V_0$  is the Van der Waals volume of the molecule.

Using the Nernst-Einstein equation

$$\sigma = \frac{q^2 n D}{kT} \quad (1.7)$$

It follows that

$$\sigma = \frac{q^2 n g a^* u}{kT} \exp\left(\frac{-\gamma V^*}{V_f}\right) \quad (1.8)$$

In this equation,  $n$  and  $q$  are the concentration and charge of the charge carriers respectively;  $k$  is the Boltzmann's constant.

Free volume theory in this form has been applied to polymer electrolytes by several workers [188, 189]. This theory predicts that at a constant free volume, the conductivity should decrease weakly with increasing temperature because kinetic theory requires that  $u$  vary as  $T^{1/2}$ . Since the remaining terms in equation (1.8) are approximately temperature independent, equation (1.8) can be rewritten as

$$\sigma = \frac{C}{T^{1/2}} \exp\left(\frac{-\gamma V^*}{V_f}\right) \quad (1.9)$$

where  $C$  includes the charge carrier concentration. But the experimental data show that the electrical conductivity at constant specific volume increases strongly with temperature. The conclusion that equation (1.9) is not supported by the data is based on the assumption that the free volume is proportional to the macroscopic volume.

Cohen and Turnbull made the assumption that

$$V_f = V_0 \left( \exp\left[ \int_{T_0}^T \alpha dT \right] - 1 \right) \quad (1.10)$$

where  $\alpha$  is the thermal expansion coefficient. A slightly different approximation often made is that the thermal expansion of free volume is the difference in thermal expansion coefficient of bulk material above and below  $T_g$  [189]. However, when the microscopic volume is held constant, the ionic conductivity increases strongly with temperature. Consequently, if the free volume varies as microscopic volume, as follows from the definition given in equation (1.6), free volume theory is not capable of representing the constant volume electrical conductivity

for a typical polymer electrolyte. The disagreement between theory and experiment is not surprising since the theory was originally developed for simple Van der Waals liquid and metallic liquids [187]. Inability of free volume theory to account for the phenomena governed by segmental motions has been wisely pointed out in literature [190,191].

One of the first attempts to modify the free volume theory to account for the temperature variation of physical phenomena was made by Macedo and Litovitz [192]. They employed the reaction rate theory of Eyring [193] to arrive at the following equation for the shear viscosity

$$\eta = \left( \frac{RT}{E_v} \right)^{1/2} \frac{(2mkT)^{1/2}}{V^{2/3}} \exp \left[ \frac{\gamma V^*}{V_f} + \frac{E_v}{kT} \right] \quad (1.11)$$

where  $r$  is gas constant,  $E_v$  is the height of potential barrier between equilibrium positions,  $V$  is a quantity roughly equal to the volume of a molecule and  $m$  is the molecular mass. Next, the Stokes-Einstien equation

$$\eta = \frac{kT}{6\pi Dd} \quad (1.12)$$

where  $d$  is the molecular radius, is used. It is known that Stokes-Einstien equation breaks down for fragile glasses near  $T_g$  [194]. The Nernst-Einstien equation is used to obtain the following equation for the conductivity

$$\sigma = \frac{q^2 n V^{2/3}}{6\pi d (2mkT)^{1/2}} \left( \frac{E_v}{kT} \right)^{1/2} \exp \left[ -\frac{\gamma V^*}{V_f} - \frac{E_v}{kT} \right] \quad (1.13)$$

At constant volume, equation (1.3) can be written as

$$\sigma = \frac{B}{T} \exp \left[ -\frac{E_v}{kT} \right] \exp \left[ -\frac{\gamma V^*}{V_f} \right] \quad (1.14)$$

Because the temperature dependence in the first exponential term, this equation can account for a strong increase of the conductivity at constant volume and was used by Macedo and Litovitz to successfully reproduce the pressure and temperature dependence of the shear viscosity of several liquids [192]. These include several materials exhibiting VTF or WLF behavior. Equation (1.14) can account for VTF or WLF behavior because both types of behavior are represented by the free volume factor.

## 1.4 Swift Heavy Ion Irradiation of Polymer Electrolytes

Ion beams have become an integral part of various surface processing schemes and in modification of surface layers of solids [195]. Recently there has been enormous growth of interest in high energy ion irradiation polymers and other insulating materials [196-201]. Swift heavy ion (SHI) irradiation can modify the molecular structure in polymers in a controlled way leading to changes in their chemical, electronic, electrical, tribological and optical properties [202, 203]. SHI (energy > 1 MeV/u) irradiation deposits the energy in the material in the near surface region mainly due to the electronic excitation [204]. Ion irradiation of polymers can induce irreversible changes in their macroscopic properties. Electronic excitation, ionization, chain scission and cross-links as well as mass losses are the events that give rise to the observed macroscopic changes. The impinging ions do not get implanted in the material due to their large range typically a few tens of  $\mu\text{m}$ . Ionization trail produced by SHI causes bond cleavages producing free radicals, which are responsible for most of the chemical transformations in polymers: chain scission, cross linking, and double and triple bond formation. The structural modifications in polymers depend on electron energy loss  $S_e$  and ion fluence. At low fluence, small value of  $S_e$  produces decrease in free volume i.e. densification occurs. Beyond a threshold  $S_e$  value SHI produces zone of reduced density along its trajectory (ion track).

An important parameter, which characterizes ion-to-target energy transfer, is the energy loss  $dE/dx$  ( $\text{eV}/\text{\AA}$ ), defined as the energy deposition per unit length along ion track. The value of  $dE/dx$  changes with ion energy. When an energetic ion penetrates into a polymer material, it loses energy during their passage through the material, which is either spent in displacing atoms (of the sample) by elastic collisions (referred to as nuclear stopping) or exciting the atoms by inelastic collisions (referred to as electronic stopping).

### 1.4.1 Nuclear Energy Loss

Nuclear energy loss  $S_n$  arises from collisions between the energetic particle and the target nuclei, which cause atomic displacement and phonons [205]. Displacement takes place when the colliding particle imparts energy greater than certain displacement threshold energy,  $E_d$ , to target atom.  $E_d$  is the energy that recoil requires to overcome the binding forces and to move more than one atomic spacing away from its original site. At low energies ( $= 1 \text{ keV/nucleon}$ )

the incident ion primarily undergoes nuclear energy loss ( $S_n$ ) [206]. Nuclear energy loss is derived with consideration of momentum transfer from ion to target atom and inner atomic potential between two atoms. Thus  $S_n$  varies with ion velocity as well as the charges of two colliding atoms. Nuclear energy loss becomes important when an ion slows down to approximately the Bohr velocity. Therefore nuclear energy loss occurs near the end of the ion track for high-energy ions.

#### **1.4.2 Electronic Energy Loss**

Electronic energy loss  $S_e$  arises from electromagnetic interaction between the positively charged ion and the target electrons. One mechanism is called glancing collision (inelastic scattering, distant resonant collisions with small momentum transfer) and the other one is called knock-on collision (elastic scattering, close collisions with large momentum transfer). Both the collisions transfer energy in two ways: electronic excitation and ionization. All excited electrons lose energy as they thermalize. Glancing collisions are quite frequent but each collision involves a small energy loss ( $< 100$  eV). On the other hand, knock on collisions are very infrequent but each collision imparts a large energy to the target electrons ( $> 100$  eV). Theoretical and experimental evidence suggested that approximately one half of electronic energy loss is due to glancing collisions and other half is due to knock-on collisions [205]. At high energies (100 keV/nucleon) the incident ion undergoes electronic energy loss  $(dE/dx)_e$ , and if the films are sufficiently thin compared to stopping range of the ion, the electronic energy loss is reasonably uniform throughout the film thickness.

The passage of the ion through an insulator produces a positively charged cylinder, which explodes radially due to Coulomb force, causing coherent radial atomic movements until the ions are screened by the conduction of electrons. Due to the resulting cylindrical shock wave, which is known as Coulomb explosion [207], columnar defects are formed. The other competing process, which can lead to the formation of the columns, is thermal spike [207]. According to this model, during the passage of SHI kinetic energy of the ejected electrons is transmitted to the lattice by electron-phonon interaction, resulting in the increase of local lattice temperature above the melting point of the material. A rapid quenching follows the temperature increase, which results in an amorphous columnar structure when the melt solidifies.

## 1.5 Scope of the Thesis and Statement of Thesis Problem

Tremendous research efforts have been made worldwide in the last four decades to develop new ion conducting membranes with improved electrical, electrochemical and mechanical properties. The most widely studied poly(ethylene oxide) (PEO) based solid polymer electrolytes (SPEs) complexed with lithium salts have not yet been used for practical applications because they possess very low ionic conductivity ( $10^{-7}$  to  $10^{-8}$  Scm<sup>-1</sup>) at ambient temperature [8], despite a high solvating power for lithium salts and compatibility with lithium electrode [207]. Addition of nanofillers leads to enhancement of ionic conductivity as well as mechanical property in SPEs. However the conductivity value still falls far away to be used in practical applications. Plasticized or gel polymer electrolytes (GPEs) have high ambient temperature ionic conductivity by immobilizing a large amount of liquid electrolyte in the polymer host [4, 5]. The conductivity and mechanical stability of GPEs are mutually exclusive i.e. the ionic conductivity in GPEs increases at the expense of mechanical strength and vice versa [17]. Moreover, leakage of organic liquid solvents from the polymer electrolyte is yet another problem for GPEs when used in a device over a long period of time. This leakage leads to a decrease in ionic conductivity with damage to the lithium electrode and other components. Nanocomposite gel polymer electrolytes, on the other hand combine the high ambient conductivity of conventional gel electrolytes with the excellent stability toward the metal electrode and the good mechanical properties of nanocomposite electrolytes [152]. Nanocomposite gel polymer electrolytes can be obtained either from a nanocomposite polymer electrolyte by incorporating a conventional liquid electrolyte into a porous structure of a nanocomposite polymer or from a GPE containing dispersed nanoparticles. However due to the absence of exact structure–property correlations in nanocomposites gel polymer electrolytes, a complete understanding of the ion conduction phenomenon is still lacking. In the present work, an attempt has been made to gain an insight into the ion conduction mechanism (ion-polymer, ion-ion and polymer–filler interfacial interaction) in the polymer electrolytes and develop new nanocomposites gel polymer electrolytes with: (i) high ionic conductivity (ii) good thermal, electrochemical and interfacial stability (iii) mechanically strong and flexible (iv) ease of processing and (v) high affinity with organic liquid electrolytes.

To achieve the aforesaid objectives, in the present work the following polymer electrolytes systems have been investigated:

- (i) PMMA-(PC+DEC)-LiClO<sub>4</sub>-dedoped (insulating) polyaniline nanofibers.
- (ii) P(VdF-HFP)-(PC+DEC)-LiClO<sub>4</sub>-dedoped (insulating) polyaniline nanofibers.
- (iii) PEO/P(VdF-HFP)-(PC+DEC)-LiClO<sub>4</sub>.
- (iv) PEO/P(VdF-HFP)- LiClO<sub>4</sub>-dedoped (insulating) polyaniline nanofibers.
- (v) PMMA-(PC+DEC)-LiClO<sub>4</sub>-modified montmorillonite (MMT).
- (vi) PVdF-(PC+DEC)-LiClO<sub>4</sub>-modified montmorillonite (MMT).
- (vii) PEO- modified montmorillonite (MMT) single ion conductor.

Ionic conductivity of the polymer electrolytes was measured by complex impedance spectroscopy. Wagner polarization technique was employed to measure the total ionic transport number of the polymer electrolytes. Structural characterization was done by X-ray diffraction analysis. FTIR was carried out to investigate the different bond interactions among polymer-ion-filler so as to understand dynamics of ion conduction processes in the polymer electrolytes. Scanning electron microscopy studies were carried out to investigate the microstructure and surface morphology (SEM) of polymer electrolytes. Tunneling electron microscopy studies (TEM) were carried out to observe the size, shape and distribution of the nanofillers used in the present work.

Swift heavy ion irradiation (SHI) on polymers plays an important role in modifying chemical structure and physical properties of polymers. Intensive research efforts are going on in the field to study the irradiation effects on polymers. With a view to increase the ionic conductivity, P(VdF-HFP)-(PC+DEC)-LiClO<sub>4</sub>-dedoped (insulating) polyaniline nanofibers and PEO- modified montmorillonite (MMT) electrolyte systems were irradiated with 90 MeV O<sup>7+</sup> ion beams of several different fluences. Results show that in case of P(VdF-HFP)-(PC+DEC)-LiClO<sub>4</sub>-dedoped (insulating) polyaniline nanofibers polymer electrolytes irradiation with swift heavy ion increases the ionic conductivity of the composite gel polymer electrolyte films at lower fluences ( $\leq 10^{11}$  ions/cm<sup>2</sup>) and decrease at higher fluences ( $\geq 10^{11}$  ions/cm<sup>2</sup>) as compared to that of the unirradiated film. At lower fluence scissioning of polymer chain takes place, which leads to faster ionic transport through the polymer matrix assisted by larger segmental motion of the polymer backbone. However at higher fluence a combined effect of phase separation and cross-linking of polymer chains seems to dominate

resulting in decrease in ionic conductivity. Swift heavy ion irradiation on PEO-MMT nanocomposites results in intercalation of PEO chains at lower fluence and exfoliation above a critical fluence. This has been explained on the basis of shifting and disappearance of (001) diffraction peak of MMT in XRD patterns. Strain calculations reveal that the compressive strain increases with the increase of ion fluence, which ultimately leads to the exfoliation of MMT layers. About 1.5 orders of magnitude enhancement in ionic conductivity has been observed for the sample irradiated with the fluence of  $5 \times 10^{12}$  ions/cm<sup>2</sup> as compared to that of the unirradiated sample. FTIR and XRD analyses have been carried out to investigate the interactions and change of structure after SHI irradiation in these two systems.



## CHAPTER II

### Theoretical Aspects

---

---

*The present thesis deals with the ionic transport phenomena in gel, composite and layered silicate nanocomposites polymer electrolytes. This chapter describes the theoretical aspects of complex impedance spectroscopy, models and mechanisms that explain the ion transport kinetics in solvent-free, gel, composite and polymer/layered silicate nanocomposite electrolytes. Salient points of dielectric spectroscopy and its different formalisms have also been discussed in this chapter.*

---

---

#### 2.1 Electrical Conductivity and Impedance Spectroscopy

Generally, the expression for conductivity ' $\sigma$ ' is given as

$$\sigma = G \cdot \frac{l}{A} = \frac{1}{R} \left( \frac{l}{A} \right) S cm^{-1} \quad (2.1)$$

where  $G$  (1/Resistance) is the conductance of the sample,  $R$  is the resistance,  $l$  is the sample's thickness or separation between electrodes and  $A$  is the area of the electrode.

Measuring the ionic conductivity of materials is not as straightforward as is the case for electronic conductors. In the case of electronic conductors, conductivity can be measured directly by applying a d.c. potential by using either two-probe or four-probe methods. In the case of ionic conductors, the d.c. potential cannot be applied as it leads to the occurrence of fast interfacial polarization, which results in the continuous increase in resistance as a function of time. In order to avoid these problems, two different methods have been adopted for the measurement of ionic conductivity of solids: d.c. method and a.c. method.

##### 2.1.1 Direct Current Method (D.C. Method)

In this method, a constant d.c. potential or current is applied across a cell comprising of electrolyte sandwiched between two reversible electrodes, and the resulting current or potential are monitored. By putting  $R = (V/I)$  in the equation 2.1, the conductivity can be written as

$$\sigma = \frac{I}{V} \cdot \frac{l}{A} \quad (2.2)$$

where  $V$  is the voltage and  $I$  is the current.

Two types of d.c. conductivity techniques can be used to measure the ionic conductivity:

- (i) Two probe, and
- (ii) Four probe methods.

In the two probe method, a known d.c. potential is applied across the cell, (in which electrolyte material is sandwiched between the two reversible electrodes) and a resulting current is measured to determine the d.c. resistance. Whereas, in the four probe method, a known d.c. current is applied between two outer electrodes and the potential is measured between two inner electrodes. Conductivity can be calculated by measuring the area of the two inner electrodes and the distance between them. The experimental set-up for the four-probe method is given in figure 2.1.

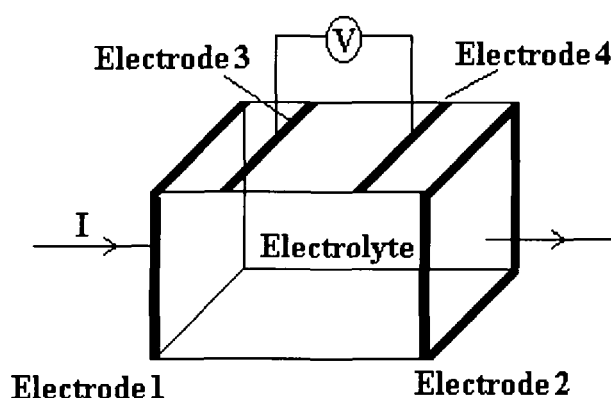


**Figure 2.1:** Experimental set-up for four probes method.

Though the d.c. technique for the measurement of ionic conductivity appears quite simple, it possesses many practical difficulties, e.g. it is very difficult to get reversible electrodes for both the cations and anions, there is also a contribution of electrode-electrolyte interfacial resistances to the overall conductivity, presence of grain boundary conduction, formation of a double layer due to concentration polarization etc. Further, the interpretation of the electrical conductivity data is also very difficult due to the presence of more than one phase in the polymeric materials. Combination of all the above difficulties led the researchers to switch over to a.c. methods rather than the d.c. methods.

### 2.1.2 Alternating Current Method (A.C. Method)

The a.c. methods are used for the determination of electrical conductivity to minimize the various polarization effects. The technique is called “Impedance Spectroscopy” according to which a sinusoidal voltage is applied to a cell, comprising of an electrolyte sandwiched between two blocking or non-blocking electrodes, and the resulting cell current passing through the cell as a result of this perturbation is determined. The resulting current is related with the applied sinusoidal voltage by two different parameters, which are

- (i) The ratio of the current and voltage maxima,  $V_{\max}/I_{\max}$  (analogous to resistance in d.c. measurements), and
- (ii) The phase difference ‘ $\theta$ ’ between the voltage and the current.

The combination of these two parameters represents the impedance ‘ $Z$ ’ of the cell. Both the magnitude of impedance ( $|Z| = V_{\max}/I_{\max}$ ) and the phase angle ‘ $\theta$ ’ are the functions of applied frequency. The impedance of a cell is measured as a function of applied frequencies, over a wide range of frequencies, typically, 1 mHz - 1 MHz [208]. The Impedance Spectroscopy enables us to evaluate and separates the contribution of different electrical parameters in different frequency regions such as bulk phenomena, i.e. the migration of ions through the bulk and across the grain boundaries within the electrolyte, interfacial phenomena due to electrode reactions at the electrode/electrolyte interfaces [209, 210] etc. This study was also applied successfully for the study of dielectric properties of the materials by Cole and Cole [211]. Bauerly [212] was the first to propose a generalized complex impedance/admittance plot method to extract the true bulk conductivity from the a.c. conductivity measurement. The subsequent developments in this field have been reviewed extensively in the literature [213-220].

Impedance of a cell is a vector quantity and this vector may be represented by its  $x$  and  $y$  components:  $|Z| \cos\theta$  and  $|Z| \sin\theta$ .  $Z^*$  represents complex impedance.  $Z'$  and  $Z''$  are the real and imaginary components of the complex impedance  $Z^*$ . It can be displayed in a complex plane in several different forms:

$$\text{Complex impedance } Z^*(\omega) = Z' - j Z'' = R_s - j / \omega C_s \quad (2.3)$$

$$\text{Complex admittance } Y(\omega) = Y' + j Y'' = 1 / R_p + j \omega C_p = G(\omega) + j B(\omega) \quad (2.4)$$

$$\text{Complex modulus } M(\omega) = 1 / \varepsilon(\omega) = M' + j M'' = j \omega C_0 Z(\omega) \quad (2.5)$$

$$\text{Complex permittivity (Dielectric constant), } \varepsilon(\omega) = \varepsilon' - j\varepsilon'' \quad (2.6)$$

$$\text{Loss Tangent } \tan \delta = \varepsilon'' / \varepsilon' = M'' / M' = -Z'' / Z' = Y'' / Y' \tag{2.7}$$

$$\text{Complex resistivity } \rho(\omega) = \rho' + j \rho'' = Z \times (C_0 / \varepsilon_0) \tag{2.8}$$

$$\text{Complex conductivity } \sigma(\omega) = \sigma' - j \sigma'' = Y \times (\varepsilon_0 / C_0) \tag{2.9}$$

where  $j = \sqrt{-1}$ ,  $C_0$  is vacuum capacitance of the cell,  $G$  is the conductance and  $B$  is susceptance (subscripts  $s$  and  $p$  are for series and parallel combinations of the circuit elements, respectively).

Out of these parameters, the impedance and admittance plane representations provide useful information when various processes within the cell have different relaxation times as in the case with the solid electrolyte cells. In this regard, Randles [221] was the first to successfully show that the electrical processes occurring within the cell could be represented by an electrical equivalent circuit comprising of resistors, capacitors, inductors and their series and parallel combinations. This equivalent circuit shows almost the same phenomenological processes within the cell. Practically the equivalent circuit consists of resistors and capacitors in terms of which the charge migration and polarization occurring within the cell can be represented. A general practice is to represent one charge polarization or migration process by one parallel RC combination. Hence, a model of equivalent circuit for a general solid electrolyte consists of three parallel RC circuits connected in series. Each of the parallel combinations represents contributions due to the bulk properties of the material, electrode-electrolyte interfacial processes and grain boundary conduction in different frequency ranges respectively as shown in figure 2.2.

The simplest possible circuit in an electrochemical cell consists of an overall resistance ( $R$ ) due to electrolyte, electrodes and lead wires in series with a parallel circuit comprising charge transfer resistance ( $R_{ct}$ ) at the electrode/electrolyte interface and Warburg impedance ( $W$ ) representing diffusion polarization in parallel with the double layer capacitance as shown in figure 2.3

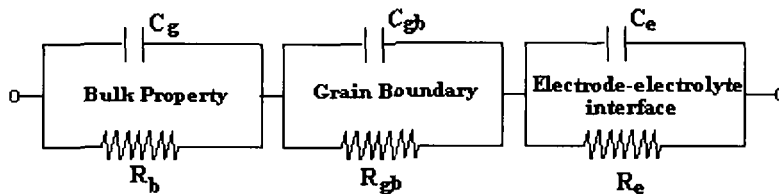


Figure 2.2: Equivalent circuit model of a typical electrolyte.

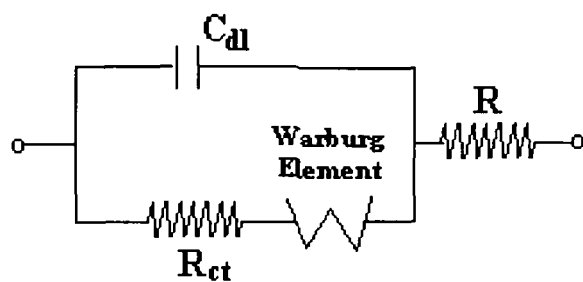
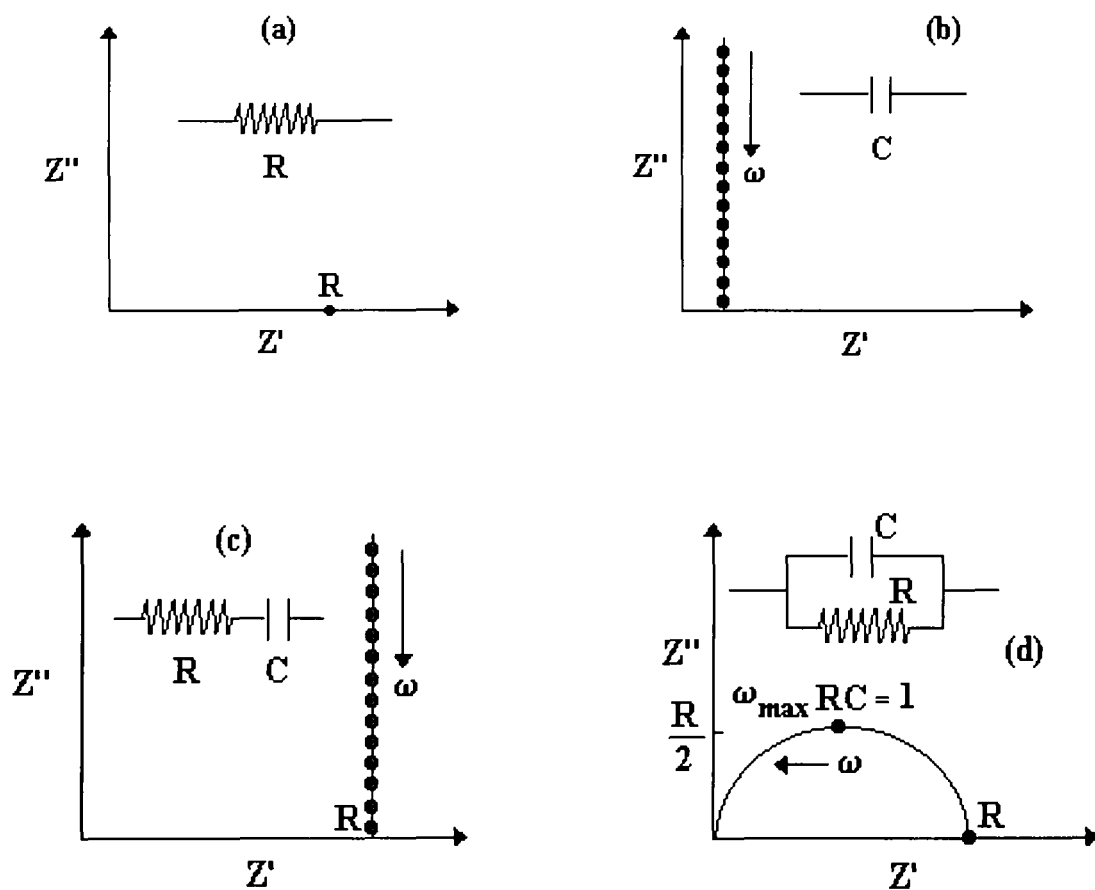


Figure 2.3: Equivalent circuit representation of an electrochemical cell.

The impedance plots of some simple electrical circuits are shown in figures 2.4 (a-f).



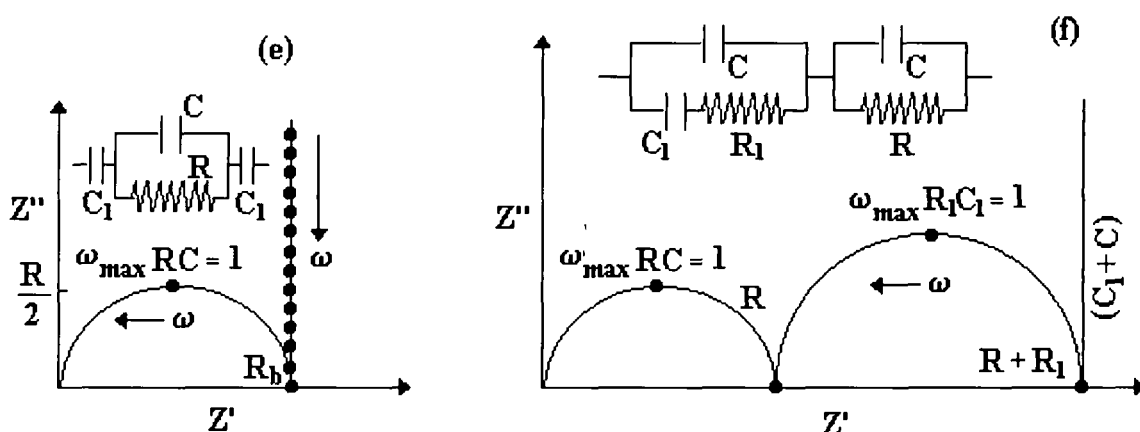


Figure 2.4: Impedance plots of some simple RC circuits.

Let us consider a cell comprising of a polymeric gel electrolyte sandwiched between two identical electrodes under a small input signal perturbation. The electrical behavior of such a cell is controlled by the bulk electrolyte resistance, the charge transfer (double layer) capacitance at the electrode-electrolyte interface and the geometrical capacitance, which can be represented in the form of an equivalent circuit. The geometrical capacitance would arise due to an analogous capacitor comprising of two electrodes separated by a dielectric medium. Depending on the types of electrodes used (i.e. either blocking or non-blocking electrodes) and types of electrolytes having single mobile ion species (in conventional solid electrolytes) or double mobile ion species (both cations and anions as observed in the liquid or polymer electrolytes), the behavior of the cells, their impedance patterns and hence their equivalent circuits are distinctly different, which are described briefly as follows:

### 2.1.2.1 Blocking Electrodes

Figures 2.5 (a & b) show the cell with blocking electrodes and single ion conducting electrolyte, its ideal impedance pattern and the equivalent circuit representing its a.c. response. The bulk polarization and ion migration in the electrolytes are reflected as a semicircle in the impedance plot, generally observed in the middle/high frequency range. This semicircular spur indicates that the representative components  $R_b$  (bulk resistance) and  $C_g$  (geometrical capacitance) are connected in parallel combination. The double layer capacitance  $C_e$ , built up due to the charge accumulation at electrode-electrolyte interfaces, appears as a spike rising at right angle parallel to imaginary axis in the low frequency region

of impedance plot as shown in the figure 2.5 (b) and connected in series with parallel combination of  $R_b$  and  $C_g$  as shown in inset in the figure 2.5 (b).

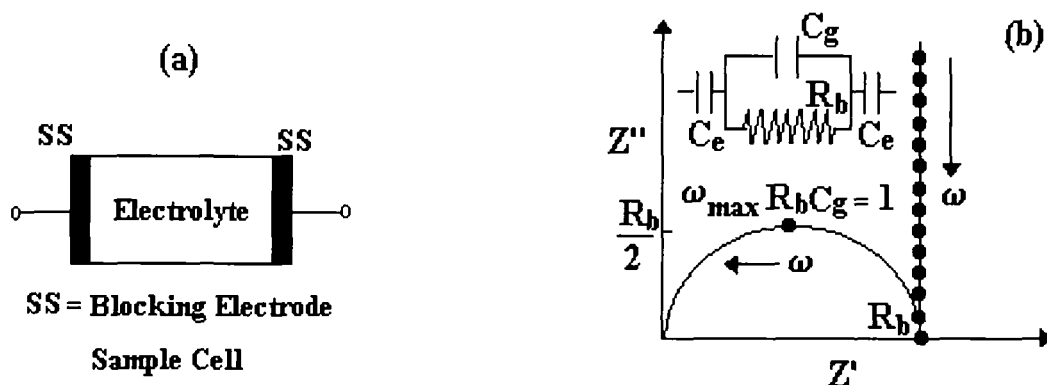


**Figure 2.5:** Schematic representation of (a) an electrochemical cell with blocking electrodes, (b) impedance plot. The equivalent circuit is shown in inset.

It is generally observed that the middle/high frequency response gives information about the properties of the electrolyte, whereas the low frequency response carries information about the electrode-electrolyte interfaces. Overall, the magnitude of all the fundamental electrical properties of the cell may be obtained from the complete impedance data. Particularly, the bulk resistance  $R_b$ , of the electrolyte can easily be evaluated by sandwiching the electrolyte between two blocking electrodes.

Generally, the equivalent circuit and the impedance plot, as shown in the figure 2.5 (b), are equally applicable to the liquid/polymer electrolytes having more than one mobile ionic species, sandwiched between the two blocking electrodes.

### 2.1.2.2 Non-Blocking Electrodes (Reversible Electrodes)

In the case of non-blocking electrodes or reversible electrodes, there is a finite reversible electrode reaction at the electrode-electrolyte interfaces, which allow the dissolution of mobile ionic species in the electrodes. Figures 2.6 (a & b) show the impedance plots of the cell consisting of (a) single ion conducting electrolyte, and (b) both the cation and anion conducting electrolyte (e.g. liquid / polymeric gel electrolyte). The equivalent circuits are shown in their corresponding insets.

In the case of single ion conducting electrolyte, the high frequency semicircle in the impedance plot is observed due to the parallel combination of  $R_b$  and  $C_g$  (representing bulk

properties of the electrolyte) similar to the pattern observed in case of the cell with blocking electrodes. In addition to this another semicircle is observed in the middle frequency region, which is the representation of a.c. response of the electrode/electrolyte interface. This is represented by a parallel combination of a finite charge-transfer resistance  $R_e$  and charging-discharging double layer capacitance  $C_e$ .

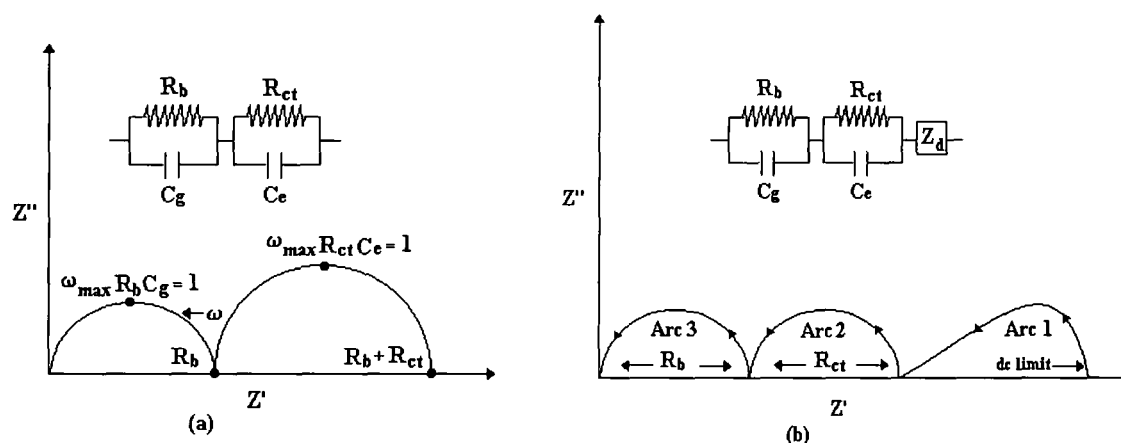


**Figure 2.6:** Schematic representation of impedance plots for the cells with non-blocking electrodes consisting of (a) single ion conducting electrolyte, and (b) both the cation and anion conducting electrolyte (e.g. liquid/polymer gel electrolyte). The equivalent circuits are shown in their corresponding insets.

On the other hand, in the case of a cell with non-blocking electrodes and electrolyte having two mobile ions (cation and anion), there appears three semicircles corresponding to the bulk (high frequency), electrode-electrolyte interfaces (middle frequency), and diffusion impedance due to the concentration gradient of anions developed at sufficiently low frequency, as shown in the above figure 2.6 (b). The low frequency semicircle is skewed and is inclined at an angle of  $45^\circ$  to the real axis. However, all the three features may not be observed in all the cases [210].

In actual practice, it is observed that there is a significant flattening of the ideal semi-circular pattern and tilting of the spike in the impedance spectrum contrary to the ideal spectrum obtained from the equivalent circuit model based on the processes within the polymer electrolyte cell as shown in figures 2.7 (a & b). The effect may be related to the presence of crystalline non-conducting regions interlocked with the conducting amorphous materials within the spherulites of a polymer electrolyte system.



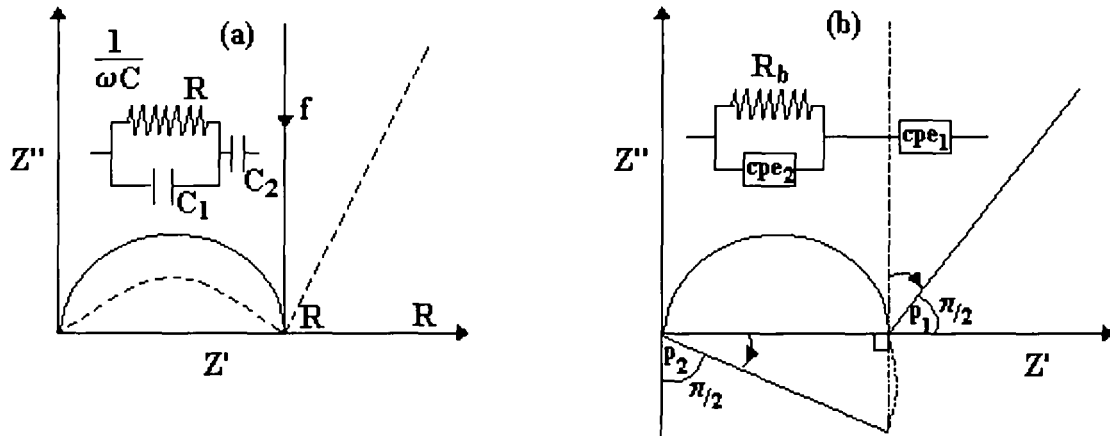


**Figure 2.7:** (a) Equivalent circuit and impedance spectrum (bold line = spectrum for ideal equivalent circuit. Dotted line = Experimental impedance spectrum for gel electrolytes), (b) Depression of semicircle and tilting of spike caused by replacing capacitors by constant phase elements.

The cell behaves as a “leaky capacitor” resulting in the semicircle flattening and spike tilting as shown in the figure 2.7 (a). The effect has also been attributed to a variety of physical phenomena such as the multiple or coupled reaction sequences, roughening of the electrode and frequency dependent ohmic resistances caused by a non-uniform charging of the double layer [222]. In order to account for such effects, a generalized impedance element known as the “constant phase angle element (CPE)” is introduced into the equivalent circuit model, which is shown in the figure 2.7 (b) as inset.

The impedance of the constant phase angle element is given by

$$Z_{CPE} = k (j\omega)^{-p}, \quad 0 \leq p \leq 1 \quad (2.10)$$

When  $p = 0$ ,  $Z$  is frequency independent and ‘ $k$ ’ represents the resistance  $R$ . When  $p = 1$ ,  $Z = k / j\omega = -j / \omega k^{-1}$ , in such a case  $Z$  is now frequency dependent and  $k^{-1}$  represents the capacitance. For  $0 \leq p \leq 1$ , the ‘CPE’ acts, in a way, intermediate between a resistor and a capacitor, which is the case for polymeric materials.

## 2.2 Dielectric Relaxation in Amorphous Materials

Dielectric relaxation in solids is one of the most intensely researched topics in physics, yet there is no satisfactory theoretical understanding of the relaxation phenomena. Relaxation consists of the recovery of strain on removal of stress and it implies therefore time

dependence, typically under sudden removal or sudden application of a steady stress. This is the basis of the time-domain (TD) measurements [223]. An equivalent and often preferable method is to subject the material to a harmonically varying stress of an angular frequency  $\omega$  and this forms the basis of frequency-domain (FD) measurements [224, 225]. Materials are polarized in ac fields by various polarization mechanisms and their permittivity, as a measure of the polarization, shows frequency dependence, namely dielectric relaxation or dielectric dispersion. Dielectric spectroscopy is a technique that measures permittivity and conductivity as a function of frequency in a non-invasive way and can provide insights into the structures and electrical properties of materials at molecular and macroscopic levels.

According to Maxwell's equations,  $\varepsilon^*$  is time (or frequency) dependent if a time dependent process takes place within the sample. Resonance phenomena are due to atomic or molecular vibrations and can be analyzed by optical spectroscopy. Relaxation phenomena, on the other hand, are related to molecular fluctuations of dipoles due to molecules or part of them in a potential landscape. Moreover, drift motion of mobile charge carriers viz., electrons, ions or charged defects also contribute to the dielectric response. Complex dielectric permittivity  $\varepsilon^*$  is defined as

$$\varepsilon^*(\omega) = \varepsilon'(\omega) - j\varepsilon''(\omega) \quad (2.11)$$

where  $\varepsilon'(\omega)$  and  $\varepsilon''(\omega)$  are, respectively, the real and imaginary parts of complex permittivity  $\varepsilon^*$ . The real part  $\varepsilon'(\omega)$  and the imaginary part  $\varepsilon''(\omega)$  of complex permittivity though not always, show dielectric relaxation (or dielectric dispersion) in which  $\varepsilon'(\omega)$  decreases and  $\varepsilon''(\omega)$  increases with increasing frequency. Single dielectric relaxation is characterized by a set of parameters (called relaxation parameters):  $\varepsilon_1$  and  $\varepsilon_h$  are the low- and the high-frequency limits of relative permittivity, respectively,  $\Delta\varepsilon = \varepsilon_1 - \varepsilon_h$  the relaxation intensity (or the relaxation magnitude),  $f_0$  the characteristic frequency and  $\tau (= 1/2\pi f_0)$  the relaxation time. The complex plane plot (or the Cole–Cole plot) is also used for analysis of dielectric relaxation. In the complex plane plot the imaginary part of the complex permittivity or the loss factor  $\varepsilon''(\omega)$  is plotted against the real part of the complex permittivity or the relative permittivity  $\varepsilon'(\omega)$ , tracing a semicircle if the dielectric relaxation

has a single relaxation time, viz., the Debye type relaxation. The complex plane plots, however, often deviate from a semicircle, which indicates a distribution of relaxation times.

### 2.2.1 Formalism of Dielectric Data

Dielectric information may be formulated in a number of equivalent ways and it is important to use the most appropriate form of presentation to match the particular requirement [226]. The following important dielectric functions may be defined.

#### (a) Permittivity formalism

The complex permittivity  $\varepsilon^*(\omega)$  and susceptibility  $\chi^*(\omega)$ ,

$$\chi^*(\omega) \equiv [\varepsilon^*(\omega) - \varepsilon_\infty] / \varepsilon_0 = \chi'(\omega) - i\chi''(\omega) \quad (2.12)$$

where  $\varepsilon_0 = 8.854 \times 10^{-12} \text{ Fm}^{-1}$  is the permittivity of free space,  $\varepsilon_\infty$  is a suitable high-frequency permittivity and the physical emphasis is on parallel processes contributing to the real and imaginary components of the polarization.

#### (b) Modulus formalism

The electric modulus, which is the reciprocal of  $\varepsilon^*(\omega)$ ,

$$M^*(\omega) = M'(\omega) + iM''(\omega) = \frac{1}{\varepsilon^*(\omega)} = \frac{\varepsilon'(\omega) + i\varepsilon''(\omega)}{[\varepsilon'(\omega)]^2 + [\varepsilon''(\omega)]^2} \quad (2.13)$$

which emphasizes series processes that may be acting in the material.

#### (c) Capacitance formalism

The complex capacitance

$$C^*(\omega) = (A/d)\varepsilon^*(\omega) \quad (2.14)$$

which relates to a sample of planar geometry of area  $A$  and thickness  $d$ , or some other appropriate geometrical factor for other geometries. Susceptance is the quantity corresponding to susceptibility

$$X^*(\omega) = C^*(\omega) - C_\infty \quad (2.15)$$

Their use is recommended wherever the geometry of the sample is not well defined. They both emphasize parallel processes acting in the sample.

#### (d) Admittance formalism

The admittance of the sample representing the equivalent parallel conductance  $G(\omega)$  and capacitance  $C(\omega)$

$$Y^*(\omega) = I/V = i\omega C^*(\omega) \equiv G(\omega) + i\omega C(\omega) \quad (2.16)$$

The frequency dependence of these elements arises from the fact that they represent an equivalent circuit of a system that is not necessarily a parallel combination of frequency-independent elements.

*(e) Impedance formalism*

The impedance of the sample, which is the reciprocal of admittance

$$Z^*(\omega) = V/I = 1/Y^*(\omega) \quad (2.17)$$

which emphasizes series processes.

These different formalisms are often used to study different relaxation processes occurring in solids. Electrical relaxation phenomena are usually analysed in terms of the dielectric permittivity by the relaxation of the electric displacement vector,  $D$ , under the constraint of constant electric field,  $E$ . However, in dielectrics containing mobile charges, it seems convenient to concentrate on the relaxation of the electric field,  $E$ , under the constraint of a constant displacement vector,  $D$ , which leads to the inverse dielectric permittivity and the definition of electric modulus. An advantage of using the electric modulus to interpret bulk relaxation properties is that variations in the large values of permittivity and conductivity at low frequencies are minimized. In this way the familiar difficulties of electrode nature and contact, space charge injection phenomena and absorbed impurity conduction effects, which appear to obscure relaxation in the permittivity presentation, can be resolved or even ignored.

There are several ways of presenting the data and the most common ones are as follows.

- (1) Plots of the real and imaginary components either in logarithmic or in linear coordinates against frequency, usually on a logarithmic presentation in view of the very large range of frequencies involved. The log-log form is particularly useful in representing dielectric functions, which are often power-law functions of frequency:

$$\chi^*(\omega) \propto (i\omega)^{n-1} \quad \text{where } 0 < n < 1 \quad (2.18)$$

in the frequency region above any loss peaks, which is referred to as the 'universal' law.

- (2) Polar plots of the imaginary component against the real component, typically on a linear presentation, but the logarithmic presentation introduced by the Chelsea

research Group [227] can be very useful. The usefulness of polar plots is limited mainly to characterization by shape as Debye, Cole–Cole, Cole–Davidson etc. and also as a means of finding series combinations of elements in  $Z$  plots.

### 2.3 Kinetics of Ion Transport in Solid Polymer Electrolytes

The conductivity of any material can be expressed by the relation

$$\sigma = \sum_i n_i q_i \mu_i \quad (2.19)$$

where  $n_i$  is the concentrations of charge carriers of type  $i$ ,  $q$  is the charge and  $\mu$  the mobility. The polymer electrolytes contain no significant conjugation within the polymer backbone, and the salts on which they are based have negligible electronic conductivities, hence electrons and holes do not contribute to the summation in equation (2.19). Both cations and anions contribute to the conductivity. This represents a complication in the simple interpretation of the temperature dependence of conductivity.

For transport in amorphous systems, the temperature dependence of a number of relaxation and transport processes in the vicinity of the glass transition temperature can be described by the Williams-Landel-Ferry (WLF) equation [185] given by

$$\log \frac{\eta(T)}{\eta(T_s)} = \log a_T = \frac{-C_1(T - T_s)}{C_2 + (T - T_s)} \quad (2.20)$$

where  $T$ , is an arbitrary reference temperature, usually  $T_s = T_g + 50$  K,  $a_T$  is called the mechanical shift factor, and  $C_1$  and  $C_2$  are universal constants. Often the WLF equation is coupled with the empirical observation known as Walden's rule [228]

$$D\eta = \text{Const}/r_i \quad (2.21)$$

Stokes-Einstein relationship can be written as

$$D = kT/6\mu\eta r_i \quad (2.22)$$

where  $D$  is the diffusion coefficient and  $r_i$  is the radius.

The Nernst-Einstein relationship can be written as

$$\sigma = DNq^2/kT \quad (2.23)$$

where  $N$  is the number of charge carriers and  $q$  is the charge. Putting the value of  $D$  of equation (2.22) in equation (2.23) one can get

$$\log \frac{\sigma(T)}{\sigma(T_s)} = \frac{C_1(T - T_s)}{C_2 + (T - T_s)} \quad (2.24)$$

Equation (2.24) holds reasonably well for a number of polymer electrolyte systems and a decrease in the  $T_g$  leads to an increase in conductivity.

The WLF relation was an extension of the Vogel-Tamman-Fulcher (VTF) empirical equation [180-182] that was originally formulated to describe the properties of super cooled liquids and, given in its original form, is

$$\eta^{-1} = A \exp \left[ \frac{-B}{k(T - T_0)} \right] \quad (2.25)$$

where  $A$  is a prefactor proportional to  $T^{1/2}$ , which is determined by the transport coefficient (in this case  $\eta^{-1}$ ) at a given reference temperature.  $B$  is a constant, whose dimensions are in fact energy, but which is not simply interpreted as an activation term and  $k$  is Boltzmann's constant. Equation (2.25) holds for many transport properties and, by making the assumption of a fully dissociated electrolyte, it can be related to the diffusion coefficient through the Stokes-Einstein equation giving the form to which the conductivity,  $\sigma$ , in polymer electrolytes is often fitted,

$$\sigma = \sigma_0 \exp \left[ \frac{-B}{k(T - T_0)} \right] \quad (2.26)$$

This form of the equation suggests that thermal motion above  $T_0$  contributes to relaxation and transport processes and low  $T_g$  gives faster motion and faster relaxation.

Writing equation (2.26) in the form

$$\log \frac{\sigma(T)}{\sigma(T_s)} = -\frac{B}{k} \left[ \frac{1}{T - T_0} - \frac{1}{T_s - T_0} \right] \quad (2.27)$$

Comparing equations (2.24) and (2.27)

$$\frac{C_1(T - T_s)}{C_2 + (T - T_s)} = -\frac{B}{k} \left[ \frac{1}{T - T_0} - \frac{1}{T_s - T_0} \right]$$

$$\text{Or, } C_1 = \frac{B}{k(T_s - T_0)} \left[ \frac{C_2 + (T - T_s)}{T - T_0} \right] \quad (2.28)$$

$$\text{Identifying } C_2 = T_s - T_0 \quad (2.29)$$

$$C_1 = \frac{B}{k(T_s - T_0)} \quad (2.30)$$

$$\text{Or, } B = KC_1C_2 \quad (2.31)$$

In an attempt to understand how the conductivity mechanism works, quasi-thermodynamic theories [229-233], originally developed to deal with molten salts and neat polymers, have been applied with some success to consideration of transport properties in polymer electrolytes. These theories are based on considerations involving the critical role of the glass transition temperature  $T_g$  and of the so-called “equilibrium” glass transition temperature  $T_0$ . Above  $T_g$ , the polymeric material becomes macroscopically rubbery rather than glassy [229-233]. The concept of equilibrium glass transition temperature  $T_0$  is based on the kinetic feature of  $T_g$  depending on the rate of cooling, one can observe different glass transition temperatures, and  $T_0$  is idealized as the temperature at which all “free volume” vanishes or at which all polymer segment motion disappears or at which the excess configurational entropy of the material vanishes. The theoretical scheme, which treats  $T_0$  in terms of volume, is called the free volume theory [187, 229].

The free volume model is the simplest way to understand the polymer segmental mobility. It states that as temperature increases, the expansivity of the material produces local empty space, free volume, into which ionic carriers, solvated molecules, or polymer segments themselves can move. The overall mobility of the material is determined by the amount of volume present in the material. One can obtain, for diffusivity  $D$ , the form

$$D = BRT \exp\left(\frac{-V^*}{V_f}\right) \quad (2.32)$$

where  $B$  and  $V^*$  are constant,  $R$  is gas constant and  $V_f$  is the free volume

When the volume is expanded in terms of the volume at glass transition temperature plus a linear term, the free volume yields the form [31, 234, 235]

$$D = D_0 T \exp\left(\frac{-a}{T - (T_g - C_2')}\right) \quad (2.33)$$

where the constant  $a$  and  $C_2'$  are both inversely related to the free volume thermal expansion factor.

Rewriting equation (2.33) as

$$D = D_0 T \exp\left(\frac{-a}{C_2 + T - (T_g - C')}\right) \quad (2.34)$$

where  $C_2 = C_2' - C'$ . If  $C' = 0$ , the free volume argument yields the WLF relation of equation (2.20).

Motion of ions in polymer electrolytes is strongly dependent on segmental motion of the polymer host. Based on this and assuming a weak dependence of the conductivity on interionic interactions, Druger, Nitzan and Ratner proposed a microscopic model based on dynamic bond percolation (DBP) theory [25, 235]. For conductivity in polymer electrolytes, cation and anion motions are considered to be fundamentally different. The former is visualized as the making and breaking of coordinate bonds with motion between coordinating sites, while anion motion is regarded as a hopping between an occupied site and a void, which is large enough to contain the ion. Conductivity is visualized as being due to a combination of cooperative motion with the occasional independent ion movement; the time scale for the latter is much shorter than for polymer relaxation.

The rate of jumping (i.e. of ion motion) between any two sites is represented in terms of simple first order chemical kinetics, using the master equation

$$\frac{dP_i}{dT} = \sum_j (P_j W_{ji} - P_i W_{ij}) \quad (2.35)$$

$P_i$  is the probability of finding a mobile ion at site  $i$ ,  $W_{ij}$  is the probability per unit time that an ion will hop from site  $j$  to site  $i$  and is equal to zero except between neighboring sites. It is then assumed that  $W_{ij}$  may take two values,

$$\begin{aligned} W_{ij} &= 0 \text{ (probability } 1-f) \\ W_{ij} &= w \text{ (probability } f) \end{aligned} \quad (2.36)$$

with  $W_{ij}$  equal to zero, if all sites are already filled. Jumps are available with a relative probability  $f$  ( $0 \leq f \leq 1$ ). Because of polymer motion, the configuration is continually changing and sites move with respect to each other. Therefore hopping probabilities readjust or renew their values on a time scale  $\tau_{\text{ren}}$ , which is determined by the  $r$  motion of the polymer. The  $W_{ij}$  values are thus fixed by the parameters  $w$ ,  $f$  and  $\tau_{\text{ren}}$ . A number of results can be obtained from this model:



- (i) For an observation time  $\gg \tau_{ren}$ , with  $f > 0$ , ionic motion is always diffusive i.e. the mean squared displacement is always proportional to time.
- (ii) The diffusion coefficient is, in general, proportional to  $(\lambda)$ , the average rate of renewal. This corresponds well both to the wealth of experimental data indicating that the ionic motion is modulated by the segmental motions of the polymer host and to the expectation, that structural reorganization and conductivity arise from the same underlying motion mechanism.
- (iii) It is possible to show in great generality that

$$D_0(\omega + i\lambda) = D(\omega) \quad (2.37)$$

That is, the diffusion coefficient at frequency  $\omega$  in the renewing (dynamic) percolation problem may be found from the diffusion coefficient in the static (non renewing) percolation problem, analytically continued to frequency  $\omega + i\lambda$ .

- (iv) The factor  $f$ , giving the number of available jumps, will be substantially different for cationic (strongly solvated) and anionic (weakly solvated) motions.

This model does have the attractive feature of including the effects of segment motion on ionic conduction; it does not directly include interionic interaction. Thus while it is the best microscopic model currently available for understanding ionic conduction in polymer electrolytes, it is inadequate in several ways (no inertial dynamics, no interionic interaction).

## 2.4 Kinetics of Ion Transport in Gel Polymer Electrolytes

The gel polymer electrolytes are prepared by immobilizing a nonaqueous electrolyte solution within an inactive structural polymer matrix or by increasing the viscosity of liquid electrolyte by adding a soluble polymer. They are basically salt-solvent-polymer hybrid systems in which first a salt solution is prepared and then it is immobilized with the help of suitable polymer matrix. The salt generally provides free/mobile ions, which take part in the conduction process, and the solvent helps in solvating the salt and also acts as a conducting medium whereas the polymer provides mechanical stability by increasing the viscosity of the electrolyte.

Writing the conductivity relation in terms of concentration, charge and mobility [236]

$$\sigma = \sum_i n_i q_i \mu_i \quad (2.38)$$

where  $n_i$  is the concentrations of charge carriers of type  $i$ ,  $q$  is the charge and  $\mu$  the mobility. The ionic conductivity here is also a function of temperature and pressure, and this equation is suitable for homogenous polymer electrolytes [236]. With the assumption that the dissolved salt completely dissociates into cations and anions in the electrolyte system, the determination of ion conductivity depends only on the evaluation of ion mobility.

The ionic mobility  $\mu$  can be calculated by the Stokes-Einstein equation

$$\mu = \frac{q}{6\pi\eta r_s} \quad (2.39)$$

Here  $q$  is the electronic charge on each charge carrier,  $\eta$  is the solution viscosity,  $r_s$  is the effective hydrodynamic (Stokes) radius. Ionic diffusion coefficient  $D$  is assumed to relate to the Stokes-Einstein (Equation 2.39) and can also be used to evaluate the ionic mobility. This is Nernst-Einstein relationship between the ionic diffusion coefficient and the ionic mobility [86]

$$\mu = \frac{qD}{kT} \quad (2.40)$$

where  $k$  is the Boltzmann constant. Ionic conductivity from Nernst-Einstein equation is then described as following [237]

$$\sigma_{diff} = \frac{Nq^2}{kT} (D_+ + D_-) \quad (2.41)$$

where  $N$  is the number of charge carriers per  $\text{cm}^3$  on the assumption of complete dissociation, and  $D_+$  and  $D_-$  are the diffusion coefficient of the cation and anion, respectively. The ionic transfer (transport) number is an important parameter in describing the mechanism of ion conduction in polymer electrolyte as well as its application. It represents the fraction of the total current carried by the mobile ions. The ionic transfer number of cation,  $t_+$ , can be estimated by the equation as follows

$$t_+ = \frac{\mu_+}{\mu_+ + \mu_-} = \frac{q_+ D_+}{q_+ D_+ + q_- D_-} \quad (2.42)$$

where  $\mu_+$  ( $\mu$ ) and  $q_+$  ( $q$ ) are ionic mobility and electronic charge on the cation (anion), respectively.

## 2.5 Kinetics of Ion Transport in Composite Polymer Electrolytes

### *Effectitive Medium Approach*

It has been recognized that in composite polymer electrolytes enhancement of ionic conductivity is connected with the existence of a highly conductive layer at the polymer filler interface [98, 238]. Therefore, in composite systems there are three components with different electrical properties. These are (Figure 2.8)

- (i) Highly conductive interface layers coating the surfaces of grains.
- (ii) Dispersed insulating grains.
- (iii) Matrix polymer ionic conductors.

The dispersed grain may be considered as covered with the thin layer as a unit and call it a composite grain (Figure 2.8). According to the Maxwell-Garnett rule [239] the equivalent conductivity  $\sigma_c$  of the composite unit can be expressed as

$$\sigma_c = \sigma_1 \frac{2\sigma_1 + \sigma_2 + 2Y(\sigma_2 - \sigma_1)}{2\sigma_1 + \sigma_2 - Y(\sigma_2 - \sigma_1)} \quad (2.43)$$

where  $\sigma_1$  and  $\sigma_2$  being, respectively, the conductivity of the interface layer and that of the dispersed grain.  $Y$  is a volume fraction of a dispersed phase in a composite unit for spherical geometry calculated as

$$Y = \frac{1}{\left(1 + \frac{t}{R}\right)^3} \quad (2.44)$$

where  $t$  is the thickness of interlayer and  $R$  is the radius of dispersed grain

According to the assumption above, the composite electrolyte can be treated as a quasi two-phase mixture consisting of an ionically conductive pristine polymer matrix with dispersed composite units. Such a quasi two-phase mixture can simply be described by the Bruggeman equation [240] or the simple effective medium equation introduced by Landauer [241]. These simple approaches ignore local field effects and are suitable only for the description of quasi two-phase mixtures for volume fractions of composite units lower than 0.1. In our system as the volume fraction of composite units increases, the composite grains join each other and form complicated clusters for which local field effects have to be considered. Therefore, the simple Landauer approach was improved according to the method proposed by Nan [242, 243] and Nakamura [244]. Two limiting situations are considered

- (i) The matrix phase is the polymeric electrolyte and isolated composite units are scattered throughout.
- (ii) The matrix phase consists of overlapping or touching composite units with a small amount of dispersed polymeric electrolyte in the interstices.



**Figure 2.8:** Schematic drawing of morphology of composite polymer–nonconductive filler electrolytes. Numbers are attributed to (1) highly conductive interface layers coating the surfaces of grains, (2) dispersed insulating grains, (3) matrix polymer ionic conductor [238].

Only for these two boundary situations used for calculations of the corrected value of the  $\sigma_c$  and  $\sigma_3$ , the local field effect is a geometrical effect and has no relation to the conductivity of the two phases. “The matrix phase” screens in these two cases the effect of the “dispersed phase” in the limiting composite unit [243]. Thus, the conductivity limits of the two limiting cases mentioned above can be calculated according to a simplified form of Nakamura’s equations [244].

$$\sigma_c^a = \frac{\sigma_c(d-1)V_c}{(d-V_c)} = \frac{2\sigma_c V_c}{(3-V_c)} \quad (2.45a)$$

$$\sigma_3^a = \frac{\sigma_3[(d-1) - (d-1)V_c]}{(d-1+V_c)} \quad (2.45b)$$

where  $V_c = V_2/Y$  is the volume fraction of composite units,  $V_2$  is the volume fraction of the dispersed grains,  $\sigma_3$  is the conductivity of the matrix polymeric electrolyte, and  $d$  is the dimensionality of the system ( $d=3$  for spherical grains). After introducing the improved conductivity parameters in the EMT equation one obtains two equivalent equations allowing finding  $\sigma_m$  (the conductivity of the composite polymeric electrolyte).

$$\frac{\left(\frac{V_2}{Y}\right)(\sigma_c^a - \sigma_m)}{\left[\sigma_c^a + \left(\frac{1}{p_c} - 1\right)\sigma_m\right]} + \frac{\left(\frac{1-V_2}{Y}\right)(\sigma_3^a - \sigma_m)}{\left[\sigma_3^a + \left(\frac{1}{p_c} - 1\right)\sigma_m\right]} = 0 \quad (2.46)$$

$$\frac{V_2/Y(\sigma_c^a - \sigma_m)}{\left[\sigma_m + p_c(\sigma_c^a - \sigma_m)\right]} + \frac{(1-V_2/Y)(\sigma_3^a - \sigma_m)}{\left[\sigma_m + p_c(\sigma_3^a - \sigma_m)\right]} = 0 \quad (2.47)$$

where  $p_c$  is the continuous percolation threshold for the composite grains. Since the composite grains are allowed to overlap in the region of interface layer,  $p_c$  can be taken to be 0.28 for this random mixture on the basis of general percolation theory [242, 245]. The highest enhancement of ionic conductivity is reached for the volume fraction of the dispersed grains equal to

$$V_2^* = \left(1 + \frac{t}{R}\right)^3 \quad (2.48)$$

For concentrations of grains exceeding  $V_2^*$  the quasi two-phase system consists of a mixture of composite grains and dispersed bare insulating grains. For such a situation, equation (2.47) can be rewritten in the following form

$$\frac{(1-V_2)(\sigma_c^a - \sigma_m)}{\left[\sigma_m + P_c(\sigma_c^a - \sigma_m)\right]} + \frac{(V_2 - V_2^*)(\sigma_2^a - \sigma_m)}{\left[\sigma_m + P_c(\sigma_2^a - \sigma_m)\right]} = 0 \quad (2.49)$$

where  $\sigma_c^a$  and  $\sigma_2^a$  (the modified conductivity parameters for second limiting case) are calculated according to the method proposed by Nan [242] and Nakamura [244]

$$\sigma_c^a = \frac{2\sigma_c(1-V_2+V_2^*)}{[2(1+V_2)-V_2^*]} \quad (2.50)$$

$$\sigma_2^a = \frac{2\sigma_2(V_2-V_2^*)}{(3-V_2+V_2^*)} \quad (2.51)$$

Equations (2.50) and (2.51) also consider local field effects. Here  $P_c$  is the percolation threshold of the dispersed bare insulating grains that are not allowed to overlap. Therefore  $P_c$  in equation (2.49) is different from  $p_c$  in equation (2.47) and was taken as the percolation threshold equal to 0.15 [238] for a general random mixture. Equations (2.47) and (2.49) are used to calculate the conductivity  $\sigma_m$  of composite polymer electrolytes. Three characteristic volume fractions of the dispersed grains can be observed

$V_2^I = P_c/(1 + t/R)^3$  is the critical volume fraction at which composite grains join to form a composite cluster and thus a continuous percolation threshold is reached.

$V_2^{II} = 1/(1 + t/R)^3$  is the volume fraction of the filler at which the continuous composite grain cluster fill the total electrolyte volume at which point the conductivity of a composite electrolyte reaches the maximum.

$V_2^{III} = 1 - P_c + P_c V_2$  is the volume fraction of the filler at which transition from conductor to insulator occurs.

The applicability of the model presented above has been tested by Wieczorek and co-workers [98, 238, 246-249] for PEO based composite polymer electrolytes dispersed with inorganic and organic fillers. They showed that  $t/R$  ratio decreases for concentrations of filler higher than  $V_2^{II}$  e.g. the concentration for which the maximum of the conductivity is reached. Moreover, the conductivity of an interface amorphous layer also depends on the fraction of the additive. They predicted the decrease in conductivity by a model, which considered the effect of a decrease in the surface layer conductivity with an increase in grain concentration. Since the structure of the interface layer is highly amorphous the temperature dependence of conductivity was assumed to follow VTF relation

$$\sigma = AT^{-1/2} \exp\left[\frac{-B}{k(T - T_0)}\right] \quad (2.52)$$

Here,  $B$  is pseudo-activation energy for conduction,  $A$  is a pre-exponential factor and  $T_0$  is a quasi equilibrium glass transition temperature usually 30-50 K lower than  $T_g$ . It is also assumed that the pseudo-activation energy  $B$  and the pre-exponential factor  $A$  are independent of the concentration of fillers. Therefore, the interface layer conductivity is only dependent on  $T_g$  and decreases with an increase in  $T_g$ . Values of  $T_g$  taken from DSC experiments were used for the calculation of  $\sigma_1$  for electrolytes with various concentrations of the filler. To generalize the model, the variation of  $T_g$  as a function of grain size and volume fraction of filler should be considered. The effect of the dissolved salt on  $T_g$  should also be taken into account. It was found [250, 251] that for several composite systems  $T_g$  could be approximated by the following equation

$$T_g = K_0 + K_1[f(V_2/S_2)] + K_2[f(C_s, V_2)] \quad (2.53)$$

where  $V_2$  and  $S_2$  are respectively volume fraction and surface area of the dispersed phase,  $C_S$  is the molar concentration of the dopant salt added, and  $K_0$ ,  $K_1$ , and  $K_2$  are adjustable constants. It has been found that for a system with different concentrations of filler additive and a fixed concentration of dopant salt, the best fit to the experimental data can be obtained when  $T_g$  is approximated by the relation

$$T_g = K_0 + K_1 V_2 + K_2 V_2^2 \quad (2.54)$$

In this equation, the effect of salt is included in  $K_0$ , which is identical to the  $T_g$  for pristine polymer electrolyte.  $K_1$  describes the influence of filler added on  $T_g$  of the composite system and  $K_2$  is connected with polymer-filler-salt interaction.

## 2.6 Kinetics of Intercalation and Ion Transport in Polymer/Clay Nanocomposite Electrolytes

Polymer–clay nanocomposites comprise polymer chains intercalated into the inter layer galleries stacked in a regular arrangement. In recent years it has been shown that the ground state of polymer–clay nanocomposites corresponds to phase-separated, intercalated or exfoliated state depending on the external conditions. The mechanism of structural transitions between these states is a subject of great scientific and practical importance [252].

To study the kinetics of polymer intercalation in layered silicates Ginzburg et al. [253] proposed a simple model according to which the intercalation process is driven by the motion of localized excitations (“kinks”), which open up the tip between the clay sheets. A system of two adjacent clay platelets was considered as shown in figure 2.9. In the absence of polymer, they are in the aggregated (Ag.) state, and the distance between them is zero. When mixed with a polymer, the platelets can separate and form a narrow “gallery” of width  $U = U_0$ , which is filled by polymer chains. It is possible to calculate the potential energy per unit area  $V(U)$  (Figure 2.10); such a potential takes into account the enthalpic and entropic terms in the free energy of the confined polymers as well as Van der Waals and electrostatic interaction between the clay platelets [254-257]. In the model they have restricted themselves by considering this potential having a double-well shape, i.e.  $V(U)$  has a minimum at some point  $U_0 > 0$  in addition to the minimum at  $U_0 = 0$ . Then, the transition between the aggregated (Ag.) state ( $U = 0$ ) and the intercalated (Int.) state ( $U = U_0$ ) can be described as a “switching” process in a bistable potential. Assuming the potential to be symmetric, the

equations of motion for the plate separation  $U$  can be derived in one-dimensional case [ $U = U(x, t)$ ] in the following form [258]

$$\eta \frac{\partial U}{\partial T} + EI \frac{\partial^4 U}{\partial x^4} - T \frac{\partial^2 U}{\partial x^2} + \frac{\partial V}{\partial U} = 0 \tag{2.55}$$

where  $E$  is the Young’s modulus of the clay,  $I = d^3/12$  ( $d$  being the thickness of a clay sheet) is the moment of inertia of a unit length of a clay sheet,  $\eta$  is the “friction coefficient” (proportional to the bulk viscosity of the polymer), and  $T$  is the effective external force. On an average, one can estimate the magnitude of  $T$  as  $T = 2\tau d$ , where  $\tau$  is the effective shear stress. Positive values of  $T$  correspond to the elongation while negative values describe compression. Inertial forces have been neglected, which are small in comparison with the viscous forces however, adding them would not qualitatively change the results.

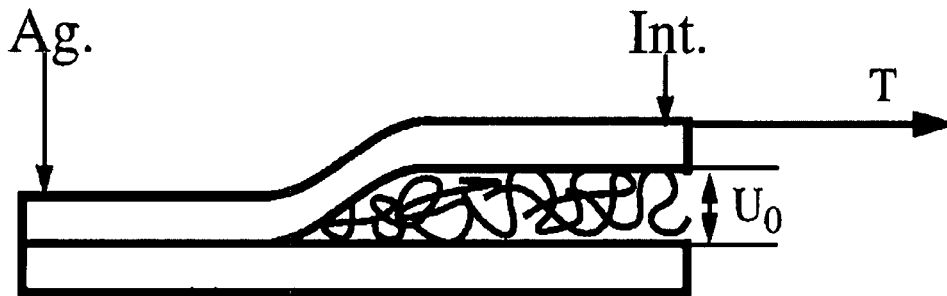


**Figure 2.9:** Sketch of the polymer–clay system. Here, Ag. denotes the agglomerated (immiscible) state, and Int. denotes the intercalated state;  $U_0$  is the plate separation in this state.  $T$  is the external longitudinal force applied to the upper plate [253].

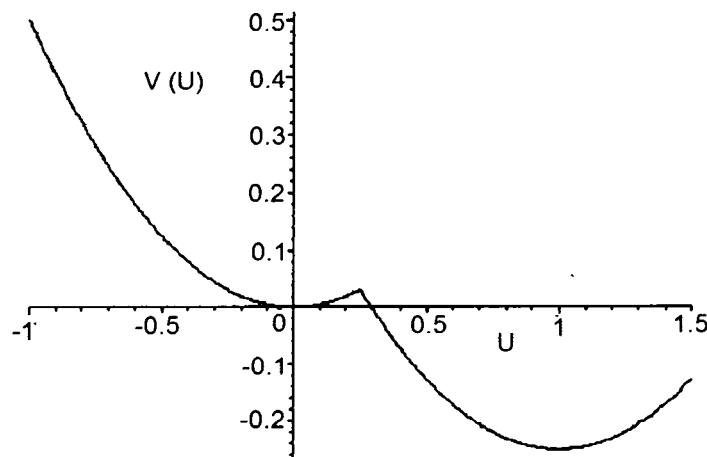


**Figure 2.10:** Sketch of the plate–plate interaction potential  $V(U)$  [252].



To obtain an exact analytical solution of equation (2.55), a piecewise parabolic form for the potential  $V(U)$  can be adapted [253]:

$$V(U) = \begin{cases} \frac{A}{2} \left( \frac{U}{U_0} - 1 \right)^2, & U > 3U_0/4 \\ \frac{A}{16} - \frac{A}{2} \left( \frac{U}{U_0} - \frac{1}{2} \right)^2, & U_0/4 \leq U \leq 3U_0/4 \\ \frac{A}{2} \left( \frac{U}{U_0} \right)^2, & U < U_0/4 \end{cases} \quad (2.56)$$

After introducing dimensionless variables  $u = U/U_0$ ,  $X = x(A/EIU_0^2)^{1/4}$ ,  $\tau = tA/U_0^2 \eta$ , equation (2.55) can be written as

$$\frac{\partial^4 U}{\partial X^4} - K \frac{\partial^2 U}{\partial X^2} + \frac{\partial U}{\partial \tau} + f(u) = 0 \quad (2.57)$$

where  $f(u) = u$ , if  $0 < u < \frac{1}{4}$ ,

$$\left. \begin{aligned} & -\left(u - \frac{1}{2}\right), \text{ if } \frac{1}{4} \leq u \leq \frac{3}{4} \text{ and} \\ & (u-1), \text{ if } \frac{3}{4} < u < 1. \end{aligned} \right\} \quad (2.58)$$

The rescaled tension

$$K = TU_0 / (AEI)^{1/2} \quad (2.59)$$

Let us consider solutions in the form  $u = u(\xi)$ , with  $\xi = X - V\tau$ , corresponding to a kink moving from left to right with velocity  $V$ . In this case, equation (2.57) becomes an ordinary differential equation

$$\frac{d^4 u}{d\xi^4} - K \frac{d^2 u}{d\xi^2} - V \frac{du}{d\xi} + f(u) = 0 \quad (2.60)$$

with boundary condition  $u(\xi) \rightarrow 0$  for  $\xi \rightarrow -\infty$ ;  $u(\xi) \rightarrow 1$  for  $\xi \rightarrow +\infty$ . Moreover, all derivatives of  $u(\xi)$  must vanish at  $\pm\infty$ .

Considering static solutions ( $V = 0$ ), it can be shown that the solution satisfying equation (2.58) and all boundary conditions has the form

$$u = \begin{cases} C_1 \exp(\lambda_1 \xi) + C_2 \exp(\lambda_2 \xi), & u < 1/4 \\ \frac{1}{2} + D_1 \sin(\lambda_3 \xi) + D_2 \sinh(\lambda_4 \xi), & 1/4 \leq u \leq 3/4 \\ 1 - C_1 \exp(-\lambda_1 \xi) \\ - C_2 \exp(-\lambda_2 \xi), & u < 3/4 \end{cases} \quad (2.61)$$

where  $C_1$ ,  $C_2$ ,  $D_1$  and  $D_2$  are determined based on the requirement that  $u(\xi)$  and its first, second, and third derivatives are continuous functions everywhere. The exponents  $\lambda_1$  and  $\lambda_2$  are the positive roots of the following equation

$$\lambda^4 - K\lambda^2 + 1 = 0 \quad (2.62)$$

while  $\lambda_3$  and  $\lambda_4$  are the absolute values of one imaginary and one real root of the following equation

$$\lambda^4 - K\lambda^2 - 1 = 0 \quad (2.63)$$

Equation (2.62) has real roots if and only if  $K \geq 2$ , while equation (2.63) always has both real and imaginary roots. Thus, for existence of the kink solutions the elongational force  $T$  should be larger than some threshold value  $T = 2(AEI)^{1/2}/U_0$  (equation 2.59). This is in a qualitative agreement with numerous experiments suggesting that strong shear flow is almost always necessary to exfoliate or intercalate clay sheets in the polymer.

For  $K > 2$  an analytical solution can be easily constructed. Ginzburg et al. [253] plotted the kink profile for several values of  $K$ . They observed that as  $K$  becomes larger the kinks become broader. Quantitatively they showed that such a kink could easily emerge and propagate in clay. Thus intercalation process in polymer/clay nanocomposites could be carried by the soliton like excitations—kinks. These kinks result from the balance between the bending elasticity of the clay sheets, the polymer-induced interaction between the sheets and the external elongational force.

To discuss the cation transport in polymer/clay nanocomposites Moon et al. [259] developed a simplified one-dimensional model for the transport of lithium ions in the clay-polymer membrane. Figure 2.11 shows the idealized structure of the nanocomposites films, which consists of intercalated poly(ethylene oxide) (PEO) in the synthetic layered hectorite (SLH). A schematic representation of a typical Li-ion battery cell is shown in figure 2.12.

To simplify the model, they have made certain assumptions:

- (i) Only lithium ions transported through the film.

- (ii) The electroneutrality of the active lithium ions is maintained by coordination of one to six oxygen's in the PEO chain present in the film [260].
- (iii) The total lithium concentration in the membrane,  $C_0$ , is a constant parameter.
- (iv) The transport of  $\text{Li}^+$  ions through the film is described by concentration solution theory [261].
- (v) The diffusion coefficient and the transference number of the  $\text{Li}^+$  are concentration independent.
- (vi) Only cations are electroactive at the electrolyte-electrode interfaces.

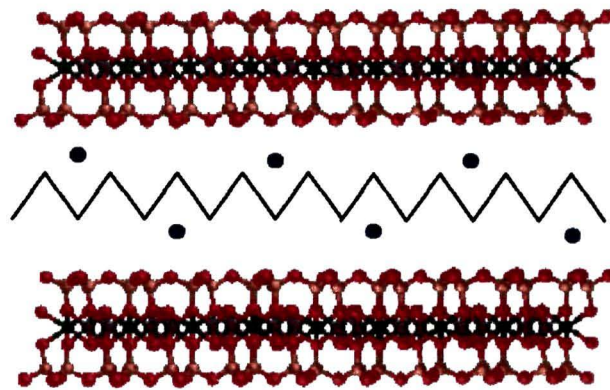


**Figure 2.11:** Idealized clay-polymer membrane structure of intercalated PEO in the synthetic lithium hectorite (SHL). Circle dots are represented by the lithium ions, and the PEO chain is shown between the Li ions [259].

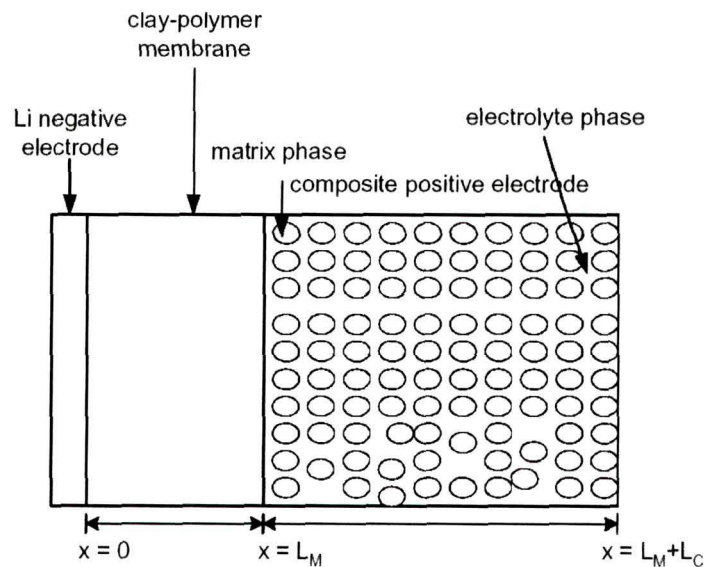


**Figure 2.12:** One-dimensional model of lithium clay-polymer membrane battery cell.

The flux of lithium ions,  $N_+$ , within the polymer-clay membrane is given by

$$N_+ = -D \frac{\partial C}{\partial x} + \frac{i_2 t_+}{v_+ F} \quad (2.64)$$

where  $C$  is the concentration of lithium ions,  $D$  is the diffusion coefficient,  $i_2$  is the current density in the clay-polymer membrane and is equal to the applied current density,  $t_+$  is the lithium transference number.  $F$  is faraday's constant. A material balance on the lithium ions in the clay-polymer membrane is then given by

$$\frac{\partial C}{\partial t} = D \frac{\partial^2 C}{\partial x^2} \text{ and the boundary condition } N_+ = \frac{i_{app}}{F} \text{ at } x = 0 \quad (2.65)$$

At the Li electrode ( $x = 0$ ), the flux of lithium ions is equal to the dissolution rate of Li, which yields the boundary condition

$$-D \frac{\partial C}{\partial x} \Big|_{x=0} = \frac{i_{app}}{F} \quad (2.66)$$

The variation in potential in the membrane is calculated from [262],

$$\nabla \Theta_2 = -\frac{i}{\sigma} - \frac{RT(1+t_+)}{v_+ F} \quad (2.67)$$

where  $\nabla \Theta_2$  and  $\sigma$  are the potential and the lithium conductivity in the clay-polymer membrane, respectively. The flux and the concentration of the lithium ion and the potential in the membrane are taken to be continuous from  $x = 0$  to  $x = L_M$ .

There are various reports in literature describing cation dynamics in polymer-clay nanocomposites. An initial simulation study of the dynamics of  $\text{Li}^+$  in a PEO–montmorillonite system was carried out by Yang and Zax [263], who used spectral simulation methods to elucidate the line shape of the  $^7\text{Li}$  NMR spectra. The study concluded that the main limitation on diffusion in the polymer–clay system was the inefficient coordination of the cations to the PEO backbone oxygen atoms, which resulted in the  $\text{Li}^+$  moving along the clay sheets in short jumps, or “hops”. Giannelis and co-workers [264, 265] performed Monte Carlo (MC) and molecular dynamics (MD) simulations to examine the  $\text{Li}^+$  dynamics of PEO intercalated between layers of montmorillonite, under varying hydration and layer charge conditions. They showed that the polymer chains form a bilayer structure, but are relatively disordered in the plane parallel to the interlayer surface. The authors also observed that in the absence of water, the cations bind to the interlayer surface. When water is present two types of cation environment are noticeable, those bound to the

interlayer surface and those hydrated by water in the interlayer region. In both cases, coordination of cations by PEO was minimal. To study the  $\text{Li}^+$  dynamics, Kuppa and Manias [266] performed MD simulation of both bulk polymer and intercalated polymer into the galleries of montmorillonite. As in the previous studies, the authors showed that the lithium cations motion in the nanocomposites was independent of temperature and followed a hopping mechanism, whereby they go from one ditrigonal cavity to another. This is in contrast to what was observed in simulations of lithium cations in bulk PEO, reported in the same paper, which showed a hopping motion at low temperatures and random Brownian-like diffusion at higher temperatures. In the simulations the authors found that the  $\text{Li}^+$  dynamics was driven by competitive adsorption of the  $\text{Li}^+$  between the PEO chains and the clay surface, with correlation between the  $\text{Li}^+$  dynamics and the PEO segment dynamics. This study was backed by further experimental studies of  $^7\text{Li}$  and  $^{23}\text{Na}$  NMR by Reinholdt et al. [267], which confirmed that the dynamics of  $\text{Li}^+$  described a hopping type motion.

# CHAPTER III

## Experimental Details

*This chapter primarily deals with the methods and materials used for synthesizing different types of polymer electrolyte membranes. Synthesis techniques for the preparation of polymer electrolytes have been discussed in detail. This is followed by the discussion of the principles and specifications of different analytical techniques employed for the physico-chemical characterization of the synthesized materials. Various parameters related to Swift Heavy Ion (SHI) irradiation are mentioned in this chapter.*

### 3.1 Parent Materials

Poly(ethylene oxide) PEO ( $M_w = 600000$ ), Poly(vinylidene fluoride) ( $M_w = 275000$ ) PVdF, Poly(vinylidene fluoride-co-hexafluoropropylene) P(VdF-HFP) ( $M_w = 400000$ ) polymers were procured from Aldrich Chemical Inc. (USA). Poly(methyl methacrylate PMMA) ( $M_w = 15000$ ) polymer was obtained from Himedia (India). The lithium salt, lithium perchlorate ( $\text{LiClO}_4$ ) was obtained from Aldrich Chemical Inc. (USA). Organic solvents propylene carbonate (PC) and diethyl carbonate (DEC) were procured from E-Merck (Germany). Aniline monomer for synthesis of polyaniline nanofibers was obtained from E-Merck (Germany). Montmorillonite (MMT) nanoclay was purchased from Aldrich Chemical Inc. (USA).

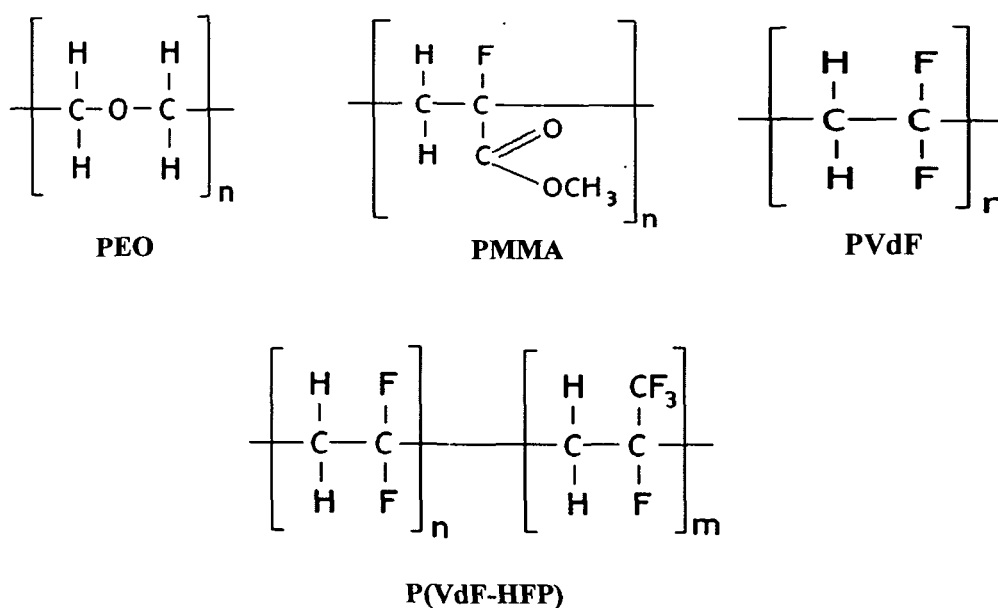
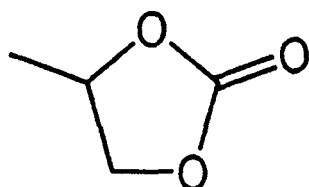
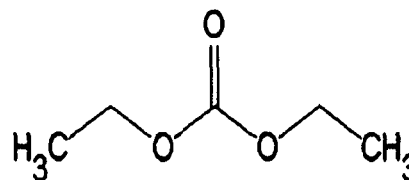


**Figure 3.1:** Chemical structure of different polymers used in the present work

Figures 3.1 and 3.2 show the structure of different polymers and plasticizers, respectively used to synthesize polymer electrolytes. Tables 3.1 and 3.2 show the basic physical properties of polymers and plasticizers.



Propylene carbonate (PC)



Diethyl carbonate (DEC)

**Figure 3.2:** Chemical structure of plasticizers used in the present work

**Table 3.1:** Some physical properties of polymers used to synthesize polymer electrolytes.

Polymer	Glass transition temperature $T_g$ ( $^{\circ}\text{C}$ )	Melting point ( $^{\circ}\text{C}$ )	Tensile strength ( $\text{N}/\text{mm}^2$ )	Dielectric constant at 1 MHz	Density ( $\text{gm}/\text{cm}^3$ )
PEO	-73	65	16-13	3.3	1.15-1.25
PMMA	105	160	2.9-2.3	2.9	1.19
PVdF	-40 – (-30)	170	30-50	8.5	1.77
P(VdF-HFP)	-100 – (-90)	140	28-41	7.5	1.78

**Table 3.2:** Some physical properties of organic plasticizers used to synthesize polymer electrolytes.

Plasticizers	Mol. weight	Melting point ( $^{\circ}\text{C}$ )	Boiling point ( $^{\circ}\text{C}$ )	Viscosity $\eta$ at 25 $^{\circ}\text{C}$ ( $\text{mPa}\cdot\text{s}$ )	Density ( $\text{gm}/\text{cm}^3$ )	Dielectric constant
PC	102.09	-48.8	242	2.53	1.2047	64.6
DEC	118.13	-43.0	126	0.748	0.9752	2.82

### 3.2 Sample Preparation

Dedoped polyaniline (PAni) nanofibers were synthesized by the interfacial polymerization technique [268]. The interfacial polymerization reaction was carried out in 30 ml glass vials. 1M amount of aniline was dissolved in 10ml of organic solvent carbon tetrachloride ( $\text{CCl}_4$ ). Ammonium peroxydisulfate  $\{(\text{NH}_4)_2\text{S}_2\text{O}_8\}$  (0.25M) was dissolved in 10ml of double distilled water and dopant acid (HCl). The polyaniline nanofibers were dedoped with 1M NaOH. The electronic conductivity of PAni nanofibers was measured with Keithley 2400 LV source meter. The electronic conductivity of doped nanofibers is of the order of  $10^{-4} \text{ Scm}^{-1}$ , whereas after dedoping with NaOH solution the electronic conductivity was found to be of the order of  $10^{-11} \text{ Scm}^{-1}$ . This confirms the insulating nature of dedoped polyaniline nanofibers.

In polyaniline nanofiber reinforced polymer electrolytes solution casting technique was used, which consists of the following steps:

- (i) All the polymers and the salt were vacuum dried for 24 hours prior to use
- (ii) PEO polymer as required was dissolved in acetonitrile.
- (iii) PVdF polymer was dissolved in dimethyl sulfoxide (DMSO).
- (iv) PMMA and P(VdF-HFP) polymers were dissolved in acetone or tetrahydrofuran.
- (v) Salt  $\text{LiClO}_4$  was dissolved in propylene carbonate (PC) and/ or diethyl carbonate (DEC). PC has high dielectric constant ( $\epsilon = 64.6$ ) but has high viscosity ( $\eta = 2.53$ ), whereas DEC has low dielectric constant ( $\epsilon = 2.82$ ) but has low viscosity ( $\eta = 0.748$ ). Combination of PC and DEC (1:1 by volume) solvent was used as optimization for high dielectric constant ( $\epsilon = 33.71$ ) and low viscosity ( $\eta = 1.639$ ) to achieve high ionic conductivity.
- (vi) Both polymers and salt solution were mixed together in a beaker and magnetically stirred during continuous heating for 7-8 hours at  $50^\circ\text{C}$ .
- (vii) Polyaniline (PAni) nanofibers as filler were added to the above polymer-salt solution as required and continuously heated and stirred at  $50^\circ\text{C}$  for another 7-8 hours to make the solution homogenous and viscous.



- (viii) Above viscous solution was finally cast on glass plates / patri dishes and allowed to dry under vacuum.

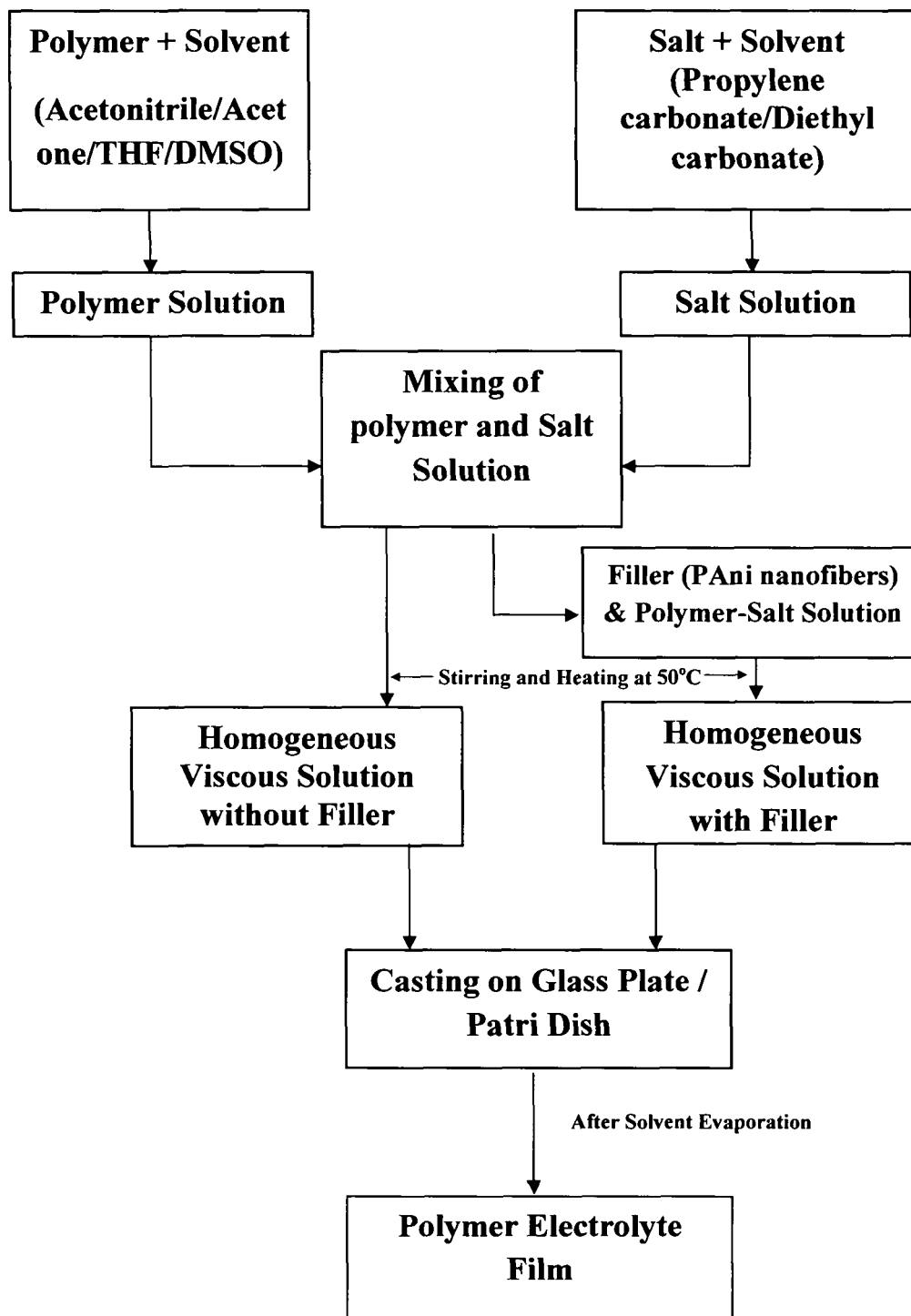


Figure 3.3: Block diagram of solution casting technique for sample preparation.

In case of layered silicate (MMT) based nanocomposite electrolytes, solution intercalation technique was used, which consists of the following steps:

- (i) All the polymers, montmorillonite (MMT) clay and the salt were vacuum dried for 24 hours prior to use.
- (ii) PEO polymer as required was dissolved in acetonitrile.
- (iii) PVdF polymer was dissolved in dimethyl sulfoxide (DMSO).
- (iv) PMMA and P(VdF-HFP) polymers were dissolved in acetone or tetrahydrofuran.
- (v) MMT was dispersed in THF.
- (vi) Both polymers and MMT were mixed together in a beaker and magnetically stirred during continuous heating for 7-8 hours at 50 °C and then shear is supplied via sonication for half an hour.
- (vii) The viscous solution thus obtained was cast onto glass plates/patri dishes.
- (vi) The films thus obtained were dipped into a solution containing 1M LiClO<sub>4</sub> in 1:1 (v/v) of PC and DEC.

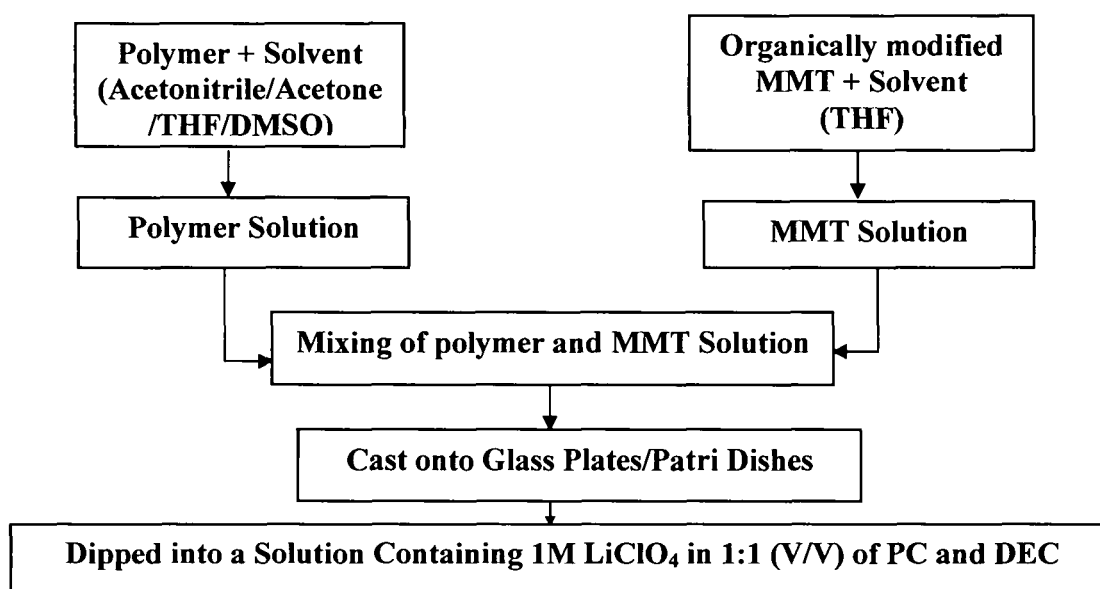


Figure 3.4: Block diagram of solution intercalation technique of sample preparation.

Figures 3.3 and 3.4 show the block diagrams of solution casting and solution intercalation techniques, respectively to synthesize nanocomposites polymer electrolyte films. These procedures provided mechanically stable, free standing and flexible films of thickness in the range of 30  $\mu\text{m}$  -1 mm.

### 3.3 Furnace and Temperature Controller

An indigenously built electrical resistive heating furnace comprising of an insulated heating element (Kanthal) uniformly wound on an alumina tube has been used. The resistance of the heating element was 30  $\Omega$ . High temperature cement was applied over the windings to fix them in place. This tube was kept in cylindrical stainless steel container with one end closed, and the space between the tube and the wall of the container was filled with glass wool and plaster of paris to make it perfectly insulating to prevent heat loss. Fixing circular asbestos followed by a wooden plate covered top end.

A PID temperature controller (Nutronics, Model pp-3040) and a chromel-alumel thermocouple were used to control and measure the furnace temperature, respectively. The temperature was controlled to within  $\pm 1^\circ\text{C}$ .

### 3.4 Sample Holder

Figure 3.5 shows the photograph of the sample holder made up of stainless steel/copper and polymer (PVC) block. A stainless steel (SS) / Cu rod fixed with stainless steel / Cu base plate was passed through the center hole of the PVC block and fixed with a nut. Four stainless steel / copper rods were fixed on the four corners of the PVC block such that it touches the base plate. Spring arrangement was attached with lower part of each of the four rods to apply uniform pressure due to spring action to ensure a firm contact between the electrodes and the sample. In this sample holder conductivity measurement on four samples can be done simultaneously. These four rods and the base plate serve as blocking electrodes in measuring the ionic conductivity. The diameter of the bottom disc is  $\approx 1$  cm. The sample is placed between the rod and base plate as shown in the figure 3.5.

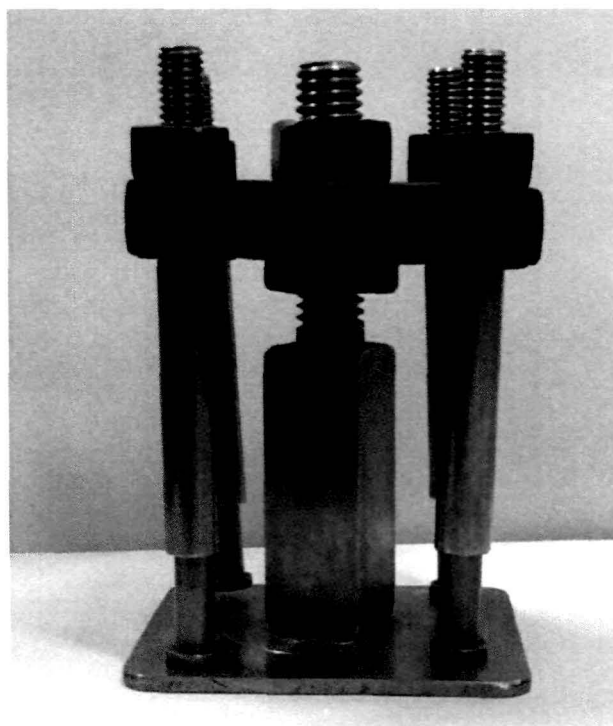


**Figure 3.5:** Sample holder used in the present work.

### 3.5 Conductivity Measurements

Figure 3.6 shows the set-up for conductivity measurement employed in this work. Hioki 3532-50 LCR HiTester has been employed for the complex impedance (modulus  $Z$  and phase angle  $\theta$ ) measurements. The instrument is interfaced with a computer to collect the data. It has a built-in frequency synthesizer and has a frequency range 42 Hz to 5 MHz. The impedance measurements were carried out at a temperature interval 5 °C from room temperature to 150 °C. Sufficient time was allowed at each temperature for thermal equilibrium and reproducibility of data. The ionic conductivity was subsequently obtained from the relation

$$\sigma = \frac{L}{R_b A} \quad (3.1)$$

where  $L$  is the thickness and  $A$  is the cross-sectional area of the polymer electrolyte sample disc.  $R_b$  is the bulk resistance obtained from the complex impedance plot.

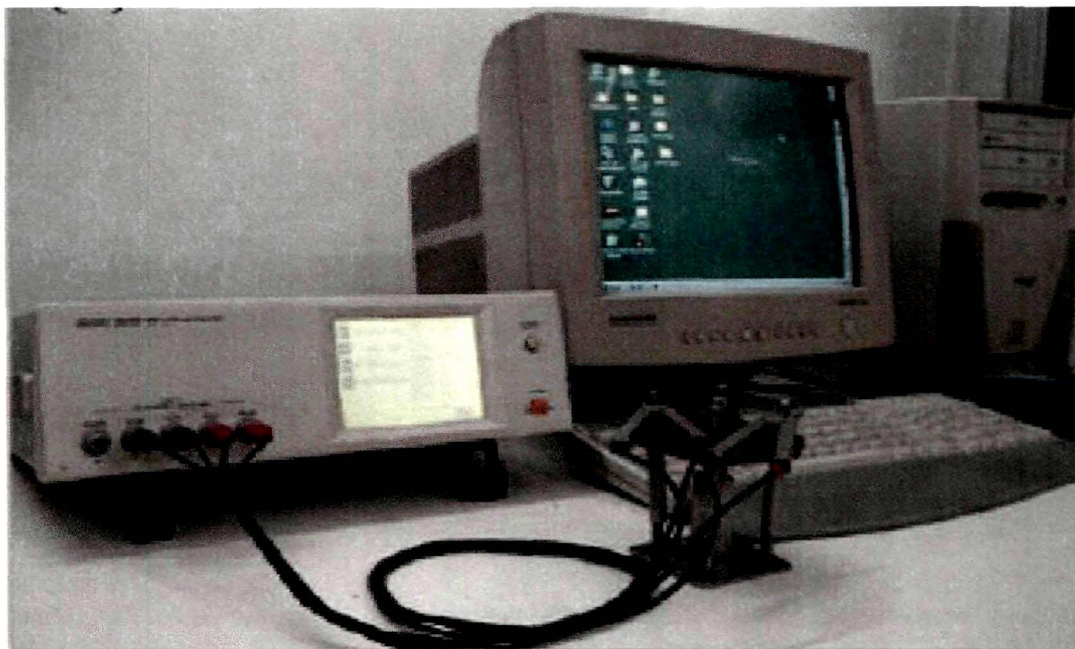


**Figure 3.6:** Conductivity measurement set-up.

### 3.6 Transport Number Measurements

Total ionic transference number of the nanocomposites gel polymer electrolytes was measured by Wagner's polarization technique [269], which is used to determine the ionic contribution to the total charge transport by measuring the residual electronic current passing through the electrolytes. The Wagner polarization cell Ag/nanocomposites polymer electrolyte/Ag was prepared to measure the transport number. A fixed small dc potential (300 mV) was applied across the blocking electrodes and the current passing through the cell was measured as a function of time for 6 hours to allow the samples to become fully polarized. Initial total current ( $I_T$ ), which is the sum of ionic ( $I_i$ ) and electronic ( $I_e$ ) currents ( $I_T = I_i + I_e$ ) and final current after polarization, which is only the electronic current  $I_e$  were measured. The transference numbers ( $t_{ion}$  and  $t_{ele}$ ) have been calculated using the relations

$$t_{ion} = I_i / I_{total} = (I_T - I_e) / I_T \quad (3.2)$$

$$t_{\text{elc}} = I_{\text{e}} / I_{\text{T}} \quad (3.3)$$

### 3.7 X-ray Diffraction

X-ray scattering and spectroscopy methods can provide a wealth of information concerning the physical and electronic structure of crystalline and non-crystalline materials in a variety of external conditions and environments. X-ray diffraction is one of the most widely used probes for crystal structure determination. This technique is based on the scattering of X-rays by crystals governed by the Bragg's law. Powder X-ray diffraction is used to determine the atomic structure of crystalline, semi-crystalline and amorphous materials without the need for large ( $\sim 100 \mu\text{m}$ ) single crystals. X-ray diffraction patterns give information about crystal structure parameters like crystallite size (domain length in case of semi-crystalline polymers),  $d$ -spacing, diffraction planes, structure, phase and lattice constants. In addition to the crystal structure, XRD is applied for various other purposes such as chemical analysis, stress, strain, particle size measurements, phase equilibrium, determination of orientation for single crystals or the ensemble of orientations in a polycrystalline or polymeric aggregate, order-disorder transformation etc. The intensities and angles of the diffracted X-ray beams are related to the atomic arrangement of the crystal. In case of polymeric materials, XRD is used to determine the proportions of the crystalline and amorphous phases in terms of the degree of crystallinity. X-ray diffraction is also used to determine the domain length in case of polymers. Polymers are semicrystalline materials. Their crystallinity is attributed to chain folding or to the formation of single or double helices, for at least part of their chain length [270]. This local range of order in polymer chains is referred to as the domain length ( $L$ ) and can be in the range of angstroms ( $\text{\AA}$ ). The X-ray diffraction patterns for the polymer electrolyte films reported in the present work have been recorded using a Rigaku Miniflex diffractometer with Cu  $K_{\alpha}$  radiation ( $\lambda = 1.5406 \text{\AA}$ ) shown in figure 3.7. The angular range spread over the region between 100 and 700 in  $2\theta$ , in steps of 0.050. The X-ray diffraction patterns have been used to determine the degree of crystallinity,  $d$ -spacings, domain length ( $L$ ) and strain ( $\varepsilon$ ). The methodology adopted for the quantitative estimation of these structural details of the electrolyte films specifically the degree of crystallinity,  $d$ -spacings, domain length ( $L$ ) and strain ( $\varepsilon$ ) are discussed in the next two subsections (Sections 3.7.1 and 3.7.2).

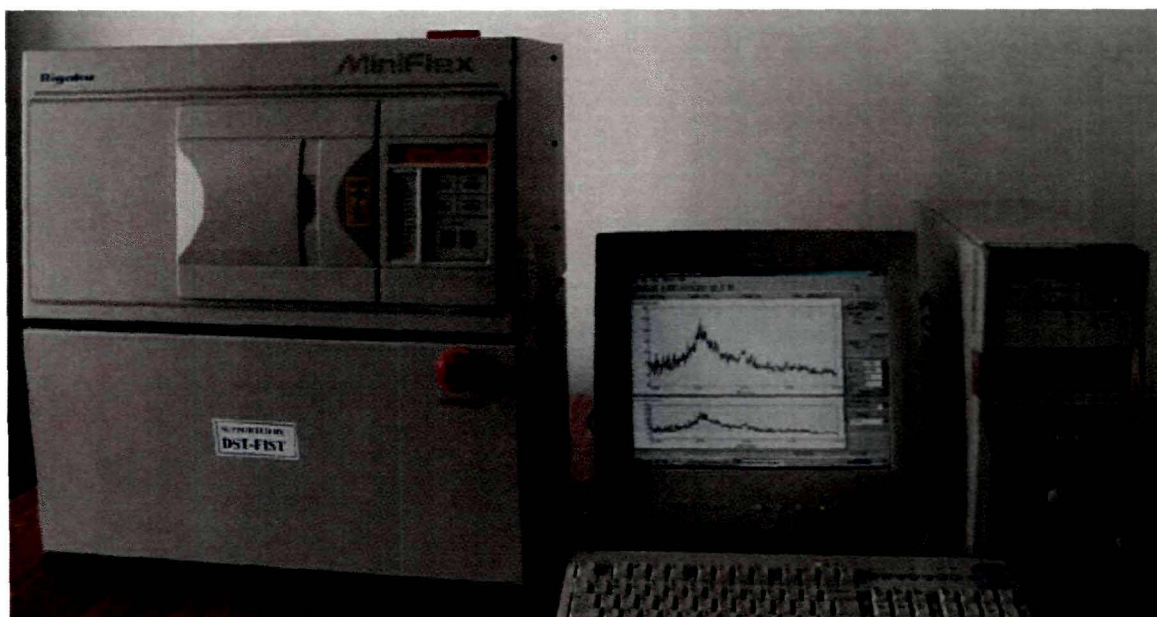


**Figure 3.7:** Rigaku Miniflex X-ray diffractometer installed at the Department of Physics, Tezpur University.

### 3.7.1 Degree of Crystallinity

Domain length ( $L$ ) is a measure of the local range of order (ordering in a single polymer chain) of a polymer whereas the overall ordering in the polymer samples are generally described in terms of the degree of crystallinity. The degree of crystallinity gives quite a good estimation of the amount of crystalline phase present in a polymer sample. A typical X-ray diffractogram for a polymeric material consist of a broad amorphous hump superimposed with some sharp peaks as shown in the figure 3.8 (a). The total area under the diffractogram is the sum of the crystalline peaks and broad amorphous hump.

If a typical X-ray diffractogram has two crystalline peaks with areas  $A_1$  and  $A_2$  superimposed on a broad amorphous hump with an area  $A_3$  as shown in figure 3.8 (b), then the degree of crystallinity ( $K$ ) of the polymer will be

$$K = \frac{\alpha_C(A_1 + A_2)}{\alpha_C(A_1 + A_2) + \alpha_A A_3} \quad (3.4)$$

where  $\alpha_C$  and  $\alpha_A$  are proportionality constant for the crystalline and amorphous phases, respectively. Assuming  $\alpha_C = \alpha_A$  for reasonable accuracy in polymers, the equation (3.4) for the degree (percentage) of crystallinity may be written as

$$K = \frac{A_1 + A_2}{A_1 + A_2 + A_3} \times 100\% = \frac{A}{A_0} \times 100\% \quad (3.5)$$

where  $A$  is the sum of the areas of all the crystalline peaks in the diffractogram and  $A_0$  is the total area under the diffractogram. In the present work, the area has been calculated by dividing the X-ray diffractogram into minute square grids ( $0.5 \times 0.5 \text{ mm}^2$ ) and counting the number of grids. The degree of crystallinity of a polymer is affected by the secondary valence bonds that can be formed, the structure of the polymer chain (range of order), the physical treatment and the molecular weight of the polymer.

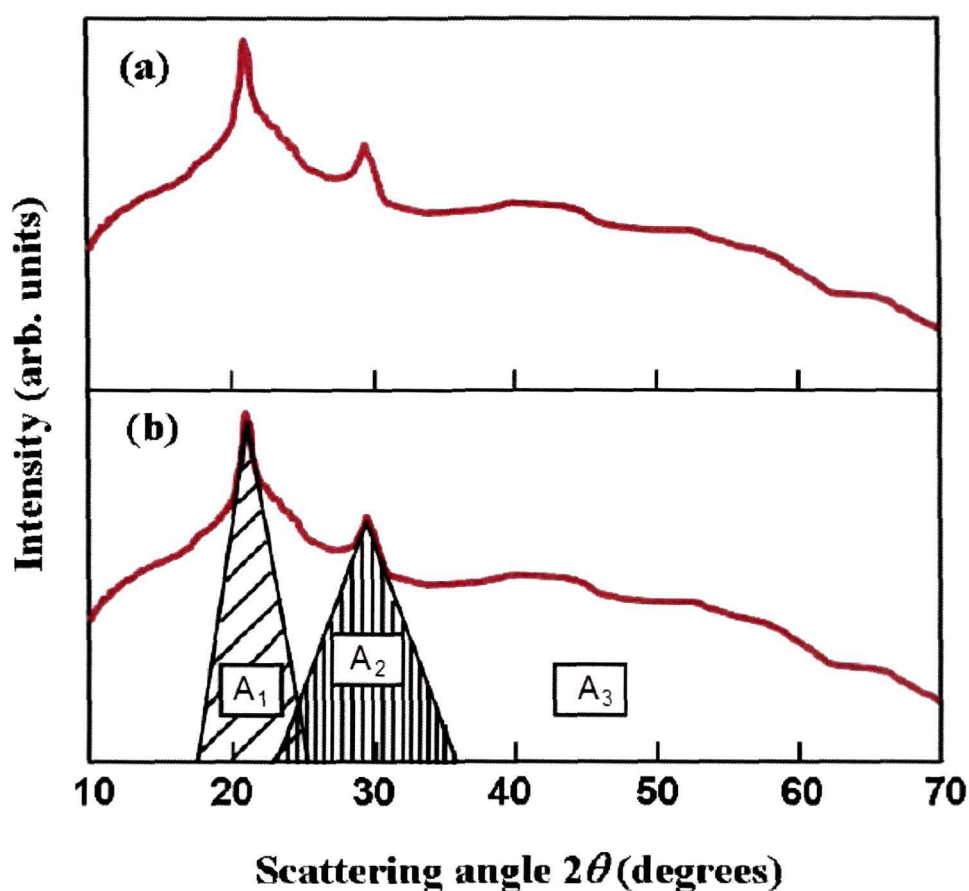


**Figure 3.8:** (a) Typical X-ray diffractogram of a semi-crystalline polymer and (b) XRD patterns showing the superposition of crystalline peaks and an amorphous hump.

### 3.7.2 Calculation of $d$ -spacing, Domain length ( $L$ ) and Strain ( $\epsilon$ )

The  $d$ -spacings have been deduced from the angular position  $2\theta$  of the observed peaks in the X-ray diffraction patterns of the polymer electrolytes, according to the Bragg's formula



$$\lambda = 2d\sin\theta \quad (3.6)$$

Line broadening in the X-ray diffraction patterns may be attributed to two major factors: the size and strain components. The former depends on the size of coherent domains (or incoherently diffracting domains), which is not limited to the grains but may include effects of stacking and twin faults and sub-grain structures (small-angle boundaries, for instance); and the latter is caused by any lattice imperfection (dislocations and different point defects) [271]. The theory is quite general and has been successfully applied to all forms of materials, including oxides and polymers [272].

In the present work, the domain length ( $L$ ) and strain ( $\epsilon$ ) of polymer electrolytes have been calculated using a single line approximation technique employing Voigt function [273]. The measures of dispersion used in earlier studies of crystal imperfections by means of diffraction broadening have been the width of the line profile at half the maximum intensity (FWHM,  $2w$ ) and the integral breadth ( $\beta$ ). However, uncertainties arising from the correction of the instrumental broadened in the profile have led to the introduction of the Fourier and variance methods [274]. These methods allow a detailed and accurate analysis of imperfections to be undertaken, but are solely dependent on the quality of the data, necessary expertise and computing facilities that are available to analyze the data.

A limitation in the use of the FWHM or integral breadth is the need to ascribe an analytical function to the line profiles. Earlier workers have assumed that they are Cauchy (Lorentzian) or Gaussian in form, but it has been demonstrated later on [275] that a closer approximation is given by the convolution of these curves, namely the Voigt function. The Voigt function has been adopted by many groups for an analysis of diffraction broadening based on the integral breadth of a single line and the approach has also been used to obtain the domain size and strain in deformed tungsten [273 and refs. therein]. Langford has introduced an explicit equation for the Voigt function in 1978 [276], which shows that the breadths of the Cauchy and Gaussian components can easily be found from the ratio of the FWHM of the broadened profile to its integral breadth ( $2w/\beta$ ). Later on Keijser et al. [273] reported that graphical methods or interpolation from tables can be avoided by using empirical formulae and thus the required calculations can be simplified greatly. While it is always desirable to use data from several reflections whenever practicable, the method can be used in single-line analysis.

The measured line profile  $h$  is the convolution of the standard profile  $g$  with the structurally broadened profile  $f$ . Assuming,  $h, f$  and  $g$  to be Voigt functions [276], we get,

$$h_C = g_C \otimes f_C \text{ and } h_G = g_G \otimes f_C \quad (3.7)$$

where subscripts  $C$  and  $G$  denote the Cauchy and Gaussian components of the respective Voigt profiles. From equation (3.7) it follows that the integral breadths of  $f_C$  and  $f_G$  are given by

$$\beta_C^f = \beta_C^h - \beta_C^g \text{ and } (\beta_G^f)^2 = (\beta_G^h)^2 - (\beta_G^g)^2 \quad (3.8)$$

The constituent Cauchy and Gaussian components can be obtained from the ratio  $2w/\hat{a}$  for the  $h$  and  $g$  profiles. However, to avoid graphical methods or interpolation from tables, an empirical formula has been given as [273]

$$\beta_C = (a_0 + a_1\varphi + a_2\varphi^2)\beta \quad (3.9)$$

and

$$\beta_G = \left[ b_0 + b_{12} \left( \varphi - \frac{2}{\pi} \right)^{1/2} + b_1\varphi + b_2\varphi^2 \right] \beta \quad (3.10)$$

where  $\varphi = 2w/\beta$ ,  $a_0 = 2.0207$ ,  $a_1 = -0.4803$ ,  $a_2 = -1.7756$ ,  $b_0 = 0.6420$ ,  $b_{12} = 1.4187$ ,  $b_1 = -2.2043$  and  $b_2 = 1.8706$ .

The maximum error introduced by equations (3.9) and (3.10) is about 1%, and in the majority of cases the error is much less than this. In order to separate size and strain effects, it has been assumed that the size and strain profiles have a Voigtian profile. If two or more reflections are available, size and strain effects can be determined from the variation of  $\beta_C^f$  and  $\beta_G^f$  with  $hkl$  [276]. However in single line analysis it is assumed that the Cauchy component of the  $f$  profile is solely due to crystallite size (domain length in case of polymers) and that the Gaussian contribution arises from strain [277]. In a single-line analysis the apparent crystallite or domain length ( $L$ ) is given by [273]

$$L = \frac{\lambda}{\beta_C^f \cos \theta} \quad (3.11)$$

and the strain ( $\varepsilon$ ) is given as

$$\varepsilon = \frac{\beta_G^f}{4 \tan \theta} \quad (3.12)$$

where  $\beta$  is measured on  $2\theta$  scale and,  $\lambda$  is the wavelength of the radiation used and  $\theta$  is the angular position of the line.

### 3.8 Fourier Transform Infrared Spectroscopy (FTIR)

Fourier Transform Infrared Spectroscopy (FTIR) is a powerful analytical tool for characterizing and identifying organic molecules, chemical bonds (functional groups) and the molecular structure of organic compounds. Figure 3.9 describes the layout of a simple FTIR spectrometer. The key modules of a FTIR spectrometer are the source, the Michelson interferometer and the detector. To use the FTIR instrument, the IR radiation from a continuous source is directed onto the sample of interest and the intensity is measured using an infrared detector. The Michelson interferometer provides the means for the spectrometer to measure all optical frequencies simultaneously. The interferometer modulates the intensity of the individual frequencies of radiation before the detector picks up the signal.

Part of the infrared radiation is absorbed by the sample and the rest is transmitted. The wavelength of infrared radiation absorbed is characteristic of stretching/bending vibrational modes of a chemical bond. The most useful range for identification of the compounds is the near and mid-infrared region as most of the molecular vibrations lie in these frequency regions. The resulting spectrum represents the molecular absorption and transmission, creating a molecular fingerprint of the sample with absorption peaks, which correspond to the frequencies of vibrations between the bonds of the atoms making up the material. Because each material is a unique combination of atoms, no two compounds produce exactly similar infrared spectra. Therefore, infrared spectroscopy can result in a positive identification (qualitative analysis) of different kind of materials. A single vibrational energy change is accompanied by a number of rotational energy changes, consequently vibrational spectra appear as bands rather than as discrete lines.

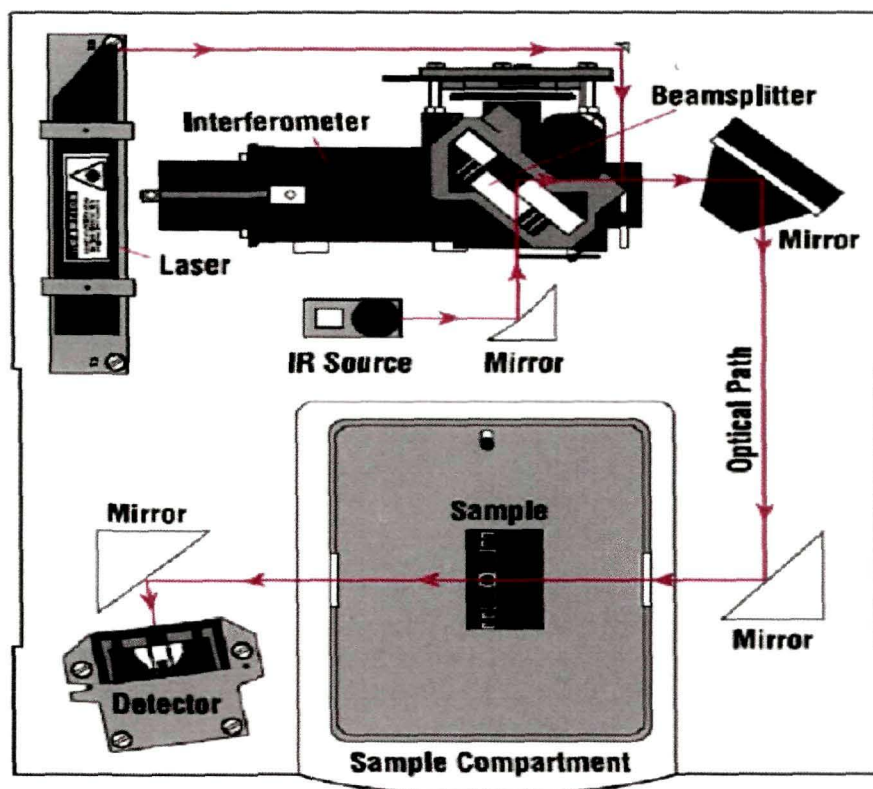


Figure 3.9: layout of a typical FTIR spectrometer.

Band positions are presented as wave numbers (in  $\text{cm}^{-1}$ ). Band intensities are expressed either as transmittance ' $T$ ', the ratio of the radiant power transmitted by the sample or the absorbance ' $A$ ', logarithm to the base 10 of the reciprocal of the transmittance,  $A = \log_{10}(1/T)$ . Determination of frequencies, at which the sample absorbs IR radiation, allows the identification of the sample's chemical make-up, since functional groups are known to absorb radiation at specific frequencies. In addition, the size of the peaks in the spectrum is a direct indication of the amount of material present. With modern software algorithms, infrared is an excellent tool for quantitative analysis.

The FTIR spectroscopy study of the various polymer electrolytes and their nanocomposites have been conducted for understanding the bond structure and different interactions taking place among the various constituents of polymer electrolytes. The FTIR spectra have been recorded using a Perkin Elmer spectrum 100 spectrophotometer and Nicolet Impact 410 spectroscopy installed at Tezpur University, Assam, India.

### 3.9 Transmission Electron Microscopy (TEM)

Transmission electron microscopy (TEM) is the premier tool for understanding the internal microstructure of materials at the nanometer level. Electrons have an important advantage over X-rays in that they can be focused using electromagnetic lenses. One can obtain real-space images of materials with resolutions on the order of a few tenths to a few nanometers, depending on the imaging conditions, and simultaneously obtain diffraction information from specific regions in the images (e.g. small precipitates) as small as 1 nm [278].

Transmission electron microscope (TEM) uses a high voltage electron beam to create an image. The electrons are emitted by an electron gun, commonly fitted with a tungsten filament cathode as the electron source. The electron beam is accelerated by an anode typically at +100 keV (40 to 400 keV) with respect to the cathode, focused by electrostatic and electromagnetic lenses, and transmitted through the specimen that is in part transparent to electrons and in part scatters them out of the beam. When it emerges from the specimen, the electron beam carries information about the structure of the specimen that is magnified by the objective lens system of the microscope. The spatial variation in this information (the “image”) is viewed by projecting the magnified electron image onto a fluorescent viewing screen coated with a phosphor or scintillator material such as zinc sulfide. The image can be photographically recorded by exposing a photographic plate directly to the electron beam, or a high-resolution phosphor may be coupled by means of a lens optical system or a fiber optic light-guide to the sensor of a CCD (charge-coupled device) camera. The image detected by the CCD may be displayed on a monitor or computer. Resolution of the TEM is limited primarily by spherical aberration, but a new generation of aberration correctors has been able to partially overcome spherical aberration to increase resolution. Hardware correction of spherical aberration has allowed the production of images with resolution below 0.5 Å (50 pm) at magnifications above 50 millions [279]. The TEM studies have been carried out using JEOL JEM 100 CX II transmission electron microscope installed at the Sophisticated Analytical Instrumentation Facility (SAIF), North-Eastern Hill University (NEHU), Shillong, Meghalaya, India shown in figure 3.10. The micrographs have been taken at 100 kV accelerating voltage at different magnifications according to need.

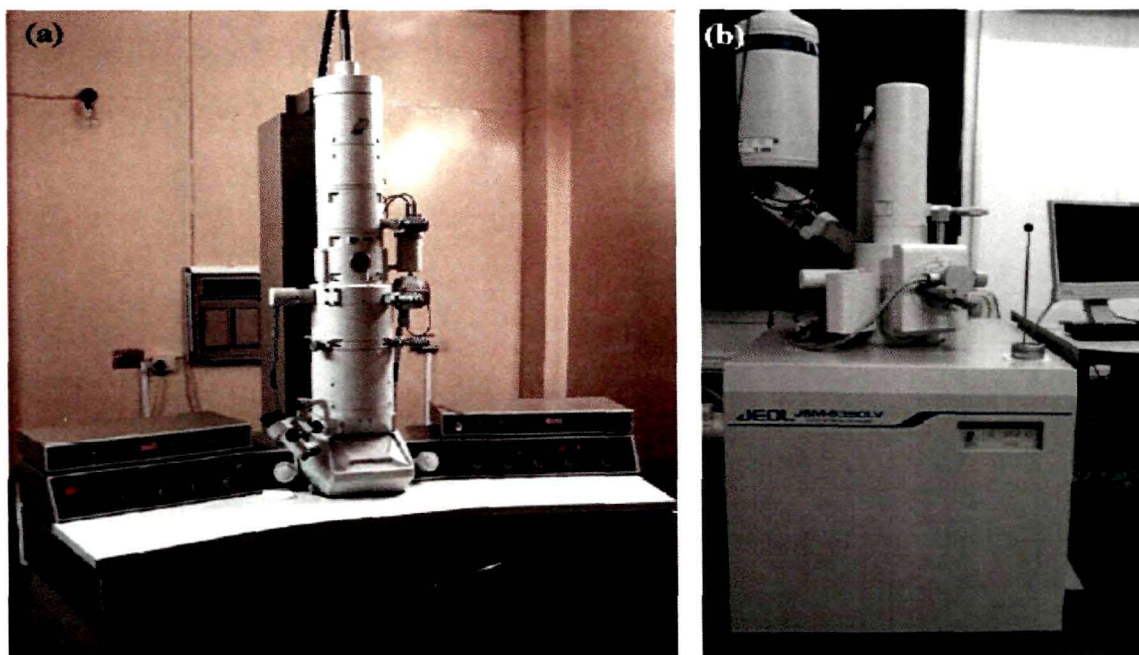


**Figure 3.10:** (a) Transmission electron microscope (JEOL JEM 100 CXII) at SAIF, NEHU, Shillong and (b) Scanning electron microscope (JEOL JSM 6390 LV) installed at Tezpur University used for acquiring electron micrographs in the present work.

### 3.10 Scanning Electron Microscopy (SEM)

The scanning electron microscope (SEM) is one of the most widely used instruments in materials research laboratories and is common in various forms in fabrication plants. The SEM study has been carried out using a JEOL JSM 6390 LV model scanning electron microscopy [shown in figure 3.10 (b)] installed at Central Instrumentation Facility (CIF), Tezpur University, Assam, India to examine the surface morphology and porosity. The micrographs have been taken at an accelerating voltage varying between 5-15 kV and magnification is fixed according to need from 2000X to 10000X.

Scanning electron microscopy is central to microstructural analysis and therefore important to any investigation relating to the processing, properties, and behaviour of materials that involve their microstructure. The SEM provides information relating to topographical features, morphology, phase distribution, compositional differences, crystal structure, crystal orientation, and the presence and location of electrical defects [280]. The SEM electron beam is a focused probe of electrons accelerated to moderately high energy and positioned onto the sample by electromagnetic fields. The SEM optical column is

utilized to ensure that the incoming electrons are of similar energy and trajectory. These beam electrons interact with atoms in the specimen by a variety of mechanisms when they impinge on a point on the surface of the specimen. For inelastic interactions, energy is transferred to the sample from the beam, while elastic interactions are defined by a change in trajectory of the beam electrons without loss of energy. Since electrons normally undergo multiple interactions, the inelastic and elastic interactions result in the beam electrons spreading out into the material (changing trajectory from the original focused probe) and losing energy. This simultaneous energy loss and change in trajectory produces an interaction volume within the bulk. The signals resulting from these interactions (e.g. electrons and photons) will each have different depths within the sample from which they can escape due to their unique physical properties and energies.

Lenses in the SEM are not a part of the image formation system but are used to demagnify and focus the electron beam onto the sample surface. This gives rise to two of the major benefits of the SEM: range of magnification and depth of field in the image. Depth of field is that property of SEM images where surfaces at different distances from the lens appear in focus, and thus provide three-dimensional information about the image [280].

The interaction of high energy electrons with the sample results in the generation of Backscattered electrons (BSEs) and Secondary Electrons (SEs). BSEs are electrons from the incident probe that undergo elastic interactions with the sample, change trajectory, and escape the sample. These make up the majority of electrons emitted from the specimen at high beam voltage and their average energy is much higher than that of the SEs. The intensity of the BSE signal is a function of the average atomic number ( $Z$ ) of the specimen, with heavier elements (higher  $Z$  samples) producing more BSEs. The BSE intensity and trajectory are also dependent upon the angle of incidence between the beam and the specimen surface. The topography or physical features of the surface are then imaged by using these properties of the BSE signal to generate BSE topographic images. Secondary electrons (SEs) of low energy (typically 2 to 5 eV), on the other hand, are due to inelastic interactions and are influenced more by surface properties than by atomic number. The SE is emitted from an outer shell of a specimen atom upon impact of the incident electron beam. The depth from which SEs escape the specimen is generally between 5 and 50 nm due to their low energy. Secondary electrons are generated by both the beam entering the specimen and BSEs as they

escape the specimen; however, SE generation is concentrated around the initial probe diameter. Secondary electron intensity is a function of the surface orientation with respect to the beam and the SE detector and hence produces an image of the specimen morphology [280].

### 3.11 Swift Heavy Ion (SHI) Irradiation

Swift heavy ion (SHI) irradiation experiments have been carried out in the Material Science (MS) beam line at Inter University Accelerator Centre (IUAC), New Delhi under ultrahigh vacuum  $\sim 10^{-6}$  Torr. The swift heavy ions having high energies ( $> 1$  MeV/u) are provided by the 15 UD Pelletron accelerator at IUAC [281].

The schematic view of the 15 UD Pelletron at IUAC and its different parts are shown in figure 3.11. It is basically a tandem electrostatic Van de Graff type accelerator, in vertical configuration, which can go up to a maximum terminal voltage of 16 MV and capable of accelerating any ion from proton to uranium up to an energy of around 200 MeV depending upon the suitable negative ion source and the charge state. The pelletron accelerator consists mainly of two parts: (a) ion source and (b) the accelerating column with many auxiliary parts in between. In the top portion of the tank there are three different ion sources, viz., R.F. source (ALPHATROSS), Source of Negative Ions by Cesium Sputtering (SNICS) and direct extraction negative ion source (Duoplasmatron), which can produce different negative ions to be injected in pelletron tank. These three ion sources working on three different principles can produce almost every type of negative ions. Duoplasmatron works on the principle of gas discharge, SNICS uses surface ionization and R.F. source utilizes high frequency gas discharge.

The negative ions emerging from the ion source are first accelerated to 250 keV by the high voltage deck potential and different optical elements focus and inject the same into the vertical accelerating tube. The injector magnet does mass selection by bending the ions by  $90^\circ$  and then injects them into the accelerating tube. The singly ionized negative ions then follow a vertical downward path and get accelerated through the accelerating tube path. It consists of a vertical insulating cylindrical tank of height 26.5 m and diameter 5.5 m, filled with  $\text{SF}_6$  (Sulphur hexafluoride) at high pressure ( $> 200$  psi) as an insulating gas. In the top portion of the tank there is an ion source system consisting of a high negative potential deck,



SNICS, vacuum system, power supplies and controls of the ion source required to produce and inject the negative ions into accelerating tank. The ion source system is followed by the high voltage accelerating terminal of height 3.18 m and diameter 1.52 m inside the tank. The terminal is connected to the tank vertically through ceramic titanium tubes called accelerating tubes. A potential gradient is maintained through these tubes from high voltage to ground, from top of the tank to the terminal as well as from the terminal to the bottom of the tank. The insulating column which supports the high potential terminal consists of thirty 1 MV modules, 15 on either side of the terminal. The upper portion of the column is referred to as low energy section and the portion below the terminal as the high energy section. The shorted section with no potential gradient, commonly known as the Dead Section, is provided each in the low and high energy sections for equipment housing. Both are provided with an electron trap and a sputter ion pump.

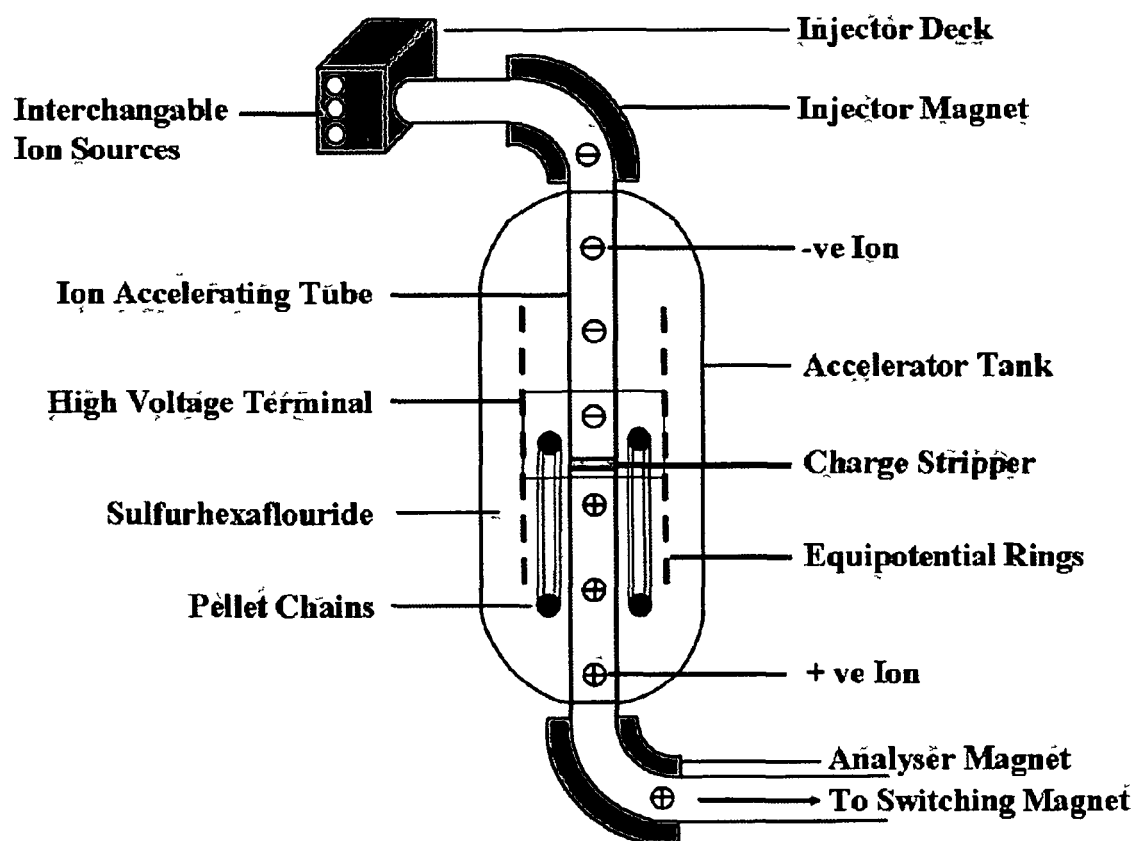


**Figure 3.11:** Schematic diagram showing the principle of acceleration of ions in a Pelletron (Courtesy: <http://www.iuac.res.in/infrastructure/accelerators/pelletron/index.htm>)

The beam energy gained by the ion in the accelerating tube at the end of the tube is determined by,

$$E_{beam} = (q + 1)V_T \quad (3.13)$$

where  $V_T$  is the terminal voltage,  $q$  is the number of positive charges on the ion after stripping. These high energy ions were analyzed to the required energy with the help of  $90^\circ$  bending magnet known as analyzer magnet and directed to the desired experimental area with the help of switching magnet, which can deflect the beam into any one of the seven beam lines in the beam hall for the experiments.

Figures 3.12 (a, b) shows the Materials Science (MS) beam line and the samples loaded on a ladder. For ion irradiation, the samples of area  $1\text{cm} \times 1\text{cm}$  are mounted on a sample holder (ladder) made up of copper. The ladder in the Material Science (MS) chamber is rectangular and 24 samples can be loaded with six samples on each side at a time. After sample loading the ladder is inserted in the MS vacuum chamber. Vacuum inside the irradiation chamber is maintained with the help of a rotary and turbo-molecular pump at  $\sim 10^{-6}$  torr during irradiation. All the samples in the present work have been irradiated at normal beam incidence.

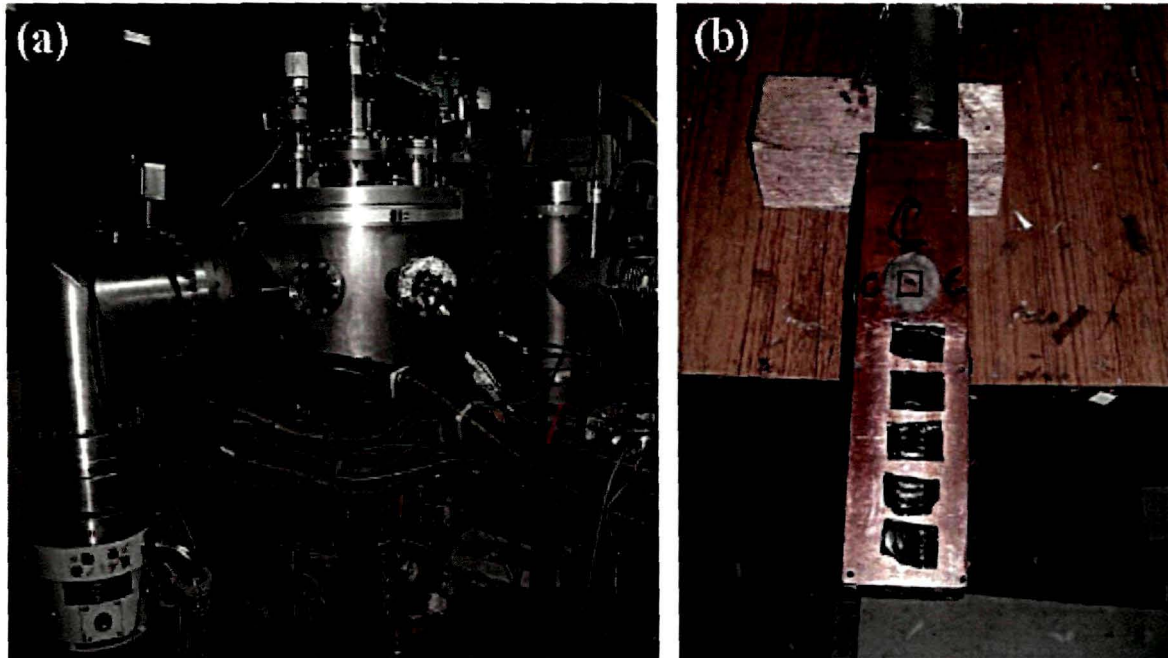


**Figure 3.12:** Photographs of (a) the high vacuum irradiation chamber in the Materials Science (MS) beam line at IUAC and (b) sample loaded in the ladder used for irradiating the samples.

### 3.11.1 Parameters Related to Ion Irradiation

#### Fluence ( $\phi$ )

It is defined as the total number of irradiating ions incident per square centimeter (ions/cm<sup>2</sup>) of sample. It varies from sample to sample depending upon its size and material.

Fluences are calculated using the following formula

$$\text{Fluence} = [\text{Time } (t) \times \text{beam Current} \times \text{pnA}] / \text{Charge State} \quad (3.14)$$

Beam currents for ion irradiation experiments are usually taken in the range from 2-5 nA.

$$\begin{aligned} 1 \text{ pnA (particle nano-ampere)} &= 10^{-19} \text{ Coul/sec} / 1.6 \times 10^{-19} \text{ Coul} \\ &= 6.25 \times 10^9 \text{ particles / sec} \end{aligned} \quad (3.15)$$

#### Counts

During ion irradiation process, fluences are recorded by using a counter. Following relation relates the counts and the fluences

$$\text{Counts} = \phi q e / S \quad (3.16)$$

Where  $\phi$  is the fluence

$q$  is the charge state of ion beam,

$e$  is the electronic charge ( $1.6 \times 10^{-19}$  Coulomb)

$S$  is the scale of counter

#### Beam energy

The energy of the accelerated ion beam depends on charge state ( $q$ ) of the ion and the terminal potential  $V_T$

$$E \text{ (meV)} = (q + 1) V_T + V_{inj} \quad (3.17)$$

For the 15 UD Pelletron at Inter University Accelerator Center (IUAC), New Delhi, the terminal potential ( $V_T$ ) is in the range of 10 MeV to 15 MeV and Injector potential ( $V_{inj}$ ) is in the range 250 to 350 keV. The projected range of 90 MeV O<sup>7+</sup> ions that has been used to irradiate polymer electrolyte films in the present work is 100  $\mu\text{m}$  as calculated from SRIM-98 code (Stopping and Range of ions in matter). The thickness of polymer electrolyte

samples (30-90  $\mu\text{m}$ ) was kept less than the range calculated by SRIM programme so that all the incident ions cross the sample.

## CHAPTER IV

### ***[PMMA/ P(VdF-HFP)] based Nanocomposite Gel Polymer Electrolytes Dispersed with Dedoped (Insulating) PANi Nanofibers***

---

*The aim of the present chapter is to investigate whether the dispersion of dedoped (insulating) polyaniline (PANi) nanofibers affect the ion transport properties of PMMA P(VdF-HFP) based composite polymer electrolytes. By analysis of SEM, XRD, impedance spectroscopy and FTIR results it has been demonstrated that the incorporation of dedoped PANi nanofibers up to a moderate concentration to PMMA/P(VdF-HFP)-(PC+DEC)-LiClO<sub>4</sub> gel polymer electrolyte system significantly enhance the ionic conductivity and interfacial stability of the electrolyte system. At higher concentration dedoped nanofibers appear to get phase separated and form insulating clusters, which impede ionic transport. The pores in the polymer matrix are greatly widened by the nanofibers due to their high aspect ratio (>50) and the ions get extra free volume for movement.*

---

Nanocomposite gel polymer electrolytes can be formed by polymer, plasticizer, salt and dispersed inorganic or organic nano-sized particles have been the subject of great deal of research in the last few years because of their potential importance in the development of solid state batteries as discussed in chapter I.

In this chapter an attempt has been made to study the electrical and electrochemical properties of P(VdF-HFP)-(PC+DEC)-LiClO<sub>4</sub> and PMMA-(PC+DEC)-LiClO<sub>4</sub> based gel electrolytes dispersed with dedoped (insulating) polyaniline (PANi) nanofibers. Ionic conductivity of the nanocomposite gel polymer electrolytes have been measured by complex impedance analysis described in Chapter II. The nature of conductivity of the nanocomposite gel polymer electrolytes was determined by transference number measurements using Wagner polarization technique with polymer electrolyte films sandwiched between graphite blocking electrodes. The transference number was found to be  $\approx 0.98$  indicating that conductivity was essentially ionic in nature. X-ray diffraction patterns of the prepared films were obtained by Rigaku miniflex diffractometer at room temperature. Surface morphology of the composite electrolytes was studied by using scanning electron microscope (SEM) (JEOL 6390 LV). The size of PANi nanofibers was determined by TEM (JEOL-TEM-100 CXII). The interfacial stability of nanocomposite polymer electrolytes was studied by

fabricating stainless steel/polymer electrolyte/stainless steel cells at room temperature and was monitored for 18-20 days. The anodic decomposition voltage was determined by linear sweep voltammetry using electrochemical workstation. FTIR was conducted using Perkin Elmer spectrum 100 spectrophotometer using KBr pellets.

#### 4.1 TEM Studies

Figure 4.1 shows the TEM micrograph of PANi nanofibers. From the figure it is observed that nanofibers are composed of randomly packed polymer chains. As the PANi nanofibers are synthesized by interfacial polymerization, no overgrowths of polyaniline on the nanofiber scaffolds take place and nanofibrillar morphological units are formed. The diameter and length of the nanofibers are in the range of 20 to 30 nm and more than 1,000 nm, respectively.

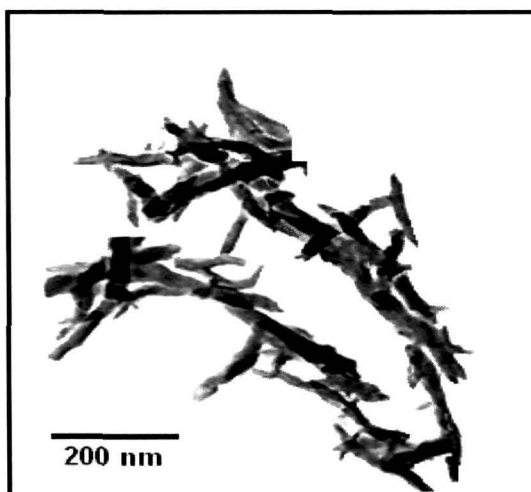
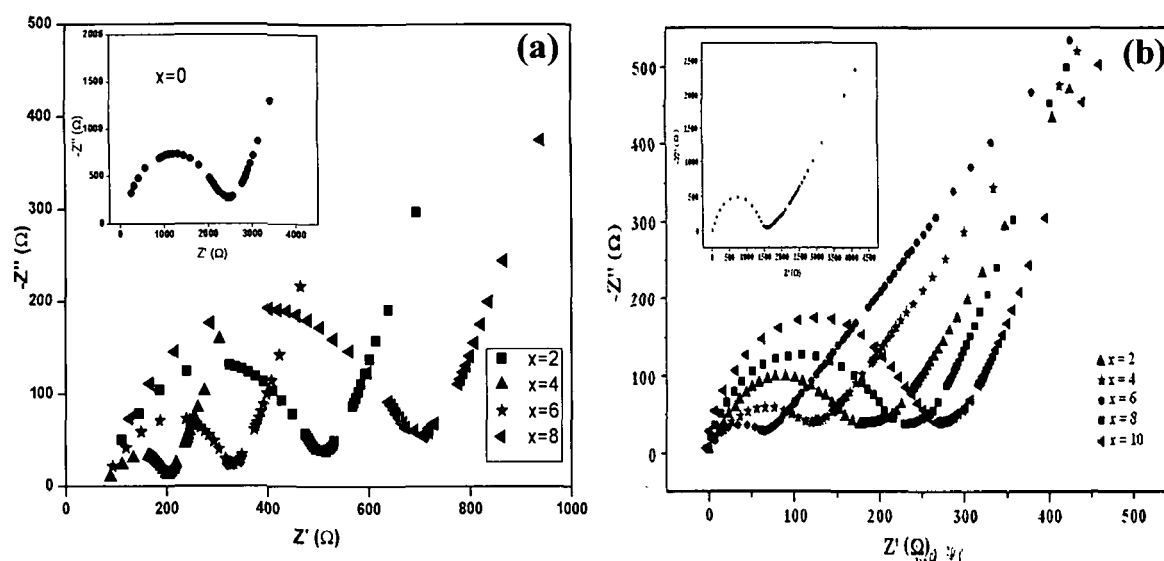


Figure 4.1: TEM image of dedoped PANi nanofibers.

#### 4.2 Ionic Conductivity Measurements

Ionic conductivity of as-prepared nanocomposite gel polymer electrolytes was obtained from the complex impedance measurements as described in Chapter II. Figures 4.2 (a & b) show the impedance plot of PMMA-(PC + DEC)-LiClO<sub>4</sub>-x% dedoped PANi nanofibers ( $x = 2, 4, 6$  and  $8$ ) and P(VdF-HFP)-(PC + DEC)-LiClO<sub>4</sub>-x% dedoped PANi nanofibers ( $x = 2, 4, 6, 8$  and  $10$ ) composite polymer electrolytes at room temperature, respectively. The impedance spectra comprise a distorted semicircular arc in the high frequency region followed by a

spike in the lower frequency region. The high frequency semicircle is due to the bulk properties and the low frequency spike is due to the electrolyte and electrode interfacial properties. The bulk electrical resistance value ( $R_b$ ) is calculated from the intercept at high frequency side on the  $Z'$  axis. The ionic conductivity is calculated from the relation  $\sigma = l/R_b r^2 \pi$ ; where  $l$  and  $r$  are thickness of polymer electrolyte membrane and radius of the sample membrane discs and  $R_b$  is the bulk resistance obtained from complex impedance measurements.



**Figure 4.2:** Complex impedance spectra of (a) PMMA-(PC+DEC)-LiClO<sub>4</sub>- $x$ % dedoped PANi nanofibers ( $x = 2, 4, 6$  and  $8$ ) and (b) P(VdF-HFP)-(PC+DEC)-LiClO<sub>4</sub>- $x$ % dedoped PANi nanofibers ( $x = 2, 4, 6, 8$  and  $10$ ). Insets show the Nyquist plots for  $x=0$ .

It is observed that the  $\sigma_{\text{ionic}}$  increases with increase in concentration of nanofibers in both the cases. Maximum conductivity was found to be  $2.1 \times 10^{-3} \text{ Scm}^{-1}$  for PMMA-(PC + DEC)-LiClO<sub>4</sub> - $x$ % dedoped PANi nanofibers at  $x = 4$  wt. % while P(VdF-HFP)-(PC + DEC)-LiClO<sub>4</sub> - $x$ % dedoped PANi nanofibers exhibits the highest conductivity of  $6.3 \times 10^{-3} \text{ Scm}^{-1}$  for  $x = 6$  wt. % at room temperature. These conductivity values are over one order higher as compared to that for polymer electrolyte without nanofibers in both the cases. However, as the filler (dedoped nanofibers) concentration increases beyond that, the ionic conductivity decreases. The variation of ionic conductivity as a function of nanofibers is shown in figures 4.3 (a & b).

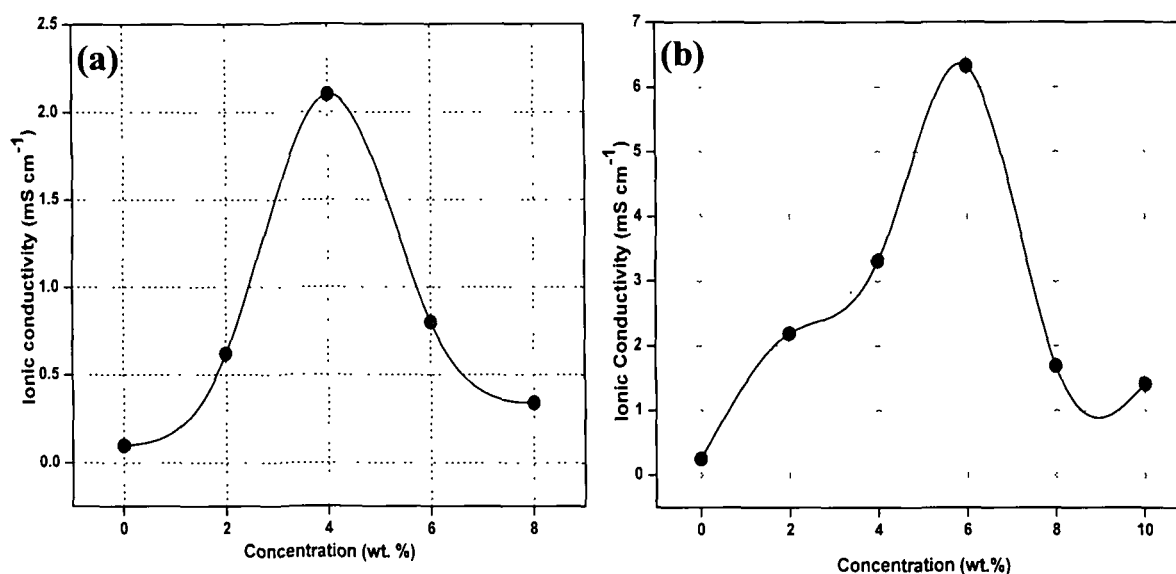


**Figure 4.3:** Variation of ionic conductivity with nanofiber concentration (a) PMMA-(PC+DEC)-LiClO<sub>4</sub>-x% dedoped PANi nanofibers ( $x = 0, 2, 4, 6$  and  $8$ ) and (b) P(VdF-HFP)-(PC+DEC)-LiClO<sub>4</sub>-x% dedoped PANi nanofibers ( $x = 0, 2, 4, 6, 8$  and  $10$ ).

The enhancement up to a certain wt. % of nanofiber concentration seems to be correlated with the fact that the dispersion of dedoped PANi nanofibers to the polymer matrix prevents chain reorganization due to the high aspect ratio of nanofibers resulting in reduction in polymer crystallinity, which gives rise to an increase in ionic conductivity. The reduction in crystallinity upon addition of PANi nanofibers up to 4 wt. % and 6 wt. % in case of PMMA and P(VdF-HFP), respectively is consistent with XRD results, which will be discussed in the next section. For gel polymer electrolyte systems porosity is one of the main factors that govern the ionic transport properties by the movement of ions through the liquid environment in the porous structure of the polymer. It is known that plasticized polymer electrolytes show highly porous structure created by plasticized rich phase [163]. When dedoped PANi nanofiber is incorporated in the porous membrane, the movement of Li<sup>+</sup> ion through the pores is facilitated by the filler due to formation of conduction path at the polymer-filler interface resulting in higher conductivity. The filler-polymer interface is a site of high defect concentration providing channels for faster ionic transport. The structure and chemistry of filler-polymer interface may have even more important role than the formation of amorphous phase in the electrolyte [114].

On the other hand, the decrease in ionic conductivity for nanofibers at higher fraction of nanofibers can be attributed to the blocking effect on the transport of charge carriers due to



the phase separation of nanofibers. The phase separation phenomenon will be discussed with the help of XRD results in the next section.

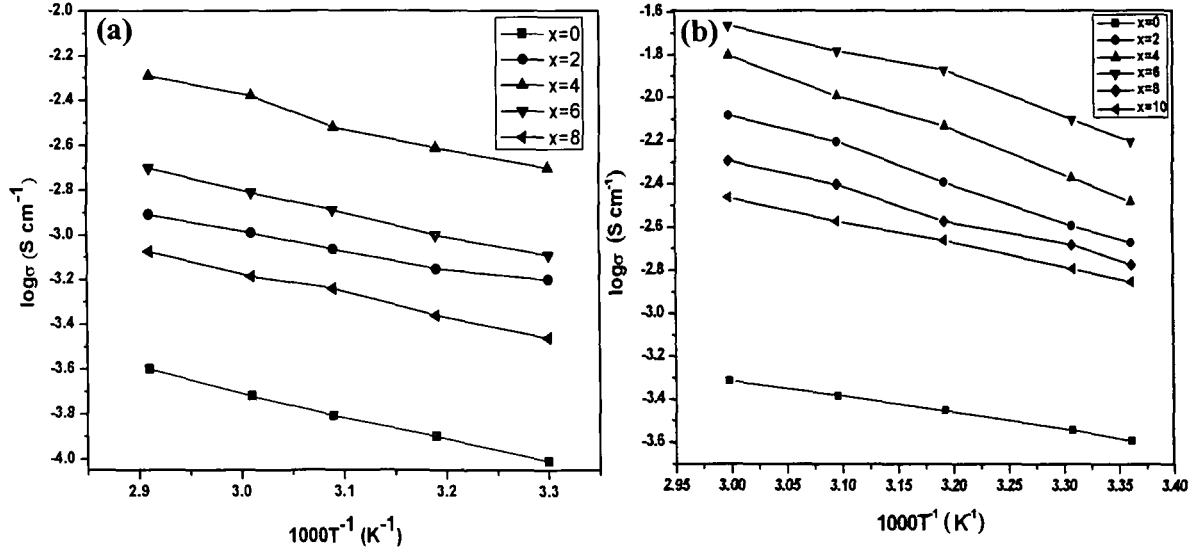


**Figure 4.4:**  $\log \sigma$  vs. temperature inverse curves of (a) PMMA-(PC+DEC)-LiClO<sub>4</sub>-x% dedoped PANi nanofibers ( $x = 0, 2, 4, 6$  and  $8$ ) and (b) P(VdF-HFP)-(PC+DEC)-LiClO<sub>4</sub>-x% dedoped PANi nanofibers ( $x = 0, 2, 4, 6, 8$  and  $10$ ).

Figures 4.4 (a & b) show the conductivity versus temperature inverse plots of polymer electrolyte films in the temperature range from 25 °C to 80 °C. The figures show that the ionic conduction in nanocomposite polymer electrolytes obeys the Arrhenius relation [282]

$$\sigma = \sigma_0 \exp(-E_a/kT) \quad (4.1)$$

where  $\sigma$ ,  $\sigma_0$ ,  $E_a$ ,  $k$  and  $T$  are the ionic conductivity, pre exponential factor, activation energy, Boltzmann constant and absolute temperature, respectively. As expected the increase in temperature leads to increase in ionic conductivity because as the temperature increases the polymer chains flex at increased rate to produce larger free volume, which leads to enhanced polymer segmental and ionic mobilities. The enhancement of ionic conductivity by the dedoped PANi nanofibers can be explained by the fact that the nanofibers inhibit the recrystallization kinetics, helping to retain the amorphous phase down to relatively low temperatures.

### 4.3 X-Ray Diffraction (XRD) Analysis

X-ray diffraction patterns of pure PMMA, pure P(VdF-HFP) and pure dedoped PANi nanofibers are presented in figure 4.5. Figure 4.6(i) shows the XRD patterns of PMMA-(PC+DEC)-LiClO<sub>4</sub>-x% dedoped PANi nanofibers ( $x = 2, 4, 6$  and  $8$ ) while figure 4.6(ii) shows the XRD patterns of pure P(VdF-HFP) and P(VdF-HFP)-(PC+DEC)-LiClO<sub>4</sub>-x% dedoped PANi nanofibers ( $x = 2, 4, 6, 8$  and  $10$ ). Two characteristics peaks are observed at

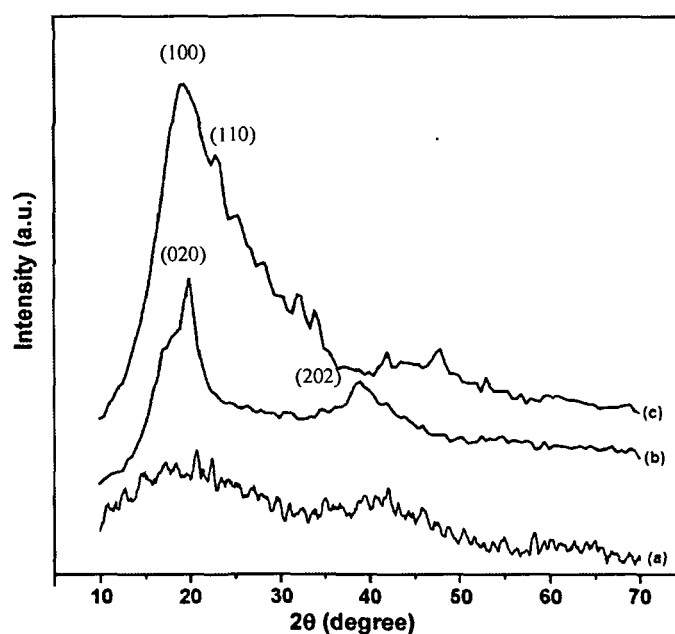


**Figure 4.5:** XRD patterns of (a) pure PMMA, (b) pure P(VdF-HFP) and (b) pure dedoped PANi nanofibers.

$2\theta=19.5^\circ$  and  $23^\circ$  for pure dedoped PANi nanofibers. However, there is hardly any peak observed in case of pure PMMA. In case of pure P(VdF-HFP) the peaks at  $2\theta=20^\circ$  and  $38^\circ$  correspond to (020) and (202) crystalline peaks of P(VdF) [283]. This is a confirmation of partial crystallization of the PVdF units in the copolymer to give an overall semi-crystalline morphology for P(VdF-HFP). Addition of dedoped PANi nanofibers in polymer electrolytes increases the amorphicity of the composites up to  $x = 4$  wt. % for PMMA and  $x = 6$  wt. % for P(VdF-HFP) based electrolytes. This is due to fact that addition of nanofibers prevents polymer chain reorganization causing significant disorder in the polymer chains, which promotes the interaction between them [164].

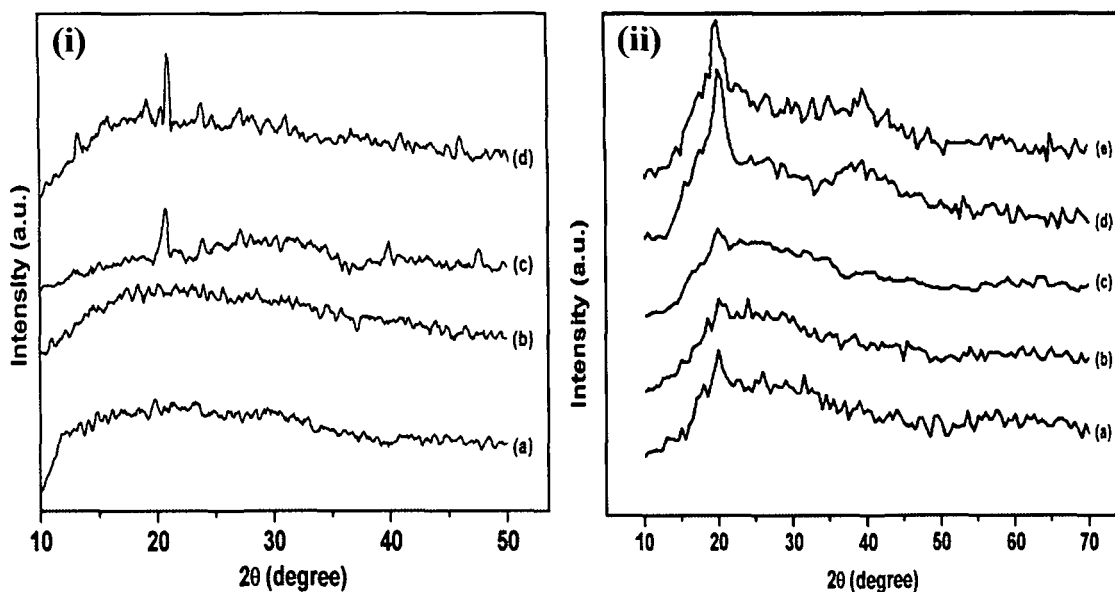


**Figure 4.6:** XRD patterns of (i) PMMA-(PC+DEC)-LiClO<sub>4</sub>-x% dedoped PANi nanofibers: (a) x=2, (b) x=4, (c) x=6 and (d) x=8 and (ii) P(VdF-HFP)-(PC+DEC)-LiClO<sub>4</sub>-x% dedoped PANi nanofibers: (a) x=2, (b) x=4, (c) x=6, (d) x=8 and (e) x=10.

However, beyond 4 wt. % of nanofibers for PMMA and 6 wt. % for P(VdF-HFP) concentration the peaks due to PANi nanofibers reappear and the crystallinity of the composite increases. This reveals that beyond the critical concentration, nanofibers get phase separated from polymer electrolyte phase and start forming insulating clusters, which impede the ion motion resulting in decrease in ionic conductivity.

#### 4.4 Morphological Studies

Scanning electron micrographs of pure PMMA, PMMA-(PC + DEC)-LiClO<sub>4</sub> -x% dedoped PANi nanofibers (x = 4 and 8), pure P(VdF-HFP) and P(VdF-HFP)-(PC + DEC)-LiClO<sub>4</sub> -x% dedoped PANi nanofibers (x = 4 and 8) composite gel polymer electrolytes are shown in figures 4.7 (a-f). It is observed that pure PMMA and pure P(VdF-HFP) show highly porous structure with uniform pore distribution. With the addition of plasticizer and filler (PANi nanofibers) up to 4 wt. % in PMMA and 6 wt. % in P(VdF-HFP) based electrolytes, pore distribution on the surface of the polymer electrolytes becomes denser with larger pore size [Figures 4.7(b & e)] while porous structure is almost vanished at 8 wt. % of nanofibers content for PMMA and 10 wt. % of nanofibers content for P(VdF-HFP). In composite gel polymer electrolytes the porous structure gives conducting pathways for Li<sup>+</sup> ions movement

[163]. The high aspect ratio of nanofibers remarkably increases the pore density and widens the porous structure of the polymer electrolytes.

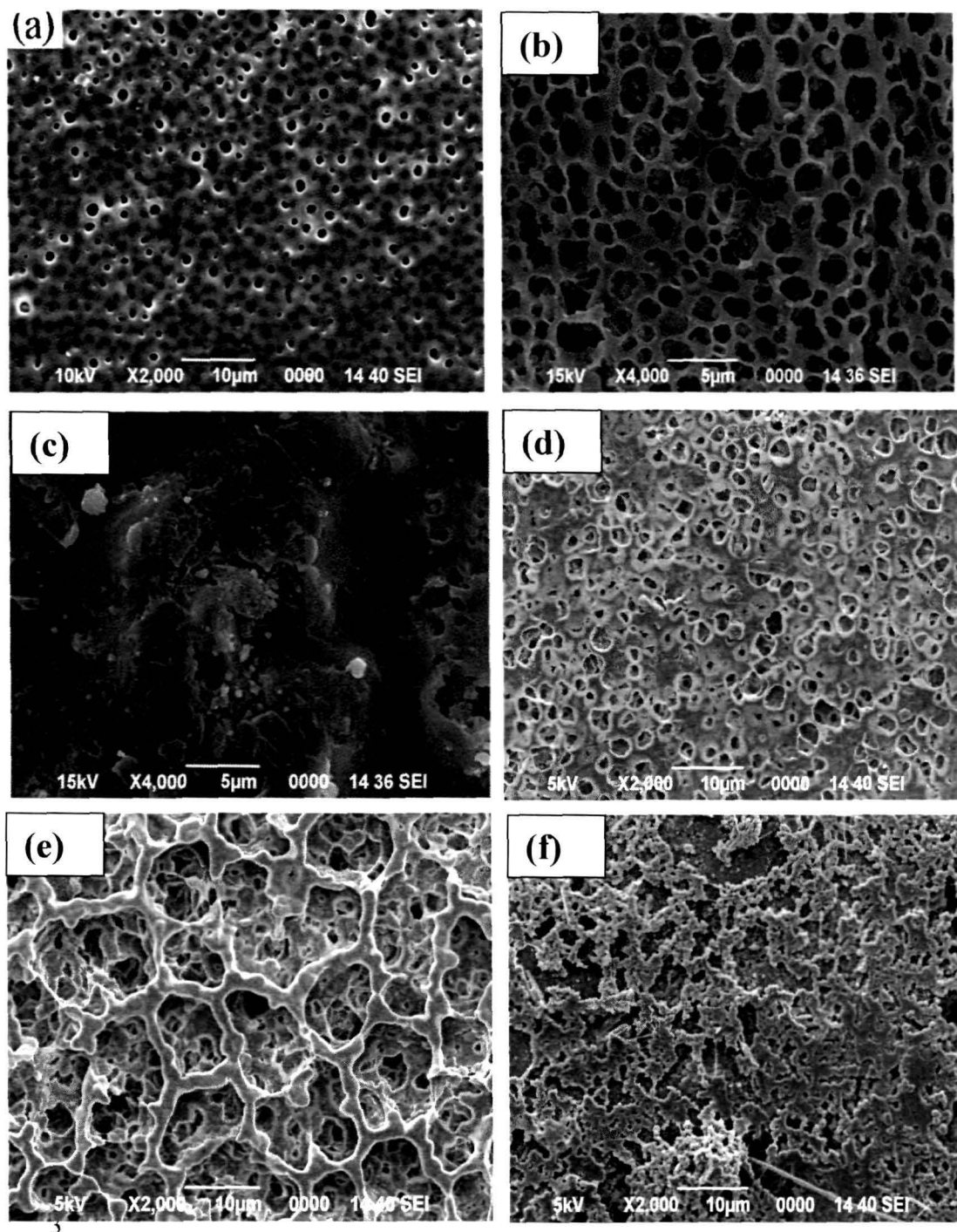


**Figure 4.7:** SEM image of (a) pure PMMA, PMMA-(PC+DEC)-LiClO<sub>4</sub>-x% dedoped PANi nanofibers: (b) x=4, (c) x=8, (d) pure P(VdF-HFP), P(VdF-HFP)-(PC+DEC)-LiClO<sub>4</sub>-x% dedoped PANi nanofibers: (e) x=6 and (f) x=10.

The above phenomenon is possibly due to the fact that the dedoped nanofibers try to occupy the pores in the gel polymer electrolyte and in the process pore distribution becomes denser. Highly porous structure leads to better connectivity of the liquid electrolyte through the pores accounting for the increase in ionic conductivity. Highly porous surface morphology of the polymer electrolytes is effectively formed on account of the interaction of dispersed PANi nanofibers with polymer component as well as the affinity with solvent molecules [284]. However, beyond the critical concentration of filler content the nanofibers get phase separated from the PMMA matrix and form insulating clusters, which leads to the decrease of pore size.

#### 4.5 FTIR Analysis

FTIR has been used to study the chain structure of polymers and has led the way in interpreting the reaction of multifunctional monomers including rearrangements and isomerizations. The wavelength and frequency of the peak represents the electronic structure of an atom in a compound. Therefore, the interactions among the atoms or ions in the electrolyte system will induce changes in the electronic and vibrational levels of the atoms, resulting in the influence of the spectrum [285]. The FTIR spectra of pure PMMA and PMMA-(PC+DEC)-LiClO<sub>4</sub> at different fraction of nanofiber concentration are shown in figure 4.8. Since the carbonyl group (C=O) is a strong electron donor within the PMMA-based polymer electrolyte, the Li<sup>+</sup>-ions tends to form a complex with the oxygen atom of the carbonyl group [286]. For pure PMMA the peak at 1730 cm<sup>-1</sup> is due to the free C=O group of the PMMA. With the addition of nanofibers the peak intensity decreases up to 4 wt. % of nanofibers content and then again increases with further increase of nanofibers. The decrease of this peak intensity can be ascribed to the strong interaction between C=O group of polymer and Li<sup>+</sup> cation [287]. The peak at 1242 cm<sup>-1</sup> is assigned to symmetric vibrations of C-O-C bond. Here also a decrease of peak intensity is observed with addition of nanofibers due to the interaction between Li<sup>+</sup> ion and oxygen atom of C-O-C bond in the polymer chain, the peak at 780 cm<sup>-1</sup> and 650 cm<sup>-1</sup> are assigned to CH<sub>2</sub> rocking mode and Li<sup>+</sup>, ClO<sub>4</sub><sup>-</sup> ion pair, respectively.

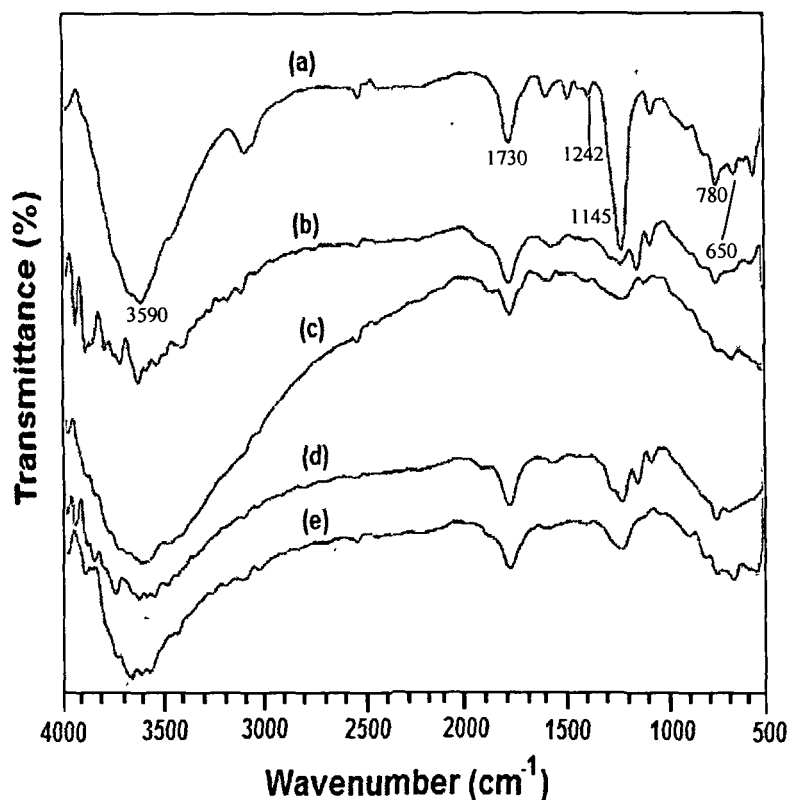


**Figure 4.8:** FTIR spectra of (a) pure PMMA and PMMA-(PC+DEC)-LiClO<sub>4</sub>-x% doped PANi nanofibers: (b) x=2, (c) x=4, (d) x=6 and (e) x= 8.

The intensity of the ion pair decreases gradually with increasing the nanofibers content and it indicates the higher dissociability of the lithium salt. After incorporation of LiClO<sub>4</sub> peak at 3590 cm<sup>-1</sup> due to C-H stretching of pure PMMA gets shifted to 3600 cm<sup>-1</sup>. As the concentration of nanofibers increases this peak is shifted to the higher frequency of 3670 cm<sup>-1</sup> indicating a strong interaction between various constituents of polymer electrolytes.

Figure 4.9 shows the FTIR spectra of P(VdF-HFP) and P(VdF-HFP)-(PC+DEC)-LiClO<sub>4</sub>-x% doped PANi nanofibers at different fraction of nanofiber concentration. Frequency 1790 cm<sup>-1</sup> is assigned -CF=CF<sub>2</sub>, -C-O-CO-O-C- group. Frequencies 1486 cm<sup>-1</sup> and 1394 cm<sup>-1</sup> are assigned to -CH<sub>3</sub> asymmetric bending and C-O stretching vibration of plasticizer propylene carbonate and diethyl carbonate. Frequencies 1286-1066 cm<sup>-1</sup> are assigned to -C-F- and -CF<sub>2</sub>- stretching vibration. Frequency 881 cm<sup>-1</sup> is assigned to vinylidene group of polymer. The vibrational peaks of PVdF are shifted to (1786, 1391, 882,

837  $\text{cm}^{-1}$ ) in the polymer electrolyte. The C-H symmetric and asymmetric bending frequencies are observed around 3000  $\text{cm}^{-1}$  in pure P(VdF-HFP). However, after incorporating dedoped PANi nanofibers the corresponding bands in the electrolyte systems show a large shift (3021  $\text{cm}^{-1}$ ) in higher frequency region, which is a characteristic of highly disordered conformation [288]. This is in good agreement with the XRD results.

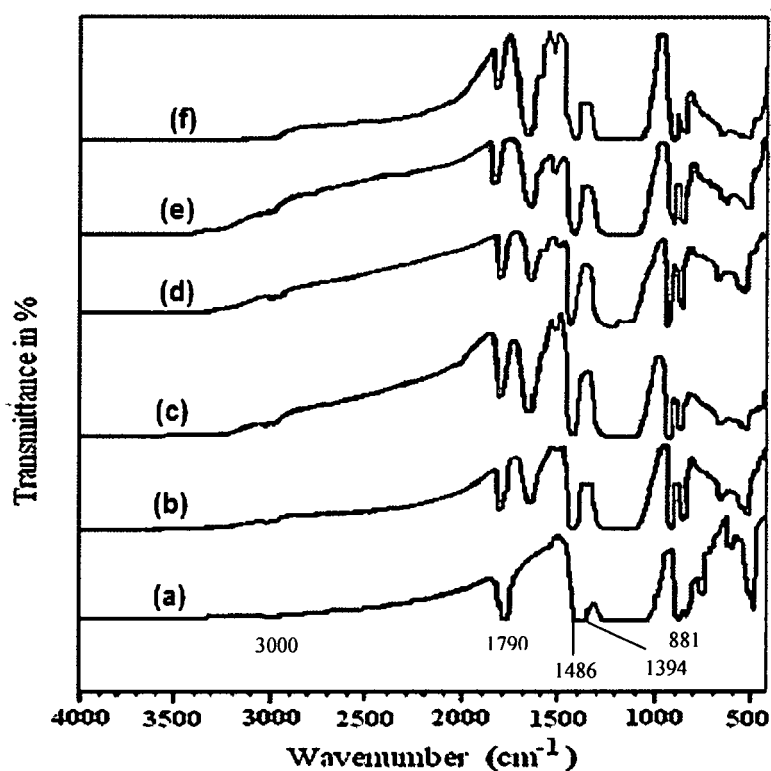


**Figure 4.9:** FTIR spectra of (a) pure P(VdF-HFP) and P(VdF-HFP)-(PC+DEC)-LiClO<sub>4</sub>-x% dedoped PANi nanofibers: (b) x=2, (c) x=4, (d) x=6, (e) x= 8 and (f) x=10.

## 4.6 Electrochemical Analysis

Linear sweep voltammetry (LSV) measurements conducted using the Li|CPE|Li cell configuration for determination of the electrochemical stability window of the electrolyte systems are presented in figures 4.10 (a & b). The measurements were carried out from 2 to 6 V at a scan rate of 0.1mVs<sup>-1</sup>. The onset of the current identifies the anodic decomposition voltage of the electrolytes. It is observed that for PMMA based electrolyte system (Figure 4.10a) the decomposition voltage increases with increase in nanofiber loading and commences at about 4.6 V for 4 wt. % nanofiber content, as compared with 4.3 V for the nanofiber-free electrolyte. Similarly for P(VdF-HFP) based electrolyte system (Figure 4.10b)

the decomposition voltage commences at about 4.7 V for a 6 wt. % nanofiber content, as compared with 4.5 V. Thus there is an improvement in the voltage stability factor in the electrolyte films containing nanofibers. It is well known that the anodic stability window is limited by irreversible oxidation of the salt anion [289]. The Lewis acid sites on the anionic surface of nanofibers can interact with  $\text{ClO}_4^-$  (Lewis base), thereby enhancing the electrochemical potential window by retarding decomposition of the lithium salt anion. This working voltage range (i.e., electrochemical potential window) appears to be sufficient for application of the nanocomposite gel polymer electrolyte films as a solid-state separator/electrolyte in Li-ion batteries.

Compatibility of nanocomposites polymer electrolyte with electrode materials is an important factor for polymer battery applications. In order to improve the interfacial stability of polymer electrolytes before and after incorporating dedoped PANi nanofibers, the ionic conductivity was measured by fabricating stainless steel/polymer electrolyte membrane/stainless steel cells at room temperature and monitored for 18-20 days. Polymer electrolytes without nanofibers and containing 4 wt. % and 6 wt. % of dedoped PANi nanofibers for PMMA based nanocomposites electrolytes and P(VdF-HFP) based nanocomposites electrolytes have been selected to observe the effect of nanofiber on interfacial stability and the results are shown in figures 4.11 (a & b).

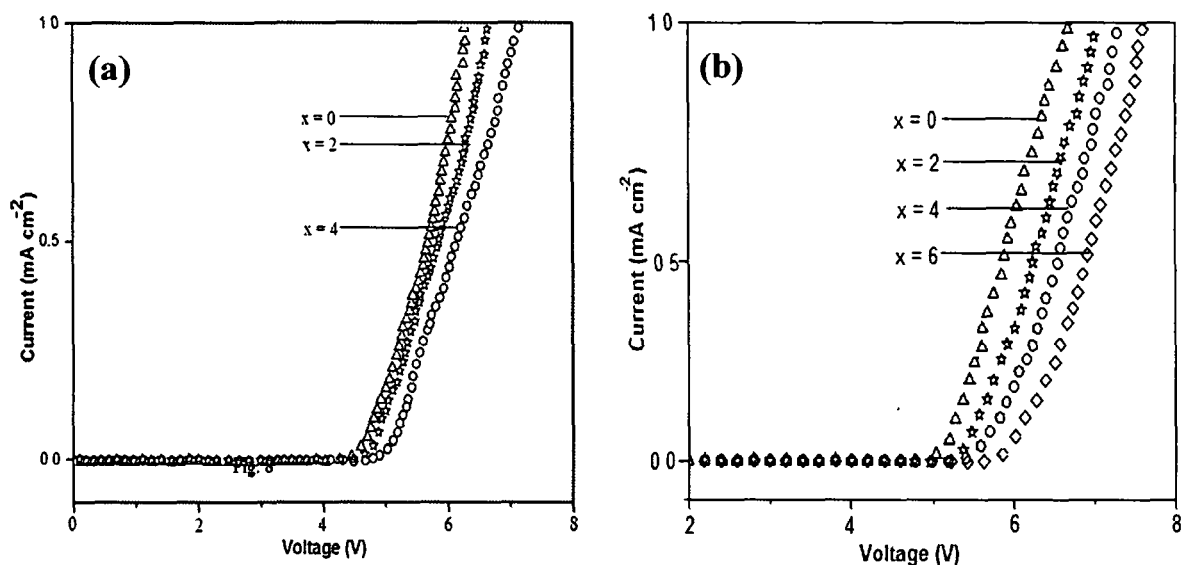


**Figure 4.10:** Linear sweep voltammetry (LSV) of (a) PMMA-(PC+DEC)-LiClO<sub>4</sub>-x% dedoped PANi nanofibers (x = 0, 2 and 4) and (b) P(VdF-HFP)-(PC+DEC)-LiClO<sub>4</sub>-x% dedoped PANi nanofibers (x = 0, 2, 4 and 6).



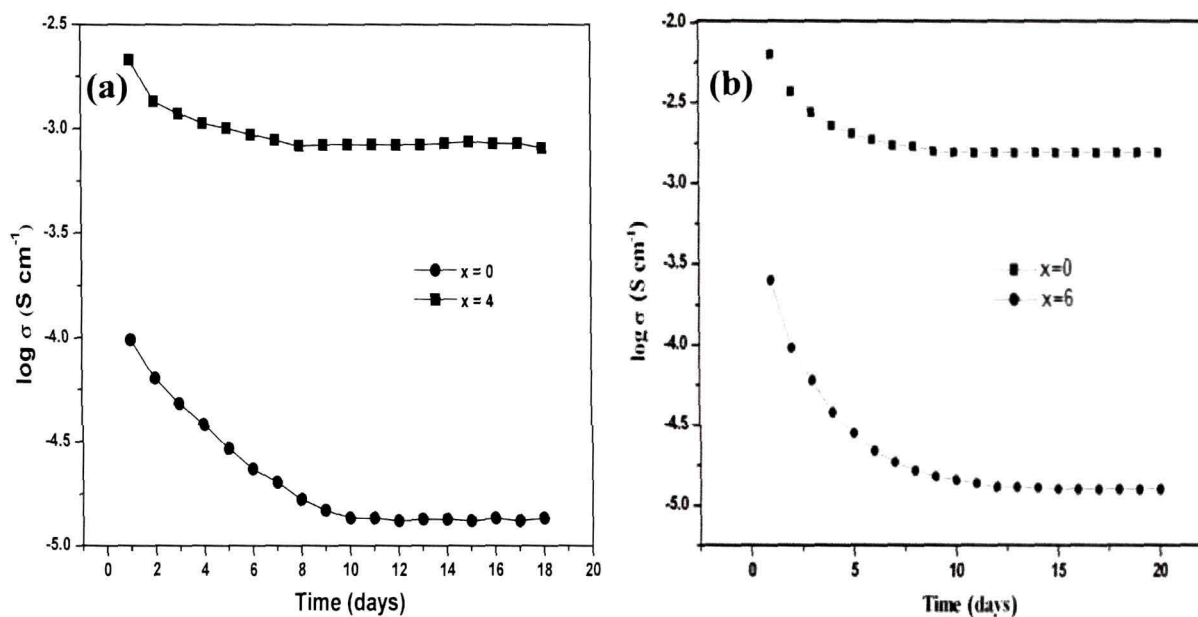


**Figure 4.11:** Interfacial stability of (a) PMMA-(PC+DEC)-LiClO<sub>4</sub>-x% dedoped PANi nanofibers ( $x = 0$  and 4) and (b) P(VdF-HFP)-(PC+DEC)-LiClO<sub>4</sub>-x% dedoped PANi nanofibers ( $x = 0$  and 6).

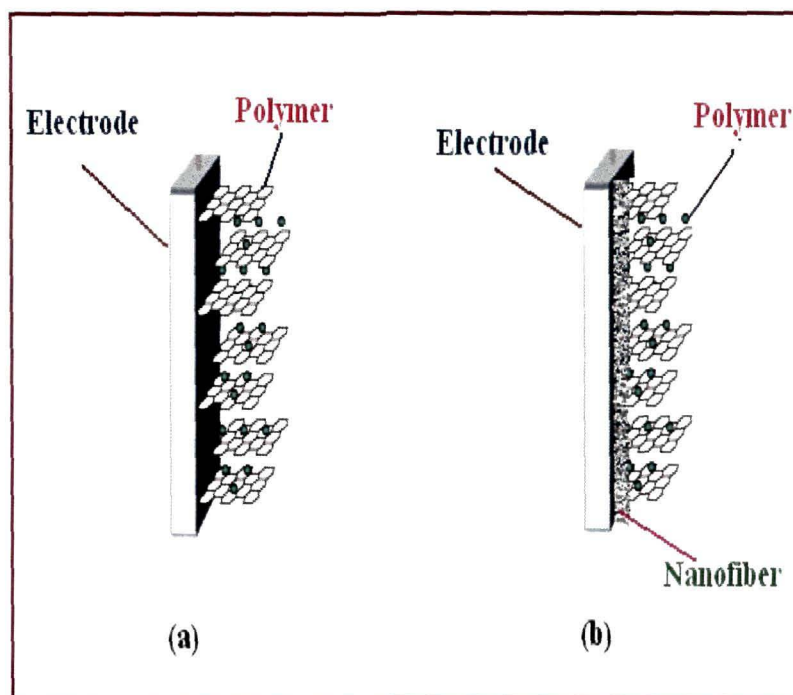


**Figure 4.12:** Schematic representation of electrode/polymer electrolyte interfacial passivation (a) without and (b) with dedoped PANi nanofibers.

It reveals that ionic conductivity of both the electrolytes decreased with time but decrease of ionic conductivity in the polymer electrolyte without nanofibers is much larger as compared to that of polymer electrolytes containing nanofibers. This result confirms that the interfacial stability of the polymer electrolyte containing nanofibers is better than that of without nanofibers. This can be attributed to the fact that when nanofibers are added passivation of polymer electrolyte due to reaction with electrode material decreases. High aspect ratio ( $> 50$ ) nanofibers get accumulated on the surface of the electrode and effectively impede the electrode electrolyte reaction [290]. Figure 4.12 schematically depicts that when dedoped (insulating) nanofibers are incorporated in the polymer electrolyte the electrolyte does not make direct contact with the electrode, which increases the interfacial stability.

#### 4.7 Summary

Dedoped PANi nanofibers have been dispersed in PMMA and P(VdF-HFP)-based gel electrolytes to modify the electrical and electrochemical properties. The addition of dedoped PANi nanofibers on PMMA-(PC+DEC)-LiClO<sub>4</sub> system significantly enhances the ionic conductivity up to 4 wt. % and 6 wt. % of nanofibers fraction for PMMA and P(VdF-HFP), respectively as revealed by ac impedance analysis. XRD analysis reveals that amorphicity increases upon addition of nanofibers, which could be attributed to the reduction in chain reorganization of polymer by nanofibers. Higher amorphicity provides higher flexibility to the polymer chains and mobile ions achieve greater free volume giving rise to higher ionic conductivity. However, at higher filler content [ $> 4$  wt. % for PMMA and  $> 6$  wt. % for P(VdF-HFP)] conductivity decreases because the dedoped nanofibers get phase separated out and start forming insulating clusters that encumber ion movement. SEM results show that nanofibers remarkably increase the pore density and widens the porous structure of the polymer electrolytes. This has been attributed to the fact that the dedoped nanofibers try to occupy the pores in the gel polymer electrolyte and in the process pore distribution becomes denser. Highly porous structure leads to better connectivity of the liquid electrolyte through the pores accounting for the increase in ionic conductivity. The interfacial stability and electrochemical potential window of the nanofibers dispersed polymer gel electrolyte membranes are observed to be higher than that of gel polymer electrolytes without nanofibers. FTIR spectra reveal various interactions, which take place among different

constituents of polymer electrolytes. The enhanced properties like higher ionic conductivity at ambient temperature and improved interfacial stability make PMMA-(PC + DEC)-LiClO<sub>4</sub>-4% dedoped PANi nanofibers and P(VdF-HFP)-(PC + DEC)-LiClO<sub>4</sub>-6 wt. % particularly attractive for technological applications in rechargeable lithium batteries.

## CHAPTER V

### ***PEO/P(VdF-HFP) Blend based Microporous Gel and Nanocomposite Polymer Electrolytes***

---

---

*This chapter mainly describes the ionic transport properties of PEO/P(VdF-HFP) blend based polymer electrolyte systems. The chapter consists of two parts. First part deals with the microporous polymer electrolyte (MPE) comprising blends of PEO and P(VdF-HFP) prepared by phase inversion technique. Addition of PEO improved the pore configuration, such as pore size, pore connectivity and porosity of P(VdF-HFP) based membranes. The liquid electrolyte uptake was found to increase with increase in porosity and pore size. The highest porosity of about 65% and ionic conductivity of about  $6.85 \times 10^{-4} \text{ Scm}^{-1}$  was obtained when the weight ratio of PEO was 40 wt. %. In the second part effect of dedoped polyaniline (PAni) nanofibers on the ionic transport and electrochemical properties of PEO/P(VdF-HFP) based electrolytes have been discussed. The ionic conductivity of PEO-P(VdF-HFP)-LiClO<sub>4</sub> electrolyte system increases with increase in the fraction of dedoped PAni nanofibers up to a critical fraction. Beyond the critical concentration the PAni nanofibers get phase separated out as discussed in the previous chapter.*

---

---

Polymer blends often exhibit properties that are superior compared to the properties of the individual components [291-293]. Main advantages of blend systems are simplicity of preparation and ease of control of physical properties by compositional change [293, 294]. The miscibility of polymer blend is an important factor for obtaining the desired properties. There are several specific factors contributing to the miscibility of polymer blends, such as polarity, specific group attraction, molecular weight, blend ratio and crystallinity of the components [295]. Choi et al. [296] developed a model based on modified perturbed hard sphere chain theory and melting point depression theory to describe the phase behaviors of the blend-based polymer electrolyte composed of polyethylene oxide, polypropylene and salts. Unfortunately, these models only described the phase diagram between the polymer and salt, and did not give any suggestion on the miscibility of polymers in polymer blend in the presence of salts (such as the miscibility of PEO and PPO). For polymer blend based electrolytes, the addition of salt into polymer blend can influence the miscibility of the polymer blend via forming multi polymer/cation coordination. However, there are no thermodynamic models to describe miscibility for polymer blend electrolytes with salts.

Experimentally, the techniques used in the study of the miscibility and morphology of polymer blends include optical microscopy, DSC, FTIR, SAXS, SEM, TEM and AFM. Among them, optical microscopy, SEM, TEM and AFM can directly provide the observation of the phase morphology of the immiscible or miscible blends. They are selectively used depending on the phase separation scales. In DSC, the  $T_g$  shift, melt temperature depression and heat of fusion of the blends can indicate the interaction between polymer pairs. If they are completely miscible, only one  $T_g$  can be found which is between the  $T_g$  of the each parent component.

The conception of blended polymers for the use of lithium-ion cell electrolyte was demonstrated by Rhoo et al. [297] with a poly(vinyl chloride) (PVC)/poly(methyl methacrylate) (PMMA). Furthermore, Kim et al. [298] examined the electrochemical characteristics of a Li-ion polymer cell, which used a PVC/PMMA polymer electrolyte. PVC is able to provide a rather rigid framework in the polymer electrolyte films because of its poor solubility in the liquid electrolyte. Recently, some of the polymer blend electrolytes such as (PVC–PVdF) [299] and (PVA–PAN) [300] etc. has been studied by adopting solvent casting technique. These polymer electrolytes satisfy most of the properties required for battery applications.

In recent years microporous polymer films have been found to have high ionic conductivity [301-304]. The pores are believed to trap liquid electrolyte [301]. Methods to produce microporous morphology include use of solvent/non-solvent mixtures [301] or highly volatile plasticizers [303]. Huang et al. proposed a new polymer electrolyte based on PVDF-HFP/PS (PS: polystyrene) blends [305]. When cast from a solvent/nonsolvent (BuOH) mixture, micron size pores are created from a phase separation process. This is a novel way to prepare polymer films with different porosity.

In this chapter we have investigated the ionic transport properties of two systems viz. PEO-P(VdF-HFP)-(PC+DEC)-LiClO<sub>4</sub> synthesized by phase inversion technique with varying PEO content and PEO-P(VdF-HFP)-(PC+DEC)-LiClO<sub>4</sub>-dedoped PANi nanofibers synthesized by solution casting technique with varying nanofibers content. In the first system samples were prepared by dissolving P(VdF-HFP) and PEO in a mixture of acetone (solvent) and ethanol (non-solvent) (v/v = 8/2). After stirring for 4-5 hours at 40 °C, the resulting homogeneous mixture was cast onto ultrasonically cleaned glass plate and allowed to dry at

room temperature for 5-6 hours. In the drying process, solvent (acetone) and non-solvent (ethanol) evaporated and the empty locations of ethanol form micro-pores. Finally opaque freestanding membranes were obtained. The concentration of PEO was varied from 10 to 60 wt. % and the membranes used in the study were denoted as P(VdF-HFP)-x% PEO ( $x = 10, 20, 30, 40, 50, 60$ ).

The liquid electrolyte used in this study was 1M LiClO<sub>4</sub> in 1:1 (v/v) mixture of propylene carbonate (PC) and diethyl carbonate (DEC). Weight uptake of P(VdF-HFP)-x % PEO blend microporous membranes were measured as a function of soaking time in liquid electrolyte to activate porous polymer membranes for 6 h and calculated as follows [306]

$$\text{Weight uptake (\%)} = (W_t - W_0)/W_0 \times 100 \quad (5.1)$$

where  $W_t$  and  $W_0$  are the weight of the wet and dry polymer membranes, respectively

Porosity of P(VdF-HFP)-x% PEO membranes was measured by immersing the membrane into 1-butanol for 2 h and calculated using the following equation [307]

$$\text{Porosity (\%)} = (W_t - W_0)/\rho V \times 100 \quad (5.2)$$

where  $W_t$  and  $W_0$  are the weight of the wet and dry polymer membranes, respectively.  $V$  is the apparent volume of the membrane.  $\rho$  is the density of 1-butanol.

In the second system the samples were prepared by solution casting method by varying the ratio of nanofibers as discussed in chapter III. The surface morphology of P(VdF-HFP)-x% PEO blend microporous membranes and PEO-P(VdF-HFP)-(PC+DEC)-LiClO<sub>4</sub>-dedoped PANi nanofibers electrolytes were studied by scanning electron microscopy (SEM) using Jeol model JSM 6390 LV. The ionic conductivity of the microporous polymer electrolytes were determined from the complex impedance plots obtained by using a Hioki 3532-50 LCR Hitester in the frequency range 42 Hz to 5MHz. X-ray diffractograms were studied by Rigaku miniflex diffractometer. FTIR studies have been conducted to investigate the structural and complexation in the microporous polymer electrolytes.

## 5.1 PEO-P(VdF-HFP) based Microporous Electrolytes

### 5.1.1 Morphology, Porosity and Electrolyte Uptake of the Microporous Membranes

The microporous membranes prepared in this work were composed of two materials: mechanically strong P(VdF-HFP) [308] and flexible PEO. Figures 5.1 (a-f) show the surface morphology of P(VdF-HFP)-x % PEO porous membranes. It is observed that pore size of the

membranes increases with increase in PEO concentration up to 40 wt. % (Figure 5.1a-d) and then decreases with further increase in PEO content (Figure 5.1e-f).

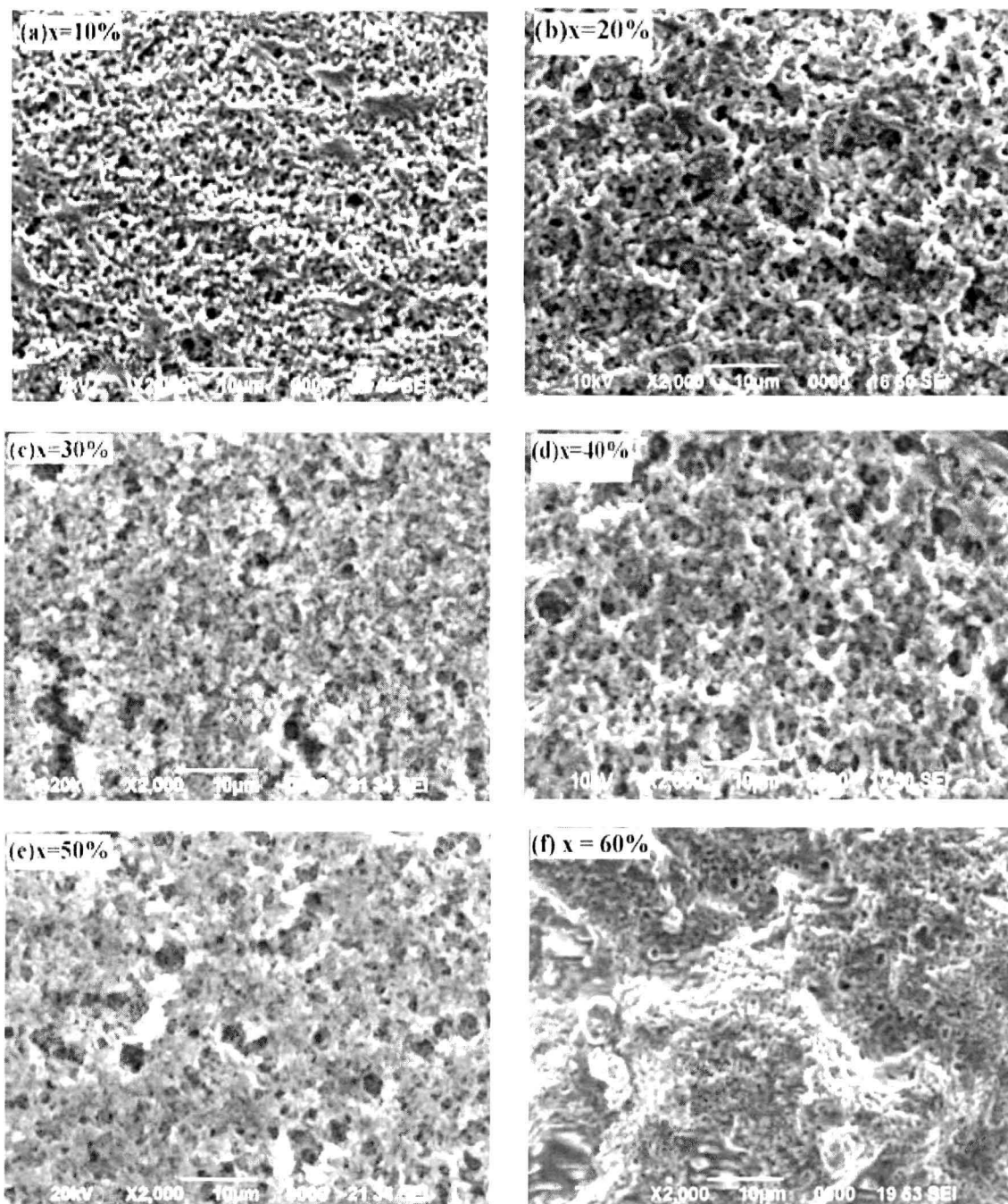


**Figure 5.1:** Surface SEM micrographs of P(VdF-HFP)-x% PEO porous membranes: (a)  $x = 10$ , (b)  $x = 20$ , (c)  $x = 30$ , (d)  $x = 40$ , (e)  $x = 50$  and (f)  $x = 60$ .

The increase in pore size up to 40 wt. % of PEO content is possibly due to easier evaporation of non-solvent (ethanol) from flexible PEO than from rigid P(VdF-HFP) [309]. Figure 5.1 reveals the decrease in pore size of as prepared membranes at 50 and 60 wt. % of PEO. Decrease in pore size beyond 40 wt. % of PEO could be attributed to conglomeration of PEO near the pores [310]. This conglomeration occurs due to the inversion effect of host matrix from a P(VdF-HFP) rich phase to a PEO-rich phase, which results in decrease in pore size and porosity at PEO concentration greater than 40 wt. %.

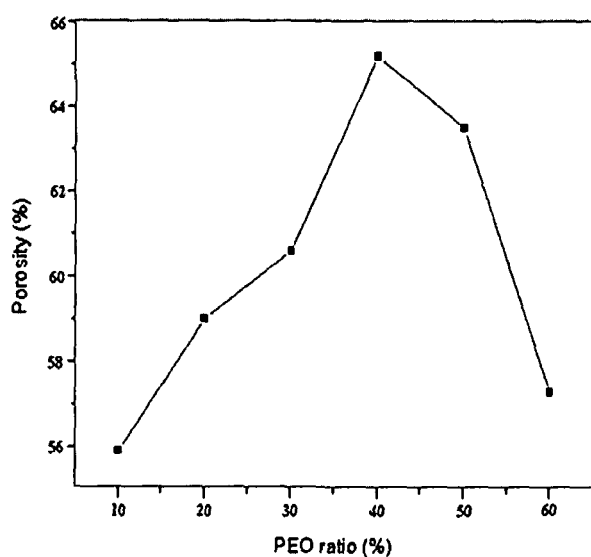


**Figure 5.2:** Porosity of P(VdF-HFP)-x% PEO microporous membranes as a function of PEO weight ratio.

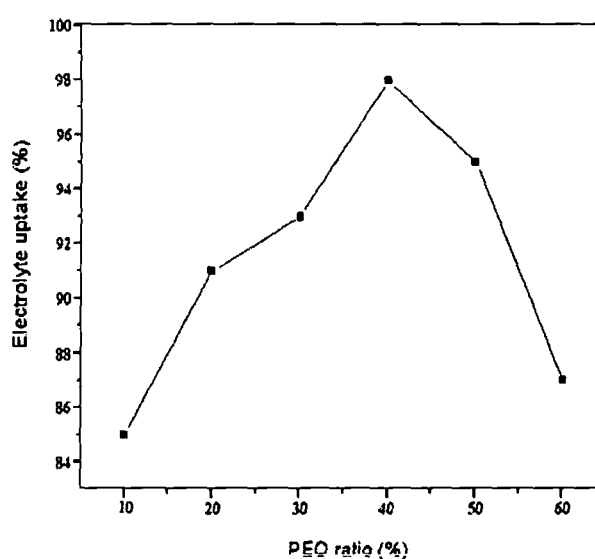


**Figure 5.3:** Liquid electrolyte uptake of P(VdF-HFP)-x% PEO microporous membranes as a function of PEO weight ratio.

Figure 5.2 displays the variation of porosity of P(VdF-HFP)-x% PEO microporous membranes with gradual increase of PEO concentration. It is seen that porosity first increases as a function of PEO concentration and reaches maximum (65.2%) when the weight ratio of PEO is 40%, subsequently decreases at higher weight ratio of PEO. This variation in porosity is consistent with the change of pore configuration as observed in SEM images (Figure 5.1).

The liquid electrolyte uptake plots of P(VdF-HFP)-x% PEO microporous membranes are shown in figure 5.3. The figure shows that the liquid electrolyte uptake of P(VdF-HFP)-x% PEO microporous membranes are greatly influenced by PEO concentration and is consistent with the variation of porosity of the membranes. As PEO content increases resulting in greater porosity, the liquid electrolyte uptake also increases, suggesting that



P(VdF-HFP)- $x$ % PEO microporous membranes can store more liquid electrolytes when its porosity increases. Beyond 40 wt. % of PEO content both porosity and liquid electrolyte uptake decreases, which is attributed to conglomeration of PEO near the pores as mentioned earlier.

### 5.1.2 Ionic Conductivity Measurements

Figure 5.4 shows the room temperature complex impedance spectra of P(VdF-HFP)- $x$ % PEO microporous polymer electrolytes at different concentrations of PEO. The ionic conductivity of P(VdF-HFP)- $x$ % PEO microporous polymer electrolytes is calculated from  $\sigma = l/R_b r^2 \pi$ , where  $l$  and  $r$  are thickness and radius of the sample membrane discs and  $R_b$  is the bulk resistance obtained from complex impedance plots. It is accepted that  $R_b$  could be obtained from the intercept on the real axis at the high frequency end of the Nyquist plot of complex impedance.

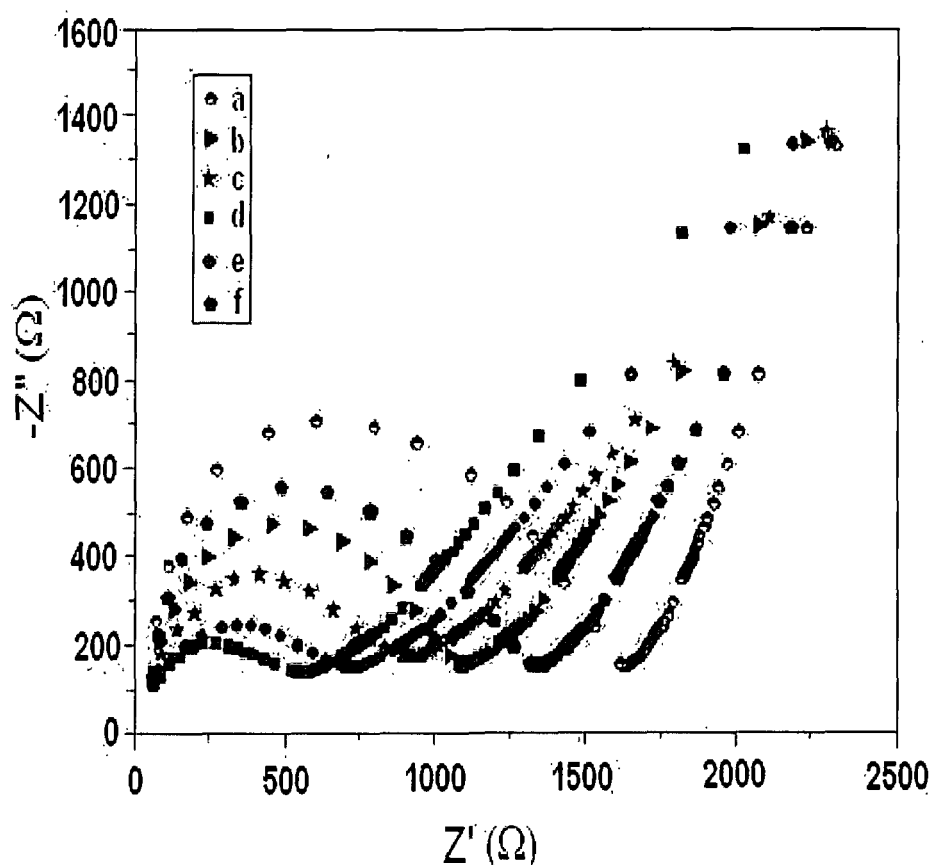


**Figure 5.4:** Room temperature impedance plots of P(VdF-HFP)- $x$  % PEO microporous membranes: (a)  $x = 10$ , (b)  $x = 20$ , (c)  $x = 30$ , (d)  $x = 40$ , (e)  $x = 50$  and (f)  $x = 60$ .

The variation of room temperature ionic conductivity with different weight ratio of PEO is shown in figure 5.5. From the plot it is seen that room temperature ionic conductivity of the microporous polymer electrolytes follow the same trend as that of porosity and liquid electrolyte uptake as a function PEO content. It is worth mentioning that with increase in PEO content the ionic conductivity increases and becomes maximum ( $6.85 \times 10^{-4} \text{ Scm}^{-1}$ ) at 40 wt. % of PEO and decreases at higher PEO content (> 40 wt. %). This result confirms that uptake is dependant on pore size as well as on porosity because liquid electrolyte can more easily penetrate into the membrane with larger pores resulting in higher ionic conductivity [311, 312]. The enhancement in ionic conductivity upon addition of PEO up to 40 wt. % could also be due to improved pore connectivity, which is very important for charge carrier transport in microporous polymer electrolyte [313].

The decreased ionic conductivity at higher PEO content (> 40 wt. %) can be explained by the conglomeration effect as mentioned earlier. The conglomeration of PEO near the pores reduces the pore size and porosity, which resists further uptake of liquid electrolyte in P(VdF-HFP)-x% PEO microporous membranes resulting in lower ionic conductivity. Moreover at higher PEO content the phase separation between PEO and P(VdF-HFP) happens leading to the decrease in ionic conductivity. The phase separation effect is confirmed by XRD results.

Figure 5.6 shows the conductivity versus temperature inverse plots of P(VdF-HFP)-x% PEO microporous polymer electrolytes. The curvature shown in this plot indicate that the ionic conduction obeys the VTF (Vogel-Tamman-Fulcher) relation [180] given by

$$\sigma = \sigma_0 \exp \left[ \frac{-B}{k(T-T_0)} \right] \quad (5.3)$$

where  $B$  is a constant, whose dimensions are that of energy,  $T_0$  is the temperature at which the probability of configurational transition tends to zero. The above equation describes the transport properties in a viscous matrix. The conductivity enhancement behavior with temperature can be understood by free volume model [81]. As the temperature increases, the polymer chains flex and expand at increasing rate and produce free volume leading to an increase in ion and segmental mobility, which facilitates ion transport [81].

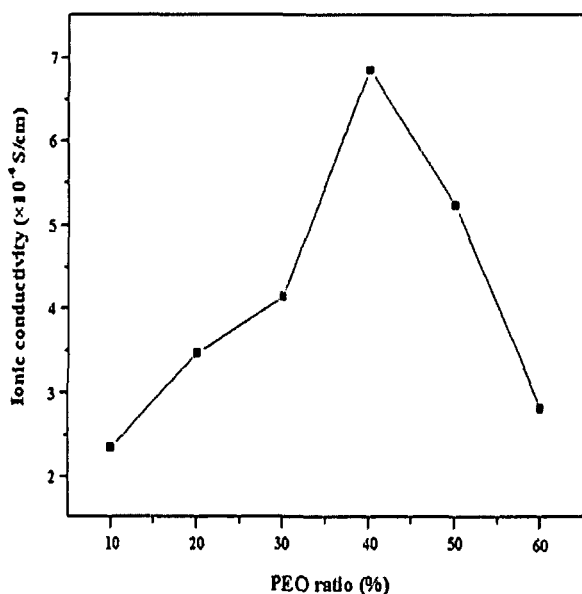


**Figure 5.5:** Ionic conductivity of P(VdF-HFP)-x% PEO microporous membranes as a function of PEO weight ratio.

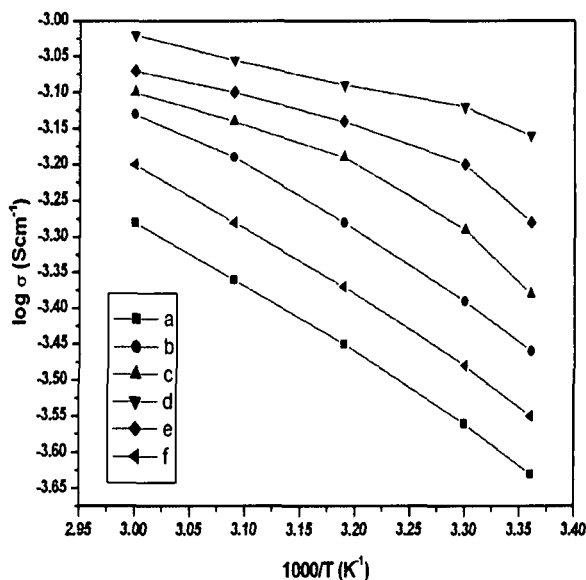


**Figure 5.6:** Temperature dependence of ionic conductivity of P(VdF-HFP)-x% PEO microporous polymer electrolytes: (a)  $x=10$ , (b)  $x=20$ , (c)  $x=30$ , (d)  $x=40$ , (e)  $x=50$  and (f)  $x=60$ .

### 5.1.3 XRD Analysis

X-ray diffraction patterns of pure PEO and P(VdF-HFP) are presented in figure 5.7(a-b). In figure 5.7b the peaks at  $2\theta=20^\circ$  and  $38^\circ$  correspond to (020) and (202) crystalline peaks of P(VdF-HFP). This confirms the partial crystallization of PVdF units in the copolymer and gives a semi crystalline structure of P(VdF-HFP) [81]. PEO shows characteristic peaks at  $2\theta=19.5^\circ$  and  $23^\circ$  corresponding to the ( $hkl$ ) values of (120) and (112), respectively [148] (Figure 5.7a). Figure 5.8 shows the XRD patterns of P(VdF-HFP)-x% PEO microporous membranes with different weight ratio of PEO. It is observed that when P(VdF-HFP) is blended with PEO, no additional peak appears up to 40 wt. % of PEO; only the intensity of crystalline peaks decreases suggesting that the amorphicity increases [314]. In addition, at 50 and 60 wt. % of PEO concentration additional peak appears at  $2\theta=23^\circ$ , which can be assigned to characteristic peak of PEO {Figure 5.8(e, f)}, which indicates that above 40 wt. %, PEO get phase separated from the polymer electrolyte phase. The degree of crystallinity of the microporous membranes was determined by using a method described in chapter III.

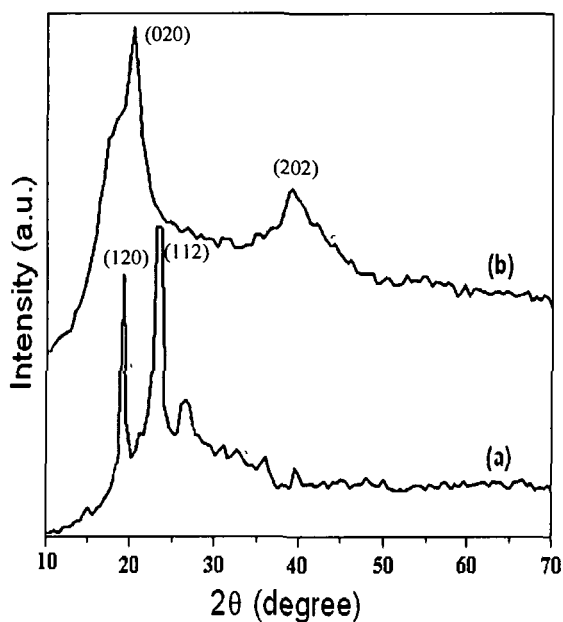


**Figure 5.7:** XRD patterns of (a) PEO and (b) P(VdF-HFP).

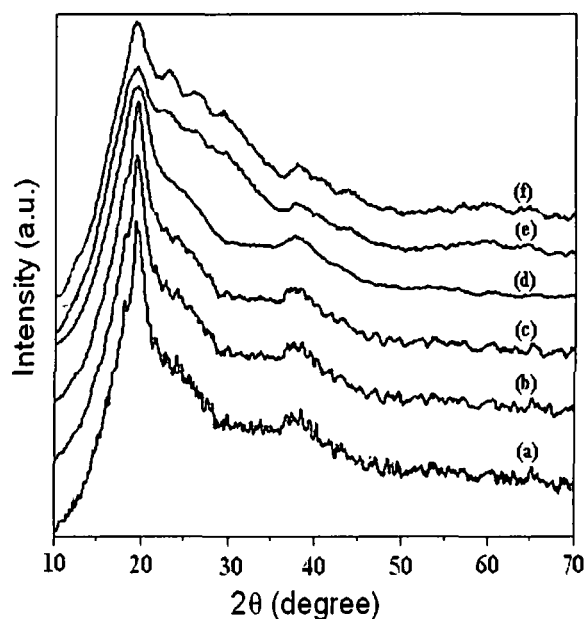


**Figure 5.8:** XRD patterns of P(VdF-HFP)-x % PEO microporous membranes: (a) x =10, (b) x =20, (c) x =30, (d) x =40, (e) x =50 and (f) x =60.

It is observed that degree of crystallinity decreases with increasing PEO content and becomes a minimum (15.2%) when the weight ratio of PEO is 40%. The broadening of the peaks confirms this result (Figure 5.8). This reduction in crystallinity upon addition of PEO could be attributed to the increase in porosity and liquid electrolyte uptake of the microporous membranes. The ionic conductivity increases with decrease in crystallinity due to the fact that ionic conduction essentially occurs through the amorphous phase in the polymer electrolytes [315].

#### 5.1.4 FTIR Analysis

FTIR is a powerful tool to study the local structural changes. The infrared spectrum is sensitive to both situations where complexations occur in crystalline or amorphous phase. The FTIR spectra as shown in figure 5.9 are evidence for interactions between the polymer and salt. Comparing with the pure PEO FTIR spectra, stretching and bending modes of  $(\text{CH}_2)_n$  are at  $1470 \text{ cm}^{-1}$  and  $1353 \text{ cm}^{-1}$  respectively get shifted to  $1455 \text{ cm}^{-1}$ ,  $1351 \text{ cm}^{-1}$  in 30 wt. % of PEO concentration (Figure 5.9d) and  $1454 \text{ cm}^{-1}$ ,  $1351 \text{ cm}^{-1}$  in 50 wt. % of PEO concentration (Figure 5.9e). The peak at  $1104 \text{ cm}^{-1}$  is assigned to  $\nu(\text{C-O-C})$  of PEO

molecule, which also get shifted to  $1113\text{ cm}^{-1}$  and  $1080\text{ cm}^{-1}$  for 30 wt. % and 50 wt. % of PEO concentration in P(VdF-HFP)-x % PEO microporous polymer electrolytes. The frequency  $3000\text{ cm}^{-1}$  is assigned to C-H stretching vibration of PVdF.

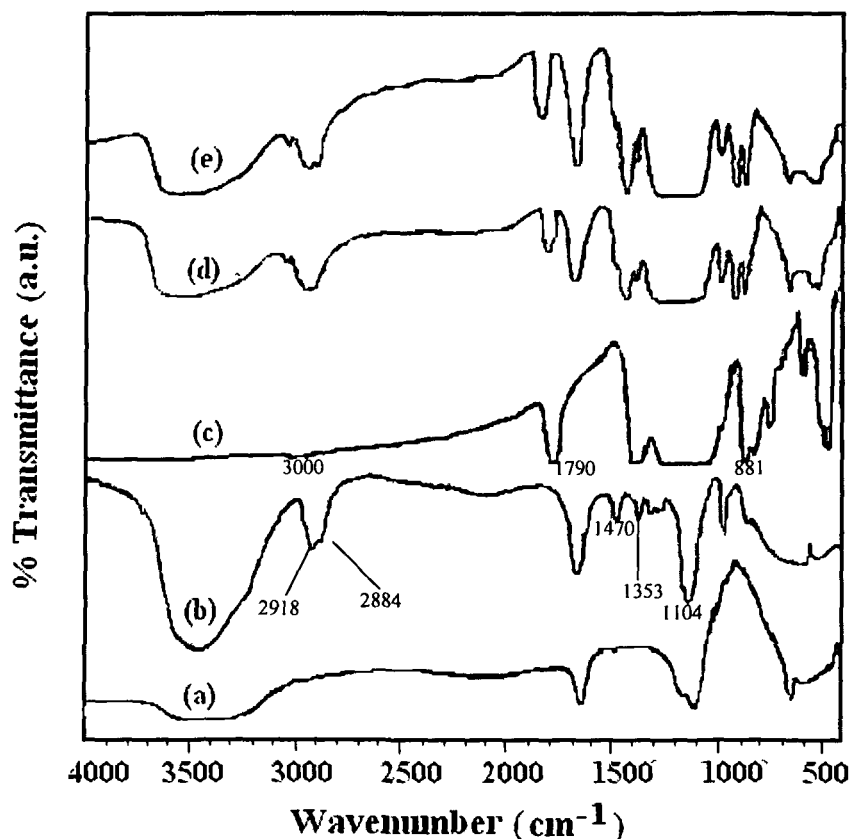


**Figure 5.9:** FTIR spectra of (a)  $\text{LiClO}_4$ , (b) Pure PEO, (c) Pure P(VdF-HFP), (d) P(VdF-HFP)-30 wt. % PEO and (e) P(VdF-HFP)-50 wt. % PEO.

The frequency  $1790\text{ cm}^{-1}$  is assigned to  $-\text{CF}=\text{CF}_2$ ,  $-\text{C}-\text{O}-\text{CO}-\text{O}-\text{C}-$  group [81]. Frequency  $881\text{ cm}^{-1}$  is assigned to vinylidene group of PVdF. All these peaks are shifted in the polymer electrolyte to  $3020\text{ cm}^{-1}$ ,  $1765\text{ cm}^{-1}$  and  $882\text{ cm}^{-1}$  in 30 wt. % of PEO and that to  $3021\text{ cm}^{-1}$ ,  $1777\text{ cm}^{-1}$ ,  $880\text{ cm}^{-1}$  in 50 wt. % of PEO. The peak at  $626\text{ cm}^{-1}$  is due to the salt  $\text{LiClO}_4$  and because of polymer-salt interaction it gets shifted to  $625\text{ cm}^{-1}$  and to  $626\text{ cm}^{-1}$  in 30 wt. % and 50 wt. % of PEO respectively. The increase or decrease manner of shifting of frequency from pure PEO and pure P(VdF-HFP) shows the interaction of the two polymers and salt in P(VdF-HFP) based microporous polymer electrolytes.

## 5.2 PEO-P(VdF-HFP)-(PC+DEC)-LiClO<sub>4</sub>-dedoped PANi Nanofibers Composite Polymer Electrolytes

### 5.2.1 XRD Analysis

X-ray diffraction patterns of pure PEO, P(VdF-HFP) and dedoped PANi nanofibers are presented in figure 5.10. High intensity peaks at  $2\theta=20^\circ$  and  $2\theta=23^\circ$  are observed in the XRD pattern of dedoped PANi nanofibers (Figure 5.10c). The peaks at  $2\theta=20^\circ$  and  $38^\circ$  correspond to (020) and (202) crystalline peaks of P(VdF-HFP). This confirms the partial crystallization of PVdF units in the copolymer and semi crystalline structure of P(VdF-HFP) [81]. PEO shows characteristic peaks at  $2\theta=19.5^\circ$  and  $2\theta = 23^\circ$  corresponding to the  $(hkl)$  values of (120) and (112), respectively [148] (Figure 5.10a). Figure 5.11 shows the XRD patterns of PEO-P(VdF-HFP)-LiClO<sub>4</sub>- $x\%$  dedoped PANi nanofibers composite polymer electrolytes.

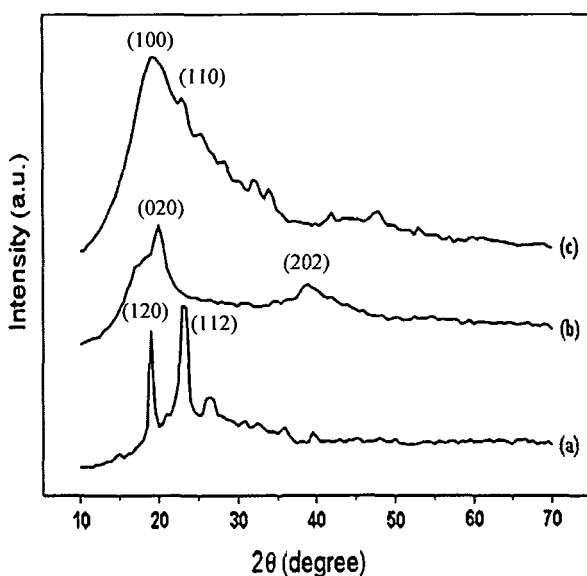


**Figure 5.10:** XRD patterns of (a) PEO, (b) P(VdF-HFP) and (c) dedoped PANi nanofibers.

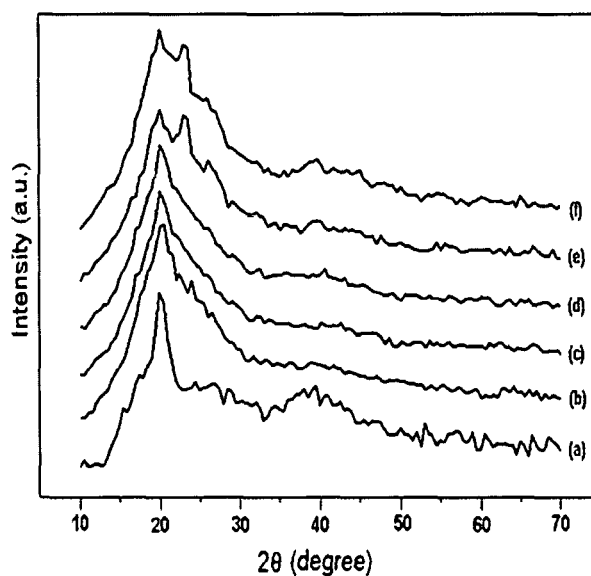


**Figure 5.11:** XRD patterns of PEO-P(VdF-HFP)-LiClO<sub>4</sub>- $x\%$  dedoped PANi nanofibers: (a)  $x = 0$ , (b)  $x = 2$ , (c)  $x = 4$ , (d)  $x = 6$ , (e)  $x = 8$  and (f)  $x = 10$ .

It is observed that when P(VdF-HFP) is blended with PEO, no additional peak appears; only the intensity of crystalline peaks slightly decreases and broadens as compared to pure PEO suggesting that the amorphicity increases [314]. When dedoped PANi nanofibers are incorporated in the PEO-P(VdF-HFP)-LiClO<sub>4</sub> the crystalline peak further broadens while the intensity of the small peak at  $2\theta=38^\circ$  decreases significantly as shown in figure 5.11(b-f).

The degree of crystallinity is determined by the method described in Chapter III. Calculated values of degree of crystallinity with increasing fraction of dedoped PANi nanofibers are given in table 5.1.

**Table 5.1:** Degree of crystallinity of PEO-P(VdF-HFP)-LiClO<sub>4</sub>-x% dedoped PANi nanofibers polymer electrolytes at different concentration of PANi nanofibers.

Fraction of dedoped PANi nanofibers (wt. %)	Degree of crystallinity (%)
0	34.5
2	30.1
4	25.4
6	19.3
8	21.7
10	27.3

It is observed that the degree of crystallinity decreases with increasing nanofibers content and reaches a minimum at 6 wt. % nanofibers fraction. This reduction in crystallinity upon addition of nanofibers is attributed to the suppression of the reorganization of polymer chains by the nanofibers [164]. However, at higher fraction of nanofibers (>6 wt. %), the degree of crystallinity increases with increasing nanofibers content indicating that crystalline phase starts increasing above 6 wt. % of nanofibers fraction due to reorganization of polymer chains in PEO-P(VdF-HFP)-LiClO<sub>4</sub> electrolyte system. At 8 wt. % and 10 wt. % of nanofibers fraction an additional peak appears at  $2\theta=23^{\circ}$ , which can be assigned to dedoped PANi nanofibers suggesting that above 6 wt. %, PANi nanofibers get phase separated from the PEO-P(VdF-HFP)-LiClO<sub>4</sub> polymer electrolyte phase.

### 5.2.2 Ionic Conductivity Measurements

The complex impedance plots for PEO-P(VdF-HFP)-LiClO<sub>4</sub> polymer electrolyte membranes with different weight fraction of PANi nanofibers are presented in figure 5.12(a-f). All plots comprise a semicircular arc in the high frequency region and an oblique line in the low frequency region. The ionic conductivity is calculated from the relation  $\sigma = l/R_b r^2 \pi$ ; where  $l$

and  $r$  are thickness and radius of the sample membrane discs and  $R_b$  is the bulk resistance obtained from complex impedance measurements. The variation of ionic conductivity with increasing fraction of nanofibers is shown in figure 5.13. It is observed that the  $\sigma_{\text{ionic}}$  increases with the increase of weight fraction of nanofibers. Maximum conductivity was found to be  $3.1 \times 10^{-4} \text{ Scm}^{-1}$  at room temperature for 6 wt. % dedoped PANi nanofiber fillers, which is over seven times higher as compared to that ( $4.5 \times 10^{-5} \text{ Scm}^{-1}$ ) for polymer electrolyte without nanofibers. However, as the filler (dedoped nanofibers) fraction increases beyond 6 wt. %, the ionic conductivity decreases.

The enhancement up to 6 wt. % of nanofibers content seems to be correlated with the fact that the dispersion of dedoped PANi nanofibers to PEO-P(VdF-HFP) prevents polymer chain reorganization due to the high aspect ratio ( $>50$ ) of nanofibers, resulting in reduction in polymer crystallinity, which gives rise to an increase in ionic conductivity. The increase in ionic conductivity may also result from Lewis acid-base interaction [65, 120, 316]. In the present composite polymer electrolytes, the oxygen atom in PEO has two lone pair of electrons and nitrogen atom in PANi nanofibers has one lone pair of electrons, which act as strong Lewis base centers and  $\text{Li}^+$  cations as strong Lewis acid giving rise to numerous acid-base complexes in the composite polymer electrolyte. Accordingly three types of Lewis acid-base complexes can be formed [103].

First type of complexes involve PEO- $\text{Li}^+$ -PEO interaction, which leads to the transient cross-linking of PEO chains via  $\text{Li}^+$  cations resulting in the reduction of ionic conductivity. Second type of interaction is due to mixed PEO- $\text{Li}^+$ -PANi nanofibers complexes, which involves Lewis base oxygen from PEO chain and Lewis base nitrogen from PANi. The third type of interaction involves only the Lewis base nitrogen from PANi and  $\text{Li}^+$  cations. The formation of second and third type of complexes leads to lowering of concentration of first type of complexes and hence density of transient cross-linking is reduced. [103]. This allows mobile ions to move more freely either on the surface of the nanofibers or through a low-density polymer phase at the interface, which results in enhanced ionic conductivity. The reduction in crystallinity upon addition of PANi nanofibers up to 6 wt. % is consistent with XRD results. Enhancement in ionic conductivity can also be attributed to the creation of polymer-filler interface. The filler-polymer interface is a site of high defect concentration providing channels for faster ionic transport and the structure and



chemistry of filler-polymer interface may have even more important role than the formation of amorphous phase in the electrolyte [114].

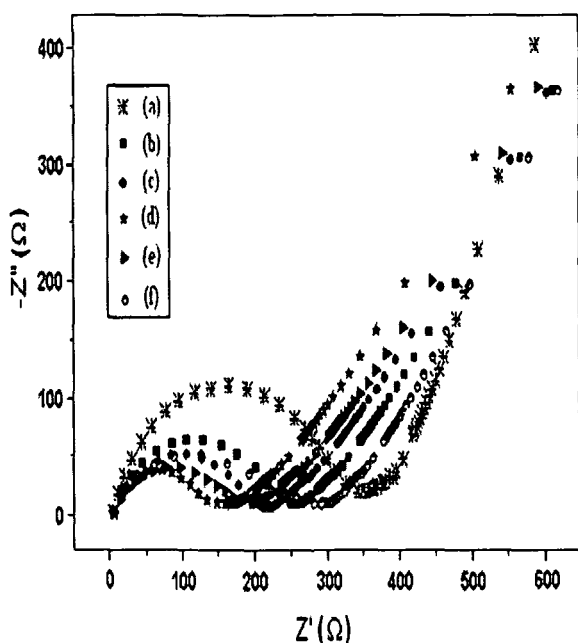


**Figure 5.12:** Complex impedance spectra of PEO-P(VdF-HFP)-LiClO<sub>4</sub>-x% dedoped PANi nanofibers: (a)  $x = 0$ , (b)  $x = 2$ , (c)  $x = 4$ , (d)  $x = 6$ , (e)  $x = 8$  and (f)  $x = 10$ .

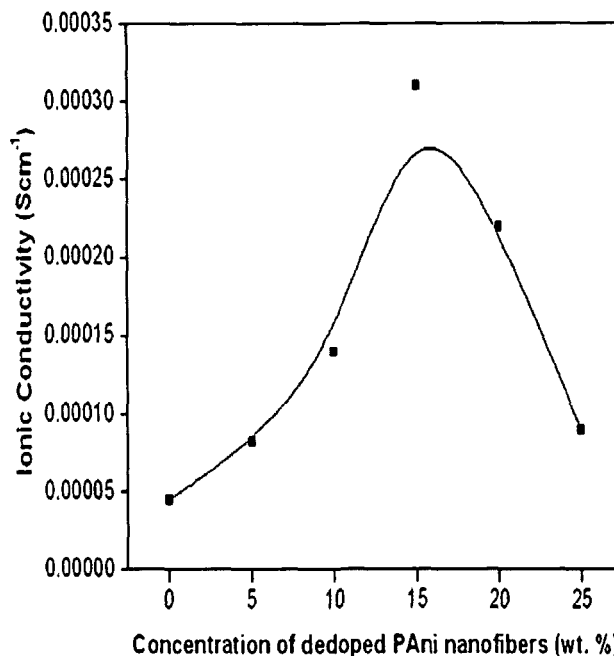


**Figure 5.13:** Variation of ionic conductivity with different weight fraction of dedoped PANi nanofibers.

On the other hand, the decrease in ionic conductivity for fraction of nanofibers higher than 6 wt. % can be attributed to the blocking effect on the transport of charge carriers resulting from the phase separation of nanofibers [133]. Besides, above 6 wt. % a depressed semicircle is seen in the impedance spectra, which is characteristic of a system where more than one conduction processes are present simultaneously [144]. SEM micrographs show that, at higher wt. fraction of nanofibers (6 wt. %), a two-phase microstructure is observed. This could be attributed to the fact that at higher fraction of nanofibers, uniform dispersion of nanofibers in PEO-P(VdF-HFP) matrix is difficult to achieve due to formation of phase-separated morphologies. This is expected to affect the conductivity of the system, since a large number of Li<sup>+</sup> cations are trapped in the phase separated nanofibers. Thus the decrease of ionic conductivity above 6 wt. % nanofibers content can be attributed to the effect of phase separation, which is consistent with the XRD and SEM results.

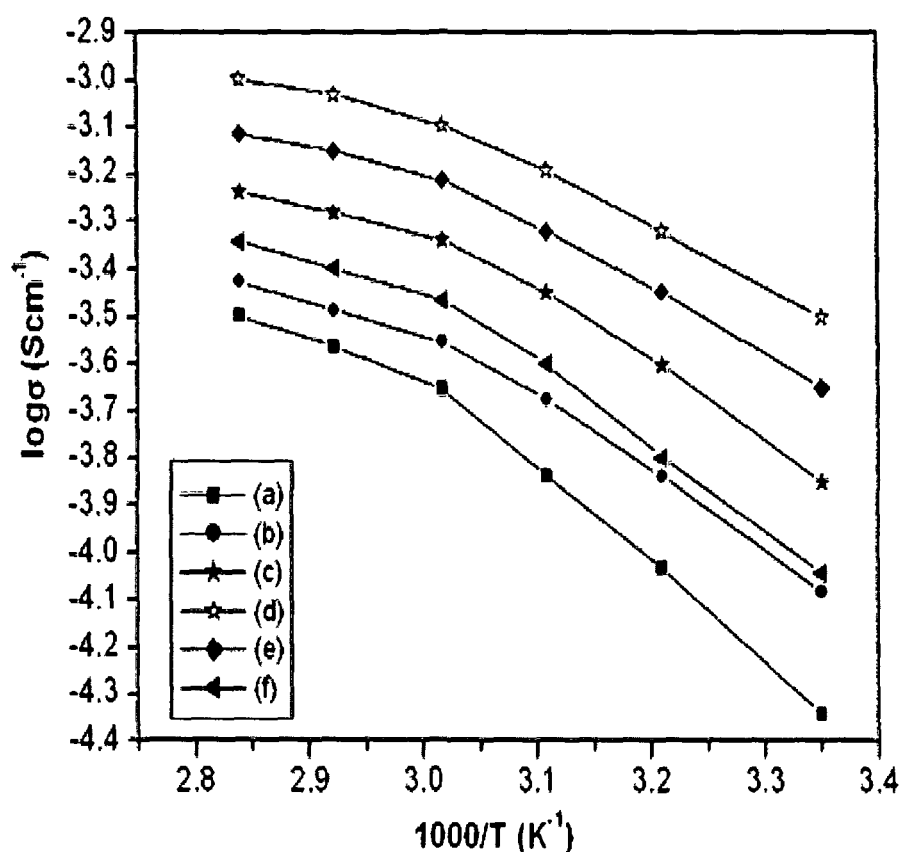


Figure 5.14:  $\log \sigma$  vs. temperature inverse curve PEO-P(VdF-HFP)-LiClO<sub>4</sub>-x% dedoped PANi nanofibers: (a)  $x = 0$ , (b)  $x = 2$ , (c)  $x = 4$ , (d)  $x = 6$ , (e)  $x = 8$  and (f)  $x = 10$ .

Figure 5.14 shows the conductivity versus temperature inverse plots of polymer electrolyte films in the temperature range from 25 °C to 80 °C. The figure shows that the ionic conduction in nanocomposite polymer electrolytes obeys the Arrhenius relation with two degree of slopes

$$\sigma = \sigma_0 \exp(-E_a/kT) \quad (5.4)$$

where  $\sigma$ ,  $\sigma_0$ ,  $E_a$ ,  $k$  and  $T$  are the ionic conductivity, the pre exponential factor, the activation energy, the Boltzmann constant and the absolute temperature respectively. All the samples show a break point at around 60 °C, near the melting temperature of PEO, reflecting the well-known transition from PEO crystalline to amorphous phase. As expected the increase in temperature leads to increase in ionic conductivity because as the temperature increases the polymer chains flex at increased rate to produce larger free volume, which leads to enhanced polymer segmental and ionic mobilities. The enhancement of ionic conductivity by the dedoped PANi nanofibers can be explained by the fact that the nanofibers inhibit the

recrystallization kinetics, helping to retain the amorphous phase down to relatively low temperatures.

### 5.2.3 Morphological Studies

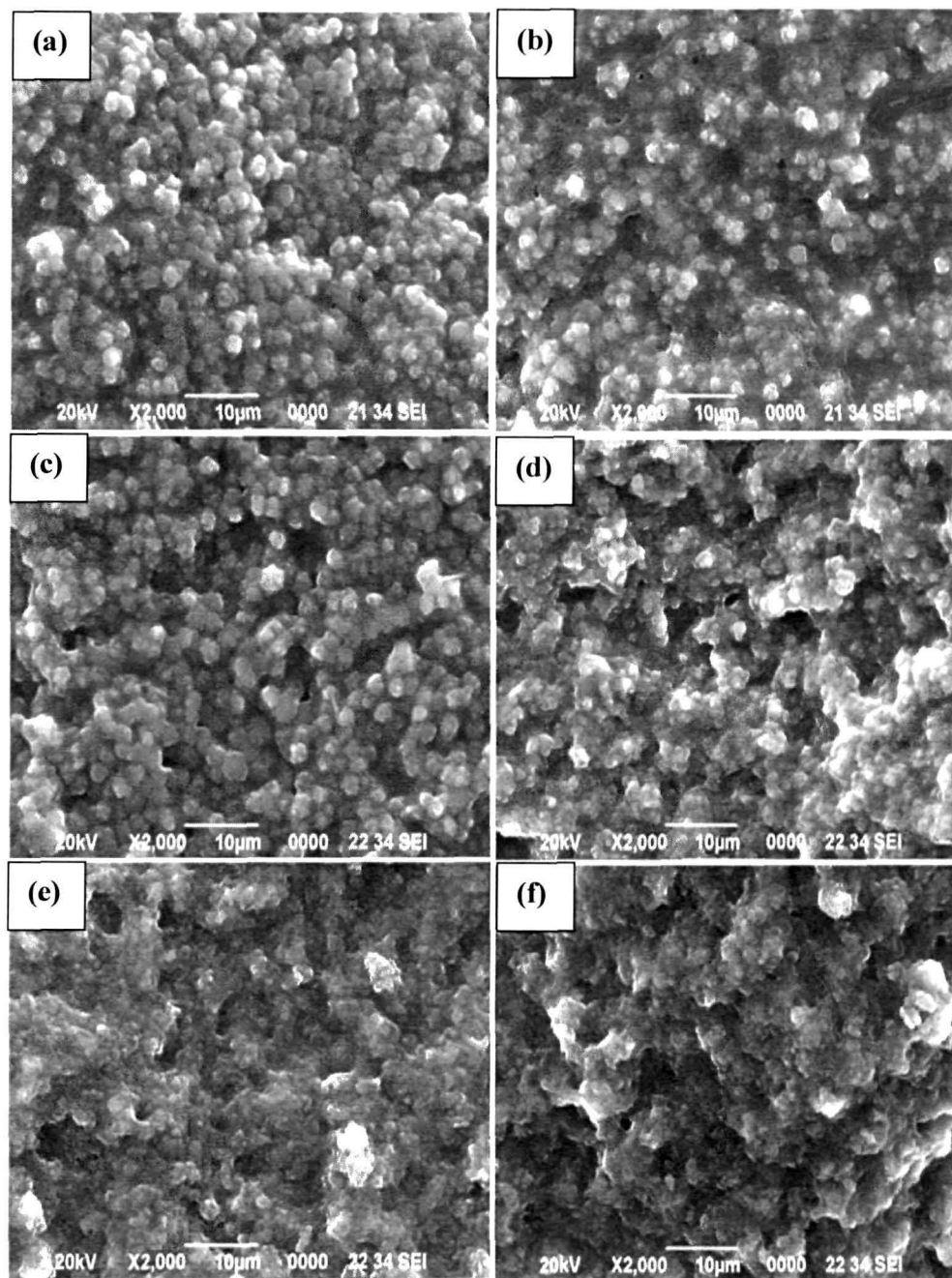


**Figure 5.15:** SEM micrographs of PEO-P(VdF-HFP)-LiClO<sub>4</sub>-x% dedoped PANi nanofibers: (a)  $x = 0$ , (b)  $x = 2$ , (c)  $x = 4$ , (d)  $x = 6$ , (e)  $x = 8$  and (f)  $x = 10$ .

The SEM micrographs for PEO-P(VdF-HFP)-LiClO<sub>4</sub>-x% dedoped PANi nanofibers membranes are presented in figure 5.15(a-f). In general three-four phases are known to coexist in the PEO based polymer electrolytes viz. crystalline PEO phase, crystalline PEO-Li salt complex phase and amorphous PEO phase. It is observed that below 6 wt. % nanofibers content in PEO-P(VdF-HFP) matrix (Figure 5.15a-c), the surface morphology is granular and smooth, which could be attributed to the reduction of PEO crystallinity due to complexation with lithium salt and PANi nanofibers.

At 6 wt. %, rough morphology and sharp interfaces are observed (Figure 5.15d) which may facilitate lithium ion conduction along the interface [317]. Figure 5.15e shows that at 8 wt. % of nanofibers content a two-phase microstructure is observed due to phase segregation of nanofibers. Phase separation becomes more prominent at 10 wt. % of nanofibers as shown in figure 5.15f. The nanofibers get phase separated from the PEO-P(VdF-HFP) polymer matrix and form domain like regions, which may act as physical barriers to the effective motion of the ions leading to decrease in ionic conductivity.

#### 5.2.4 FTIR Analysis

FTIR spectra of LiClO<sub>4</sub>, dedoped PANi nanofibers, P(VdF-HFP), PEO and polymer complexes are shown in figure 5.16. The symmetric and asymmetric C-H stretching vibrations of pure P(VdF-HFP) are observed at 3000 cm<sup>-1</sup>. Frequencies 1286-1066 cm<sup>-1</sup> are assigned to -C-F- and -CF<sub>2</sub>- stretching vibration of P(VdF-HFP). Frequency 881 cm<sup>-1</sup> is assigned to vinylidene group of polymer. Stretching and bending modes of (CH<sub>2</sub>)<sub>n</sub> for pure PEO are observed at 1470 cm<sup>-1</sup> and 1353 cm<sup>-1</sup> respectively. The peak at 1104 cm<sup>-1</sup> is assigned to  $\nu$  (C-O-C) of PEO molecule [318]. Frequency 1120 cm<sup>-1</sup> is assigned to the in-plane C-H bending of PANi nanofibers [319]. The ammonium ion displays broad absorption in the frequency region 3350-3050 cm<sup>-1</sup> because of N-H stretching vibration. The N-H bending vibration of secondary aromatic amine of PANi nanofibers occurs at 1507 cm<sup>-1</sup>. The frequency 1650 cm<sup>-1</sup> of PANi nanofibers is assigned to C=C of aromatic ring. The assigned peaks of dedoped PANi nanofibers get shifted towards lower frequency after incorporation into the polymer electrolyte system signifying their effect on the electrolyte system. The peak for in-plane C-H bending of PANi nanofibers at 1120 cm<sup>-1</sup> is shifted to 1170 cm<sup>-1</sup> for 2 wt. % and to 1185 cm<sup>-1</sup> for 6 wt. % of dedoped nanofibers. The peak at 1507 cm<sup>-1</sup> due to N-H

bending vibration of secondary aromatic amine of PANi nanofibers gets shifted in case of composite polymer electrolytes to  $1550\text{ cm}^{-1}$  (for 2 wt. %) and  $1580\text{ cm}^{-1}$  (for 6 wt. %). The peaks at  $1690\text{ cm}^{-1}$  (for 2 wt. %) and  $1730\text{ cm}^{-1}$  (for 6 wt. %) are evidence of shifting of C=C of aromatic ring peak ( $1650\text{ cm}^{-1}$ ) of pure dedoped PANi nanofibers.

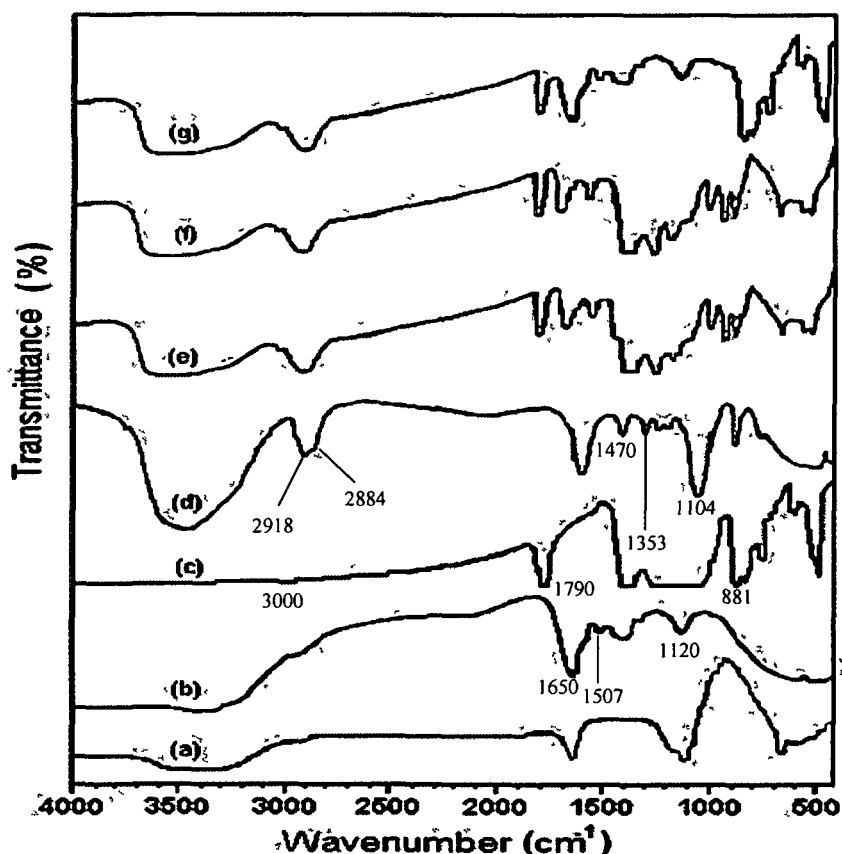


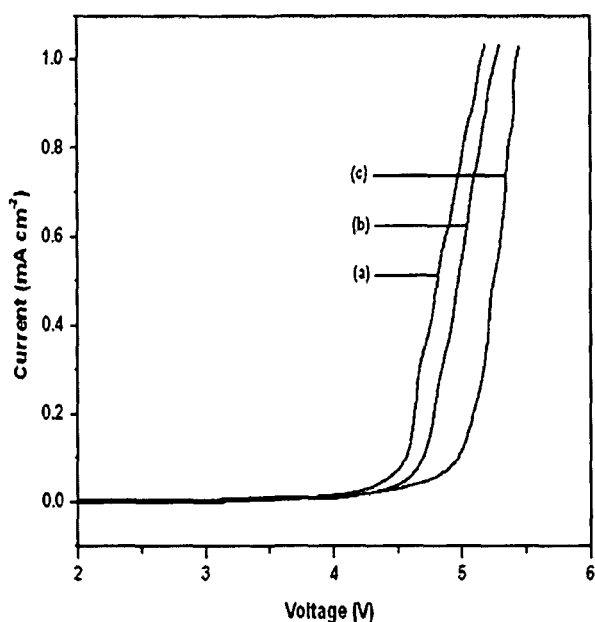
**Figure 5.16:** FTIR spectra of (a)  $\text{LiClO}_4$ , (b) dedoped PANi nanofibers: (c) P(VdF-HFP), (d) PEO and PEO-P(VdF-HFP)- $\text{LiClO}_4$ -x% dedoped PANi nanofibers (e) x=2, (f) x=6 and (g) x=8.

However FTIR spectra of PEO-P(VdF-HFP) polymer electrolyte containing 8 wt. % of dedoped nanofibers show all the peaks of the dedoped nanofibers at their original assigned positions. This result strongly corroborates the occurrence of phase separation at higher fraction of nanofibers ( $> 6\text{ wt. \%}$ ) and is consistent with XRD and SEM results.

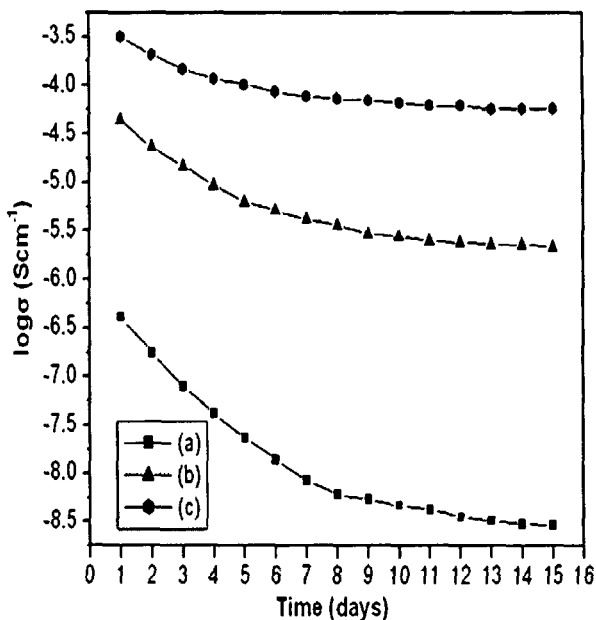
### 5.2.5 Electrochemical Analysis

Figure 5.17 displays the current-voltage response obtained for PEO- $\text{LiClO}_4$ , PEO-P(VdF-HFP)- $\text{LiClO}_4$  and PEO-P(VdF-HFP)- $\text{LiClO}_4$ -6 wt. % dedoped PANi nanofibers composite.

The ongoing of the current identifies the anodic decomposition voltage of the electrolytes. It is observed that PEO-LiClO<sub>4</sub> shows decomposition voltage at 4.3 V whereas after blending with P(VdF-HFP), the decomposition voltage is slightly increased (4.4 V). However after incorporation of dedoped PANi nanofibers (6 wt. % in this case) in the blend system the value of decomposition voltage increases significantly and sets at about 4.8 V. Thus there is a clear improvement in the voltage stability factor in the electrolyte films containing dedoped PANi nanofibers. This value of working voltage range (i.e., electrochemical potential window) appears to be high enough to use the nanocomposite polymer electrolyte films as a solid-state separator/electrolyte in Li-batteries.



**Figure 5.17:** Linear sweep voltammetry plots of (a) PEO-LiClO<sub>4</sub>, (b) PEO-P(VdF-HFP)-LiClO<sub>4</sub> and (c) PEO-P(VdF-HFP)-LiClO<sub>4</sub>-6 wt. % dedoped PANi nanofibers.



**Figure 5.18:** Interfacial stability of (a) PEO-LiClO<sub>4</sub>, (b) PEO-P(VdF-HFP)-LiClO<sub>4</sub> and (c) PEO-P(VdF-HFP)-LiClO<sub>4</sub>-6 wt. % dedoped PANi nanofibers.

Compatibility of nanocomposite polymer electrolyte with electrode materials is an important factor for polymer battery applications. In order to examine the interfacial stability of polymer electrolytes before and after incorporating dedoped PANi nanofibers, the ionic conductivity was measured by fabricating stainless steel/polymer electrolyte membrane/stainless steel cells at room temperature and monitored for 15 days. Three systems viz. PEO-LiClO<sub>4</sub>, PEO-P(VdF-HFP)-LiClO<sub>4</sub> and PEO-P(VdF-HFP)-LiClO<sub>4</sub>-6 wt. % dedoped PANi nanofibers have been selected for the compatibility study and the results are

shown in figure 5.18. It reveals that ionic conductivity of all the electrolyte systems decreases with time but decrease of ionic conductivity in PEO-LiClO<sub>4</sub> electrolyte is much larger than the other two systems. It is well known that PEO-LiClO<sub>4</sub> exhibits highly crystalline structure at room temperature. The existence of crystallites in PEO-LiClO<sub>4</sub> affects the charge transfer reaction, because the interface between the electrode and crystalline polymer function as a barrier for electrochemical reaction [320], which gives rise to increase in interfacial resistance. When PEO is blended with P(VdF-HFP) the crystallinity of the system is greatly reduced, as confirmed by XRD results, resulting in higher interfacial stability than PEO-LiClO<sub>4</sub>. On the other hand PEO-P(VdF-HFP)-LiClO<sub>4</sub>-6 wt. % dedoped PANi nanofibers membrane shows highest interfacial stability (Figure 5.18c). The highest interfacial stability of nanofibers dispersed polymer electrolyte seems to be associated with the fact that, the high aspect ratio (> 50) nanofibers form a barrier layer at the electrode, which effectively impedes the electrode-electrolyte reaction [314]. This in turn reduces the passivation layer on the electrode leading to better interfacial stability between electrode and electrolyte.

### 5.3 Summary

In the first part of this chapter we have discussed microporous polymer electrolytes (MPEs) based on P(VdF-HFP)-PEO blend prepared by a phase inversion method wherein PEO has been added to effectively control the pore size and porosity, which are strongly correlated with electrolyte uptake and ionic conductivity of the MPEs. The liquid electrolyte uptake and room temperature ionic conductivity are greatly enhanced upon addition of PEO and become a maximum at 40 wt. % PEO. SEM micrographs display the increase in pore size with increase in PEO content. The increased pore size results in an increase in ionic conductivity and decrease in degree of crystallinity as confirmed by ac impedance analysis and XRD pattern respectively. Beyond 40 wt. % of PEO, conglomeration takes place, which decreases the pore size as observed in SEM results. The conglomeration effect predominates at higher concentration of PEO and as a result ionic conductivity, porosity and liquid electrolyte uptake exhibit a descending trend.

In the second part, blend based polymer electrolyte nanocomposite membranes based on PEO-P(VdF-HFP)-LiClO<sub>4</sub>-dedoped polyaniline (PANi) nanofibers have been investigated. The ac impedance analysis shows that the ionic conductivity of the polymer electrolyte

membranes increases when dedoped PANi nanofibers are added as filler up to a fraction of 6 wt. %. XRD results show a gradual decrease in degree of crystallinity with increase in dedoped PANi nanofibers up to 6 wt. %. At higher fraction (> 6 wt. %), the PANi nanofibers get phase separated from the polymer matrix as revealed by the occurrence of PANi peaks in the XRD patterns. SEM studies reveal two-phase morphology above 6 wt. % nanofibers indicating the phase separation of PANi nanofibers. FTIR spectra also confirm the phase separation at nanofibers fraction greater than 6 wt. % showing peaks for dedoped PANi nanofibers at their assigned positions. The three moieties PEO, P(VdF-HFP) and dedoped PANi nanofibers no longer remain a miscible uniform phase and nanofibers get phase separated from the polymer matrix giving the domain like structures. These domains may create barrier in the conduction path leading to the decrease in ionic conductivity. The interfacial stability of the nanofibers dispersed composite polymer electrolytes is observed to be better than that of PEO-P(VdF-HFP)-LiClO<sub>4</sub> and PEO-LiClO<sub>4</sub>. Incorporation of dedoped (insulating) nanofibers up to a critical fraction increases the ionic conductivity of the polymer electrolyte system.



## CHAPTER VI

### ***[PMMA/ P(VdF-HFP)]-MMT based Nanocomposite Gel Polymer Electrolytes***

---

---

*In this chapter, effect of organically modified montmorillonite (MMT) clays on PMMA and PVdF based electrolytes has been investigated. The nanocomposites have been prepared by solution intercalation technique with varying clay loading from 0 to 5 wt. %. The formation of partially exfoliated nanocomposites has been confirmed by XRD and TEM analyses. The obtained nanocomposites were soaked with 1M LiClO<sub>4</sub> in 1:1 (v/v) solution of propylene carbonate (PC) and diethyl carbonate (DEC) to get the required gel electrolytes. Surface morphology and structural conformation of the nanocomposite electrolytes have been examined by SEM and FTIR analyses, respectively. It has been observed that the ionic conductivity of the nanocomposite gel polymer electrolytes increases with the increase in clay loading as revealed by ac impedance spectroscopy. Improvement of electrochemical and interfacial stabilities has also been observed in the gel electrolytes containing MMT fillers.*

---

---

Organic-inorganic hybrids based on the intercalation of a polymer into layered inorganic matrices have received much attention, among others because of its potential as electrolyte or electrode materials in electrochemical devices [321]. Resulting materials exhibit only the electrical properties of the guest polymer, but also the mechanical strength, thermal stability, and electronic properties of the inorganic host. It is believed that the dispersion of inorganic nano-sized components, more specifically mineral clays, provides an interesting approach to improve the polymer electrolyte characteristics. Intercalated or exfoliated structures based on the conductive polymer and various layered silicates are expected to improve the mechanical properties on account of the large interfacial area, as well as the high aspect ratio of the clay [322].

Layered clay mineral, particularly montmorillonite (MMT), is one of the most interesting layered hosts owing to its unique layered structure, cation exchangeability and expandability [323]. MMT belongs to the general family of 2:1 phyllosilicates. Its crystal structure consists of layers formed by sandwiching an aluminium octahedron sheet between two silicon tetrahedron sheets. Stacking of the layers leads to a van der Waals gap between the layers. Substitution of aluminium (Al<sup>3+</sup>) for magnesium (Mg<sup>2+</sup>) in the octahedron sheet gives each three-sheet layer an overall negative charge (in the range 0.2–0.6 per formula

unit), which is normally counterbalanced by exchangeable metal cations residing in the interlayer space. The interlayer cations hold the individual negatively charged silicate layers together through electrostatic forces. Due to the weak interaction between layers, organic monomers can be intercalated into these interlayer galleries and interact with the interlayer cations.

Recently many related works have reported the use of polymer/clay nanocomposites in solid-state electrolytes, where the intercalated or exfoliated state of MMT plays an important role in ion conduction in these electrolytes [324, 325]. Additionally, the dispersion of mineral clay was found to enhance the thermal stability, mechanical strength, molecular barrier and flame-retardant properties of polymers [326-329].

In this chapter we have studied the electrical and electrochemical properties of PMMA-(PC+DEC)-LiClO<sub>4</sub>- MMT and PVdF-(PC+DEC)-LiClO<sub>4</sub>- MMT nanocomposites gel electrolytes. The synthesis technique for the preparation of the samples has been explained in Chapter III. Different amounts of modified MMT (1, 2.5, 4 and 5 wt. %) were dispersed in 5 ml of THF by ultrasonication. The dispersed MMT solution was then mixed with polymer solution (15% solid content (w/v) in THF for PMMA and in DMSO for PVdF) by mechanical stirring at 50 °C followed by ultrasonication for half an hour. The nanocomposite films were obtained by solution casting method and dried under vacuum at room temperature. The dried films were denoted as PMMA1, PMMA2.5 and PMMA5 and PVdF1, PVdF2.5 and PVdF4 corresponding to nanoclay loading of 1, 2.5 and 5 wt. % respectively for PMMA and 1, 2.5 and 4 wt. %, respectively for PVdF .

The nanocomposite gel polymer electrolytes were prepared by immersing the films into a liquid electrolyte solution containing 1M LiClO<sub>4</sub> in PC:DEC = 1:1 (v/v), for a period of 20 h. The films swell quickly, and the percentage of electrolyte uptake was calculated by the relation

$$\text{Uptake (\%)} = (W_t - W_0)/W_0 \times 100 \quad (6.1)$$

where  $W_t$  and  $W_0$  are the weight of the wet and dry films, respectively. The nanocomposite gel polymer electrolytes used in this study were denoted as gel PMMA, gel PMMA1, gel PMMA2.5 and gel PMMA5; figure in the end corresponding to the % of MMT. Similarly in case of PVdF the electrolytes were denoted as gel PVdF, gel PVdF1, gel PVdF2.5 and gel PVdF4.

Ionic conductivity of the nanocomposites gel polymer electrolytes have been measured by complex impedance analysis described in Chapter II. X-ray diffraction patterns of the prepared films were obtained by Rigaku miniflex diffractometer at room temperature. The distribution of the clay layers was studied using TEM. The ionic conductivity of the nanocomposite polymer electrolyte films was determined by ac impedance measurements using Hioki 3532-50 LCR HiTester in the frequency range from 42 Hz to 5 MHz. The temperature dependence of ionic conductivity was also measured by heating the samples from room temperature (25 °C) to higher temperature. The nature of conductivity of the nanocomposites gel polymer electrolytes was determined by transference number measurements using Wagner polarization technique with polymer electrolyte films between graphite blocking electrodes. The transference number was found to be  $\approx 0.98$  indicating that conductivity was essentially ionic in nature. The interfacial stability of nanocomposite polymer electrolytes was studied by fabricating stainless steel/polymer electrolyte/stainless steel cells at room temperature and monitoring the ionic conductivity for 18 days. The anodic decomposition voltage was determined by linear sweep voltammetry by using electrochemical workstation. FTIR was conducted using Nicolet Impact 410 (Madison, USA) spectroscopy using KBr pellets.

## 6.1 TEM Studies

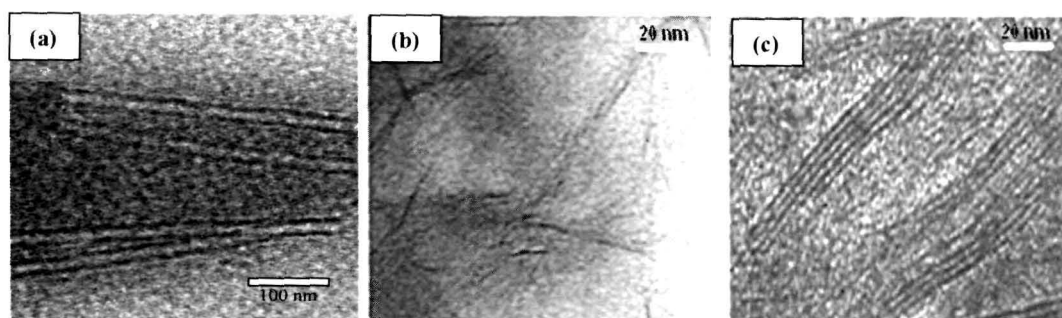


**Figure 6.1:** TEM image of (a) PMMA1, (b) PVdF1 and (c) PVdF4.

The partial exfoliated structure of the clay layers in the nanometer range can be observed from the TEM image as shown in figures 6.1(a-c). The distribution pattern of the clay layers inside the matrix (PMMA1, PVdF1 and PVdF4) is seen in the figure. It is observed that for PMMA1 and PVdF1 (Figures 6.1a & b) most of the clay layers are well dispersed and are

found to be disordered in a random fashion in the polymer matrix. This indicates that the extent of exfoliation is more than that of intercalation in case of PMMA1 and PVdF1. On the other hand, micrograph of PVdF4 (Figure 6.1c) exhibits mostly intercalated morphology with well diffused clay layers in the polymer chains.

## 6.2 XRD Analysis

XRD patterns shown in figures 6.2 (i & ii) reveal that the MMT exhibits (001) diffraction peak at  $2\theta = 4.4^\circ$  corresponding to the interlayer spacing of 20 Å. Upon addition of MMT into the polymers (PMMA and PVdF), shifting of peaks towards lower  $2\theta$  value is observed. This shifting of peak is a result of the insertion of polymer chains into the nanometric channels of layered MMT. However at low clay content (1 wt. %), the intercalation of the polymer leads to the disordering of the layered clay structure leading to a decrease in the XRD scattering intensity as shown in figures 6.2 (i & ii). The peak positions and the corresponding interlayer spacing are tabulated in table 6.1. The nanocomposite containing 1 wt. % clay content demonstrates both the exfoliation and intercalation properties. With the further addition of clay, the intensity of the  $d_{001}$  peak increased, indicating intercalation of the polymer in the layers without disruption of the ordered structure [330]. However the intensity of the (001) diffraction peaks for 2.5 and 4 wt. % clay loading is low as compared to that of pure MMT suggesting that some clay layers still exist in the form of exfoliated nanostructures.

As polymer intercalates into the galleries of MMT, a significant compressive strain is expected in MMT layers. This strain has been calculated quantitatively for (001) reflection of MMT and the values are presented in table 6.1. The single-line approximation method [275] has been employed to compare this contribution. This procedure involves the extraction and analysis of Gaussian ( $\beta_G$ ) and Lorentzian ( $\beta_L$ ) component of integral breadth of a single Bragg peak corrected for instrumental broadening as discussed in chapter III. It is observed from table 1 that the value of microstrain  $\epsilon = 0.155$  for pure MMT is increased to 0.231 and 0.295 for PMMA2.5 and PMMA5 respectively for PMMA-clay based system while PVdF-clay based system exhibits microstrain value of 0.242 and 0.275 for PVdF2.5 and PVdF4, respectively.

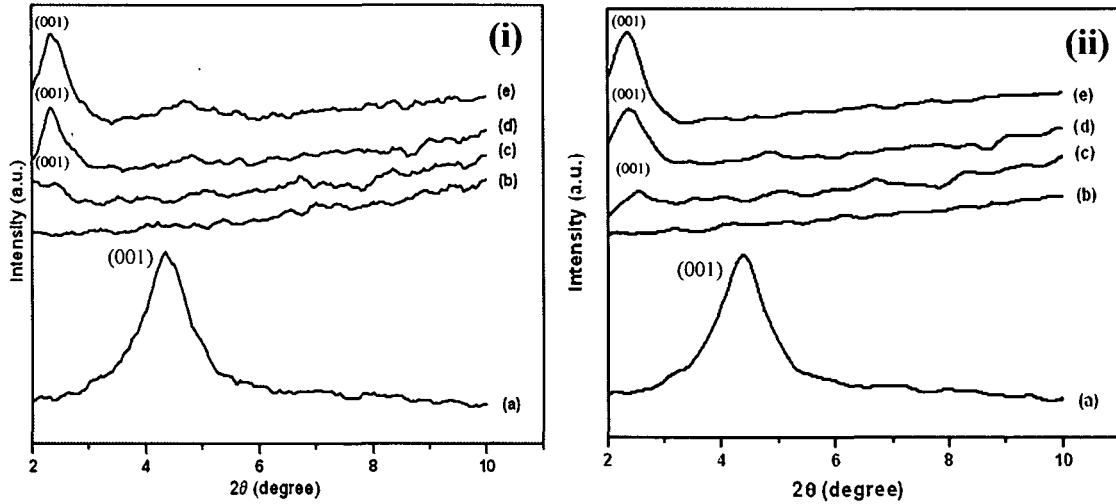


**Figure 6.2:** XRD patterns in the range  $2\theta = 2-10^\circ$  of (i) : (a) pure MMT, (b) pure PMMA, (c) PMMA1, (d) PMMA2.5 and (e) PMMA5 and (ii): (a) pure MMT, (b) pure PVdF, (c) PVdF2.5 and (d) PVdF4.

**Table 6.1:**  $d$ -spacing and microstrain ( $\varepsilon$ ) value of different samples calculated from (001) reflection of MMT.

Sample	$d$ -spacing (nm)	$\varepsilon$
Pure MMT	2	0.155
PMMA1	-	
PMMA2.5	3.85	0.231
PMMA5	3.94	0.295
PVdF1	3.46	0.213
PVdF2.5	3.65	0.242
PVdF4	3.75	0.275

Pure PVdF exhibits the characteristic peaks at  $2\theta$  values  $17.8^\circ$ ,  $18.6^\circ$  and  $20^\circ$  corresponding to (100), (110) and (020) reflections, respectively as shown in figure 6.3. These three peaks are attributed to  $\alpha$  phase of PVdF [331]. With the addition of clay in PVdF the peaks at  $17.8^\circ$  and  $20^\circ$  due to  $\alpha$  phase diminish while the intensity of the peak at  $18.6^\circ$  decreases significantly. On the other hand one new peak at  $20.6^\circ$  is observed in the composites, which could be attributed to the unresolved (110) and (200) reflections of  $\beta$

phase of PVdF [331]. Thus the addition of MMT clays in PVdF leads to the formation of  $\beta$  phase. The  $\alpha$  and  $\beta$ -phases of PVdF have the TGTG' and TT molecular conformations, respectively, as shown in figures 6.4 (a & b). The TGTG' conformation of the  $\alpha$  phase is known to be the most common and thermodynamically stable phase than TTTT conformation of the  $\beta$  phase of PVdF. The  $\beta$ -phase can be induced by several techniques, the most common being the mechanical stretching of the  $\alpha$ -phase films at a suitable temperature [332].

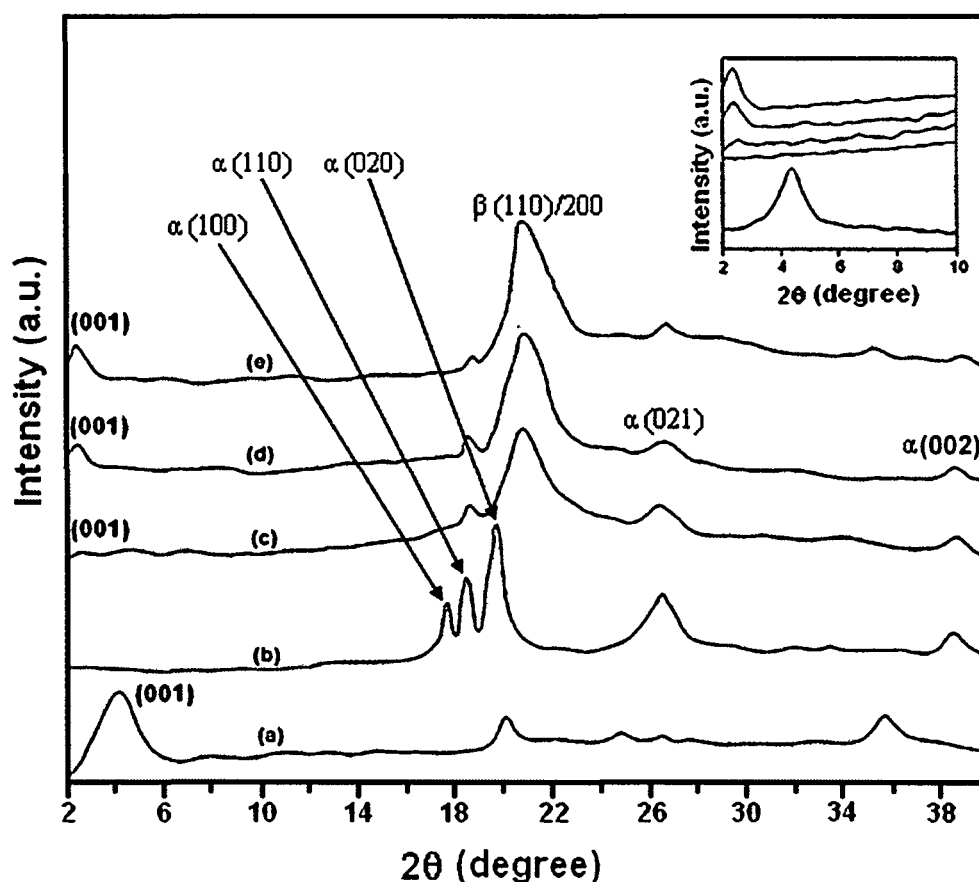


**Figure 6.3:** XRD patterns (a) pure organophilic MMT, (b) pure PVdF, (c) PVdF1, (d) PVdF2.5 and (e) PVdF4. Inset shows reflection of (001) in the range  $2\theta = 2$ - $10^\circ$ .

In the present case the  $\alpha$  to  $\beta$  phase formation of PVdF upon inclusion of MMT can be explained on the basis of stretching of PVdF chains during intercalation into the galleries of MMT. Thermodynamically a decrease in the Gibbs free energy ( $\Delta G$ ) is required for the overall intercalation process. The driving force for direct polymer intercalation from solution is the entropy gained by desorption of solvent molecules, which compensates for the entropy decrease of confined, intercalated chains [333]. On the other hand, the conformational energy

cost of stretching the chains resulting in the formation of  $\beta$  phase, in addition to the topographical constrains and the adsorption on the surfaces are expected to impose severe limitations on diffusion of chains diffusing in a pseudo-two dimensional slit. The  $\alpha$  phase peaks (021) ( $2\theta = 26.4^\circ$ ) and (002) ( $2\theta = 38.5^\circ$ ) obviously decrease in intensity suggesting that MMT clays disturb the ordered structure perpendicular to the planes (021) and (002).

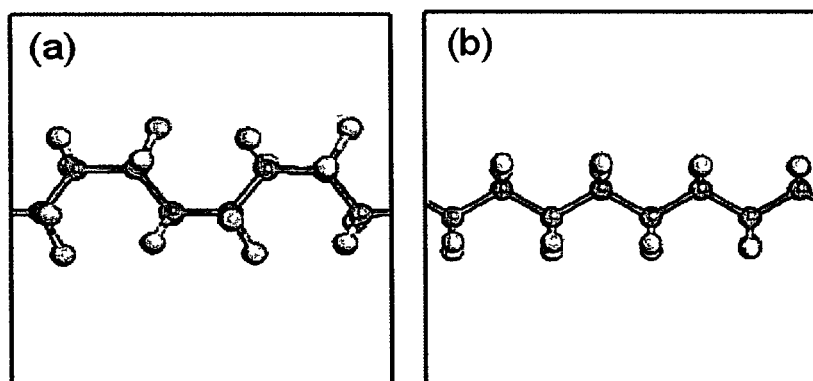


**Figure 6.4:** Molecular conformation of PVdF (a) TG TG' and (b) TT where the white cyanine balls denote the hydrogen and fluoride atoms and the gray balls represent carbon atoms [331].

### 6.3 Swelling Behavior of Nanocomposites

The major difference between gel polymer electrolytes and solid polymer electrolytes lies in the presence plasticizer in the polymer system [4]. The dynamic swelling behavior of PMMA, PMMA-clay, PVdF and PVdF-clay nanocomposite films in 1M LiClO<sub>4</sub> containing 1:1 (v/v) ratio of plasticizers PC and DEC at room temperature is shown in figures 6.5 (a & b). PC has high dielectric constant ( $\epsilon = 64.6$ ) but has high viscosity ( $\eta = 2.53$ ), whereas DEC has low dielectric constant ( $\epsilon = 2.82$ ) and low viscosity ( $\eta = 0.748$ ). Combination of PC and DEC (1:1 v/v) solvents was used as optimization for high dielectric constant ( $\epsilon = 33.71$ ) and low viscosity ( $\eta = 1.639$ ) to achieve high ionic conductivity. It can be observed from figure that the % of swelling or solvent uptake as calculated using equation 6.1 for both PMMA and PMMA-clay nanocomposites increases with the increase of soaking period up to 11 h, but the increase of % of swelling for nanocomposites is more as compared to that of PMMA at the same time scale. Same kind of swelling behavior is observed for PVdF and PVdF-clay nanocomposites. But the saturation of swelling decreases 6 h in case of PVdF-based nanocomposites while the % of swelling is more as compared to that of PMMA-based

nanocomposites. This may be attributed to the fact that PVdF exhibits larger pore size and better pore connectivity than PMMA, which leads to faster impregnation of liquid electrolytes into the pores resulting in the decreased saturation time and increased swelling ratio. On the other hand increase of % of swelling in the nanocomposites as compared to the pure one implies that the presence of MMT clays in the polymer matrix can enhance electrolyte absorption, due to the high active surface and high affinity of the oxides present in the organoclays towards PC/DEC molecules (solvent of the electrolyte). Moreover the high aspect ratio of nanoclays can enhance retaining of electrolyte solution in the composite films.

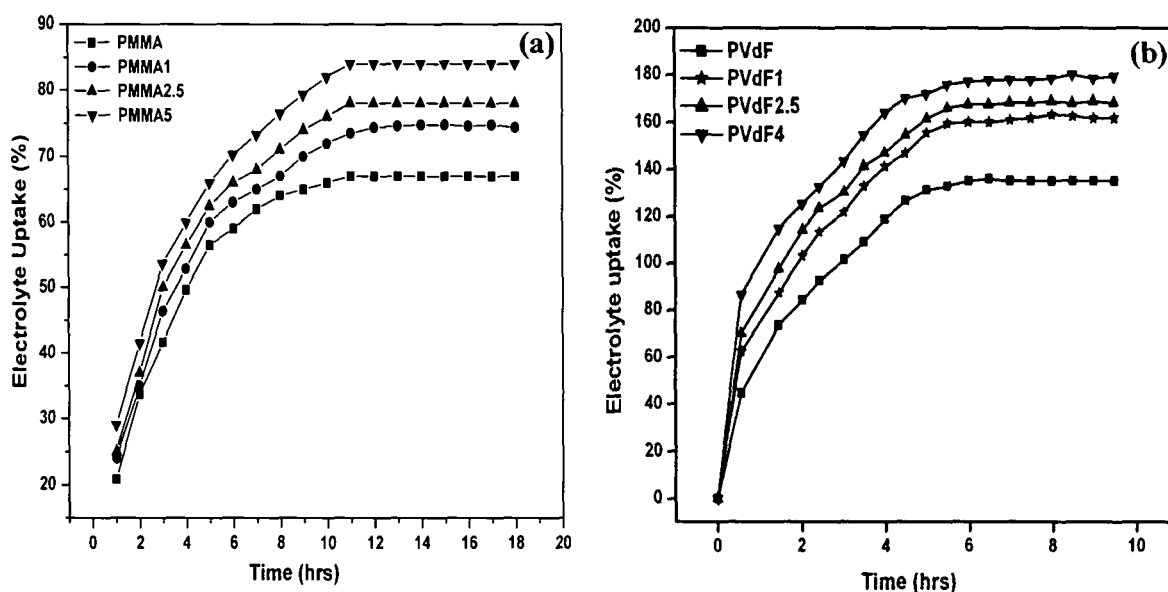


**Figure 6.5:** Swelling behavior of (a) PMMA-clay nanocomposites and (b) PVdF-clay nanocomposites at different clay loading.

## 6.4 Ionic Conductivity Measurements

As described in the previous section, electrolyte uptake of both PMMA and PVdF increased after addition of MMT into it. We may expect that ionic conductivity of PMMA/MMT will be higher than pure PMMA. The typical Nyquist plots of PMMA, PMMA/MMT, PVdF and PVdF-MMT nanocomposite gel polymer electrolyte films at room temperature are shown in figures 6.6 (a & b). All plots comprise a semicircular arc in the high frequency region and an oblique line in the low frequency region. The high frequency semicircle can be ascribed to the bulk of polymer electrolytes, whereas the low frequency spike is due to the capacitance of electric double layer formed at the electrode/electrolyte interface. The impedance spectra can



be modeled as an equivalent circuit having a parallel combination of a capacitor and a resistor in series or parallel with a constant phase element (CPE). The impedance of CPE is given by

$$Z_{CPE} = k(j\omega)^{-p} \quad \text{where } 0 < p < 1 \quad (6.2)$$

When  $p=0$ ,  $Z$  is frequency independent and  $k$  is just the resistance and when  $p=1$ ,  $Z = k/j\omega = -j/\omega(k)$ , the constant  $k^{-1}$  now corresponding to the capacitance. When  $p$  is between 0 and 1, the CPE acts in a way intermediate between a resistor and capacitor. The use of series CPE terms tilts the spike and parallel CPE terms depress the semicircle.

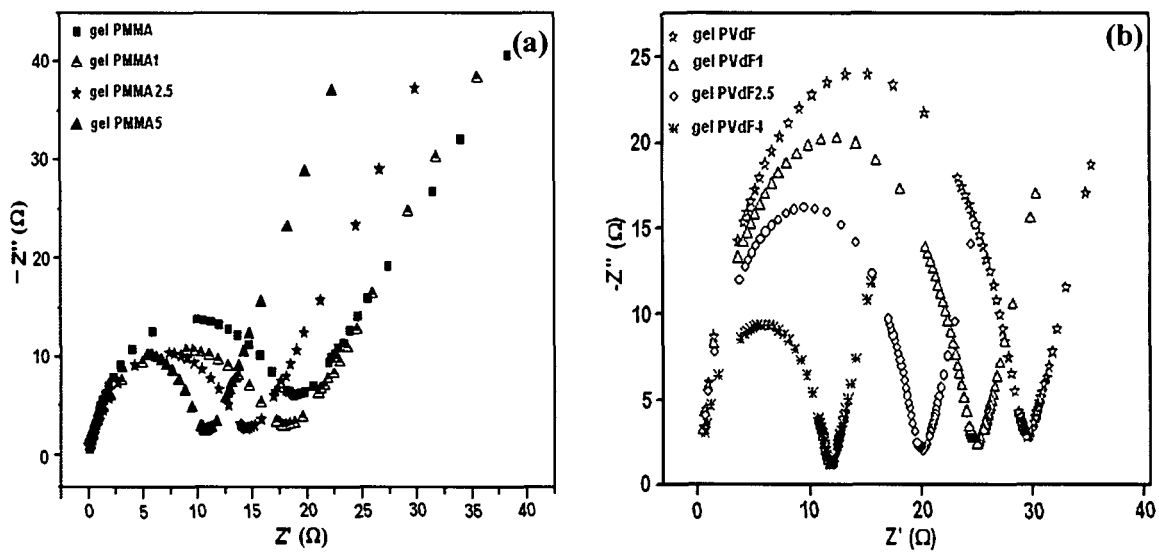


**Figure 6.6:** Nyquist plots of (a) gel PMMA and PMMA/MMT nanocomposite gel polymer electrolytes at different clay loading and (b) PVdF and PVdF/MMT nanocomposite gel polymer electrolytes at different clay loading.

The bulk resistance ( $R_b$ ) is determined from the intercept of the slanted line with the real-axis value that the arc reaches its minimum. Then the conductivity  $\sigma$  can be obtained from  $\sigma = l/R_b A$ , where  $l$  is the thickness of the polymer electrolyte film and  $A$  its area. It is observed from the figure that ionic conductivity increases (i.e. bulk resistance decreases) with increase of clay loading and attains a maximum value of  $1.3 \times 10^{-3} \text{ Scm}^{-1}$  at 5 wt. % clay content. This value of ionic conductivity at room temperature is better than that reported in literature for PMMA/clay systems [173, 286], where conductivity values were found to be of the order of  $10^{-4} \text{ Scm}^{-1}$ . The nanocomposite electrolytes, as explained in literature, were synthesized via polymerization of MMA monomer along with clay and plasticizer. However in the present work samples have been synthesized using solution intercalation method

followed by the liquid electrolyte uptake, which is more viable for mass scale production. The ionic conductivity in these systems primarily depends on the liquid electrolyte uptake amount. In case of PVdF/clay nanocomposites electrolyte maximum ionic conductivity value was found to be  $2.3 \times 10^{-3} \text{ Scm}^{-1}$  for 4 wt. % clay loading. It is worth mentioning that film formation ability of polymer-clay nanocomposites depends on the amount of clay loading in the polymer. In our case we have seen that above 5 wt. % of clay loading the PMMA-clay nanocomposite films become brittle and it is difficult for brittle films to be used in battery fabrication. For PVdF-clay nanocomposites, free standing films can be achieved only at 4 wt. % clay loading. Thus the ratio of organophilic MMT to PMMA and PVdF should be controlled up to 5 wt. % and 4 wt. % respectively.

The highest ionic conductivity for gel PMMA5 and gel PVdF4 is attributed to the highest electrolyte uptake as conductivity is related to the number of charge carriers,  $n_i$ , and their mobility,  $\mu_i$ , according to the following equation [334]

$$\sigma = \sum_i n_i q_i \mu_i \quad (6.3)$$

where  $q_i$  is the charge of each charge carrier. Higher uptake of liquid electrolytes by the nanocomposite films results in increase in the number of charge carriers at the same volume leading to higher ionic conductivity. The high aspect ratio of MMT fillers causes steric hindrance preventing polymer chains from crystallization, which favors fast ionic transport [335]. Another factor that may contribute to increase in ionic conductivity with clay loading is the increase in dielectric constant of the nanocomposite gel polymer electrolytes. It is well reported that the enhancement of ionic conductivity in PEO-based polymer electrolytes by the addition of nanoscale inorganic oxides is not due to the corresponding increase in polymer segmental motion, but more like a weakening of polymer-cation association induced by the nanoparticles [120]. The same effect can be applied to our systems. If the filler-salt interaction is the major factor in determining the ionic conductivity of the composite electrolytes, we may expect that the conductivity be related to the dielectric constant of the oxide filler at the same electrolyte uptake. Clay (MMT) is a natural mineral with high dielectric constant [286]. Presence of the high dielectric constant electronegative silicate layers in the nanocomposite could increase the dissolution of the electrolyte salt ( $\text{LiClO}_4$ ), thereby increasing the ion conduction through the solvent domain surrounding the polymer matrix. The cationic charges on the surface of MMT act as Lewis acid centers and compete

with  $\text{Li}^+$  cations (strong Lewis acid) to form complexes with the polymer host. This in turn may result in: (a) structural modifications and the promotion of  $\text{Li}^+$ -conducting pathways at the surface of filler, and (b) the lowering ionic coupling, which promotes the salt dissociation. These two effects combine to increase the free ions and account for the observed enhancement in the ionic conductivity. The evidence of salt dissociation due to the presence of clay in the nanocomposite gel polymer electrolytes is further confirmed by FTIR analysis in the next section.

As discussed in section 6.2 the clay addition in  $\alpha$ -PVdF results in the formation of  $\beta$ -PVdF due to which all the fluorine atoms are oriented on the same side of the chain and with the hydrogen atoms on the opposite side. This change in conformation will force all the H atoms to be oriented upwards inside the gallery because of their interaction with negatively charged clay platelets as schematically shown in figure 6.7. Negatively charged F-atoms will be oriented downwards and lithium ion mobility is expected to be higher along the interface lining the F atoms, which results in increase in the ionic conductivity in case of PVdF-clay based systems.

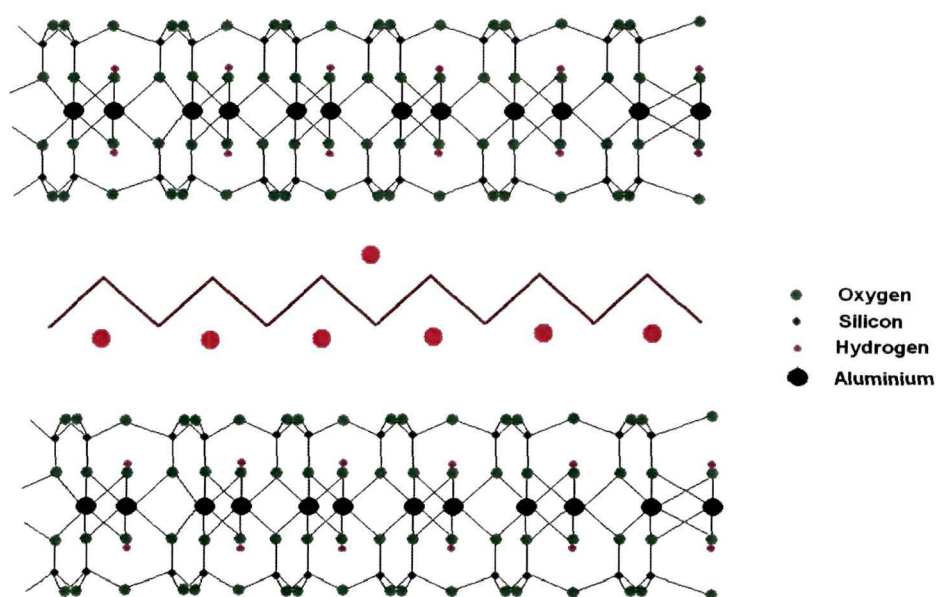


**Figure 6.7:** Lithium ion (red balls) motion inside the gallery of MMT in  $\beta$  phase of PVdF.

Figures 6.8 (a & b) show the temperature dependant ionic conductivity for both PMMA and PVdF based nanocomposite gel polymer electrolytes revealing that ionic

conductivity increases with the increase of clay concentration. Both the curves follow a linear trend i.e. Arrhenius behavior governed by the equation [282]

$$\sigma = \sigma_0 \exp(-E_a/kT) \quad (6.6)$$

where  $\sigma$ ,  $\sigma_0$ ,  $E_a$ ,  $k$  and  $T$  are the ionic conductivity, pre exponential factor, activation energy, Boltzmann constant and absolute temperature, respectively. It has been reported that ionic transport in gel polymer electrolytes obeys the VTF (Vogel–Tamman–Fulcher) relation  $\{\sigma = B \exp(-E_a/k(T-T_0))$ , where  $B$  is a constant and  $T_0$  being the idealized glass transition temperature typically 20–50 K below the glass transition temperature of the polymer}, which describes the transport properties in a viscous polymer matrix [81, 317]. However in case of gel polymer electrolytes after addition of liquid plasticizer the glass transition temperature ( $T_g$ ) drops abruptly. In that case  $T_0$  will be far below the temperature regions of measurements from room temperature to higher temperature. As expected the increase in temperature leads to increase in ionic conductivity due to increases in the polymer chain flexibility producing more free volume resulting enhanced polymer segmental mobility.

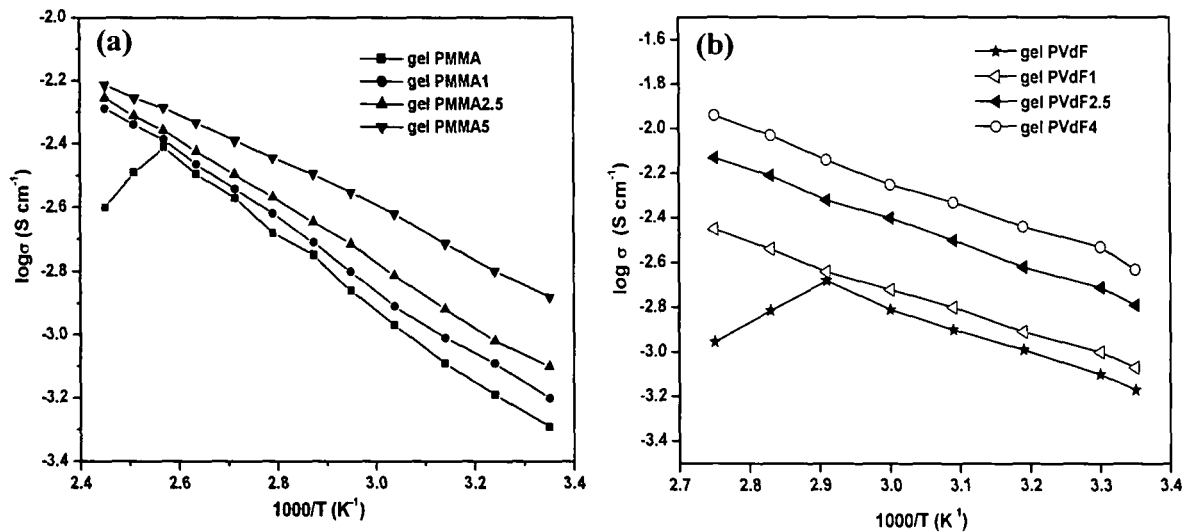


**Figure 6.8:** Temperature dependence of ionic conductivity of (a) gel PMMA and PMMA/MMT nanocomposite gel polymer electrolytes at different clay loading and (b) gel PVdF and PVdF/MMT nanocomposite gel polymer electrolytes at different clay loading.

An interesting effect occurs at higher temperature range where at about 115 °C an abrupt drop in conductivity of clay free PMMA-based electrolyte is observed. The same effect occurs at 70 °C for clay free PVdF-based system. This observation seems to be correlated with the fact that at temperature 115 °C and 70 °C the films of gel PMMA and gel

PVdF soften and the consistency of the films are lost. On the other hand the conductivity of clay loaded electrolyte systems goes on increasing up to 135 °C and 90 °C for PMMA and PVdF based electrolytes, respectively. This is attributed due to the fact that MMT fillers limit the fluidity of the polymer and thereby increases the mechanical strength of the polymer electrolytes making them suitable materials for high temperature operation [167].

## 6.5 FTIR Analysis

Vibrational spectroscopy has been identified as a powerful tool to study the interactions among the various constituents in polymer electrolytes. FTIR spectra of pure PMMA, pure PVdF, gel PMMA and gel PVdF with different clay loading is shown in figures 6.9 (i & ii). For pure PMMA [Figure 6.9(i)a], the C=O symmetric stretch gives a sharp peak at 1725 cm<sup>-1</sup>. The peaks at 1242 cm<sup>-1</sup> and 1188 cm<sup>-1</sup> are assigned to symmetric and asymmetric stretching vibrations of C-O-C bond respectively. Absorption of  $\nu(\text{C-O})$  of OCH<sub>3</sub> group and symmetrical stretch of C-O bond of PMMA appear at 1145 cm<sup>-1</sup> and 985 cm<sup>-1</sup> respectively [285]. The clay free gel PMMA exhibits a weak peak at 1700 cm<sup>-1</sup> [Figure 6.9(i)b], which corresponds to the interaction between lithium cation and C=O group [286]. As clay content increases the peak at 1700 cm<sup>-1</sup> gets intensified and shifts towards lower frequency. This indicates that the presence of MMT clays can enhance the interaction between lithium cation and carbonyl group of PMMA. Frequencies 1750 cm<sup>-1</sup> and 1644 cm<sup>-1</sup> are assigned to >C=O stretching vibration of plasticizer (PC+DEC) and >C=C< bonding respectively.

A careful analysis of FTIR spectrum of pure PVdF [Figure 6.9(ii)a] suggests that a typical vibrational band observed at 1404 cm<sup>-1</sup> corresponds to the deformed vibration of CH<sub>2</sub> group [336]. The peak appearing at 1233 is assigned to -C-F- stretching mode, whereas the peaks at 1176 and 1072 cm<sup>-1</sup> are due to the -C-F<sub>2</sub>- stretching modes. The frequency 881 cm<sup>-1</sup> corresponds to the vinylidene group of the PVdF [81]. Characteristic bands of the crystalline  $\alpha$ -phase are observed at 763 and 615 cm<sup>-1</sup>. The absorption band at 763 cm<sup>-1</sup> is assigned to a rocking vibration. The band at 615 cm<sup>-1</sup> is assigned to a mixed mode of CF bending and CCC skeletal vibration. The characteristics peaks of  $\beta$ -PVdF are observed at 834 and 510 cm<sup>-1</sup>. The band at 840 cm<sup>-1</sup> is ascribed to a mixed mode of CH<sub>2</sub> rocking and CF<sub>2</sub> asymmetric stretching vibration. The absorption band at 512 cm<sup>-1</sup> is assigned to bending mode of CF<sub>2</sub> [337].

In both the cases, the  $\nu(\text{ClO}_4^-)$  internal mode of  $\text{LiClO}_4$  shows one peak at about  $624 \text{ cm}^{-1}$ , which is assigned to the free anion, which does not interact with lithium cation. The  $\nu(\text{ClO}_4^-)$  internal mode of  $\text{LiClO}_4$  shows one peak at about  $624 \text{ cm}^{-1}$ , which can be assigned to the free anion that does not interact with lithium cation, whereas the peak at  $635 \text{ cm}^{-1}$  is due to the contact ion pair formation. The peak observed at  $635 \text{ cm}^{-1}$  is gradually reduced to a shoulder with the addition of MMT as shown in figure 9. This phenomenon may be attributed to the fact that MMT clay particles suppress the association of  $\text{Li}^+$  and  $\text{ClO}_4^-$  ions and increase the concentration of free ions leading to an increase in the ionic conductivity.

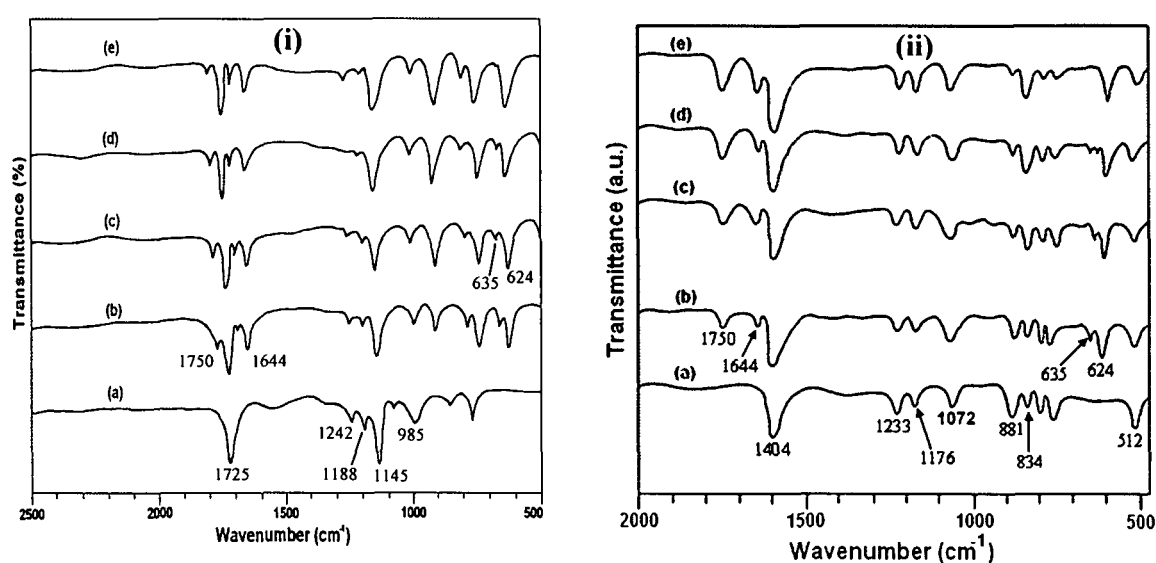


**Figure 6.9:** FTIR spectra of (i) (a) pure PMMA, (b) gel PMMA, (c) gel PMMA1, (d) gel PMMA2.5 and (e) gel PMMA5 and (ii) (a) pure PVdF, (b) gel PVdF, (c) gel PVdF1, (d) gel PVdF2.5 and (e) gel PVdF4.

## 6.6 Morphological Studies

Scanning electron micrographs for pure PMMA gel PMMA5, pure PVdF and gel PVdF4 are shown in figures 6.10 (a-d). Pure PMMA exhibits porous structure with uniform pore distribution (Figure 6.10a). Spherical granular morphology with large pores is observed in gel PVdF (Figure 6.10c). The pores in the microstructure are due to solvent removal. On the addition of clay to PMMA and PVdF matrix, the pore size is reduced and the surface becomes smoother as the concentration of MMT clay is increased to 5 wt. % for PMMA and 4 wt. % for PVdF. The results indicate that clay-loaded gel PMMA and gel PVdF electrolyte

systems have a higher solvent retention ability than clay-free electrolytes. In other words, the surface morphology of a nanocomposite polymer electrolyte without pores or any phase separation is indicative of a high affinity of the PVdF polymer for liquid electrolyte. The SEM results are consistent with the view that the higher conductivity of clay-loaded gel polymer electrolytes arises from increased solvent retention.

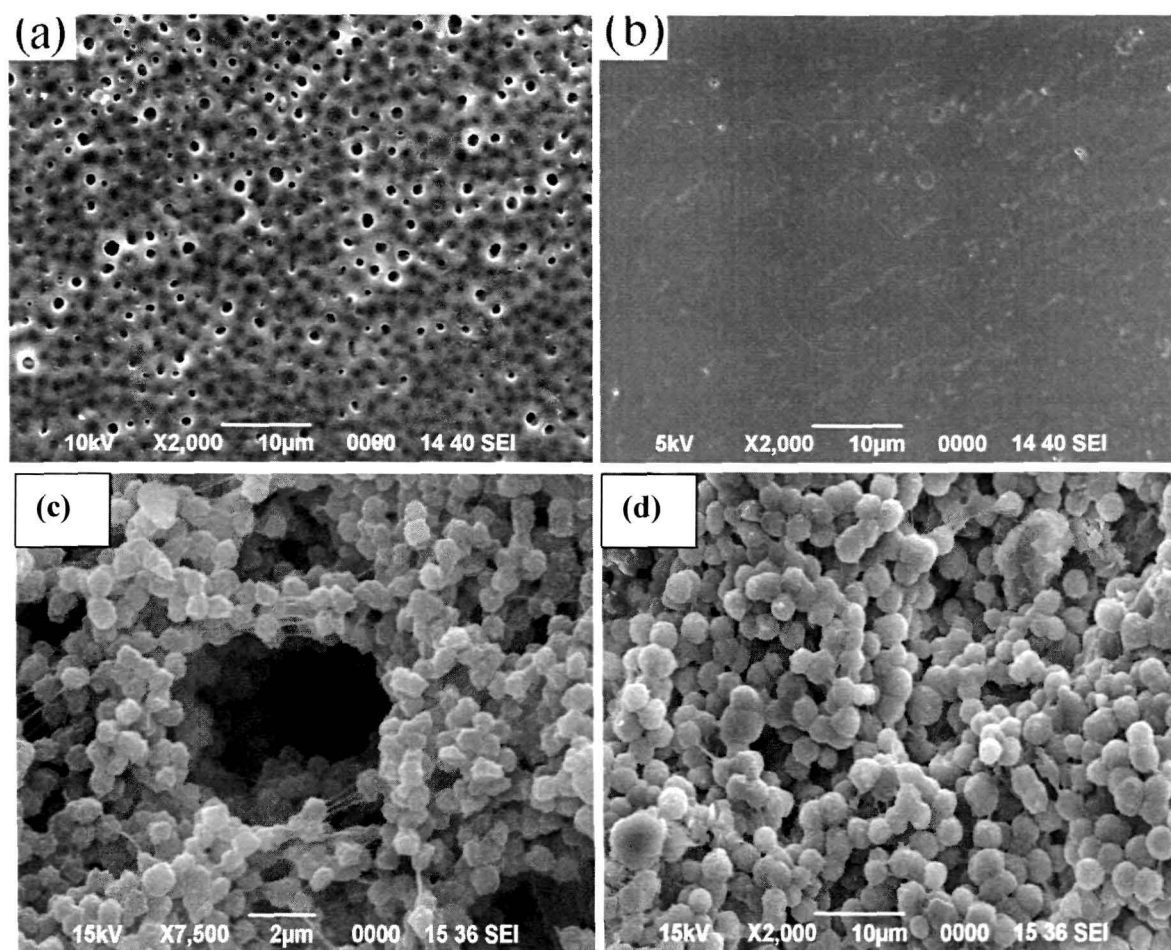


**Figure 6.10:** SEM images of (a) pure PMMA, (b) gel PMMA5, (c) pure PVdF and (d) gel PVdF4.

## 6.7. Electrochemical Analysis

The linear sweep voltammetry (LSV) measurements conducted using the Li/CPE/Li cell configurations for determination of the electrochemical stability window of the electrolyte systems are presented in figures 6.11 (a & b). The measurements were carried out in the potential range from 2V to 6V with a scan rate  $0.1 \text{ mVs}^{-1}$ . The onset of the current identifies the anodic decomposition voltage of the electrolytes. It is found that the anodic limit of

PMMA-based nanocomposite gel polymer electrolytes increases with the increase of clay loading (Figure 6.11a) and sets at about 4.9 V for 5 wt. % clay content, which is reasonably higher than that of clay free gel polymer electrolyte (about 4.5 V). In case of PVdF-based electrolytes similar kind of trend is observed, where the electrochemical potential window is found to be 4.6 V for 4 wt. % clay content (Figure 6.11b) as compared to at 4.3 V for the clay free electrolyte. Thus there is a clear improvement in the voltage stability factor in the electrolyte films containing clay. It has been well known that anodic stability window is limited by an irreversible oxidation of the salt anion [289]. The Lewis acid sites on the anionic surface of MMT can interact with  $\text{ClO}_4^-$  (Lewis base), thereby enhancing the electrochemical potential window by retarding the decomposition of lithium salt anion. These values of working voltage range (i.e., electrochemical potential window) appear to be high enough for application of the nanocomposite gel polymer electrolyte films as a solid-state separator/electrolyte in Li-ion batteries.

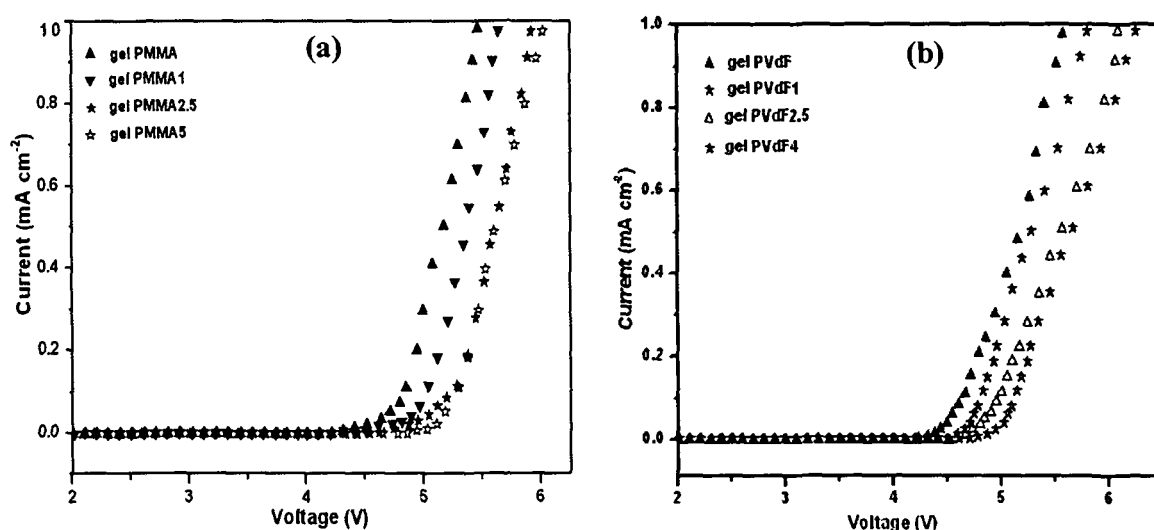


**Figure 6.11:** Linear sweep voltammetry plots of (a) gel PMMA and PMMA/MMT nanocomposite gel polymer electrolytes at different clay loading (b) gel PVdF and PVdF/MMT nanocomposite gel polymer electrolytes at different clay loading.

The compatibility of polymer electrolyte membranes with lithium metal is still an unsolved problem for their application in high power Li-ion batteries. The reactivity of the anode electrode with polymer electrolyte can lead to an uncontrolled passivation process and results in the formation of a thick and non-uniform surface layer [306]. These can in turn cause an uneven lithium deposition during the charging process eventually leading to



dendritic growth and short-circuiting of the cell [5]. Therefore, interfacial stability of polymer electrolytes in contact with electrode materials is an important factor for providing suitable performance in rechargeable lithium batteries.

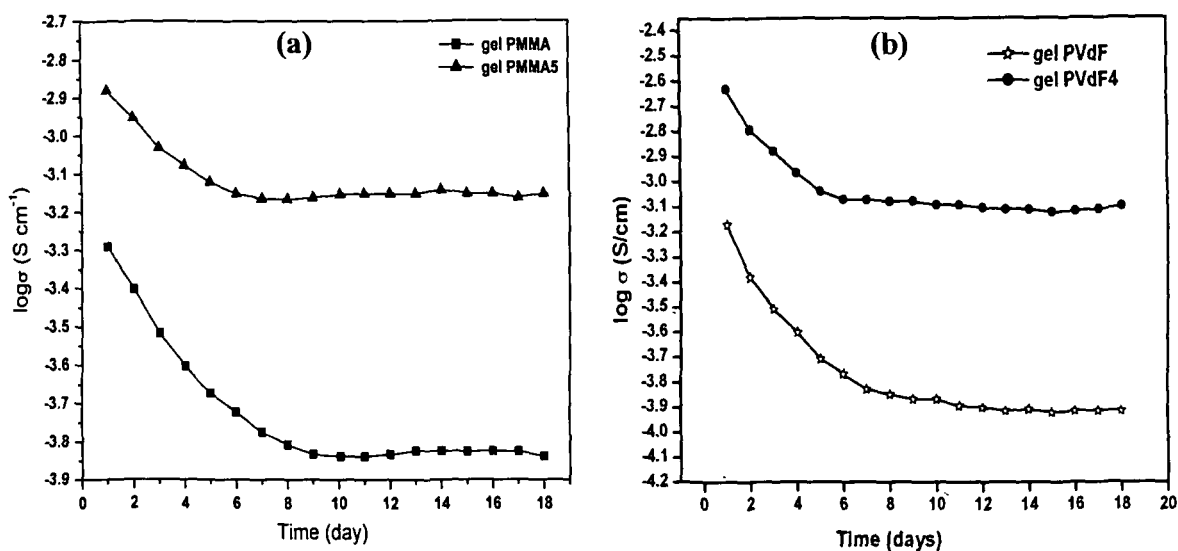


**Figure 6.12:** Interfacial stability of (a) gel PMMA and PMMA/MMT nanocomposite gel polymer electrolyte with 5 wt. % clay loading and (b) gel PMMA and PMMA/MMT nanocomposite gel polymer electrolyte with 5 wt. % clay loading.

In order to examine the interfacial stability of both PMMA-based PVdF-based gel polymer electrolytes before and after addition of organoclay, the ionic conductivity was measured by fabricating stainless steel/polymer electrolyte /stainless cells at room temperature and monitored for 18 days. Polymer electrolytes without clay and containing 5 wt. % MMT for PMMA-based electrolytes and 4 wt. % clay for PVdF-based electrolytes have been selected to observe the effect of clay on interfacial stability and the results are shown in figures 6.12 (a & b). The figures reveal that ionic conductivity of both the electrolytes decreased with time but decrease of ionic conductivity in the clay free polymer electrolytes are much larger as compared to that in the polymer electrolytes containing MMT clay. This confirms that the interfacial stability of the polymer electrolyte containing clay is better than that of the clay free electrolyte systems. To the best of our knowledge, the interfacial stability of polymer/clay nanocomposite electrolytes is not yet reported in literature. However the improvement of interfacial stability in nanocomposite polymer electrolytes due to the addition of nano-sized ceramic fillers and fibers is widely reported [167, 306, 338, 339], according to which the high surface area of nano-sized ceramic fillers

form a barrier layer at the electrode, which effectively impedes the electrode-electrolyte reaction. This in turn reduces the passivation layer on the electrode leading to better interfacial stability between electrode and electrolyte. MMT clay is a natural mineral with high aspect ratio. Presence of clay in the polymer matrix prevents the electrode material to come in direct contact with the electrolyte protecting it from passivation.

## 6.8 Summary

In this work, organically modified MMT clays have been employed to modify the electrical and electrochemical properties of PMMA and PVdF based gel electrolytes. The insertion of polymer chains into the galleries of MMT showed enhancement in the  $d$ -spacing as revealed by XRD and TEM results. Intercalation of PVdF into the galleries of MMT also results in the formation of  $\beta$  phase of PVdF. From ac impedance spectroscopy it has been shown that the ionic conductivity of the nanocomposite gel polymer electrolytes increases with increase in clay loading and exhibits a maximum value of  $1.3 \times 10^{-3} \text{ Scm}^{-1}$  for PMMA-based nanocomposite electrolytes whereas a little higher value of  $2.3 \times 10^{-3} \text{ Scm}^{-1}$  has been found in case of PVdF-based electrolytes at room temperature. This has been attributed to the higher uptake of liquid electrolytes by the nanocomposites. The SEM results are consistent with the fact that the higher conductivity of clay-loaded gel polymer electrolytes arises from increased solvent retention. The presence of high dielectric constant clay layers can dissolve more lithium salt ( $\text{LiClO}_4$ ) by disturbing the charge environment of the electrolyte systems. The cationic charges on the surface of MMT act as Lewis acid centers and compete with  $\text{Li}^+$  cations (strong Lewis acid) to form complexes with the polymer host. This in turn may result in: (a) structural modifications and the promotion of  $\text{Li}^+$ -conducting pathways at the surface of filler, and (b) the lowering ionic coupling, which promotes the salt dissociation. These two effects combine to increase the free ions and account for the observed enhancement in the ionic conductivity. Addition of MMT clays in polymers not only reduces the interfacial resistance with SS electrode but also provides better electrochemical stability window.

## CHAPTER VII

### ***Swift Heavy Ion Irradiation Effects on Nanofiber Reinforced and Layered Silicate Nanocomposite Electrolytes***

---

---

*In this chapter the effete of Swift Heavy Ion (SHI) irradiation on P(VdF-HFP) based nanocomposite gel polymer electrolytes dispersed with dedoped polyaniline (PAni) nanofibers and PEO-MMT based single ion conductor have been discussed. In case of P(VdF-HFP) based nanocomposite gel polymer electrolytes irradiation by 90 MeV  $O^{7+}$  ions results in increase of ionic conductivity by a large number up to a certain fluence ( $\leq 10^{11}$  ions/cm<sup>2</sup>) because of the chain scission effect. However at higher fluence ( $\geq 10^{11}$  ions/cm<sup>2</sup>) cross-linking of polymer chains predominates leading to decrease of ionic conductivity. On the other hand SHI irradiation on PEO-MMT nanocomposite results in the greater intercalation at lower fluence and ultimately exfoliation at the highest fluence used. With the increase of intercalation of PEO chains inside the galleries of MMT results in the increase of interaction between  $Na^+$  cation and oxygen heteroatom leading to the increase in ionic conductivity in the composite.*

---

---

High energy ion irradiation of polymers leads to remarkable changes in their physical and chemical properties [340-346]. Permanent modifications in the molecular weight distribution and solubility [345, 346], electrical [347, 348], optical [349, 350] and mechanical properties [351, 352] of polymers and other materials have been detected after ion irradiation. When an energetic ion penetrates into a polymer material, it loses energy during their passage through the material, which is either spent in displacing atoms/molecules of the sample by elastic collisions referred to as nuclear stopping or exciting the atoms by inelastic collisions referred to as electronic stopping. Nuclear stopping arises from collisions between the energetic ions and target nuclei that cause atomic displacement and chain scission. Electronic stopping is determined mainly by the charge state and velocity of the ion [205]. Energy transfer by nuclear stopping process becomes important when an ion slows down approximately to Bohr velocity. Therefore for high energy ions, the maximum energy loss occurs near the end of the ion track. Nuclear collisions create recoil atoms due to momentum transfer from ion to target atom. The recoiled atoms are thermalized by dissipating energy through phonons and collecting excitons of target atoms (plasmons). For most ion energy ranges of interest, nuclear stopping by ions of low atomic number atoms of hydrogen and helium is negligible

because the Rutherford scattering cross section and momentum transfer by low mass atom is small [205]. Nuclear stopping, however, becomes important for ion species with large number of nucleons. Polymers have fairly large free volume, often larger than 20% and the atomic density in such loose system is relatively small as compared to dense lattice structure such as metal. Therefore, in polymers, most of the nuclear displacements occur fairly independently.

The electronic energy loss takes place in two ways: electronic excitation and ionizations of the target atoms. When the electronic transfer is high, a considerable volume around the ion projectile is influenced because of the columbic field produced by glancing collisions and ionization by knock-on collisions [205]. This leads to production of active chemical species i.e. cations, anions, radicals, and electrons along the polymer chains. Columbic interactions among these active species cause violent bond stretching and segmental motion in the polymeric chain. Electronic stopping causes more cross-linking due to collective excitations of target atoms, which produce a large excited volume thereby resulting in coercive interactions among the ions and radical pairs produced within the volume.

In this chapter studies on two systems viz. P(VdF-HFP)-(PC+DEC)-LiClO<sub>4</sub>-dedoped PANi nanofibers and PEO-MMT single ion conductor irradiated with 90 MeV O<sup>7+</sup> swift heavy ion have been presented. Ion irradiation on the samples has been performed at 15 UD Pelletron accelerator available at Inter University Accelerator Center, New Delhi, India using materials science (MS) beam line facility. The ion fluence was chosen to be  $5 \times 10^{10}$ ,  $10^{11}$ ,  $5 \times 10^{11}$  and  $10^{12}$  ions/cm<sup>2</sup> for P(VdF-HFP)-(PC+DEC)-LiClO<sub>4</sub>-dedoped PANi nanofibers and  $5 \times 10^{10}$ ,  $10^{11}$ ,  $5 \times 10^{11}$ ,  $10^{12}$  and  $5 \times 10^{12}$  ions/cm<sup>2</sup> for PEO-MMT samples. The samples were loaded on four sided ladder (six samples on each side), which could be rotated and moved up and down to bring a particular sample in front of the ion beam for irradiation. Different samples were exposed to the ion beam for different time intervals as per the desired fluence. The ion current has been kept low (0.3–0.5 pna) to avoid sample burning. X-ray diffractograms were recorded by Rigaku miniflex X-ray diffractometer. Surface morphology of the composite electrolytes was studied by using Scanning Electron Microscope (Jeol model JSM 6390 LV). FTIR studies were carried out using Nicolet Impact 410 spectrophotometer. The ionic conductivity and dielectric measurement of the films was

determined from Hioki 3532-50 LCR HiTester in the frequency range of 42 Hz to 5 MHz keeping the electrolyte films between two stainless steel blocking electrodes. The nature of conductivity of the nanocomposites was determined by transference number measurements using Wagner polarization technique with polymer electrolyte films between graphite blocking electrodes. DSC measurements were carried out using Simadzu DSC-60. A heating rate of 10 °C/min was used at all samples. The transference number was found to be 0.99 for P(VdF-HFP)-(PC+DEC)-LiClO<sub>4</sub>-dedoped PANi nanofibers and 0.97 for PEO-MMT single ion conductor indicating that conductivity was essentially ionic in nature. In both the cases the best sample viz. P(VdF-HFP)-(PC+DEC)-LiClO<sub>4</sub>- 6 wt. % dedoped PANi nanofibers and PEO-20 wt. % MMT has been selected to study the irradiation effects.

## 7.1 O<sup>7+</sup> Ion Irradiated P(VdF-HFP)-(PC+DEC)-LiClO<sub>4</sub>-6 wt. % dedoped PANi Nanofibers System

### 7.1.1 Ionic Conductivity Measurements

Figure 7.1 shows the typical Nyquist plots of irradiated and unirradiated nanocomposite gel polymer electrolyte films at room temperature. All plots comprise a semicircular arc in the high frequency region and an oblique line in the low frequency region. The high frequency semicircle can be ascribed to the bulk of polymer electrolytes, whereas the low frequency spike is due to the capacitance of electric double layer formed at the electrode/electrolyte interface. The bulk resistance ( $R_b$ ) is determined from the intercept of the slanted line with the real-axis value that the arc reaches its minimum. Then the conductivity  $\sigma$  can be obtained from  $\sigma = l/R_b A$ , where  $l$  is the thickness and  $A$  is the area of polymer electrolyte film.

It is observed that the ionic conductivity of the nanocomposite gel polymer electrolytes increases with increase in fluence and attains a maximum value of  $1.2 \times 10^{-2}$  S cm<sup>-1</sup> when the fluence is  $10^{11}$  ions/cm<sup>2</sup>. Above that fluence a decreasing trend of ionic conductivity is observed as compared to that of the pristine one. The variation of ionic conductivity with different fluence is presented in figure 7.2. The increase in ionic conductivity at lower fluence could be attributed to the fact that SHI irradiation applied to the polymer matrix can force the large coil size of the polymer chains to change into smaller size due to chain scission effect [353]. This in turn induces larger segmental motion of the polymer backbone resulting in increase in ionic conductivity. However at higher fluence a

combined effect of phase separation and cross-linking of polymer chains seems to take place, which results in decrease in ionic conductivity. Phase separation occurs when PANi nanofibers-rich region in the electrolyte becomes more PANi nanofibers-rich and P(VdF-HFP)-rich phase becomes more P(VdF-HFP)-rich. This requires the mobility of the atoms or molecules in the electrolyte. The activation of the mobility is provided by the ion impact of SHI at higher fluence.

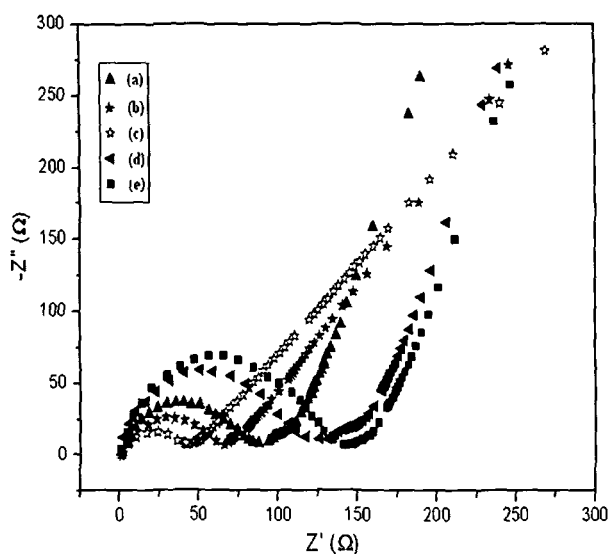


**Figure 7.1:** Nyquist plots of P(VdF-HFP)-(PC+DEC)-LiClO<sub>4</sub>-6 wt. % dedoped PANi nanofibers irradiated with fluence (a) 0, (b)  $5 \times 10^{10}$ , (c)  $10^{11}$ , (d)  $5 \times 10^{11}$  and (e)  $10^{12}$  ions/cm<sup>2</sup>.

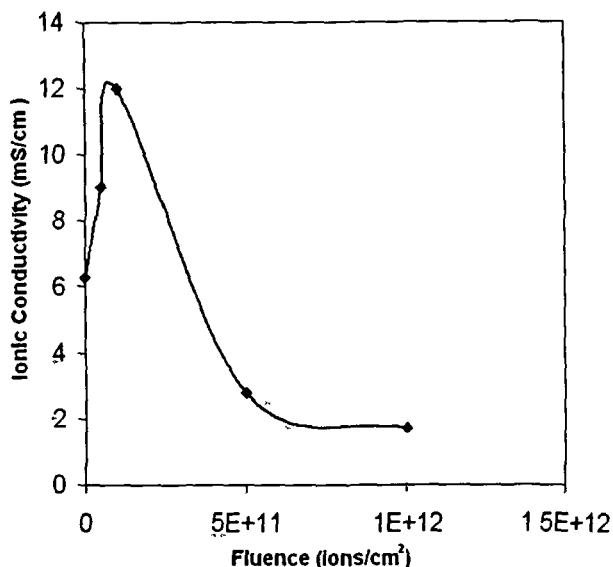


**Figure 7.2:** Variation of ionic conductivity of P(VdF-HFP)-(PC+DEC)-LiClO<sub>4</sub>-6 wt. % dedoped PANi nanofibers with different fluence.

After phase separation, it becomes easier for the polymer to contract that increases its density, which in turn results in chain folding and cross-linking of polymers, causing the formation of new crystalline regions [354] leading to decrease in ionic conductivity. It is worth mentioning that during irradiation, the energy deposited in the polymer causes chain scission or produce radicals, which subsequently decay or cross-link with neighboring radicals i.e. both chain scission and cross-linking occur during irradiation. At low fluence, chain scission predominates because of wide separation of radicals, which do not result in cross-linking. However, as fluence increases radical concentration increases resulting in formation of closely spaced radicals along the ion track. As a result coercive interaction among the radical pairs increases, which eventually allow the adjacent polymer chains to cross-link [355, 356].

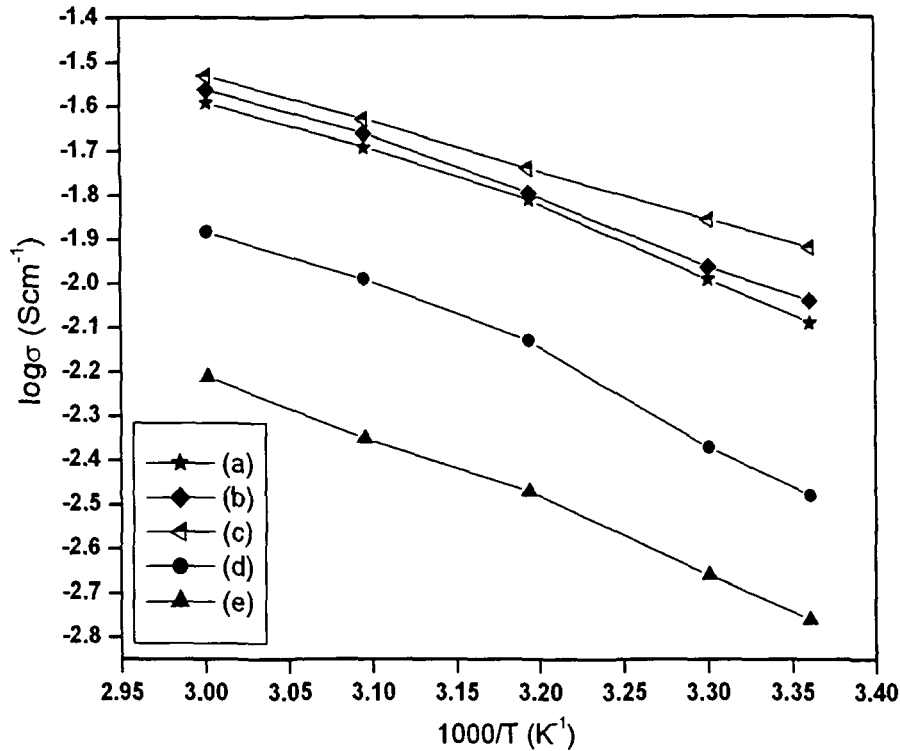


**Figure 7.3:** Temperature dependence of ionic conductivity of P(VdF-HFP)-(PC+DEC)-LiClO<sub>4</sub>-6 wt. % dedoped PANi nanofibers irradiated with fluence (a) 0, (b)  $5 \times 10^{10}$ , (c)  $10^{11}$ , (d)  $5 \times 10^{11}$  and (e)  $10^{12}$  ions/cm<sup>2</sup>.

The temperature dependant ionic conductivity of the unirradiated and irradiated nanocomposite gel electrolytes with different fluence in the temperature range from 25 °C to 70 °C is shown in figure 7.3. It is observed that the curves follow almost linear i.e. Arrhenius behavior governed by the equation [282]

$$\sigma = \sigma_0 \exp(-E_a/kT) \tag{7.1}$$

where  $\sigma$ ,  $\sigma_0$ ,  $E_a$ ,  $k$  and  $T$  are the ionic conductivity, the pre exponential factor, the activation energy, the Boltzmann constant and the absolute temperature respectively. It has been reported that ionic transport in gel polymer electrolytes obeys the VTF (Vogel–Tamman–Fulcher) relation  $\{\sigma = B \exp(-E_a/k(T-T_0))\}$ ,  $B$  is a constant and  $T_0$  being the idealized glass transition temperature of the polymer, which is 20–50 K below the glass transition temperature of the polymer}, which describes the transport properties in a viscous polymer matrix [81, 317]. Since glass transition temperature of P(VdF-HFP) is  $-100$  °C,  $T_0$  will be far below the temperature regions of measurements from room temperature (25 °C) to 70 °C.

Therefore, VTF behavior can be modeled as Arrhenius behavior as shown in figure 7.3. As expected the increase in temperature leads to increase in ionic conductivity because as the temperature increases the polymer chains flex at increased rate to produce more free volume, which leads to enhanced polymer segmental mobility.

It is well known that porosity plays an important role in determining the ionic conductivity in gel polymer electrolytes. More is the porous structure of the polymer more is the entrapment of liquid electrolytes in the pores and eventually higher is the ionic conductivity. The change in porosity in the present nanocomposite gel polymer electrolytes upon SHI irradiation at different fluence have been determined by measuring the volume occupation ( $V_p$ ) of the polymer electrolytes [357] given by

$$V_p = \sigma_{app} / \sigma_{poly} \quad (7.2)$$

where  $\sigma_{app}$  is the apparent density of the polymer electrolyte and  $\sigma_{poly}$  is the calculated density of the polymer electrolyte from the volume fraction and density of individual components in the electrolyte. The volume occupation  $V_p$  of unirradiated and  $O^{7+}$  ion irradiated P(VdF-HFP) based nanocomposite gel polymer electrolyte is given in table 7.1. It shows that porosity increases (i.e.  $V_p$  decreases) as a function of ion fluence up to  $10^{11}$  ions/cm<sup>2</sup>, which results in more entrapment of liquid electrolytes in the pores giving rise to increase in ionic conductivity. At higher fluence ( $>10^{11}$  ions/cm<sup>2</sup>) porosity decreases probably due to crystallization of polymer [358] exuding the liquid electrolyte out of the pores resulting in the decrease in the conductivity.

**Table 7.1:** Volume occupation ( $V_p$ ) of P(VdF-HFP)-(PC+DEC)-LiClO<sub>4</sub>-6 wt. % dedoped PANi nanofibers composite gel polymer electrolytes with different fluence.

Fluence (ions/cm <sup>2</sup> )	$V_p$	Degree of crystallinity (%)
$5 \times 10^{10}$	0.46	9.3
$10^{11}$	0.38	8.2
$5 \times 10^{11}$	0.67	18.6
$10^{12}$	0.71	19.7



### 7.1.2 XRD Analysis

XRD patterns of unirradiated and 90 MeV  $O^{7+}$  ions irradiated P(VdF-HFP)-(PC+DEC)- $LiClO_4$ -dedoped PANi nanofibers composite gel polymer electrolytes are shown in figure 7.4. Literature reveals that the three peaks observed at  $2\theta=18.5^\circ$ ,  $20^\circ$  and  $38^\circ$  for pure P(VdF-HFP) correspond to (100), (020) and  $(\overline{202})$  reflections of P(VdF-HFP) [256]. In the present case, the unirradiated nanocomposite gel polymer electrolyte (Figure 7.4a) exhibits a prominent peak only at  $2\theta=20^\circ$  and other peaks are decreased in intensity implying that crystallinity decreases. Normally, for pure PVdF, an increase in crystallinity is observed at lower irradiation fluence ( $<10^{11}$  ions/cm<sup>2</sup>), whereas crystallinity decreases at higher fluence [359]. However, in P(VdF-HFP) the presence of HFP units helps in reducing the crystallinity of the polymer. Moreover, the addition of high aspect ratio ( $> 50$ ) dedoped PANi nanofibers prevent polymer chain reorganization resulting in decreased crystallinity compared to pure P(VdF-HFP) [339]. As the fluence increases, the (020) peak at  $2\theta=20^\circ$  gets broadened up to a fluence of  $10^{11}$  ions/cm<sup>2</sup> indicating that degree of crystallinity is decreased. The degree of crystallinity is determined by a method described in Chapter III and the values of degree of crystallinity at different fluence are given in table 7.1. As observed from the figure 7.4, the (020) reflection of P(VdF-HFP) changes significantly upon ion irradiation. This change has been analysed quantitatively using single-line approximation method employing double Voigt function [273] and the  $d$ -spacing, crystallite size ( $l_c$ ) and strain ( $\epsilon$ ) have been calculated at different irradiation fluence, which are presented in table 7.2. This procedure involves the extraction and analysis of Gaussian ( $\beta_G$ ) and Lorentzian ( $\beta_L$ ) component of integral breadth of a single Bragg peak corrected for instrumental broadening. It is observed from the crystallite size and microstrain analysis of the irradiated polymer electrolyte films that the crystallite size and microstrain decrease with the increasing ion irradiation fluence up to  $10^{11}$  ions/cm<sup>2</sup> and increase at higher fluence ( $> 10^{11}$  ions/cm<sup>2</sup>). It appears from the size-strain analysis of the irradiated polymer electrolyte films that the crystallite size decreases with the increasing ion fluence up to  $10^{11}$  ions/cm<sup>2</sup> and then it increases with significant change in microstrain. Thus there is a strong correlation between ionic conductivity and crystallite size. The decrease of crystallite size upon low fluence ( $\leq 10^{11}$  ions/cm<sup>2</sup>) ion irradiation suggests an enhancement in the degree of disorder in the electrolyte films resulting from chain scission effect. With the increase of disorder, we can expect that generation of polymer-filler

(nanofibers) interfaces will be more. Since interfaces are the sites of high defect concentration, they can provide channels or paths for faster ionic transport [114].

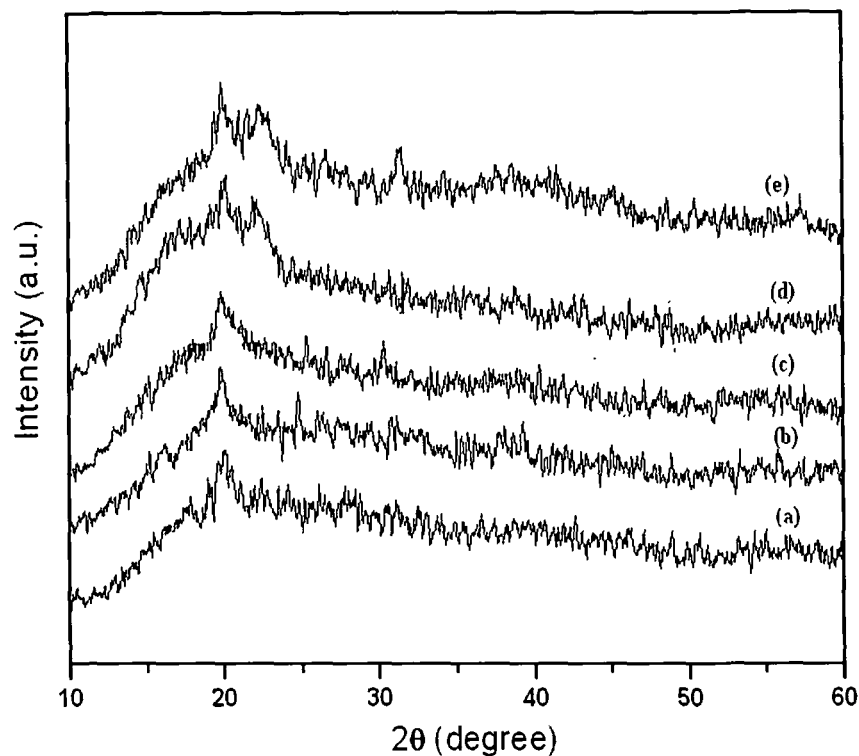


**Figure 7.4:** XRD patterns of P(VdF-HFP)-(PC+DEC)-LiClO<sub>4</sub>-6 wt. % dedoped PANi nanofibers irradiated with fluence (a) 0, (b)  $5 \times 10^{10}$ , (c)  $10^{11}$ , (d)  $5 \times 10^{11}$  and (e)  $10^{12}$  ions/cm<sup>2</sup>.

**Table 7.2:** Comparison of the values of d-spacing, crystallite size ( $l_c$ ) and strain ( $\epsilon$ ) for (020) reflection of P(VdF-HFP) with ionic conductivity ( $\sigma$ ) at different fluence.

Fluence (ions/cm <sup>2</sup> )	d-spacing (Å)	$l_c$ (nm)	$\epsilon$	$\sigma$ (mS/cm)
0	4.37	8.19	0.00378	6.3
$5 \times 10^{10}$	4.41	6.28	0.01948	8.5
$10^{11}$	4.17	6.33	0.01402	12.0
$5 \times 10^{11}$	4.18	9.22	0.00325	2.4
$10^{12}$	4.2	10.96	0.00413	1.8

An interesting effect occurs above  $10^{11}$  ions/cm<sup>2</sup> where an additional peak appears at  $2\theta=23^\circ$ , which can be assigned to dedoped PANi nanofibers as discussed in Chapter IV

indicating the phase separation PANi nanofibers at higher fluence. Therefore, one can say that there are changes in PANi matrix also, whose crystalline phase started forming at higher fluence. The  $(202)$  diffraction peak of PVdF again starts appearing at higher fluence ( $> 10^{11}$  ions/cm<sup>2</sup>) denoting recrystallization of polymer due to ion irradiation. Here recrystallization in the sense that SHI irradiation induces contraction in the polymer that increases its density resulting in chain folding and cross-linking of polymer chains, which leads to the formation of new crystalline regions. The sudden decrease of the value of microstrain at higher fluence could be attributed to the effect of phase separation. After phase separation the interfacial area between filler and polymer is greatly reduced causing the value of microstrain to decrease significantly at higher fluence.

### 7.1.3 Dielectric Loss Spectra and DSC Analysis

The evidence of phase separation is further provided by the dielectric loss spectra. Dissipation of energy due to an alternating electric field is termed as dielectric loss and is generally consists of contributions from ionic transport and polarization of dipole [360]. Figure 7.5 presents dielectric loss as a function of frequency for unirradiated and irradiated P(VdF-HFP)-(PC+DEC)-LiClO<sub>4</sub>-6 wt. % dedoped PANi nanofibers composite gel polymer electrolytes. It is observed from the figures that for unirradiated (Figure 7.5a) and irradiated samples at lower fluence ( $< 10^{11}$  ions/cm<sup>2</sup>) (Figure 7.5b-c) the dielectric loss decreases with increasing frequency and becomes constant after a certain frequency. However, for samples irradiated with higher fluence ( $> 10^{11}$  ions/cm<sup>2</sup>), a sudden rise of dielectric loss is observed giving rise to a polarization peak. The polarization peak appears when the stress given by the electric field cannot be dissipated by ionic transport. This can be attributed to the phase separation of PANi nanofibers from P(VdF-HFP matrix at higher irradiation fluence ( $> 10^{11}$  ions/cm<sup>2</sup>).

After phase separation, two phases exist in the electrolyte, one is PANi-rich phase and other is plasticizer-rich P(VdF-HFP) phase. It is difficult for the ions at the interface along the PANi-rich phase to conduct giving rise to decreased ionic conductivity and increased dielectric loss. The appearance of polarization peaks at higher irradiation fluence ( $> 10^{11}$  ions/cm<sup>2</sup>) is a strong evidence of accumulation of ions at the interface between PANi-rich phase and plasticizer-rich phase. On the other hand polarization peak is not observed in the

samples irradiated with lower fluence ( $< 10^{11}$  ions/cm<sup>2</sup>) suggesting that homogenous mixture is retained at lower fluence.

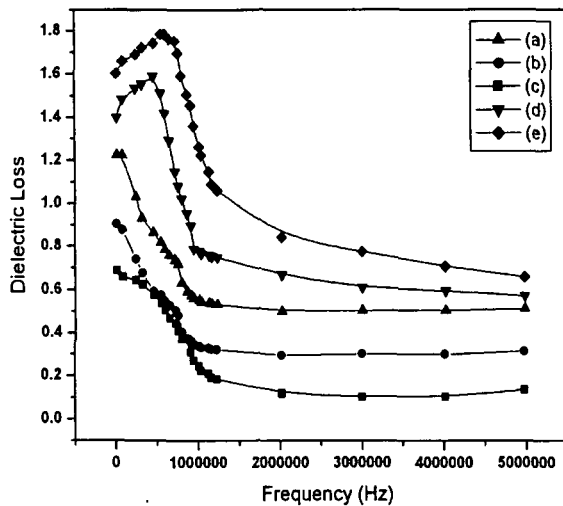


**Figure 7.5:** Dielectric loss spectra of P(VdF-HFP)-(PC+DEC)-LiClO<sub>4</sub>-6 wt. % dedoped PANi nanofibers irradiated with fluence (a) 0, (b)  $5 \times 10^{10}$ , (c)  $10^{11}$ , (d)  $5 \times 10^{11}$  and (e)  $10^{12}$  ions/cm<sup>2</sup>.

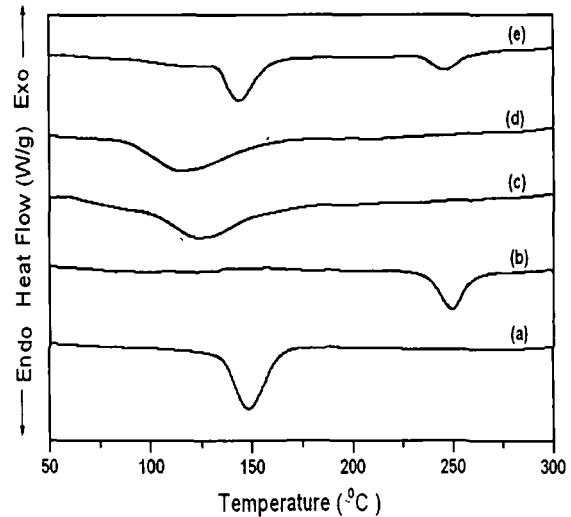


**Figure 7.6:** DSC thermograms of (a) pure P(VdF-HFP), (b) pure dedoped PANi nanofibers and P(VdF-HFP)-(PC+DEC)-LiClO<sub>4</sub>-6 wt % PANi nanofibers irradiated with fluence (c) 0, (d)  $10^{11}$  and (e)  $10^{12}$  ions/cm<sup>2</sup>.

DSC thermograms, shown in figure 7.6, reveal that the melting temperature of P(VdF-HFP) appearing at 148 °C (Figure 7.6a) is reduced and broadened upon low irradiation fluence of  $10^{11}$  ions/cm<sup>2</sup> (Figure 7.6d) suggesting that the degree of crystallinity is reduced. However, at the fluence of  $10^{12}$  ions/cm<sup>2</sup> (Figure 7.6f), peak around 250 °C, which is due to the melting peak of PANi nanofibers (Figure 7.6e) reappears, which is indicative of occurrence of phase separation.

#### 7.1.4 FTIR Analysis

FTIR spectra of unirradiated and  $O^{7+}$  irradiated P(VdF-HFP)-(PC+DEC)-LiClO<sub>4</sub>- dedoped PANi nanofibers composite gel polymer electrolytes are shown in figure 7.7. In figure 7.7a the C-N stretching vibration of secondary amine in PANi nanofiber arises at  $1289\text{cm}^{-1}$ . The ammonium ion displays broad absorption in the frequency region  $3350\text{--}3050\text{cm}^{-1}$  because of N-H stretching vibration. The N-H bending vibration of secondary aromatic amine of PANi

nanofiber occurs at  $1507\text{cm}^{-1}$ . The frequency  $1650\text{cm}^{-1}$  of PANi nanofiber is assigned to C=C of aromatic ring.

The symmetric and asymmetric stretching vibrations of crystalline  $\text{CH}_2$  of P(VdF-HFP) (Figure 7.7b) are observed at frequencies  $3025\text{cm}^{-1}$  and  $2985\text{cm}^{-1}$ . This  $\text{CH}_2$  doublet governs the overall destruction of P(VdF-HFP). The peaks at  $881$ ,  $796$ , and  $614\text{cm}^{-1}$  are due to bending vibration of  $\text{CH}_2$  group. All these peaks are shifted to  $3017$ ,  $2976$ ,  $879$ ,  $788$ ,  $609\text{cm}^{-1}$  in the nanocomposite gel polymer electrolyte (Figure 7.7c), which is indicative of polymer-salt-filler interaction [339]. It is observed from the figure that the transmission intensities of  $\text{CH}_2$  crystalline bands decrease upon low fluence irradiation ( $5 \times 10^{10}\text{ions/cm}^2$ ) indicating the breaking of C-H bond, which results in enhanced amorphization of the material. The amorphization of the polymer at low fluence is further evidenced by simultaneous decrease in transmission intensities of other bending vibration of  $\text{CH}_2$  group. At low fluence, irradiation induces defects in the crystalline zones, which are evident by a decrease of the FTIR absorption. However, at high fluence ( $10^{12}\text{ions/cm}^2$ ) the above-mentioned transmission peaks increases suggesting recrystallization of the material. The sharp increase in transmission intensities could be due to the formation of new crystalline zones, thickening of the new crystalline zones, or even growing of new lamellar stacks as a result of realignment of the molecular configuration upon high fluence ion impact. Polar group of P(VdF-HFP) plays an important role in crystallizability of the polymer. The presence of polar groups in the polymer leads to the formation of hydrogen bonds, increasing the inter chain forces of attraction [361].

The recrystallization of P(VdF-HFP) upon high ion fluence occurs during secondary electron-phonon coupling, while transferring huge amount energy into the lattice [361]. As a result the molecular dipoles forming the hydrogen bond network become realigned upon irradiation into a highly ordered state of chain cross linked molecules in the crystalline regions facilitating a tighter packing and bonding of the chain elements with each other and creating volume elements as crystallites. This is evident in the decrease in transmission intensity of  $\text{CF}_2$  bending at  $532\text{cm}^{-1}$ , which corresponds to the polar group of P(VdF-HFP). Two new peaks are observed at frequencies  $1289$  and  $1650\text{cm}^{-1}$  (Figure 7.7e) for the sample irradiated with higher fluence, which are due to C-N stretching vibration of secondary amine and C=C of aromatic ring of PANi nanofibers showing phase separation at higher fluence.

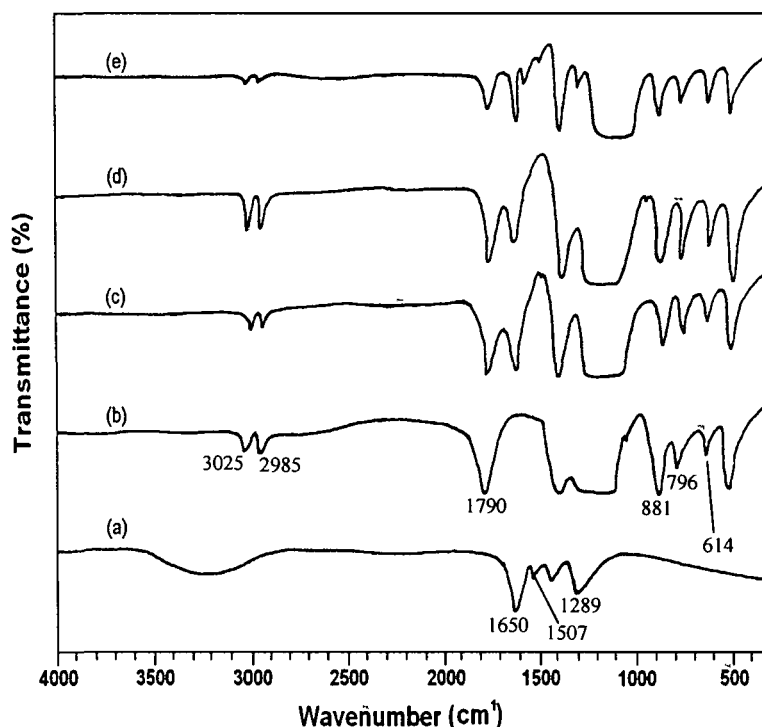


**Figure 7.7:** FTIR spectra of (a) pure PANi nanofibers, (b) pure P(VdF-HFP) and P(VdF-HFP)-(PC+DEC)-LiClO<sub>4</sub>-6 wt. % dedoped PANi nanofibers irradiated with fluence (c) 0, (d) 10<sup>11</sup> and (e) 10<sup>12</sup> ions/cm<sup>2</sup>

In figure 7.7, the  $-\text{CF}=\text{CF}_2$  group is located at around  $1790\text{ cm}^{-1}$ . Frequency  $1636\text{ cm}^{-1}$  is assigned to  $>\text{C}=\text{O}$  stretching vibration of PC and DEC. Frequencies  $1483$  and  $1400\text{ cm}^{-1}$  are assigned to  $-\text{CH}_3$  asymmetric bending and  $\text{C}-\text{O}$  stretching vibrations of the plasticizer, propylene carbonate, and diethyl carbonate. Frequencies  $1290$ – $1060\text{ cm}^{-1}$  are assigned to  $-\text{C}-\text{F}-$  and  $-\text{CF}_2-$  stretching vibrations. Frequency  $881\text{ cm}^{-1}$  is assigned to the vinylidene group of the polymer.

### 7.1.5 Morphological Studies

Scanning electron micrographs of pristine P(VdF-HFP), unirradiated and  $\text{O}^{7+}$  irradiated P(VdF-HFP)-(PC+DEC)-LiClO<sub>4</sub>-dedoped PANi nanofibers composite gel polymer electrolytes are shown in figures 7.8 (a-d). It is observed that the pure P(VdF-HFP) shows porous structure with uniform pore distribution. Addition of high aspect ratio fillers (dedoped PANi nanofibers) (Figure 7.8b) resulted in improved morphology, since the fillers occupied the pores along with the plasticizers. Highly porous surface morphology of the polymer

electrolytes (unirradiated) as compared to that of pure P(VdF-HFP) is due to the interaction of dispersed dedoped (insulating) nanofibers with polymer component as well as the affinity with solvent molecules.

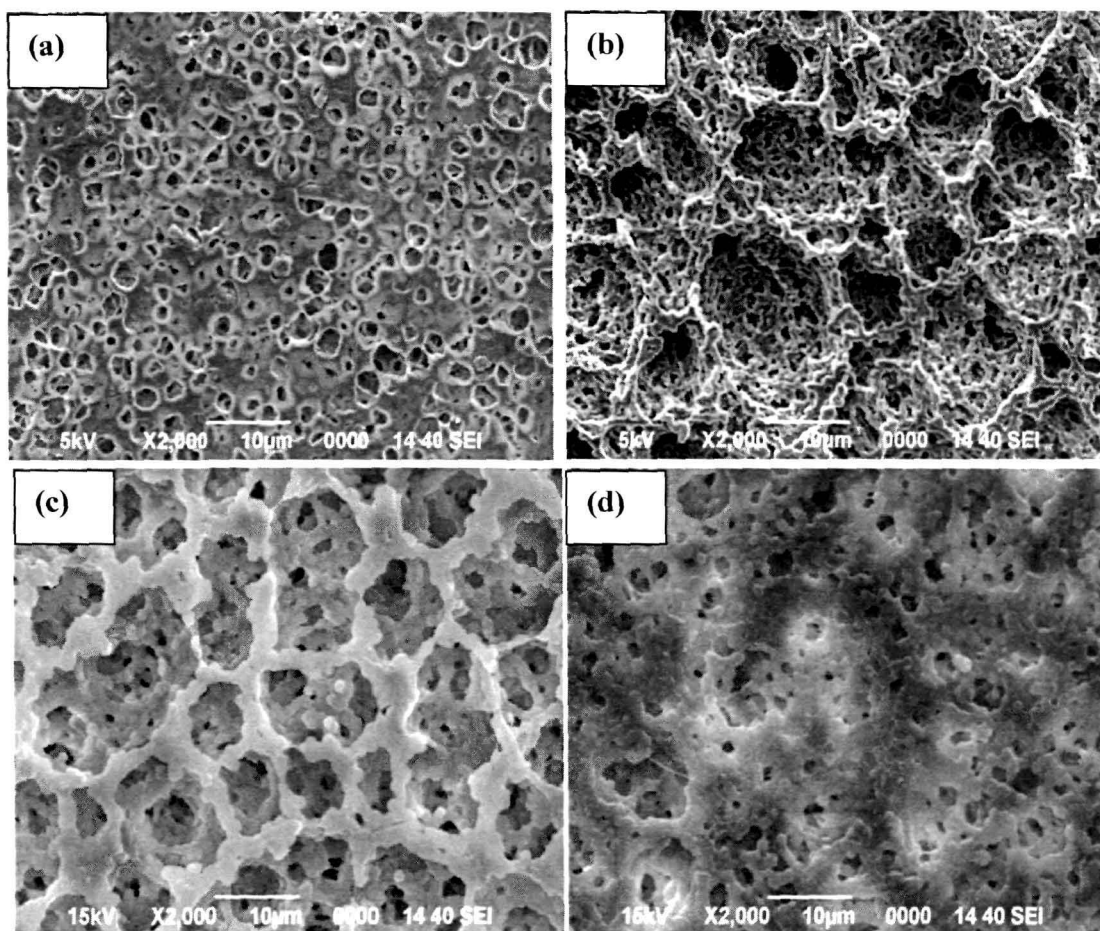


**Figure 7.8:** SEM micrographs of (a) pure P(VdF-HFP) and P(VdF-HFP)-(PC+DEC)-LiClO<sub>4</sub>-6 wt. % dedoped PANi nanofibers irradiated with fluence (b) 0, (c) 10<sup>11</sup> and (d) 10<sup>12</sup> ions/cm<sup>2</sup>.

Upon irradiation with lower fluence (10<sup>11</sup> ions/cm<sup>2</sup>) (Figure 7.8c) the porous structure becomes much denser with well dispersed pores, which leads to better connectivity of the liquid electrolyte through the pores accounting for the increase in ionic conductivity. On the other hand, at higher fluence (10<sup>12</sup> ions/cm<sup>2</sup>) irradiation the porous structure is disrupted possibly due to recrystallization of the polymer. The two-phase microstructure in the SEM image reflects the phase separation phenomenon at higher fluence.

## 7.2 O<sup>7+</sup> Ion Irradiated PEO-20 wt. % MMT System

PEO- 20 wt % MMT sample has been synthesized by solution intercalation method without adding any salt and irradiated with 90 MeV O<sup>7+</sup> to exfoliate the MMT layers so as to mobilize the non-structural Na<sup>+</sup> cations present inside the galleries of MMT. This strategy has been utilized in several studies reported in the literature that reveal that a reasonable value of single ion (cationic) conductivity can be achieved through the formation of salt free polymer/clay nanocomposites [137, 362-365]. Absence of salt ensures that there is no concentration polarization due to absence of anions in these polymer electrolytes, even though at the cost of low ionic conductivity. In the present case though the MMT clay used is organically modified, there exists some Na<sup>+</sup> cations inside the galleries, as cation exchange capacity is not 100%. Intercalation of PEO inside the galleries leads to polymer-Na<sup>+</sup> interaction resulting in movement of Na<sup>+</sup> ions responsible for single cationic conductivity in this kind of nanocomposites. For irradiation purpose the weight ratio of MMT was fixed at 20 wt. %, since at this loading of MMT in PEO, highest ionic conductivity was obtained by us as compared to that for the other compositions.

### 7.2.1 XRD Analysis

Figure 7.9 shows the X-ray diffraction pattern of pure MMT, pure PEO and PEO-20 wt. % MMT nanocomposite at different fluence. Pure MMT exhibits its (001) diffraction peak at  $2\theta = 4.4^\circ$  corresponding to the interlayer spacing of 2 nm. PEO exhibits its characteristic peaks at  $2\theta = 19.2, 22.9, 23.4$  and  $27^\circ$  corresponding to the (*hkl*) values of (120), (112), (032) and (040), respectively. Upon nanocomposite formation the (001) peak shifts towards lower angle side with interlayer spacing of 2.23 nm (Figure 7.9c), which suggests successful intercalation of PEO chains into the nanometric galleries of MMT. With the increase of irradiation fluence (Figure 7.9d-g) it is observed that the (001) peak further shifts towards lower angle side higher gallery spacing of MMT and larger intercalation of PEO. The *d*-spacing profile of MMT with different fluence has been tabulated in table 7.3. During irradiation each ion creates a cylindrical molten zone of a few nanometers, transiently along its path. At this time the temperature of the sample is quite high and the low viscous polymer gets sufficient time to diffuse into the gallery of MMT to cause higher intercalation [366]. It has to be mentioned here that the higher the fluence, the higher is the time of SHI exposure.



So, the polymer gets more time to *diffuse-in* inside the gallery at higher fluence [366]. Nonetheless, intercalation of the polymer gradually increases with the fluence.

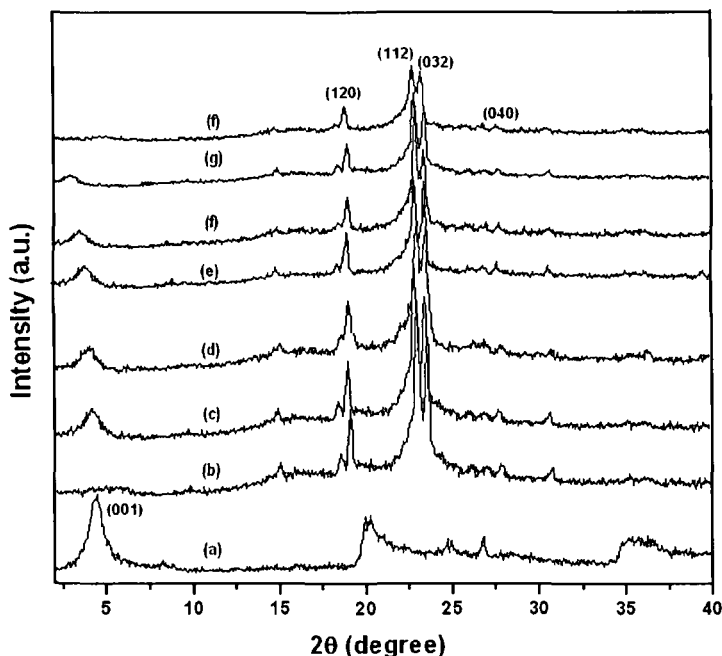


**Figure 7.9:** XRD patterns of (a) pure MMT, (b) pure PEO and PEO-20 wt. % MMT composite irradiated with fluence (c) 0, (d)  $5 \times 10^{10}$  (e)  $10^{11}$ , (f)  $5 \times 10^{11}$ , (g)  $10^{12}$  and (f)  $5 \times 10^{12}$  ions/cm<sup>2</sup>.

On the other hand, at the highest fluence ( $5 \times 10^{12}$  ions cm<sup>-2</sup>) the (001) diffraction peak is almost diminished indicating exfoliation of MMT layers in the nanocomposites. As polymer intercalates into the galleries of MMT, a significant compressive strain is expected in MMT layers. This strain arises due to the dislocation of crystal layers of MMT from their regular crystal lattice upon polymer insertion. In physical terms, the dislocation of the layers results in the increase of *d*-spacing and develops strain in the layers, which ultimately causes exfoliation of MMT layers. The intensity of the characteristics peaks due to pure PEO decreases with increase of ion fluence with no changes in their positions. The high-energy SHI irradiation initially melts the pure PEO matrix and then degrades/ cross-links most of the polymer chains. The degraded and/ or cross-linked PEO molecules cannot crystallize further and, hence, exhibit lower intense peaks in XRD patterns.

**Table 7.3:** *d*-spacing profile and microstrain ( $\epsilon$ ) of PEO-20% MMT nanocomposites at different irradiation fluence

Irradiation fluence (ions/cm <sup>2</sup> )	<i>d</i> -spacing (nm)	$\epsilon$
Pure MMT	2	0.155
Pristine PEO-MMT	2.23	0.164
$5 \times 10^{10}$	2.45	0.175
$1 \times 10^{11}$	2.79	0.189
$5 \times 10^{11}$	2.93	0.197
$1 \times 10^{12}$	3.24	0.208
$5 \times 10^{12}$	-----	-----

As polymer intercalates into the galleries of MMT, a significant compressive strain is expected in MMT layers. This strain arises due to the dislocation of crystal layers of MMT from their regular crystal lattice upon polymer insertion. In physical terms, the dislocation of the layers results in the increase of *d*-spacing and develops strain in the layers. The microstrains calculated for (001) reflections for pure MMT and PEO–MMT composites at different ion fluence are presented in table 7.3. It is observed that the value of microstrain  $\epsilon = 0.155$  for pure MMT increases significantly with SHI irradiation as shown in table 7.3, which means that as more PEO is intercalated into the galleries of MMT with increase of irradiation fluence, the compressive strain increases. The increased strain causes part of the MMT layers to exfoliate resulting in decreased X-ray peak intensity.

### 7.2.2 Ionic Conductivity Measurements

The complex impedance plots for pristine and irradiated PEO-MMT nanocomposite membranes are presented in figure 7.10. All plots comprise a semicircular arc in the high frequency region and an oblique line in the low frequency region, which has been discussed earlier. It is observed from the figure that the ionic conductivity increases (bulk resistance decreases) with the increase of ion fluence and attains a maximum value of  $5 \times 10^{-6} \text{ S cm}^{-1}$  at room temperature for the highest fluence ( $5 \times 10^{12} \text{ ions/cm}^2$ ), which is over 1.5 order higher

as compared to that ( $9.27 \times 10^{-8} \text{ S cm}^{-1}$ ) for the pristine PEO-MMT nanocomposite. The variations of ionic conductivity with different fluence are shown in figure 7.11.

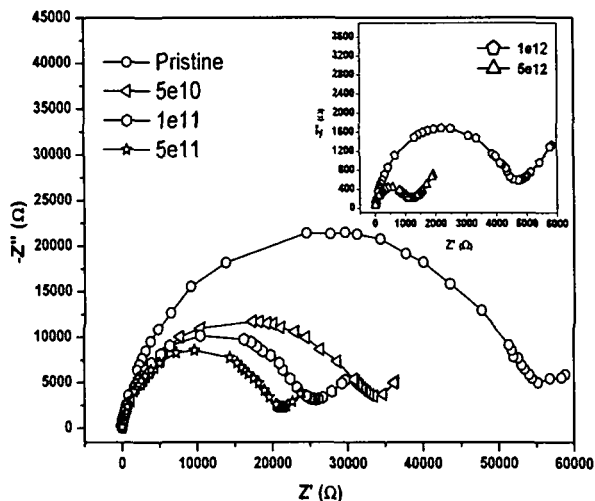


**Figure 7.10:** Impedance spectra of PEO-20 wt. % MMT nanocomposites irradiated at different fluence.

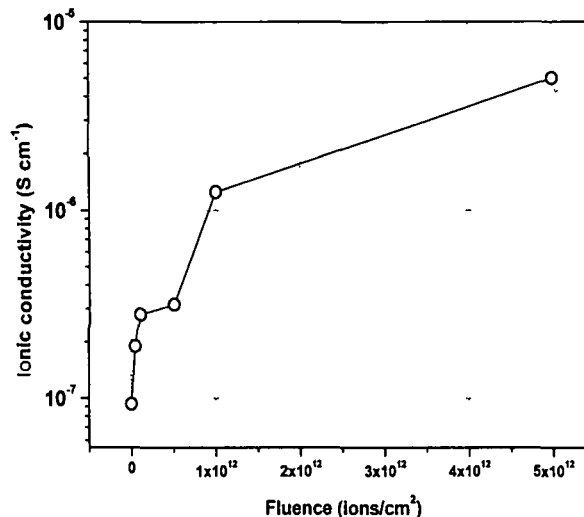


**Figure 7.11:** Variation of ionic conductivity as a function of ion fluence.

The enhancement of ionic conductivity with increasing fluence can be correlated with the fact that with the increase of fluence more polymer chains can enter into the galleries of MMT as revealed by XRD, which leads to greater interaction between heteroatom of PEO and  $\text{Na}^+$  cation residing inside the gallery resulting in higher ionic conductivity. Many related works reveal that intercalated or exfoliated state of MMT plays a distinct role in ion conduction and a complete exfoliated structure could yield the highest ionic conductivity [324, 325]. In the present case as exfoliation proceeds with increasing ion fluence more cations could be mobile and available for conduction through interaction with PEO chains. Conductivity values between  $10^{-4}$  and  $10^{-5} \text{ Scm}^{-1}$  have been reported for PEO/clay [137] nanocomposites (70–75 wt. % clay, 250 °C). PEO/ $\text{NH}_4^+$  smectic [362] composites with similarly high inorganic contents exhibited a conductivity value  $\sim 10^{-7} \text{ Scm}^{-1}$  in the temperature range 125–280 °C, while other clay/polymer systems [363] exhibited conductivities in the range of  $10^{-8}$  to  $10^{-10} \text{ Scm}^{-1}$  (10 wt.% clay, 85–110 °C). Others report conductivities of  $1.6 \times 10^{-6} \text{ Scm}^{-1}$  (60 wt. % clay, 30 °C) [364] and  $10^{-5} \text{ Scm}^{-1}$  (75 wt. % clay, RT) [365] for PEO/clay nanocomposites. In these systems conductivity values of higher order ( $\sim 10^{-5} \text{ Scm}^{-1}$ ) could be achieved only at higher clay content ( $> 70 \text{ wt. \%}$ ) and loading of

higher clay decreased the flexibility of the films. On the other hand lower clay loading resulted in lower values of ionic conductivity. In the present case under investigation we have been able to raise the ionic conductivity up to  $10^{-5} \text{ Scm}^{-1}$  at 25 wt. % of clay loading while flexibility of the films are retained at this concentration. Therefore SHI irradiation seems to be an important tool for enhancing electrical properties in these kinds of nanocomposites.

Figure 7.12 shows the temperature dependent ionic conductivity, which follows a linear trend i.e. Arrhenius behavior. The conductivity enhancement behavior with temperature can be understood by free volume model. As the temperature increases, the polymer chains flex and expand at increasing rate and produce free volume leading to an increase in ion and segmental mobility, which facilitates ion transport

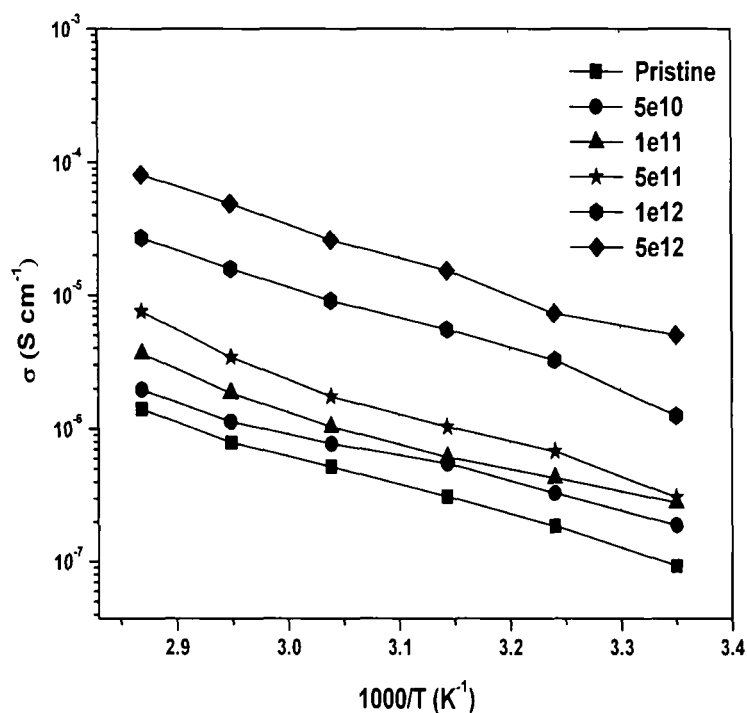


**Figure 7.12:** Temperature dependent ionic conductivity of PEO-20 wt. % MMT at different fluence.

### 7.2.3 Morphological Studies

Figures 7.13 (a-d) show the scanning electron microscope (SEM) image of pristine and irradiated PEO-MMT nanocomposites at different fluence. Unirradiated PEO-MMT

nanocomposites exhibit well-dispersed clay layers with mostly intercalated morphology (Figure 7.13a). With the increase of ion fluence the morphology of PEO-MMT nanocomposite changes and layer spacing of MMT are observed to be higher than that of the pristine one. At the highest fluence ( $5 \times 10^{12}$  ions  $\text{cm}^{-2}$ ) MMT layers exhibit almost exfoliated structure. Thus SEM results agree well with XRD results.

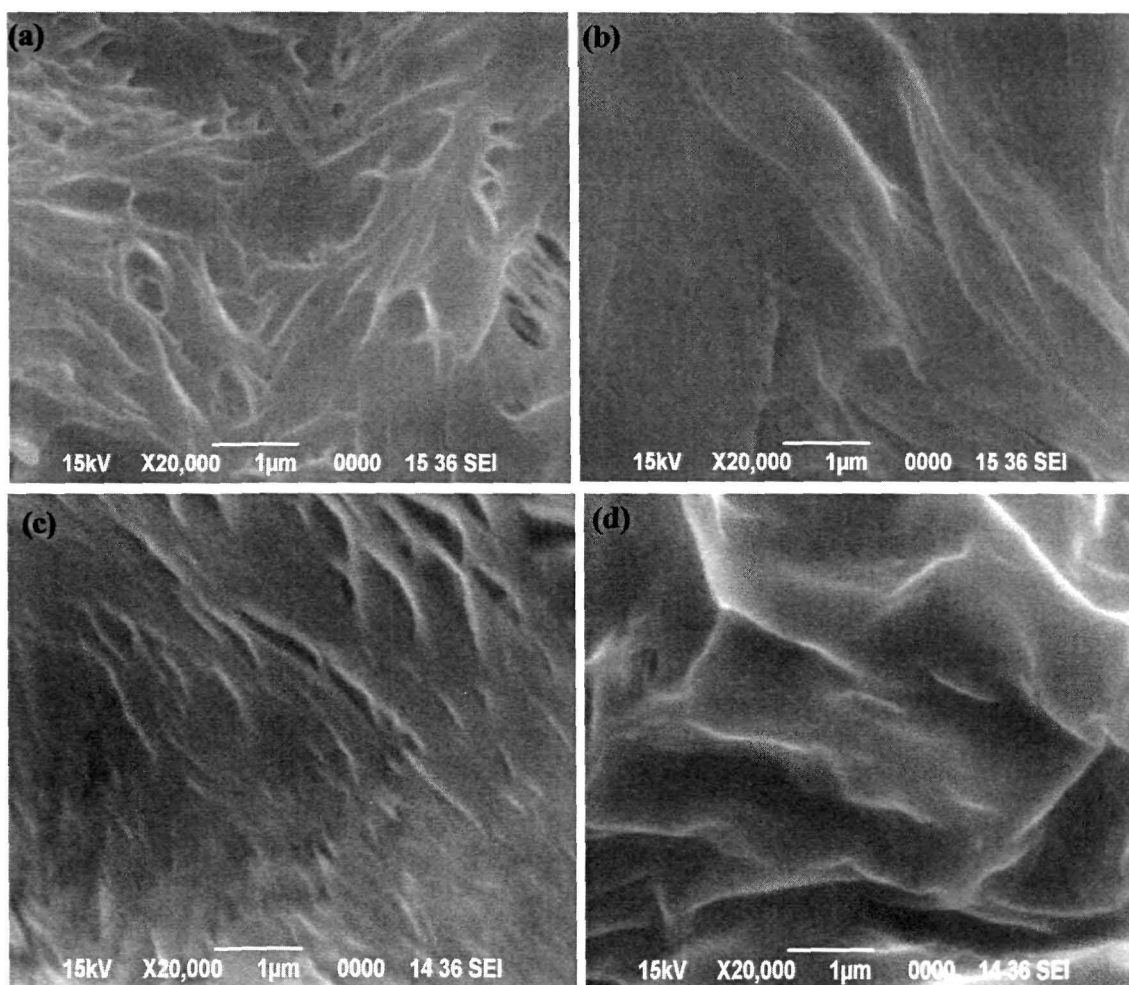


**Figure 7.13:** SEM image of PEO-20 wt. % MMT nanocomposites irradiated with fluence (a) 0, (b)  $5 \times 10^{10}$ , (c)  $5 \times 10^{11}$  and (d)  $5 \times 10^{12}$  ions/cm<sup>2</sup>.

#### 7.2.4 Complex Dielectric Function

Figures 7.14 (a & b) show the variation of real and imaginary part of permittivity ( $\epsilon'$  and  $\epsilon''$ ) for pristine and irradiated nanocomposites as a function of frequency. It is observed that  $\epsilon'$  and  $\epsilon''$  exhibit higher values for the samples irradiated with higher fluence. The  $\epsilon'$  values of

the nanocomposite films are found to be lower than that of the irradiated films and show enhancement with increase of ion fluence.

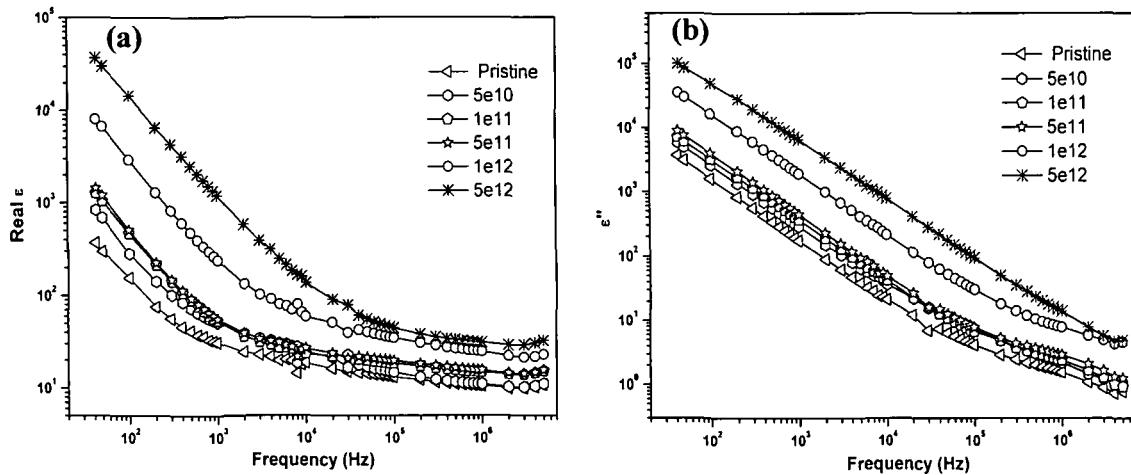


**Figure 7.14:** Real (a) and imaginary (b) part of complex permittivity of PEO- 20 wt. % MMT at different irradiation fluence.

These observations reveal that the intercalated and exfoliated MMT clay structures in PEO change dramatically with the increase of ion fluence in PEO-MMT films. The increase in the complex dielectric function values with increase in ion fluence is associated with the generation of dipolar and free charges in the nanocomposites due to intercalation and exfoliation of MMT layers [147, 367]. Further, the significant increase in  $\epsilon'$  and  $\epsilon''$  values of these materials with increase of irradiation fluence may also be related to the formation of a percolation structure of the nanoparticles, which is confirmed by dielectric investigation on nanocomposites [368]. On the other hand monotonous increase of  $\epsilon'$  with increasing ion fluence suggests enhancement in the number of free  $\text{Na}^+$  cations and their mobility in the increased clay galleries. At high frequencies, the periodic reversal of the electric field occurs so fast that there is no excess ion diffusion in the direction of the field. The polarization due to the charge accumulation decreased, leading to the observed decrease in the value of real and imaginary part of dielectric constant.

Figure 7.15 shows the variation of tangent loss with frequency of PEO-MMT films for different fluence at room temperatures. The peak appearing at loss spectra corresponds to electrode polarization (EP) relaxation frequency ( $f_{EP}$ ), which is used to separate the bulk material and EP phenomena. Appearance of peaks in the spectra suggests the presence of relaxing dipoles in all the samples. As regards the EP phenomenon, long-range drift of free

charges builds up at the interface between the electrolyte and electrode surfaces forming the electric double layer (EDL), which needs a larger space between clay galleries for intercalation [369]. It is observed that with the increase of ion fluence in the nanocomposite  $\tau_{EP}$  values decreases suggesting that the intercalated and exfoliated clay platelets speed up the long-range drift of the ions in the organic-inorganic nanocomposites resulting in faster dynamics of the EDL ions with the variation in the applied alternating electric field.

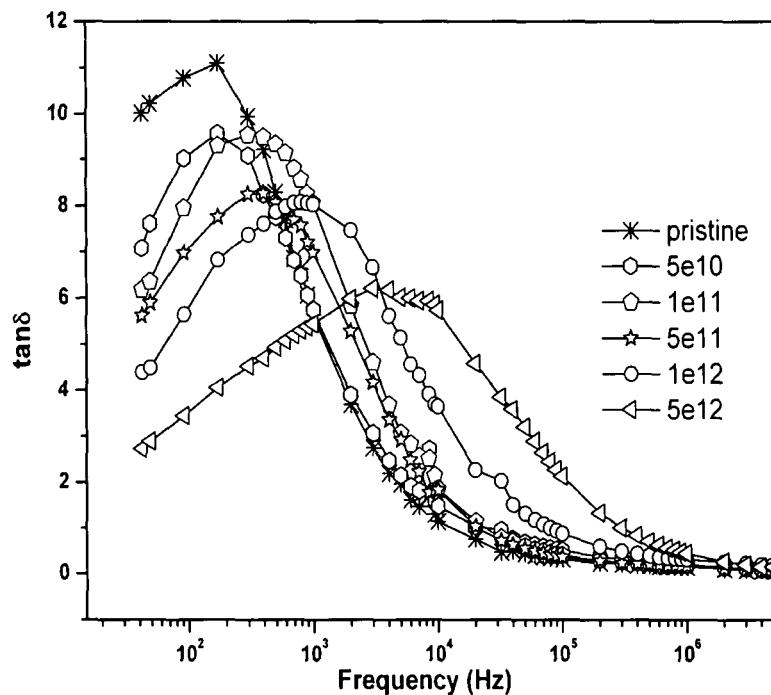


**Figure 7.15:** Tangent loss as a function of frequency for PEO-20 wt. % MMT at different irradiation fluence.

### 7.2.5 Electric Modulus Studies

The study of dielectric relaxation mechanism in the framework of complex modulus formalism is a growing interest. The main advantage of this formalism lies in the fact the effects of the contribution of the electrode and any interfacial polarization, observed in the conductivity spectra, get suppressed in this modulus representation. The  $M^*$  representation is widely used to analyze ionic conductivities by associating a conductivity relaxation time with the ionic process [370]. In the  $M^*$  representation, a relaxation peak is observed for the conductivity process in the frequency spectra of the imaginary component of  $M^*$ .

Figures 7.16 (a & b) show the complex electric modulus spectra of PEO-MMT nanocomposites irradiated with different fluence. The  $M'$  spectra of the pure and irradiated PEO-MMT shows a large dispersion in the ionic conduction region. On the other hand a relaxation peak is observed for the conductivity processes, whereas no peak is observed in the dielectric spectra suggesting that ionic motion and polymer segmental motion are strongly coupled manifesting as a single peak in the  $M'$  spectra with no corresponding feature in dielectric spectra [369]. From  $M''$  curve the conductivity relaxation time can be calculated using the relation  $\tau_{\sigma} = 1/2\pi f_{\sigma}$ , where  $f_{\sigma}$  is frequency associated to the peak appearing in  $M''$  plot. It is observed that the peak shifts towards higher frequency with the increase of ion fluence thereby decreasing the conductivity relaxation time. It can be explained on the basis of intercalation/exfoliation of MMT layers with irradiation fluence.

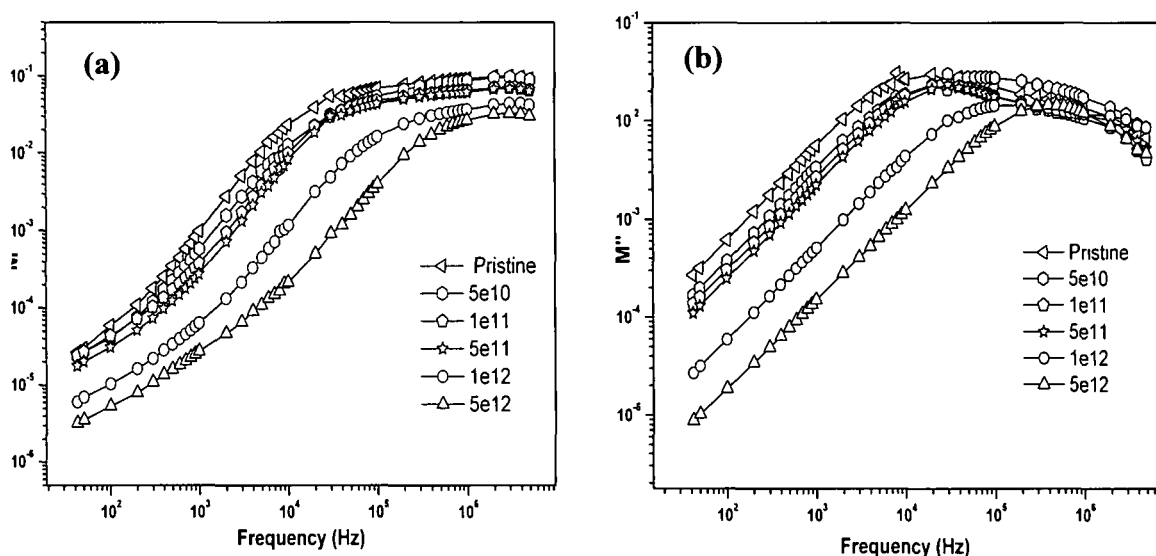


**Figure 7.16:** Real (a) and imaginary (b) part of electrical modulus of PEO-20 wt. % MMT irradiated with different ion fluence.

As exfoliation proceeds with irradiation, nano-size silicate flakes present an ever-expanding polymer/clay interface area that increases the internal capacitance of the composite where conducting ions can accumulate. Silicate flakes act as nanocapacitors in the melt polymer. In general, the MW relaxation time can be viewed as an electrical  $RC$  time constant where  $R$  is the resistance of the polymer matrix and  $C$  is the capacitance of the silicate particle. The decrease of  $\tau_{\sigma}$  value with increase of ion fluence in PEO-MMT



nanocomposites suggest that the dynamics of the films increases, which may be due to the extent of clay exfoliation in dynamic equilibrium [371].

### 7.2.6 FTIR Analysis

The FTIR spectra of pure MMT, pure PEO and PEO-MMT nanocomposites with different irradiation fluence are shown in figure 7.17. It is well known that free water molecules exist in the gallery of clay platelets and OH groups are present on the surface of clay [372]. Two different absorption bands at 2910 and 2852  $\text{cm}^{-1}$  are ascribed to O–H groups of MMT. The appearance of absorption bands (Figure 7.17a) at 1040  $\text{cm}^{-1}$  is attributed to Si–O bending modes. In FTIR spectrum of pure PEO (Figure 7.17b) the bands at 2918  $\text{cm}^{-1}$  and 2884  $\text{cm}^{-1}$  correspond to asymmetric and symmetric  $\text{CH}_2$  stretching vibration, respectively. These two bands show lower intensity in ion irradiated PEO-MMT nanocomposites. The peaks appearing at 1470  $\text{cm}^{-1}$  and 1353  $\text{cm}^{-1}$  in pure PEO correspond to asymmetric  $\text{CH}_2$  bending and symmetric  $\text{CH}_2$  wagging vibration, respectively. It is well known that the frequency, width, and intensity of these  $\text{CH}_2$  vibrations are sensitive to the intermolecular interactions and the conformational changes of the polymer backbone [373]. With the increase of irradiation fluence, the intensity of these two peaks decreases sharply, which could be attributed to the ion dipole interactions between the ether-oxygen of PEO and the interlayer cations of MMT [373]. This is further confirmed by the shifting of the band at 1638  $\text{cm}^{-1}$  of pure PEO towards lower frequency. The two bands at 1295  $\text{cm}^{-1}$  and 1252  $\text{cm}^{-1}$  corresponding to twisting vibration  $t(\text{CH}_2)_a$  and stretching vibration  $\nu(\text{C-O-C})_a$ , respectively decrease in intensity at lower fluence while these two peaks are completely absent in the sample irradiated with the highest fluence used. The bending of (C-O-C) of pure PEO is observed at 1104  $\text{cm}^{-1}$ . With the increase of irradiation fluence a broad distorted band centered at 1085  $\text{cm}^{-1}$  is observed indicating that significant interactions take place between oxygen and interlayer cations in MMT [374]. This suggests enhanced intercalation of PEO in MMT galleries with the increase in irradiation fluence leading to exfoliation at higher fluence. These results are in conformity with XRD results.

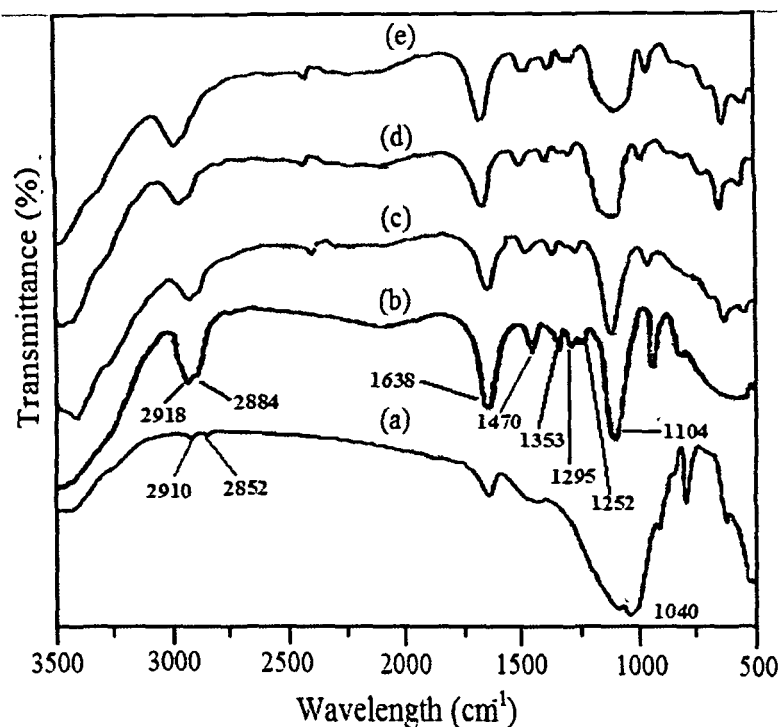


**Figure 7.17:** FTIR spectra of (a) pure MMT, (b) pure PEO and PEO-20 wt.% MMT films irradiated with fluence (c) 0, (d)  $1 \times 10^{11}$  and (e)  $5 \times 10^{12}$  ions/cm<sup>2</sup>.

### 7.3 Summary

90 MeV  $O^{7+}$  ion irradiation effects on P(VdF-HFP)-(PC+DEC)-LiClO<sub>4</sub>-dedoped PANi nanofibers composite gel polymer electrolytes and PEO-MMT single ion conductor have been investigated. In case of P(VdF-HFP)-(PC+DEC)-LiClO<sub>4</sub>-dedoped PANi nanofibers composite gel polymer electrolytes ac impedance analysis shows that the ionic conductivity of the nanocomposite gel polymer electrolytes increases with increasing ion fluence up to  $10^{11}$  ions/cm<sup>2</sup>. This has been attributed to the chain scissioning of polymer, which leads to faster ionic transport through the polymer matrix due to increased amorphicity assisted by larger segmental motion of the polymer backbone. At higher fluence ( $> 10^{11}$  ions/cm<sup>2</sup>) PANi nanofibers get phase separated out from the polymer electrolytes as revealed by XRD, DSC and dielectric loss spectra studies, leading to decrease in ionic conductivity.. SEM results show increase in porosity with uniformly dispersed pores, resulting in better connectivity of the liquid electrolytes through the polymer giving rise to higher ionic conductivity.

On the other hand swift heavy ion irradiation on PEO-MMT nanocomposites results in intercalation of PEO chains at lower fluence and exfoliation above a critical fluence. This has been explained on the basis of shifting and disappearance of (001) diffraction peak of MMT in XRD patterns. Strain calculation reveals that the compressive strain increases with the increase of ion fluence, which ultimately leads to the exfoliation of MMT layers. About 1.5 orders of magnitude enhancement in ionic conductivity has been observed for the sample irradiated with the fluence of  $5 \times 10^{12}$  ions/cm<sup>2</sup> as compared to that of the unirradiated sample as observed from ac impedance spectroscopy. Ionic conductivity enhancement has been attributed to the higher intercalation of PEO chains, which results in the increased interaction between Na<sup>+</sup> cation and oxygen atom in PEO. At low frequency, the variation of dielectric constant with frequency shows the presence of material-electrode interface polarization processes. The loss tangent peaks appearing at a characteristic frequency suggest the presence of relaxing dipoles in PEO-MMT nanocomposites. FTIR analysis confirmed that a strong interaction takes place between the ether oxygen of PEO and interlayer Na<sup>+</sup> cation of MMT.

## CHAPTER VIII

### *Conclusions and Future Prospects*

---

---

*This chapter outlines the main conclusions drawn from the present study, which deals with the synthesis and characterization of nanofibers reinforced and layered silicate nanocomposites gel polymer electrolytes with four polymers, viz. poly(ethylene oxide) (PEO), poly(methyl methacrylate) (PMMA), poly(vinylidene fluoride) (PVdF) and poly(vinylidene fluoride-co-hexafluoropropylene) [P(VdF-HFP)]. The effects of 90 MeV  $O^{7+}$  ion beam irradiation on both types of nanocomposites electrolytes have also been investigated. The chapter also presents the future prospects of research in this area.*

---

---

#### 8.1 Conclusions

The present thesis puts forth the various aspects involved in developing high ion conducting nanocomposites gel polymer electrolytes. The main conclusions drawn from different polymer electrolyte systems investigated in the present work are given below:

##### *[PMMA/ P(VdF-HFP)] based Nanocomposites Gel Polymer Electrolytes Dispersed with Dedoped (Insulating) PANi Nanofibers*

- (1) Dedoped polyaniline (PANi) nanofibers can be affectively used as filler to increase the ionic conductivity of gel polymer electrolytes. Maximum room temperature ionic conductivity for PMMA–(PC + DEC)–LiClO<sub>4</sub>–4 wt. % dedoped PANi nanofibers and P(VdF-HFP)–(PC + DEC)–LiClO<sub>4</sub>–6 wt. % dedoped PANi nanofiber is found to be  $2.1 \times 10^{-3} \text{ Scm}^{-1}$  and  $6.31 \times 10^{-3} \text{ Scm}^{-1}$ , respectively. Addition of high aspect ratio (> 50) PANi nanofibers results in the reduction of polymer crystallinity due to the prevention of chain reorganization leading to higher ionic conductivity. However, at higher filler content [ $> 4$  wt. % for PMMA and 6 wt. % for P(VdF-HFP)] a decreasing trend of ionic conductivity is observed due to the phase separation of PANi nanofibers, which form insulating clusters that encumber ion movement.
- (2) SEM results show that PANi nanofibers remarkably increase the pore density and widens the porous structure of the polymer electrolytes. This has been attributed to the fact that the dedoped nanofibers try to occupy the pores in the gel polymer electrolyte and in the process pore distribution becomes denser. Highly porous

structure leads to better connectivity of the liquid electrolyte through the pores accounting for the increase in ionic conductivity.

- (3) The interfacial stability and electrochemical potential window of the nanofibers dispersed polymer gel electrolyte membranes are observed to be higher than that of gel polymer electrolytes without nanofibers. The increase of interfacial stability due to the addition of PANi nanofibers is attributed to the fact that when nanofibers is added passivation of polymer electrolyte due to reaction with electrode material decreases. High aspect ratio (>50) nanofibers get accumulated on the surface of the electrode and effectively impede the electrode–electrolyte reaction.

#### ***PEO/P(VdF-HFP) Blend based Microporous Gel and Nanocomposite Polymer Electrolytes***

- (4) The blend based microporous membranes based on PEO-P(VdF-HFP) prepared by phased inversion technique show that the addition of PEO improved the pore configuration, such as pore size, pore connectivity and porosity of P(VdF-HFP) based membranes. The room temperature ionic conductivity was significantly enhanced. The highest porosity of about 65 % and ionic conductivity of about  $7 \times 10^{-4} \text{ Scm}^{-1}$  is obtained when the weight ratio of PEO was 40 wt. %. The liquid electrolyte uptake was found to increase with increase in porosity and pore size. However at higher weight ratio of PEO (> 40%) porosity, pore size and ionic conductivity were decreased. This descending trend with further increase of PEO weight ratio was attributed to conglomeration effect of PEO at the pores. Beyond 40 wt. % of PEO conglomeration takes place, which decreases the pore size as observed in SEM results. The conglomeration effect predominates at higher concentration of PEO and as a result ionic conductivity, porosity and liquid electrolyte uptake follow a descending trend.
- (5) Addition of dedoped PANi nanofibers in PEO-P(VdF-HFP)-LiClO<sub>4</sub> blend system results in significant enhancement of ionic conductivity up to 6 wt. % of PANi fraction as revealed by ac impedance analysis. Lewis acid-base interaction plays a dominant role in this case. The oxygen atom in PEO has two lone pair of electrons and nitrogen atom in PANi nanofibers has one lone pair of electrons, which act as

strong Lewis base centers and  $\text{Li}^+$  cations as strong Lewis acid giving rise to three types of Lewis acid-base complexes in the composite polymer electrolyte. First type of complexes involve PEO- $\text{Li}^+$ -PEO interaction, which leads to the transient cross-linking of PEO chains via  $\text{Li}^+$  cations resulting in the reduction of ionic conductivity. Second type of interaction is due to mixed PEO- $\text{Li}^+$ -PAni nanofibers complexes, which involves Lewis base oxygen from PEO chain and Lewis base nitrogen from polyaniline. The third type of interaction involves only the Lewis base nitrogen from polyaniline and  $\text{Li}^+$  cations. The formation of second and third type of complexes leads to lowering of concentration of first type of complexes and hence density of transient cross-linking is reduced. This allows mobile ions to move more freely either on the surface of the nanofibers or through a low-density polymer phase at the interface, which results in enhanced ionic conductivity. In addition reduction of crystallinity due to the dispersion of PAni nanofibers and creation of polymer filler interface also results in the enhancement of ionic conductivity in PEO-P(VdF-HFP)- $\text{LiClO}_4$  system.

- (6) SEM studies reveal two-phase morphology above 6 wt. % nanofibers indicating the phase separation of polyaniline nanofibers. FTIR spectra also confirm the phase separation at nanofibers fraction greater than 6 wt. % showing peaks for dedoped PAni nanofibers at their assigned positions. The interfacial stability of the nanofibers dispersed composite polymer electrolytes is observed to be better than that of PEO-P(VdF-HFP)- $\text{LiClO}_4$  and PEO- $\text{LiClO}_4$ .

#### ***[PMMA/ P(VdF-HFP)] / MMT based Nanocomposite Gel Polymer Electrolytes***

- (7) Organically modified MMT clays have been employed to modify the electrical and electrochemical properties of PMMA and PVdF based gel electrolytes. The insertion of polymer chains into the galleries of MMT showed enhancement in the  $d$ -spacing as revealed by XRD and TEM results. Intercalation of PVdF into the galleries of MMT also results in the formation of  $\beta$  phase of PVdF.  $\alpha$  to  $\beta$  phase formation of PVdF upon inclusion of MMT can be explained on the basis of stretching of PVdF chains during intercalation into the galleries of MMT. Thermodynamically a decrease in the

Gibbs free energy ( $\Delta G$ ) is required for the overall intercalation process. The driving force for direct polymer intercalation from solution is the entropy gained by desorption of solvent molecules, which compensates for the entropy decrease of confined, intercalated chains. On the other hand, the conformational energy cost of stretching the chains resulting in the formation of  $\beta$  phase in addition to the topographical constraints and the adsorption on the surfaces are expected to impose severe limitations on diffusion of chains diffusing in a pseudo-two dimensional slit. From ac impedance spectroscopy it has been shown that the ionic conductivity of the nanocomposite gel polymer electrolytes increases with increase in clay loading and exhibits a maximum value of  $1.3 \times 10^{-3} \text{ Scm}^{-1}$  for PMMA-based nanocomposite electrolytes, whereas a slightly higher value of  $2.3 \times 10^{-3} \text{ Scm}^{-1}$  has been found in case of PVdF-based electrolytes at room temperature. This has been attributed mainly to the higher liquid electrolyte uptake by the nanocomposite films. Higher uptake of liquid electrolytes by the nanocomposite films results in increase in the number of charge carriers at the same volume leading to higher ionic conductivity. In case of PVdF based systems the formation of  $\beta$ -PVdF due to which all the fluorine atoms are oriented on the same side of the chain and with the hydrogen atoms on the opposite side. This change in conformation will force all the H atoms to be oriented upwards inside the gallery because of their interaction with negatively charged clay platelets. Negatively charged F-ions will be oriented downwards and lithium ion mobility is expected to be higher along the interface lining the F atoms, which results in increase in the ionic conductivity in this case.

- (8) The cationic charges on the surface of MMT act as Lewis acid centers and compete with  $\text{Li}^+$  cations (strong Lewis acid) to form complexes with the polymer host. This in turn may result in: (a) structural modifications and promotion of  $\text{Li}^+$ -conducting pathways at the surface of filler, and (b) the lowering ionic coupling, which promotes the salt dissociation as revealed by FTIR. Addition of MMT clays in polymers not only reduces the interfacial resistance with electrode material but also provides larger electrochemical stability window.

***Swift Heavy Ion Irradiation Effects on Nanofiber Reinforced and Layered Silicate Nanocomposite Electrolytes***

- (9) Swift heavy ion  $O^{7+}$  irradiation effects on the ionic conduction in P(VdF-HFP)-(PC+DEC)-LiClO<sub>4</sub>-6 wt. % dedoped PANi nanofibers and PEO-MMT single Na<sup>+</sup> ion conductor have been studied extensively in the present work. In case of P(VdF-HFP)-(PC+DEC)-LiClO<sub>4</sub>-dedoped PANi nanofibers composite gel polymer electrolytes ac impedance analysis shows that the ionic conductivity of the nanocomposite gel polymer electrolytes increases with increasing ion fluence up to  $10^{11}$  ions/cm<sup>2</sup>. This has been attributed to the chain scissioning of polymer, which leads to faster ionic transport through the polymer matrix due to increased amorphicity assisted by larger segmental motion of the polymer backbone. As fluence increases radical concentration increases resulting in the formation of closely spaced radicals along the ion track. As a result coercive interaction among the radical pairs increases, which eventually allow the adjacent polymer chains to cross-link leading to decrease in ionic conductivity. XRD results show that above  $10^{11}$  ions/cm<sup>2</sup>, the PANi nanofibers peak at  $2\theta=23^\circ$  reappears indicating the phase separation PANi nanofibers at higher fluence ( $>10^{11}$  ions/cm<sup>2</sup>). The phase separation phenomenon at higher fluence has been further confirmed by DSC and dielectric loss spectra studies.
- (10) SEM results show that upon irradiation with lower fluence ( $10^{11}$  ions/cm<sup>2</sup>) the porous structure becomes much denser with well dispersed pores, which leads to better connectivity of the liquid electrolyte through the pores accounting for the increase in ionic conductivity. On the other hand, at higher fluence ( $>10^{11}$  ions/cm<sup>2</sup>) irradiation the porous structure is disrupted possibly due to recrystallization of the polymer chains. Study of volume occupation ( $V_p$ ) reveals that porosity increases (i.e.  $V_p$  decreases) as a function of ion fluence up to  $10^{11}$  ions/cm<sup>2</sup>, which results in entrapment of more liquid electrolyte in the pores giving rise to increase in ionic conductivity. At higher fluence ( $>10^{11}$  ions/cm<sup>2</sup>) porosity decreases probably due to recrystallization of polymer exuding the liquid electrolyte out of the pores resulting in the decrease in the conductivity.
- (11) Swift heavy ion irradiation on PEO-20 wt. % MMT nanocomposites results in intercalation of PEO chains at lower fluence and exfoliation above a critical fluence.



This has been explained on the basis of shifting and disappearance of (001) diffraction peak of MMT in XRD patterns. Strain calculation reveals that the compressive strain increases with the increase of ion fluence, which ultimately leads to the exfoliation of MMT layers. Maximum conductivity was found to be  $5 \times 10^{-6} \text{ Scm}^{-1}$  at room temperature for the highest fluence, which is significantly higher as compared to that for the pristine polymer electrolyte ( $9.27 \times 10^{-8} \text{ Scm}^{-1}$ ). With the increase of intercalation of PEO chains inside the galleries of MMT results in the increase of interaction between  $\text{Na}^+$  cation and oxygen heteroatom leading to the increase in ionic conductivity in the composites. Surface morphology and interactions among the various constituents in the nanocomposites at different fluence have been examined by SEM and FTIR, respectively. At low frequency, the variation of dielectric constant with frequency shows the presence of material-electrode interface polarization processes. The loss tangent peaks appearing at a characteristic frequency suggest the presence of relaxing dipoles in PEO-MMT nanocomposites. FTIR analysis depicts a strong interaction between the ether oxygen of PEO and interlayer  $\text{Na}^+$  cation of MMT.

## 8.2 Future Prospects

There is an enormous scope of further development of high ion conducting polymer electrolyte materials and fabrication of electrochemical devices such as high energy density lithium ion batteries, supercapacitors, sensors etc. using them. In lithium ion batteries undesired reactions between the battery components and the liquid organic electrolyte coupled with unpredictable events such as short circuits or local overheating lead to an exothermic reaction of the electrolyte with the electrode materials, producing a rapid increase of the battery temperature, eventually leading to fire or explosion. Keeping this prospect in view ionic-liquid based lithium-ion-conducting polymer electrolytes may greatly reduce the risk of thermal runaway since ionic liquids are practically non-flammable. This provides the lithium battery with the level of safety that is required for their large-scale application. Extensive work for testing of ionic liquids as new electrolyte media for the future is in progress worldwide. In polymer electrolytes both cations and anions contribute to the overall conductivity, where not only lithium ions but also their

counter ions migrate during the charging and discharging processes of a battery. This causes concentration polarization caused by accumulation of anions on the anode leading to the premature battery failure. Intensive research on single cationic polymer electrolytes is going on, but researchers are far away from the achieving goal. Research in this field has tremendous potential. Swift heavy ion irradiation on nanocomposites polymer electrolytes has great prospects for enhancing their properties and is a potential research field both from theoretical and applied points of views.

## References

---

- [1] Faraday, M., *Experimental Investigations in Electricity*, B. Quaritch, London, 1839.
- [2] Fergus, J.W., Ceramic and polymeric solid electrolytes for lithium-ion batteries, *J. Power Sources* **195**, 4554–4569, 2010.
- [3] Agrawal, R.C., & Pandey, G.P., Solid polymer electrolytes: materials designing and all-solid-state battery applications: an overview, *J. Phys. D: Appl. Phys.* **41**, 223001-223018, 2008.
- [4] Stephan, A.M., Review on gel polymer electrolytes for lithium batteries, *Eur. Polym. J.* **42**, 21-42, 2006.
- [5] Song, J.Y., et al., Review of gel-type polymer electrolytes for lithium-ion batteries, *J. Power Sources*, **77**, 183-197, 1999.
- [6] Fenton, B.E., et al., Complexes of alkali metal ions with poly(ethylene oxide), *Polymer* **14**, 589, 1973.
- [7] Armand, M.B., Chabagno, J.M., & Duclot, M.J., Polymer solid electrolytes, in Second International Conference on Solid Electrolytes (paper 6.5), St. Andrews, 1978.
- [8] Armand, M.B., Chabagno, J.M., & Duclot, M.J., in *Fast Ion Transport in Solids*, P. Vashishta, et al., eds., Elsevier, North Holland, New York, 1979, 131.
- [9] Gray, F.M., *Polymer Electrolytes: Fundamentals and Technological Applications*, VCH, New York, 1991.
- [10] MacCallum, J.R., & Vincent, C.A. (ed.), *Polymer Electrolyte Reviews*, vol I, II, Elsevier Applied Sciences, London, 1987–1989.
- [11] Bruce, P.G. (ed.), *Solid State Electrochemistry*, Cambridge University Press, Cambridge, 1995.
- [12] Scrosati, B. (ed.), *Applications of Electroactive Polymers*, Chapman and Hall, London 1993.
- [13] Alamgir, M., & Abraham, K.M., in *Lithium Batteries: New Materials, Developments and Perspectives*, G. Pistoia, ed., Elsevier, Amsterdam, 1994, 93.

- [14] Meyer, W.H., Polymer electrolytes for lithium-ion batteries *Adv. Mater.* **10**, 439-448 1998.
- [15] Golodnitsky, D., et al., Conduction mechanisms in concentrated LiI-P(EO)<sub>n</sub>-Al<sub>2</sub>O<sub>3</sub>-based electrolytes, *J. Electrochem. Soc.* **144**, 1997, 3484-3491.
- [16] Dai, Y., et al., Electrical, thermal and NMR investigation of composite solid electrolytes based on PEO, LiI and high surface area inorganic oxides, *Electrochim. Acta.* **43**, 1557-1561, 1998.
- [17] Stephan, A.M., & Nahm, K.S., Review on composite polymer electrolytes for lithium batteries, *Polymer* **47**, 5952-5964, 2005.
- [18] Lee, C.C., & Wright, P.V., Morphology and ionic conductivity of complexes of sodium iodide and sodium thiocyanate with poly(ethylene oxide), *Polymer* **23**, 681-689, 1982.
- [19] Payne, D.R., & Wright, P.V., Morphology and ionic conductivity of some lithium ion complexes with poly(ethylene oxide), *Polymer* **23**, 690-693, 1982.
- [20] Killis, A., et al., Mise en evidence experimentale de l'importance de la temperature de transition vitreuse sur la conductivite ionique des reseaux macromoleculaires, *Makromol. Chem., Rapid Commun.* **1** 595-598, 1980.
- [21] Berthier, C., et al., Microscopic investigation of ionic conductivity in alkali metal salts-poly(ethylene oxide) adducts, *Solid State Ionics* **11**, 91-95 1983.
- [22] Blonsky, P.M., et al., Polyphosphazene solid electrolytes, *J. Am. Chem. Soc.* **106**, 6854-6855, 1984.
- [23] Bannister, D.J., et al., Ionic conductivities of poly(methoxy polyethylene glycol monomethacrylate) complexes with LiSO<sub>3</sub>CH<sub>3</sub>, *Polymer* **25**, 1600-1602, 1984.
- [24] Nicholas, C.V., et al., Improved synthesis of oxymethylene-linked poly(oxyethylene) *Br. Polym. J.* **20**, 289-292-1988.
- [25] Ratner, M.A., & Nitzan, A., Conductivity in polymer ionics. Dynamic disorder and correlation, *Faraday Discuss. Chem. Soc.* **88**, 19-42, 1989.
- [26] Angell, C.A., Fast ion motion in glassy and amorphous materials, *Solid State Ionics* **9-10**, 3-16, 1983.
- [27] Torrel, L.M., & Angell, C.A., Ion matrix coupling in polymer electrolytes from relaxation time studies, *Br. Polym. J.* **20**, 173-179, 1988.

- [28] Cheradame, H., In: *IUPAC Macromolecules*, H. Benoit and P. Rempp eds., Pergamon, New York, 1982, 351.
- [29] Watanabe, M., & Ogata, N., In: *Polymer Electrolytes Reviews I*, J.R. MacCallum and C.A. Vincent eds., Elsevier, London, 1987, 39.
- [30]. Yamamoto, T. et al., 4.4 V lithium-ion polymer batteries with a chemical stable gel electrolyte, *J. Power Sources* **174**, 1036-1040, 2007.
- [31] Killis, A., et al., Correlation among transport properties in ionically conducting cross-linked networks, *Solid State Ionics* **14**, 231-237, 1984.
- [32] Hall, P.G., et al., Ion conductivity in polysiloxane comb polymers with ethylene glycol teeth, *Polym. Commun.* **27**, 98-100, 1986.
- [33] Nishimoto, J., Furuya, N., & Watanabe, M., in: *Extended Abstracts of 62<sup>th</sup> Meeting of Japanese Electrochemical Society*, 3J12, 1995.
- [34] Vallee, A., et al., Comparative study of poly(ethylene oxide) electrolytes made with  $\text{LiN}(\text{CF}_3\text{SO}_2)_2$ ,  $\text{LiCF}_3\text{SO}_3$  and  $\text{LiClO}_4$ : Thermal properties and conductivity behaviour, *Electrochim. Acta* **37**, 1579-1583, 1992.
- [35] Benrabah, D., et al., Perfluorosulfonate-polyether based single ion conductors, *Electrochim. Acta* **40**, 2259-2264, 1995.
- [36] Fujinami, T., Siloxyaluminate polymers with high  $\text{Li}^+$  ion conductivity, *Chem. Mater.* **9**, 2236-2239, 1997.
- [37] Angell, C.A., et al., Rubbery solid electrolytes with dominant cationic transport and high ambient conductivity, *Nature* **362**, 137-139, 1993.
- [38] Ito, Y., et al., Ionic conductivity of electrolytes formed from PEO- $\text{LiCF}_3\text{SO}_3$  complex low molecular weight poly(ethylene glycol), *J. Mater. Sci.* **22**, 1845-1849, 1987.
- [39] Sander, B., et al., Solid polymer electrolytes based on oligo(ethylene glycol)methacrylates, *Polym. Bull.* **28**, 355- 360, 1992.
- [40] Nagasubramanian, G., & Di Stefano, S., 12-Crown-4 ether-assisted enhancement of ionic conductivity and interfacial kinetics in polyethylene oxide electrolytes, *J Electrochem. Soc.* **137**, 3830-3835, 1990.

- [41] Shodai, T., et al., Thermal stability of the polymer electrolyte (PEO)<sub>8</sub>LiCF<sub>3</sub>SO<sub>3</sub>. *J. Electrochem. Soc.* **141**, 2978-2981, 1994.
- [42] Benedict, T.J., et al., Characterization of plasticized solid polymer electrolyte by XRD and AC impedance methods, *J. Power Sources* **75**, 171-174, 1998.
- [43] Kovac, M., et al., The effect of plasticizer on the microstructural and electrochemical properties of a (PEO)<sub>n</sub>LiAl(SO<sub>3</sub>Cl)<sub>4</sub> system, *Electrochim. Acta* **44**, 863-870, 1998.
- [44] Itoh, T., et al., Solid polymer electrolytes based on comblike polymers, *J. Power Sources* **163**, 252-257, 2006.
- [45] Bhide, A., & Hariharan, K., Ionic transport studies on (PEO)<sub>6</sub>:NaPO<sub>3</sub> polymer electrolyte plasticized with PEG<sub>400</sub>, *Eur. Polym. J.* **43**, 4253-4270, 2007.
- [46] Tien, C.P., et al., Electric double layer capacitors with gelled polymer electrolytes based on poly(ethylene oxide) cured with poly(propylene oxide) diamines, *Electrochimica Acta* **53**, 4505-4511, (2008).
- [47] Li, Y., et al., Conductive performances of solid polymer electrolyte films based on PVB/LiClO<sub>4</sub> plasticized by PEG<sub>200</sub>, PEG<sub>400</sub> and PEG<sub>600</sub>, *J. Power Sources* **187**, 305-311, 2009.
- [48] Watanabe, M., et al., Ionic conductivity of hybrid films based on polyacrylonitrile and their battery application, *J. Appl. Polym. Sci.* **27**, 4191-4198, 1982.
- [49] Watanabe, M., et al., Ionic conductivity of hybrid films composed of polyacrylonitrile, ethylene carbonate, and LiClO<sub>4</sub>, *J. Polym. Sci. Part B: Polym. Phys.* **21**, 939-948, 1983.
- [50] Abraham, K.M., & Alamgir, M., Li<sup>+</sup>-conductive solid polymer electrolytes with liquid-like conductivity, *J. Electrochem. Soc.* **137**, 1657-1658, 1990.
- [51] Abraham, K.M., & Alamgir, M., *Solid electrolytes*, **US Patent No. 5219679**, June 15, 1993.
- [52] Peraninage, D., et al. PAN based electrolyte with ternary solvent mixtures as plasticizers, *J. Electrochem. Soc.* **142**, 1789, 1995.
- [53] Choe, H.S., et al., Characterization of some polyacrylonitrile based Electrolytes *Chem. Mater.* **9**, 369-379, 1997.
- [54] Starkey, S.R., & Frech, R., Plasticizer interactions with polymer and salt in propylene carbonate-poly(acrylonitrile)-lithium triflate, *Electrochim. Acta.* **42**, 471-474, 1997.

- [55] Appetecchi, G.B., & Scrosati, B., A lithium ion polymer battery, *Electrochim. Acta* **43**, 1105-1107, 1998.
- [56] Sun, Y.-K., & Jin, S.H., Synthesis and electrochemical characteristics of spinel phase  $\text{LiMn}_2\text{O}_4$ -based cathode materials for lithium polymer batteries, *J. Mater. Chem.* **8**, 2399-2404, 1998.
- [57] Dissanayake, M.A.K.L., et al., A novel gel polymer electrolyte based on polyacrylonitrile (PAN) and its application in a solar cell, *Materials Research Bulletin* **37**, 867-874, 2002.
- [58] Jayathilaka, P.A.R.D., et al., Dielectric relaxation, ionic conductivity and thermal studies of the gel polymer electrolyte system PAN/EC/PC/LiTFSI, *Solid State Ionics* **156**, 179– 195, 2003.
- [59] Carol, P., et al., Preparation and characterization of electrospun poly(acrylonitrile) fibrous membrane based gel polymer electrolytes for lithium-ion batteries, *J. Power Sources* **196**, 10156– 10162, 2011.
- [60] Iijima, T., et al., Quasi-solid organic electrolytes gelatinized with poly methylmethacrylate and their applications for lithium batteries, *Denki Kagaku* **53**, 619-622, 1985.
- [61] Bohnke, O., et al., Gel electrolyte for solid-state electrochromic cell, *J. Electrochem. Soc.* **139**, 1862-1865, 1992.
- [62] Bohnke, O., et al., Fast ion transport in new lithium electrolytes gelled with PMMA. 2. Influence of lithium salt concentration, *Solid State Ionics* **66**, 105-112, 1993.
- [63] Stallworth, P.E., et al., Lithium-7 NMR and ionic conductivity studies of gel electrolytes based on poly(methylmethacrylate), *Electrochim. Acta.* **40**, 2137-2141, 1995.
- [64] Vondrak, J.M., et al., Gel polymer electrolytes based on PMMA, *Electrochim. Acta* **46**, 2047-2048, 2001.
- [65] Rajendran, S., & Uma, T., Conductivity studies on PVC/PMMA polymer blend electrolyte, *Mater. Lett.* **44**, 242-247, 2000.
- [66] Rajendran, S., et al., An electrochemical investigation on PMMA/PVdF blend-based polymer electrolytes, *Mater. Lett.* **49**, 172-179, 2001.

- [67] Kim, C.S., & Oh, S.M., Spectroscopic and electrochemical studies of PMMA-based gel polymer electrolytes modified with interpenetrating networks, *J. Power Sources* **109**, 98–104, 2002.
- [68] Hashmi, S.A., et al., Experimental studies on poly methyl methacrylate based gel polymer electrolytes for application in electrical double layer capacitors, *J. Phys. D: Appl. Phys.* **40**, 6527–6534, 2007.
- [69] Osman, Z. et al., AC ionic conductivity and DC polarization method of lithium ion transport in PMMA–LiBF<sub>4</sub> gel polymer electrolytes, *Results in Physics* **2**, 1-4, 2012.
- [70] Watanabe, M., et al., High lithium ion conductivity of polymeric solid electrolytes, *Makromol. Chem. Rapid. Commun.* **2**, 741-744, 1981.
- [71] Ohno, H., et al., Demonstration of solid-state cell based on poly(vinylidene fluoride) system containing lithium perchlorate, *Polym. Bull.* **7**, 271-275, 1982.
- [72] Tsuchida, E., et al., Conduction of lithium ions in polyvinylidene fluoride and its derivatives, *Electrochim. Acta.* **28**, 591-595, 1983.
- [73] Choe, H.S., et al., Preparation and characterization of poly(vinyl sulfone)- and poly(vinylidene fluoride)-based electrolytes, *Electrochim. Acta* **40**, 2289-2293, 1995.
- [74] Jiang, Z., et al., Studies of some poly(vinylidene fluoride) electrolytes, *Electrochim. Acta* **42**, 2667-2677, 1997.
- [75] Alex Shiao, H.C., et al., Low temperature electrolytes for Li-ion PVDF cells, *J. Power Sources* **87**, 167-173, 2000.
- [76] Mohamed, N.S., & Arof, A.K., Investigation of electrical and electrochemical properties of PVDF-based polymer electrolytes, *J. Power Sources* **132**, 229-234, 2004.
- [77] Choi, S.W., et al., Characterization of electrospun PVdF fiber-based polymer electrolytes, *Chem. Mater.* **19**, 104-115, 2007.
- [78] Rajendran, S, & Sivkaumar, P., An investigation of PVdF/PVC-based blend electrolytes with EC/PC as plasticizers in lithium battery applications, *Physica B* **403**, 509–516, 2008.
- [79] Capiglia, C., et al., Structure and transport properties of polymer gel electrolytes based on PVdF-HFP and LiN(C<sub>2</sub>F<sub>5</sub>SO<sub>2</sub>)<sub>2</sub>, *Solid State Ionics* **131**, 291-299, 2001.



- [80] Stephan, A.M. et al., Characterization of poly(vinylidene fluoride–hexafluoropropylene) (PVdF–HFP) electrolytes complexed with different lithium salts, *Eur. Polym. J.* **41**, 15-21, 2005.
- [81] Saikia, D., & Kumar, A., Ionic conduction in P(VDF-HFP)/PVDF–(PC + DEC)–LiClO<sub>4</sub> polymer gel electrolytes, *Electrochim. Acta* **49**, 2581-2589, 2004.
- [82] Ren, Z., et al., Polymer electrolytes based on poly(vinylidene fluoride-co-hexafluoropropylene) with crosslinked poly(ethylene glycol) for lithium batteries, *Solid State Ionics* **180**, 693–697, 2009.
- [83] Lalia, B.S. et al., Electrochemical performance of non-flammable polymeric gel electrolyte containing triethylphosphate, *J. Power Sources* **186**, 211-215, 2009.
- [84] Tarascon, J.M., et al., Performance of Bellcore's plastic rechargeable Li-ion batteries, *Solid State Ionics* **86-88**, 49-54, 1996.
- [85] Gozdz, A.S., Chmutz, C.N., Tarascon, J.M., & Warren, P.C., *Lithium secondary battery extraction method*, **US patent No. 5540741**, July 30, 1997.
- [86] Saito, Y., et al., Ionic conduction mechanisms of lithium gel polymer electrolytes investigated by the conductivity and diffusion coefficient, *Solid State Ionics* **160**, 149-153, 2003.
- [87] Stephan, A.M., et al., Cycling behavior of poly(vinylidene fluoride-hexafluoropropylene) (PVdF-HFP) membranes prepared by phase inversion method, *Mater. Chem. Phys.* **85**, 6-11, 2004.
- [88] Hwang, Y.J., et al., Electrochemical studies on poly(vinylidene fluoride–hexafluoropropylene) membranes prepared by phase inversion method, *Eur. Polym. J.* **43**, 65–71, 2007.
- [89] Xiao, Q, et al., Microporous polymer electrolytes based on PVdF/PEO-b-PMMA block copolymer blends for rechargeable lithium battery, *J. Membr. Sci.* **334**, 117-122, 2009.
- [90] Arvindan, V. et al., Improved performance of polyvinylidene fluoride hexafluoropropylene based nanocomposite polymer membranes containing lithium bis(oxalato)borate by phase inversion for lithium batteries, *Solid State Sciences* **13**, 1047-1051, 2011.

- [91] Dias, F.B., et al., Trends in polymer electrolytes for secondary lithium batteries, *J. Power Sources* **88**, 169-191, 2000.
- [92] Weston, J.E., & Steele, B.C.H., Effects of inert fillers on the mechanical and electrochemical properties of lithium salt-poly(ethylene oxide) polymer electrolytes, *Solid State Ionics* **7**, 75-79, 1982.
- [93] Liquan, C., in *Materials for Solid State Batteries*, Eds: B. Chowdari and S. Radhakrishna eds., World Scientific, Singapore, 1988, 69.
- [94] Wieczorek, W., Such, K., Plochanski, J., & Przulski, J., in: *Second International Symposium on Polymer Electrolytes*, B. Scrosati ed., Elsevier, Amsterdam, 1990, 339.
- [95] Capuano, F et al., Composite polymer electrolytes, *J. Electrochem. Soc.* **138**, 1918-1922, 1991.
- [96] Gang, W., et al., Comparison of NMR and conductivity in  $(\text{PEO})_8\text{-LiClO}_4\text{-}\gamma\text{LiAlO}_2$ , *Solid State Ionics* **53-56**, 1202-1205, 1992.
- [97] Appetecchi, G.B., et al., Transport and interfacial properties of composite polymer electrolytes, *Electrochim. Acta* **45**, 1481-1490, 2000.
- [98] Wieczorek, W., et al., Comparison of properties of composite polymeric electrolytes based on the oxymethylene-linked poly(ethylene oxide)  $\text{NaClO}_4$  electrolyte with polyacrylamide or  $\alpha\text{-Al}_2\text{O}_3$  Additives, *J. Phys. Chem.* **98**, 9047-9055, 1994.
- [99] Chandra, A., et al., Ion transport studies in PEO- $\text{NH}_4\text{I}$  polymer electrolytes with dispersed  $\text{Al}_2\text{O}_3$ , *J. Mater. Sci.* **30**, 3633-3638, 1995.
- [100] Li, J., & Khan, I.M, Highly conductive solid polymer electrolytes prepared by blending high molecular weight poly(ethylene oxide), poly(2- or 4-vinylpyridine), and lithium perchlorate, *Macromolecules* **26**, 4544-4550, 1993.
- [101] Zalewska, A., et al., Composite polymeric electrolytes from the PEO-PAAM- $\text{NH}_4\text{SCN}$  system, *J. Phys. Chem.* **100**, 11382-11388, 1996.
- [102] Wieczorek, W., et al., Composite polyether based solid electrolytes. The Lewis acid-base approach, *Solid State Ionics* **85**, 67-72, 1996.
- [103] Wieczorek, W., et al., Polyether, poly(*N,N*-dimethylacrylamide), and  $\text{LiClO}_4$  composite polymeric electrolytes. *Macromolecules* **29**, 143-155, 1996.
- [104] Croce, F. et al., Physical and chemical properties of nanocomposite polymer electrolytes, *J. Phys. Chem. B* **103**, 10632-10638, 1999.

- [105] Croce, F., & Scrosati, B., Nanocomposite lithium ion conducting membranes, *Ann. NY Acad. Sci.* **984**, 194-207, 2003.
- [106] Sun, H.Y., et al., Enhanced lithium-ion transport in PEO-based composite polymer electrolytes with ferroelectric BaTiO<sub>3</sub>, *J. Electrochem. Soc.* **146**, 1672-1676, 1999.
- [107] Sun, H.Y., et al., Ferroelectric materials as a ceramic filler in solid composite polyethylene oxide-based electrolytes, *J. Electrochem Soc.* **147**, 2462-2467, 2000.
- [108] Liu, Y., et al., In situ preparation of poly(ethylene oxide)-SiO<sub>2</sub> composite polymer electrolytes, *J. Power Sources* **129**, 303-311, 2004.
- [109] Panero, S., et al., Ionic conductivity and <sup>7</sup>Li NMR Study of Poly(ethylene glycol) complexed with lithium salts, *Electrochim. Acta* **37**, 1533-1539, 1992.
- [110] Khan, S.A., et al., Composite polymer electrolytes using fumed silica fillers: Rheology and ionic conductivity, *Chem. Mater.* **6**, 2359-2363, 1994.
- [111] Ji, K.S., et al., Role of functional nano-sized inorganic fillers in poly(ethylene) oxide-based polymer electrolytes, *J. Power Sources*, **117**, 124-130, 2003.
- [112] Xi, J., et al., Composite polymer electrolyte doped with mesoporous silica SBA-15 for lithium polymer battery, *Solid State Ionics* **176**, 1249-1260, 2005.
- [113] Nan, C.-W., et al., Enhanced ionic conductivity of polymer electrolytes containing nanocomposite SiO<sub>2</sub> particles, *Phy. Rev. Lett.* **91**, 266104, 2003.
- [114] Kumar, B., & Scanlon, L.G., Polymer-ceramic composite electrolytes, *J. Power Sources* **52**, 261-268, 1994.
- [115] Kumar, B., & Scanlon, L.G., Polymer-ceramic composite electrolytes: conductivity and thermal history effects, *Solid State Ionics* **124**, 239-254, 1999.
- [116] Kumar, B., et al., Ionic conductivity of polymer-ceramic composites, *J. Electrochem. Soc.* **148**, A1191-A1195, 2001.
- [117] Morita, M., et al., Ionic conductance behavior of polymeric composite solid electrolytes containing lithium aluminate, *Electrochim. Acta* **46**, 1565-1569, 2001.
- [118] Bloise, A.C. et al., Nuclear magnetic resonance study of PEO-based composite polymer electrolytes, *Electrochim. Acta* **46**, 1571-1579, 2001.
- [119] Tambelli, C.C., Characterisation of PEO-Al<sub>2</sub>O<sub>3</sub> composite polymer electrolytes, *Electrochim. Acta* **47**, 1677-1682, 2002.

- [120] Chung, S.H., et al., Enhancement of ion transport in polymer electrolytes by addition of nanoscale inorganic oxides, *J. Power Sources* **97–98**, 644-688, 2001.
- [121] Croce, F., et al., Superacid ZrO<sub>2</sub>-added, composite polymer electrolytes with improved transport properties, *Electrochem. Commun.* **8**, 364-368, 2006.
- [122] Croce, F., et al., Advanced, lithium batteries based on high-performance composite polymer electrolytes, *J. Power Sources* **162**, 685-689, 2006.
- [123] Dey, A., et al., Thermal and electric properties of CeO<sub>2</sub> nanoparticles dispersed in polyethylene oxide:NH<sub>4</sub>ClO<sub>4</sub> complex, *Solid State Ionics* **178**, 1963–1968, 2008.
- [124] Fullerton-Shirey, S.K., & Maranas, J.K., Structure and Mobility of PEO/LiClO<sub>4</sub> Solid Polymer Electrolytes Filled with Al<sub>2</sub>O<sub>3</sub> Nanoparticles, *J. Phys. Chem. C* **114**, 9196–9206, 2010.
- [125] Agrawal, R.C., & Mahipal, Y.K., Study of Electrical and Electrochemical Behaviour on Hot-press Synthesized Nano-Composite Polymer Electrolyte (NCPE) Membranes: [(70PEO: 30 KNO<sub>3</sub>) + x SiO<sub>2</sub>], *Int. J. Electrochem. Sci.* **6**, 867 – 881, 2011.
- [126] Stephan, A.M., et al., Chitin-Incorporated Poly(ethylene oxide)-Based Nanocomposite Electrolytes for Lithium Batteries, *J. Phys. Chem. B* **113**, 1963–1971, 2009.
- [127] Chen-Yang, Y.W., et al., Influence of silica aerogel on the properties of polyethylene oxide-based nanocomposite polymer electrolytes for lithium battery, *J. Power Sources* **182**, 340–348, 2008.
- [128] Zhang, J., et al., Effect of surface modified porous inorganic-organic hybrid polyphosphazene nanotubes on the properties of polyethylene oxide based solid polymer electrolytes, *Electrochim. Acta* **55**, 5966–5974, 2010.
- [129] Xi, J., et al., Conductivities and transport properties of microporous molecular sieves doped composite polymer electrolyte used for lithium polymer battery, *New J. Chem.* **29**, 1454-1460, 2005.
- [130] Xi, J., & Tang, X., Investigations on the enhancement mechanism of inorganic filler on ionic conductivity of PEO-based composite polymer electrolyte: The case of molecular sieves, *Electrochim. Acta* **51**, 4765-4770, 2006.
- [131] Xi, J., et al., Effect of molecular sieves ZSM-5 on the crystallization behavior of PEO-based composite polymer electrolyte, *J. Power Sources* **158**, 627-634, 2006.

- [132] Xi, J., et al., Enhanced electrochemical properties of poly(ethylene oxide)-based composite polymer electrolyte with ordered mesoporous materials for lithium polymer battery, *Microporous Mesoporous Materials* **88**, 1-7, 2006.
- [133] Kim, S., & Park, S.-J., Preparation and electrochemical behaviors of polymeric composite electrolytes containing mesoporous silicate fillers, *Electrochim Acta* **52**, 3477-3484, 2007.
- [134] Jeevanandam, P. & Vasudevan, S., Conductivity of a confined polymer electrolyte: Lithium-polypropylene glycol intercalated in layered CdPS<sub>3</sub>, *J. Phys. Chem. B* **102**, 4753-4758, 1998.
- [135] Yariv, S., & Cross, H., (eds.), *Organo-Clay Complexes and Interactions*, Marcel Dekker, New York, 2002.
- [136] Ray, S.S., & Okamoto, M., Polymer/layered silicate nanocomposites: a review from preparation to processing, *Prog. Polym. Sci.* **28**, 1539-1641, 2003.
- [137] Aranda, P., & Ruiz-Hitzky, E., Poly(ethylene oxide)-silicate intercalation materials, *Chem. Mater.* **4**, 1395-1403, 1992.
- [138] Vaia, R.A., et al., Microstructural evolution of melt intercalated polymer-organically modified layered silicates nanocomposites, *Chem. Mater.* **8**, 2628-2635, 1996.
- [139] Vaia, R.A., et al., Relaxations of confined chains in polymer nanocomposites glass transition properties of poly intercalated in montmorillonite, *J. Polym. Sci. B: Polym. Phys.* **35**, 59-67, 1997.
- [140] Shah, D., et al., An interface model for the prediction of Young's modulus of layered silicate-elastomer nanocomposites, *Polymer* **19**, 608-617, 1998.
- [141] Hackett, E., et al., Molecular dynamics simulations of organically modified layered silicates, *J. Chem. Phys.* **108**, 7410-7416, 1998.
- [142] Vaia, R.A., & Giannelis, E.P., Polymer melt intercalation in organically-modified layered silicates: Model predictions and experiment, *Macromolecules* **30**, 8000-8009, 1997.
- [143] Fan, L., et al., Effect of modified montmorillonites on the ionic conductivity of (PEO)<sub>16</sub>LiClO<sub>4</sub> electrolytes, *Electrochim. Acta* **47**, 3541-3544, (2002).
- [144] Kurian, M., et al., Single-ion conducting polymer-silicate nanocomposite electrolytes for lithium battery applications, *Electrochim. Acta* **50**, 2125-2134, 2005.

- [145] Thakur, A.K., et al., Studies on an ionically conducting polymer nanocomposite, *J. Power Sources* **159**, 272-276, 2006.
- [146] Zhang, H et al., Vibrational spectroscopic studies of interactions in PEO-NaSCN-montmorillonite electrolytes, *J. Phys. Chem. C* **111**, 5382-5388, 2007.
- [147] Pradhan, D.K., et al., Studies of structural, thermal and electrical behavior of polymer nanocomposite electrolytes, *Express Polymer Letter* **2**, 630-638, 2008.
- [148] Mohapatra, S.R., et al., Effect of nanoscopic confinement on improvement in ion conduction and stability properties of an intercalated polymer nanocomposite electrolyte for energy storage applications, *J. Power Sources* **191**, 601-613, 2009.
- [149] Kitajima, S., & Tominaga, Y., Enhanced cationic conduction in a polyether/clay composite electrolyte treated with supercritical CO<sub>2</sub>, *Macromolecules* **42**, 5422-5424, 2009.
- [150] Moreno, et al., Electrical and mechanical properties of poly(ethylene oxide)/intercalated clay polymer electrolyte, *Electrochimica Acta* **58**, 112-118, 2011.
- [151] Shukla, N., & Thakur, A.K., Ion transport model in exfoliated and intercalated polymer.clay nanocomposites, *Solid State Ionics* **181**, 921-932, 2010.
- [152] Jacob, M.M.E., et al., From nanocomposite to nanogel polymer electrolytes, *J. Mater. Chem.* **13**, 1-5, 2003.
- [153] Pradhan, D.K. et al., Effect of plasticizer on structure—property relationship in composite polymer electrolytes, *J. Power Sources* **139**, 384-393, 2005.
- [154] Kuila, T., et al., Enhancing the ionic conductivity of PEO based plasticized composite polymer electrolyte by LaMnO<sub>3</sub> nanofiller, *Materials Science and Engineering B* **137**, 217-224, 2007.
- [155] Johan, M.R., et al., Effects of Al<sub>2</sub>O<sub>3</sub> nanofiller and EC plasticizer on the ionic conductivity enhancement of solid PEO-LiCF<sub>3</sub>SO<sub>3</sub> solid polymer electrolyte, *Solid State Ionics* **196**, 41-47, 2011.
- [156] Krejza, O., et al., The presence of nanostructured Al<sub>2</sub>O<sub>3</sub> in PMMA-based gel electrolytes, *J. Power Sources* **178**, 774-778, 2008.
- [157] Kumar, D., & Hashmi, S.A., Ion transport and ion-filler-polymer interaction in poly(methyl methacrylate)-based, sodium ion conducting, gel polymer electrolytes dispersed with silica nanoparticles, *J. Power Sources* **195**, 5101-5108, 2010.

- [158] Ahmad, S., & Agnihotry, S.A., Effect of nano  $\gamma$ -Al<sub>2</sub>O<sub>3</sub> addition on ion dynamics in polymer electrolytes, *Current Applied Physics* **9**, 108–114, 2009.
- [159] Huang, J.-J., et al.,  $\gamma$ -Al<sub>2</sub>O<sub>3</sub> Improves the properties of gel polyacrylonitrile nanocomposite electrolytes used as electrolyte materials in rechargeable lithium batteries, *J. Appl. Polym. Sci.* **120**, 2041–2047, 2011.
- [160] Wu, C.-G., et al., PVdF-HFP/metal oxide nanocomposites: The matrices for high-conducting, low-leakage porous polymer electrolytes, *J. Power Sources* **159**, 295–300, 2006.
- [161] He, X., et al., In situ composite of nano SiO<sub>2</sub>-P(VdF-HFP) porous polymer electrolytes for Li-ion batteries, *Electrochim. Acta* **51**, 1069-1075, 2005.
- [162] Stephan, A.M., et al., Nanofiller incorporated poly(vinylidene fluoride-hexafluoropropylene) (PVdF-HFP) composite electrolytes for lithium batteries, *J. Power Sources* **159**, 1316-1321, 2006.
- [163] Aravindan, V., & Vickraman, P., Polyvinylidene fluoride-hexafluoropropylene based nanocomposite polymer electrolytes (NCPE) complexed with LiPF<sub>3</sub>(CF<sub>3</sub>CF<sub>2</sub>)<sub>3</sub>, *Eur. Polym. J.* **43**, 5121-5127, 2007.
- [164] Kumar, R., et al., Effect of MgO nanoparticles on ionic conductivity and electrochemical properties of nanocomposite polymer electrolyte, *J. Membr. Sci.* **300**, 104-110, 2007.
- [165] Kumar, D., et al., Studies on poly(vinylidene fluoride-co-hexafluoropropylene) based gel electrolyte nanocomposite for sodium-sulfur batteries, *Solid State Ionics* **202**, 45–53, 2011.
- [166] Pandey, G.P., et al., Magnesium ion-conducting gel polymer electrolytes dispersed with nanosized magnesium oxide, *J. Power Sources* **190**, 563–572, 2009.
- [167] Gentili, V., et al., Composite gel-type polymer electrolytes for advanced, rechargeable lithium batteries, *J. Power Sources* **170**, 185-190, 2007.
- [168] Zhang, P., et al., Enhanced electrochemical and mechanical properties of P(VdF-HFP) based composite polymer electrolytes with SiO<sub>2</sub> nanofibers, *J. Membr. Sci.* **379**, 80-85, 2011.
- [169] Li, Z.H., et al., Macroporous nanocomposite polymer electrolyte for lithium-ion batteries, *J. Power Sources* **184**, 562–565, 2008.

- [170] Raghavan, P., et al., Ionic conductivity and electrochemical properties of nanocomposite polymer electrolytes based on electrospun poly(vinylidene fluoride-co-hexafluoropropylene) with nano-sized ceramic fillers, *Electrochim. Acta* **54**, 228–234, 2008.
- [171] Rajendran, S., et al., Transport, structural and thermal studies on nanocomposite polymer blend electrolytes for Li-ion battery applications, *Current Applied Physics* **12**, 789-793, 2012.
- [172] Hwang, J.J., & Liu, H.J., Influence of organophilic clay on the morphology, plasticizer-maintaining ability, dimensional stability, and electrochemical properties of gel polyacrylonitrile (PAN) nanocomposite electrolytes, *Macromolecules* **35**, 7314-7319, 2002.
- [173] Meneghetti, P., et al., Synthesis of polymer gel electrolyte with high molecular weight poly(methyl methacrylate)–clay nanocomposite, *Electrochim. Acta* **49**, 4923-4931, 2004.
- [174] Kim, S., et al., Ionic conductivity of polymeric nanocomposite electrolytes based on poly(ethylene oxide) and organo-clay materials, *Colloids Surf. A: Physicochem. Eng. Aspects* **313/314**, 216-219, 2008.
- [175] Wang, M., & Dong, S., Enhanced electrochemical properties of nanocomposite polymer electrolyte based on copolymer with exfoliated clays, *J. Power Sources* **170**, 425-432, 2007.
- [176] Chen-Yang, Y.W., et al., Effect of the addition of hydrophobic clay on the electrochemical property of polyacrylonitrile/LiClO<sub>4</sub> polymer electrolytes for lithium battery, *Polymer* **50**, 2856-2862, 2009.
- [177] Linford, R.G., in *Applications of electroactive polymers*, B. Scrosati ed., Chapman and Hall, London, 1993, 1.
- [178] Chandra, S., et al., PMMA based protonic polymer gel electrolytes, *Ionics* **6**, 112-118, 2000.
- [179] Song, J.Y., et al., Microstructure of poly(vinylidene fluoride)-based Polymer electrolyte and Its effect on transport properties, *J. Electrochem. Soc.* **149**, A1230-A1236, 2002.
- [180] Vogel, H., *z. phys.* **22**, 645, 1922.



- [181] Tammann, V.G., & Hesse, H.G., *Anorg. Allg. Chem.* **19**, 245 1926.
- [182] Fulcher, G.S., Analysis of recent measurements of the viscosity of glasses, *J. Am. Ceram. Soc.* **8**, 339-355, 1925.
- [183] MacCallum, J.R., & Vincent, C.A. (ed.), *Polymer Electrolyte Reviews*, vol I, Elsevier Applied Sciences, London 1987, 185.
- [184] Singh, J. et al., Enhanced lithium-ion transport in PEG-based composite polymer electrolyte with  $Mn_{0.03}Zn_{0.97}Al_2O_4$  nanoparticles, *Solid State Ionics* **154/155**, 21-27, 2002.
- [185] Williams, M.L., et al., The temperature dependence of relaxation mechanisms in amorphous polymers and other glass-forming liquids, *J. Am. Chem. Soc.* **77**, 3701-3707, 1955.
- [186] Druger, S.D., et al., Dynamic bond percolation theory: A microscopic model for diffusion in dynamically disordered systems. I. Definition and onedimensional case, *J. Chem. Phys.* **79**, 3133-3142, 1983.
- [187] Cohen, M.H., & Trunbull, D., Molecular transport in liquids and glasses, *J. Chem. Phys.* **31** 1164-1169, 1959.
- [188] Duclot, M., et al., New alkali ionomers: transport mechanism from temperature and pressure conductivity measurements, *Solid State Ionics* **136/137**, 1153-1160, 2000.
- [189] Bamford, D., et al., The local free volume, glass transition, and ionic conductivity in a polymer electrolyte: A positron lifetime study, *J. Chem. Phys.* **115**, 7260-7270, 2001.
- [190] Williams, G., in *Dielectric Spectroscopy of Polymeric Materials, Fundamentals and Applications*, J.P. Runt & J.J. Fitzgerald, eds., American Chemical Society, Washington, DC, 1997.
- [191] Mierzwa, M., et al., Effect of pressure on the side-chain crystallization of poly(*n*-octadecyl methacrylate) studied by dielectric spectroscopy, *Phys. Rev. B* **62**, 14012-14019, 2000.
- [192] Macedo, P.B., & Litovitz, T.A., On the relative roles of free volume and activation energy in the viscosity of liquids *J. Chem. Phys.* **42**, 245-256, 1965.
- [193] Glasstone, S., Laidler, K.J., & Eyring, H., in *The Theory of Rate Processes*, McGraw-Hill, New York, 1941.

- [194] Blackburn, F.R., et al., Translational and rotational motion of probes in supercooled 1,3,5-tris(naphthyl)benzene, *J. Phys. Chem.* **100**, 18249-18257, 1996.
- [195] Ruck, D.M., Ion induced modification of polymers at energies between 100 keV and 1 GeV applied for optical waveguides and improved metal adhesion, *Nucl. Instrum. Methods Phys. Res. B* **166/167**, 602-609, 2000.
- [196] Venkatesan, T., High energy ion beam modification of polymer films, *Nucl. Instrum. Methods Phys. Res. B* **7/8**, 461-467, 1985.
- [197] Balanzat, E., et al., Physico-chemical modifications induced in polymers by swift heavy ions, *Nucl. Instrum. Methods Phys. Res. B* **91**, 140-145, 1994.
- [198] Popok, V.N., et al., Ion beam effects in polymer films: Structure evolution of the implanted layer, *Nucl. Instrum. Methods Phys. Res. B* **129**, 60-64, 1997.
- [199] Davenas, J., et al., Stability of polymers under ionising radiation: The many faces of radiation interactions with polymers, *Nucl. Instrum. Methods Phys. Res. B* **191**, 653-661, 2002.
- [200] Laskarakis, A., et al., FTIR and Vis-FUV real time spectroscopic ellipsometry studies of polymer surface modifications during ion beam bombardment, *Nucl. Instrum. Methods Phys. Res. B* **216**, 131-136, 2004.
- [201] Guenther, M., et al., Physical properties and structure of thin ion-beam modified polymer films, *Nucl. Instrum. Methods Phys. Res. B* **216**, 143-148, 2004.
- [202] Bouffard, S., et al., Basic phenomena induced by swift heavy ions in polymers, *Nucl. Instrum. Methods Phys. Res. B* **105**, 1-4, 1995.
- [203] Singh, J.P., Swift heavy ion-based materials science research at NSC, *Nucl. Instrum. Methods Phys. Res. B* **156**, 206-211, 1999.
- [204] Volkov, A.E., & Borodin, V.A., Effects of relaxation of electronic excitations from swift heavy ions in amorphous targets, *Nucl. Instrum. Methods Phys. Res. B* **193**, 381-390, 2002.
- [205] Lee, E.H., Ion-beam modification of polymeric materials – fundamental principles and applications, *Nucl. Instrum. Methods Phys. Res. B* **151**, 29-41, 1999.
- [206] Toulemonde, M., et al., Track formation and fabrication of nanostructures with MeV-ion beams, *Nucl. Instrum. Methods Phys. Res. B* **216**, 1-8, 2004.

- [206] Avasthi, D.K., Some interesting aspects of swift heavy ions in materials science, *Current Science* **78**, 1297-1306, 2000.
- [207] Zhang, S., et al., Visualization of particle distribution in composite polymer electrolyte systems, *J. Power Sources* **126**, 125-133, 2004.
- [208] S. Glasstone, Elements of Physical Chemistry (1945) 399.
- [209] Mac Donald, J.R., (ed.), *Impedance Spectroscopy*, John Wiley & Sons, Inc. New York, 1987.
- [210] Bruce, P.G., in *Polymer Electrolyte Reviews-I*, J.R. MacCallum, & C.A. Vincent, eds., Elsevier Applied Sciences, London, 1987.
- [211] Cole, K.S., & Cole, R.H., Dispersion and absorption in dielectrics I. Alternating current characteristics, *J. Chem. Phys.* **9**, 341-351, 1941.
- [212] Bauerle, J. E., Study of solid electrolyte polarization by a complex admittance method, *J. Chem. Phys.* **30**, 2657-2670, 1969.
- [213] Sluyters-Rehbach, M., & Sluyters, J.H., in *Electroanalytical Chemistry*, J. Bard, ed., Vol. 4, Marcel Dekker Inc., New York, 1970.
- [214] Epelboin, I., & Keddam, M., Faradaic impedances: Diffusion impedance and reaction Impedance, *J. Electrochem. Soc.* **117**, 1052-1056, 1970.
- [215] De Bruin, H.J., & Badwal, S.P.S., Faradaic impedance dispersion of the noble-metal/ceramic electrolyte interface, *J. Aust. Ceram. Soc.* **14**, 20-28, 1978.
- [216] Archer, W.I., & Armstrong, R.D., *Electrochemistry 7*, The Chemical Society, London, 1980, 157.
- [217] Gabrielli, C., *Identification of Electrochemical Processes by Frequency Response Analysis*, Solartron Instrumentation Group, 1980.
- [218] Mellander, B.E., & Lunden, A., in *Materials for Solid State Batteries*, B.V.R. Chowdari, & S. Radhakrishna, eds., World Scientific Publ. Co. Pvt. Ltd., Singapore, 1986, 161.
- [219] Raistrick, I.D., Application of impedance spectroscopy to problems in solid state ionics, *Solid State Ionics* **18/19**, 40-49, 1986.
- [220] Badwal, S.P.S., in *Solid State Ionics Devices*, B.V.R. Chowdari, & S. Radhakrishna, eds., World Scientific Publishing Co., Singapore, 1988, 165.

- [221] Randles, J.E.B., Kinetics of Rapid Electrode Reactions, *Discuss. Faraday Soc.* **1** 11-19, 1947.
- [222] Raistrick, I.D., Macdonald, J.R., & Franceschetti, D.R., in *Impedance Spectroscopy Characterizing Solid Materials and Analysis*, J. R. Macdonald, ed., Chap. 2, John Wiley & Sons Inc., New York, 1987.
- [223] Time domain dielectric spectroscopy: An advanced measuring system, *Rev. Sci. Instrum.* **14**, 3208-3216, 1996.
- [224] Jonscher, A.K., The universal dielectric response, *Nature* **267**, 673-679, 1977.
- [225] Iskander, M.F., et al., Time and frequency domain matrix for measuring the dielectric properties of rocks: A review, *J. Microwave Power* **18**, 55-74, 1983.
- [226] Jonscher, A.K., Dielectric relaxation in solids, *J.Phys. D: Appl. Phys.* **32**, R57-R70, 1999.
- [227] Jonscher, A.K., *Dielectric Relaxation in Solids*, Dielectric press, London, 1983
- [228] Smedly, S., *The Interpretation of Ionic Conductivity in Liquids*, Plenum, New York, 1980.
- [229] Cohen, M.H., & Grest, G.S., Liquid-glass transition: Dependence of the glass transition on heating and cooling rates, *Phys. Rev. B* **21**, 4113-4117, 1980.
- [230] Gibbs, J.H., & DiMarzio, E.A., Nature of the glass transition and the glassy state, *J. Chem. Phys.* **28**, 373-383, 1958.
- [231] Adam, G., & Gibbs, J.H., On the temperature dependence of cooperative relaxation properties in glass forming liquids, *J. Chem. Phys.* **43**, 139-146, 1965.
- [232] Goldstein, M.J., Viscous liquids and the glass transition. IV. Thermodynamic equations and the transition, *J. Phys. Chem.* **77**, 667-673, 1973.
- [233] Angell, C.A., & Sichina, W., Thermodynamics of glass transition: Empirical aspects, *Ann. N.Y. Acad. Sci.* **279**, 53-67, 1976.
- [234] Cheradame, H., in *IUPAC Macromolecules*, H. Benoit, & P. Rempp, eds., Pergamon, New York, 1982, 251.
- [235] Ratner, M.A., in *Polymer Electrolyte Reviews*, J.R. MacCallum, & C.A. Vincent, eds., Elsevier, London, 1987.
- [236] Bruce, P.G., & Gray, F.M., in *Solid State Electrochemistry*, P.G. Bruce, ed., Cambridge University Press, New York, USA, 1995, 119.

- [237] Tokuda, H., et al., Synthesis, characterization, and ion-conductive behavior in an organic solvent and in a polyether of a novel lithium salt of a perfluorinated polyimide anion, *Macromolecules* **35**, 1403-1411, 2002.
- [238] Wieczorek, W., et al., Polyether, polyacrylamide, LiClO<sub>4</sub> composite electrolytes with enhanced conductivity, *J. Phys. Chem.* **98**, 6840-6850, 1994.
- [239] Maxwell, J.C., *A Treaty on Electricity and Magnetism*, Vol. 1, Clarendon, London, Chap. 11, 1892.
- [240] Bruggeman, D.A.G., Berechnung verschiedener physikalischer konstanten von heterogenen substanzen, *Ann. Phys. (Leipzig)* **24**, 636-679, 1935.
- [241] Landauer, R., The electrical resistance of binary metallic mixtures, *J. Appl. Phys.* **23**, 779-784, 1952.
- [242] Nan, C.-W., Physics of inhomogeneous inorganic materials, *Prog. Mater. Sci.* **37**, 1-116, 1993.
- [243] Nan, C.-W., & Smith, D.M., A.c. electrical properties of composite solid electrolytes, *Mat. Sci. Eng. B* **10**, 99-106, 1991.
- [244] Nakamura, M., Conductivity for the site-percolation problem by an improved effective-medium theory, *Phys. Rev. B* **29**, 3691-3693, 1984.
- [245] DeSimone, T., et al., Continuum percolation in an interacting system: Exact solution of the Percus-Yevick equation for connectivity in liquids, *Phys Rev. Lett.* **56**, 1140-1143, 1986.
- [246] Florjanczyk, Z., et al., *Bull. Electrochem.* **8**, 524- 1992.
- [247] Przulski, J., et al., Effective medium theory in studies of conductivity of composite polymeric electrolytes, *Electrochim. Acta* **40**, 2101-2108, 1995.
- [248] Przulski et al., J., in *Solid State Ionics: Materials and Applications*, B.V.R. Chowdari, et al, eds., World Scientific Publ. Co., Singapore, 1992, 209.
- [249] Wieczorek, W., & Siekierski, M., A description of the temperature dependence of the conductivity for composite polymeric electrolytes by effective medium theory, *J. Appl. Phys.* **76**, 2220-2226, 1994.
- [250] Bares, J., Glass transition of the polymer microphase, *Macromolecules* **8**, 244-246, 1975.

- [251] Schneider, H.A., & DiMarzio, E.A., The glass temperature of polymer blends: comparison of both the free volume and the entropy predictions with data, *Polymer* **33**, 3453-3461, 1992.
- [252] Gendelman, O. V., et al., Solitonic mechanism of structural transition in polymer-clay nanocomposites, *J. Chem. Phys.* **119**, 1066-1069, 2003.
- [253] Ginzburg, V.V., et al., Simple "Kink" Model of Melt Intercalation in Polymer-Clay Nanocomposites, *Phys. Rev. Lett.* **86**, 5073-5075, 2001.
- [254] Vaia, R.A., & Giannelis, E.P., Lattice model of polymer melt intercalation in organically-modified layered silicates, *Macromolecules* **30**, 7990-7999, 1997.
- [255] Balazs, A.C., et al., Modeling the interactions between polymers and clay surfaces through self-consistent field theory, *Macromolecules* **31**, 8370-8381, 1998.
- [256] Ginzburg, V.V., et al., Theoretical phase diagrams of polymer/clay composites: The role of grafted organic modifiers, *Macromolecules* **33**, 1089-1099, 2000.
- [257] Balazs, A.C., Ginzburg, V.V., Lyatskaya, Y., Singh, C., & Zhulina, E., in *Polymer-Clay Nanocomposites*, T. Pinnavaia, & G. Beall, et al., Wiley, New York, 2000.
- [258] Landau, L.D., & Lifshitz, E.M., *Theory of Elasticity*, Pergamon, Oxford, Chap. 2, 3rd ed., 1986,
- [259] Moon, P., et al., Computational simulation of lithium ion transport through polymer nanocomposite membranes, *Journal of New Materials for Electrochemical Systems* **6**, 237-244, 2003.
- [260] Redfern, P.C., & Curtiss, L.A., Quantum chemical studies of Li<sup>+</sup> cation binding to polyalkyloxides, *J. Power Sources* **110**, 401-405, 2002.
- [261] Newman, J.S., *Electrochemical Systems*, Englewood Cliffs, New Jersey, 1991.
- [262] Prentice, G., *Electrochemical Engineering Principles*, Englewood Cliffs, New Jersey, 1991.
- [263] Yang, D.K., & Zax, D.B., Li<sup>+</sup> dynamics in a polymer nanocomposite: An analysis of dynamic line shapes in nuclear magnetic resonance, *J. Chem. Phys.* **110**, 5325-5336, 1999.
- [264] Hackett, E., et al., Computer simulation studies of PEO/layer silicate nanocomposites, *Chem. Mater.* **12**, 2161-2167, 2000.

- [265] Bujda'k, J., et al., Effect of layer charge on the intercalation of poly(ethylene oxide) in Layered silicates: Implications on nanocomposite polymer electrolytes, *Chem. Mater.* **12**, 2168-2174, 2000.
- [266] Kuppa, V., & Manias, E., Computer simulation of PEO/layered-silicate nanocomposites: 2. Lithium dynamics in PEO/Li<sup>+</sup> montmorillonite intercalates, *Chem. Mater.* **14**, 2171-2175, 2002.
- [267] Reinholdt, M.X., et al., Montmorillonite–poly(ethylene oxide) nanocomposites: Interlayer alkali metal behavior, *J. Phys. Chem. B* **109**, 16296-16303, 2005.
- [268] Huang, J., Synthesis and applications of conducting polymer polyaniline nanofibers, *Pure Appl. Chem.* **78**, 15-27, 2006.
- [269] Wagner, J.B., & Wagner, C., Electrical conductivity measurements on cuprous halides, *J. Chem. Phys.* **26**, 1597-1601, 1957.
- [270] Hussain A.M.P., *Swift heavy ion irradiation effects on electrodeposited conducting polymer based electrodes for redox supercapacitor*, Ph.D. Thesis, Tezpur University, Assam, India, 2006.
- [271] Warren B.E., & Averbach, B.L., The effect of Cold-Work distortion on X-ray patterns, *J. Appl. Phys.* **21**, 595-599, 1950.
- [272] Warren B.E., & Averbach, B.L., The separation of Cold-Work distortion and particle size broadening in X-ray patterns, *J. Appl. Phys.* **23**, 497, 1952.
- [273] de Keijer, Th. H., et al., Use of Voigt function in a single line method for the analysis of X-ray diffraction line broadening, *J. Appl. Cryst.* **15**, 308-314, 1980.
- [274] Delhez, R., et al., *Accuracy in Powder Diffraction*, Nalt. Bur. Stand. Spec. Pub., 567, Block, S., et al., eds., 1980, 213-253.
- [275] Cook, A., Hendrik Christoffel van de Hustle in de Orde van Nederlandse Leeuw, *Bigrap. Mem. Felolws of the Royal Society* **47**, 466-479, 2001.
- [276] Langford, J.I., Arapid method for analyzing the breadths of diffraction and spectral lines using Voigt function, *J. Appl. Cryst.* **11**, 10-14, 1978.
- [277] Nandi, R.K., & Sen Gupta, S.P., The analysis of X-ray diffraction profiles from imperfect solids by an application of convolution relation, *J. Appl. Cryst.* **11**, 6-9, 1978.

- [278] Ruska, E., *The Development of Electron Microscopy*, Nobel Lecture, December 8, 1986, [http://nobelprize.org/nobel\\_prize/physics/laureates/1986/ruska-lecture.pdf](http://nobelprize.org/nobel_prize/physics/laureates/1986/ruska-lecture.pdf).
- [279] Kruger, D., et. al., Helmut Ruska and visualization of viruses, *The Lancet* **355**, 1713-1717, 2000.
- [280] Kaufmann, E.N., *Characterization of Materials*, John Wiley & Sons Inc., Hoboken, New Jersey, 2003.
- [281] Singh, J.P., et al., Swift heavy ion based materials science research at NSC, *Nucl. Instrum. Methods Phys. Res. B* **156**, 206-211, 1999.
- [282] Jeon, J.-D., et al., Solvent-free polymer electrolytes based on thermally annealed porous P(VdF-HFP)/P(EO-EC) membranes, *J. Power Sources* **143**, 219–226, 2005.
- [283] Abbrent, S., et al., Crystallinity and morphology of PVdF-HFP-based gel electrolytes, *Polymer* **42**, 1407-1416, 2001.
- [284] Kim, K.M., et al., Characterization of poly(vinylidene fluoride-co-hexafluoropropylene)-based polymer electrolyte filled with rutile TiO<sub>2</sub> nanoparticles, *Solid State Ionics* **161**, 121-131, 2003.
- [285] Rajendran, S., et al., Ionic conductivity studies in composite solid polymer electrolytes based on methylmethacrylate, *J. Phys. Chem. Sol.* **63**, 303-307, 2002.
- [286] Chen H.-W., et al., Ionic conductivity enhancement of the plasticized PMMA/LiClO<sub>4</sub> polymer nanocomposite electrolyte containing clay, *Polymer* **43**, 5281-5288, 2002.
- [287] Ahmad, S., et al., The effect of nanosized TiO<sub>2</sub> addition on poly(methylmethacrylate) based polymer electrolytes, *J. Power Sources* **159**, 205-209, 2006.
- [288] Porter, M.D., et al., Spontaneously organized molecular assemblies. 4. Structural characterization of n-alkyl thiol monolayers on gold by optical ellipsometry, infrared spectroscopy, and electrochemistry, *J. Am. Chem. Soc.* **109**, 3559-3568, 1987.
- [289] Parka, C.H., et al., Electrochemical stability and conductivity enhancement of composite polymer electrolytes, *Solid State Ionics* **159**, 111–119, 2003.
- [290] Zhang, S.S., et al., Microporous poly (acrylonitrile-methyl methacrylate) membrane as a separator of rechargeable lithium battery, *Electrochim. Acta* **49** (2004) 3339-3345.
- [291] Tang, M., & Liao, W.R., Solvent effect on the miscibility of poly (4-hydroxystyrene)–poly(ethylene oxide) blends, *Eur. Polym. J.* **36**, 2597–2603, 2000.



- [292] Pielichowski, K., & Hamerton, I., Compatible poly(vinyl chloride)/chlorinated polyurethane blends: thermal characteristics, *Eur. Polym. J* **36**, 171–181, 2000.
- [293] Rocco, A.M., et al., Miscibility, crystallinity and morphological behavior of binary blends of poly (ethylene oxide) and poly(methyl vinyl ether–maleic acid), *Polymer* **42**, 5199–5205, 2001.
- [294] Acosta, J.L., & Morales, E., Structural, morphological and electrical characterization of polymer electrolytes based on PEO/PPO blends, *Solid State Ionics* **85**, 85-90, 1996.
- [295] Deanin, R.D., & Manion, M.A., in *Polymer Blends and Alloys*, G.O. Shonaike, & G.P. Simon, eds. Marcel Dekker, Inc., 1999.
- [296] Choi, Y. S., et al., Phase behaviors of polymer blend (PEO–PPO) electrolyte/LiCF<sub>3</sub>SO<sub>3</sub> systems in lithium battery, *J. Appl. Polym. Sci.* **98**, 2314-2319, 2005.
- [297] Rhoo, H.J., Ionic conduction in plasticized PVC/PMMA blend polymer electrolytes. *Electrochim. Acta* **42**, 1571-1579, 1997.
- [298] Kim, H.-T., et al., Li-ion polymer battery based on phase-separated gel polymer electrolyte, *Electrochim. Acta* **45**, 4001-4007, 2000.
- [299] Subba Reddy, Ch.V., et al., Electrochemical studies on PVC/PVdF blend-based polymer electrolytes, *J. Solid State Electrochem.* **11**, 543–548, 2007.
- [300] Subramania, A., et al., New polymer electrolyte based on (PVA–PAN) blend for Li-ion battery applications, *Ionics* **12**, 175–178, 2006.
- [301] Boudin, F., et al., Microporous PVdF gel for lithium-ion batteries, *J. Power Sources* **81-82**, 804-807, 1999.
- [302] Du Pasquier, A., Warren, P.C., Culver, D., Gozdz, A.S., Amatucci, G.G., & Tarascon, J.M., 196th the Electrochem. Soc. Meeting (B2 abs), Hawaii, 1999, 116.
- [303] Tian, Z, et al., Preparation of a microporous polymer electrolyte based on poly(vinyl chloride)/poly(acrylonitrile-butyl acrylate) blend for Li-ion batteries, *Electrochim. Acta* **52**, 3199–3206, 2007.
- [304] Quartarone, E., et al., Transport properties of porous PVDF membranes, *J. Phys. Chem. B* **106**, 10828–10833, 2002.
- [305] Huang, H., & Wunder, S.L., Ionic conductivity of microporous PVDF-HFP/PS polymer blends, *J. Electrochem. Soc.* **148**, A279-A283, 2001.

- [306] Vijayakumar, G., et al., Effect of nanoscale CeO<sub>2</sub> on PVDF-HFP-based nanocomposite porous polymer electrolytes for Li-ion batteries, *J. Solid State Electrochem.* **12**, 1135-1141, 2008.
- [307] Xi, J., et al., PVDF-PEO/ZSM-5 based composite microporous polymer electrolyte with novel pore configuration and ionic conductivity, 2006 *Solid State Ionics* **177**, 709-713, 2006.
- [308] Wu, C.-G., et al., PVdF-HFP/metal oxide nanocomposites: The matrices for high-conducting, low-leakage porous polymer electrolytes, *J. Power Sources* **159**, 295-300, 2006.
- [309] Jeon, J.-D., & Kwak, S.-Y., Pore-filling solvent-free polymer electrolytes based on porous P(VdF-HFP)/P(EO-EC) membranes for rechargeable lithium batteries, *J. Membrane Sci.* **286**, 15-21, 2006.
- [310] Jeon, J.D., et al., Solvent-free polymer electrolytes based on thermally annealed porous P(VdF-HFP)/P(EO-EC) membranes, *J. Power Sources* **143**, 219-226, 2005.
- [311] Song, J.Y., et al., Conductivity study of porous plasticized polymer electrolytes based on poly(vinylidene fluoride) A comparison with polypropylene separators, *J. Electrochem Soc.* **147**, 3219-3225, 2000.
- [312] Wang, H., et al., Novel microporous poly(vinylidene fluoride) blend electrolytes for lithium-ion batteries, *J. Electrochem Soc.* **147**, 2853-2861, 2000.
- [313] Xi, J., et al., PVDF-PEO blends based microporous polymer electrolyte: Effect of PEO on pore configurations and ionic conductivity, *J. Power Sources* **157**, 501-506, 2000.
- [314] Leo, C.J., et al., Studies on plasticized PEO-lithium triflate-ceramic filler composite electrolyte system, *Solid State Ion* **148**, 159-171, 2002.
- [315] Panero, S., et al., High voltage lithium polymer cells using a PAN-based composite electrolyte, *J. Electrochem Soc.* **149**, A414-A417, 2002.
- [316] Chung, S.H., et al., Enhancement of ion transport in polymer electrolytes by addition of nano-scale inorganic oxides, *J Power Sources* **97/98**, 644-648, 2001.
- [317] Saikia, D., et al., Ionic transport in P(VDF-HFP)-PMMA-LiCF<sub>3</sub>SO<sub>3</sub>-(PC+DEC)-SiO<sub>2</sub> composite gel polymer electrolytes, *Eur. Polym. J.* **41**, 563-568, 2005.

- [318] Yang, G., et al., A novel inorganic–organic polymer electrolyte with a high conductivity: insertion of poly (ethylene) oxide into  $\text{LiV}_3\text{O}_8$  in one step, *J. Mater. Chem.* **15**, 1369–1374, 2005.
- [319] Zhou, W., et al., Facile synthesis of polyanilinenanofibers in the presence of polyethylene glycol, *J. Polym. Res.* **14**, 1–4, 2007.
- [320] Kim, D.-W., et al., Electrochemical characteristics of blended polymer electrolytes containing lithium salts, *J. Polym. Sci. B Polym. Phys.* **34**, 2127–2137, 1996.
- [321] Bujdák, J., et al., Effect of layer charge on the intercalation of poly(ethylene oxide) in layered silicates: Implications on nanocomposite polymer electrolytes, *Chem. Mater.*, **12**, 2168–2174, 2000.
- [322] Moreno, M., et al., Poly(acrylonitrile)–montmorillonite nanocomposites: Effects of the intercalation of the filler on the conductivity of composite polymer electrolytes, *Electrochim. Acta* **55**, 1323–1327, 2010.
- [323] Zeng, Q.H., et al., Synthesis of polymer–montmorillonite nanocomposites by *in situ* intercalative polymerization, *Nanotechnology* **13**, 549–553, 2002.
- [324] Wang, M., et al., Poly(vinylidene fluoride–hexafluoropropylene)/organo–montmorillonite clays nanocomposite lithium polymer electrolytes, *Electrochim. Acta* **49**, 3595–3602, 2004.
- [325] Walls, H.J., et al., Nanocomposite electrolytes with fumed silica and hectorite clay networks: Passive versus active fillers, *Adv. Funct. Mater.* **13**, 710–717, 2003.
- [326] Lan, T., et al., On the nature of polyimide–clay hybrid composites, *Chem. Mater.* **6**, 573–575, 1994.
- [327] Tyan, H.-L., et al., Thermally and mechanically enhanced clay/polyimide nanocomposite via reactive organoclay, *Chem. Mater.* **11**, 1942–1947, 1999.
- [328] Wang, Z., & Pinnavaia, T.J., Nanolayer reinforcement of elastomeric polyurethane, *Chem. Mater.* **10**, 3769–3771, 1998.
- [329] Gilman, J.W., et al., Flammability properties of polymer–layered silicate nanocomposites. Polypropylene and polystyrene nanocomposites, *Chem. Mater.* **12**, 1866–1873, 2000.
- [330] Priya, L., & Jog, J.P., Intercalated poly(vinylidene fluoride)/clay nanocomposites: Structure and properties, *J. Polym. Sci. B: Polym. Phys.* **41**, 31–38, 2003.

- [331] Shansheng, Y., et al., Formation mechanism of  $\beta$ -Phase in PVDF/CNT composite prepared by the sonication method, *Macromolecules* **42**, 8870–8874, 2009.
- [332] Martins, P., et al., Local variation of the dielectric properties of poly(vinylidene fluoride) during the  $\alpha$ - to  $\beta$ -phase transformation, *Phys. Lett. A* **373**, 177–180, 2009.
- [333] Wen-Hua, L., et al., Preparation and characterization of wood/montmorillonite nanocomposites, *Forest. Stud. China* **8**, 35–40, 2006.
- [334] Sekhon, S.S., & Singh, H.P., Ionic conductivity of PVdF-based polymer gel electrolytes, *Solid State Ionics* **152/153**, 169-174, 2002.
- [335] Croce, F., et al., Role of the ceramic fillers in enhancing the transport properties of composite polymer electrolytes, *Electrochim. Acta* **46**, 2457–2461, 2001.
- [336] Rajendran, S., et al., Lithium ion conduction in plasticized PMMA–PVdF polymer blend electrolytes, *Mater. Chem. Phys.* **74**, 52–57, 2002.
- [337] Rajendran, S., et al., Thermal and ionic conductivity studies of plasticized PMMA/PVdF blend polymer electrolytes, *Eur. Polym. J.* **38**, 49–55, 2002.
- [338] Xie, H., et al., PVDF-HFP composite polymer electrolyte with excellent electrochemical properties for Li-ion batteries, *J. Solid State Electrochem.* **12**, 1497–1502, 2008..
- [339] Deka, M., et al., Effect of dedoped (insulating) polyaniline nano.bers on the ionic transport and interfacial stability of poly(vinylidene fluoride-hexa.uoropropylene) based composite polymer electrolyte membranes, *J. Membr. Sci.* **327**, 188–194, 2009.
- [340] Charlesby, A., *Atomic Radiation and Polymers*, Pergamon, London, 1960.
- [341] Venkatesan, T., Calcagno, L., Elman, B.B., & Foti, G., in *Ion Beam Modification of Insulators*, P. Mazzoldi, & G. Arnold, eds., Elsevier, Amsterdam, 1978, 301.
- [342] Davies, G.R., in *Physics of dielectric solids*, Ins. Phys. Conf. Ser. No. 58, Bristol and London, 1980, 50.
- [343] Osaki, S. & Kotaka, T., Electrical properties of form III poly(vinyledene fluoride), *Ferroelectrics* **32**, 1-11, 1981.
- [344] Guzman, A.M., et al., Chemical and physical changes induced in polyvinylidene fluoride by irradiation with high energy ions, *Nucl. Instrum. Methods Phys. Res. B* **7/8**, 468-472, 1985.

- [345] Mladenov, G.M., & Emmoth, B., Polymethyl methacrylate sensitivity variation versus the electronic stopping power at ion lithography exposure, *Appl. Phys. Lett.* **38**, 1000-1002, 1981.
- [346] Hall, T.M., et al., Ion beam exposure characteristics of resists: Experimental results, *J. Appl. Phys.* **53**, 3997-4010, 1982.
- [347] Hussain, A.M.P., et al., Effects of 160MeV Ni<sup>12+</sup> ion irradiation on HCl doped polyaniline electrode, *J. Phys. D: Appl. Phys.* **39**, 750-755, 2006.
- [348] Prasher, S., et al., Analysis of electrical properties of Li<sup>3+</sup> ion beam irradiated lexan polycarbonate, *Asian Journal of Chemistry* **21**, 43-46, 2009.
- [349] Kumar, V., et al., Study of chemical, optical and structural properties of 120 MeV Ni<sup>11+</sup> ions beam irradiated poly (ethylene terephthalate) film, *International J. Applied Engineering Research* **2**, 419-430, 2011.
- [350] Sarmah, S., & Kumar, A., SHI irradiation effects on electrical and optical properties of PPy-SnO<sub>2</sub> nanocomposite, *Phys. Status Solidi A* **207**, 2279-2287, 2010.
- [351] Kulshrestha, V., et al., Structural, optical, thermo-mechanical and transport properties of ion irradiated polymer membranes, *Polym. Bull.* **56**, 427-435, 2006.
- [352] Swain, M.V., et al., Influence of implantation of heavy metallic ions on the mechanical properties of two polymers, polystyrene and polyethylene terephthalate, *J. Mater. Res.* **12**, 1917-1926, 1997.
- [353] Gaafar, M., et al., Ac-electrical conductivity of poly(propylene) before and after X-ray irradiation, *Nucl. Instrum. Methods Phys. Res. B* **174**, 507-511, 2001.
- [354] Lakshmi, G.B.V.S., et al., Effects of 60 MeV C<sup>5+</sup> ion irradiation on PmT-PVC and p-TSA doped PoT-PVC blends *Nucl. Instrum. Methods Phys. Res. B* **266**, 1685-1691, 2008.
- [355] Lee, E.H., et al., Effects of electronic and recoil processes in polymers during ion implantation, *J. Mater. Res.* **9**, 1043-1050, 1994.
- [356] Lee, E.H. et al., LET effect on cross-linking and scission mechanisms of PMMA during irradiation, *Rad. Phys. Chem.* **55**, 293-305, 1999.
- [357] Michot, T., et al., Electrochemical properties of polymer gel electrolytes based on poly(vinylidene fluoride) copolymer and homopolymer, *Electrochim. Acta* **45**, 1347-1360, 2000.

- [358] Hosoi, F., et al., Preparation of highly oriented poly-diacetylene films with ion beam irradiation, *Radat. Eff. Def. Solids* **126**, 351-354, 1993.
- [359] Percolla, R., et al., Ordering induced by swift ions in semicrystalline polyvinylidene fluoride, *Appl. Phys. Lett.* **65**, 2966-2968, 1994.
- [360] Stephan, A.M., et al., Ionic conductivity and FT-IR studies on plasticized PVC/PMMA blend polymer electrolytes, *J. Power Sources* **89**, 80-87, 2000.
- [361] Biswas, A., et al., Recrystallization in polyvinylidene fluoride upon low fluence swift heavy ion impact, *Appl. Phys. Lett.* **78**, 4136-4138, 2001.
- [362] Aranda, P., & Ruiz-Hitzky, E., Poly(ethylene oxide)/NH<sub>4</sub><sup>+</sup>-smectite nanocomposites, *Appl. Clay Sci.* **15**, 119-135, 1999.
- [363] Okamoto, M., et al., Dispersed structure and ionic conductivity of smectic clay/polymer nanocomposites, *Polymer* **42**, 2685-2688, 2001.
- [364] Vaia, R.A., et al., New polymer electrolyte nanocomposites: Melt intercalation of poly(ethylene oxide) in mica-type silicates, *Adv. Mater.* **7**, 154-156, 1995.
- [365] Liao, B., et al., Polymer-layered silicate nanocomposites. 1. A study of poly(ethylene oxide)/Na<sup>+</sup>-montmorillonite nanocomposites as polyelectrolytes and polyethylene-block-poly(ethylene glycol) copolymer/Na<sup>+</sup>-montmorillonite nanocomposites as fillers for reinforcement of polyethylene, *Polymer* **42**, 10007-10011, 2001.
- [366] Tiwari, V.K., et al., Radiation-resistant behavior poly(vinylidene fluoride)/layered silicate nanocomposites, *Applied Materials and Interface* **1**, 311-318, 2009.
- [367] Pradhan, D.K., Studies of dielectric relaxation and AC conductivity behavior of plasticized polymer nanocomposite electrolytes, *International Journal of Electrochemical Science* **3**, 597-608, 2008.
- [368] Kosmidou Th.V., et al., Structural, mechanical and electrical characterization of epoxy-amine/carbon black nanocomposites, *Express Polymer Letters* **2**, 364-372, 2008.
- [369] Sengwa, R.J., et al., Dielectric behaviour and relaxation processes of montmorillonite clay nano-platelet colloidal suspensions in poly(vinyl pyrrolidone)-ethylene glycol oligomer blends, *Polym. Int.* **58**, 781-789, 2009.

- [370] Elmahdy, M.M., et al., Effect of confinement on polymer segmental motion and ion mobility in PEO/layered silicate nanocomposites, *Macromolecules* **39**, 5170-5173, 2006.
- [371] Sengwa, R.J., et al., Low frequency dielectric relaxation processes and ionic conductivity of montmorillonite clay nanoparticles colloidal suspension in poly(vinyl pyrrolidone)-ethylene glycol blends, *Express Polymer Letters* **2**, 800-809, 2008.
- [372] Xu, S, et al., The effect of MMT/modified MMT on the structure and performance of the superabsorbent composite, *Polym. Bull.* **60**, 69-78, 2008.
- [372] Zhang, H., et al., Vibrational spectroscopic studies of interactions in PEO-NaSCN-montmorillonite electrolytes, *J. Phys. Chem. C* **111**, 5382-5388, 2007.
- [374] Manoratne, C.H., et al., Ionic conductivity of poly(ethylene oxide) (PEO)-montmorillonite(MMT) nanocomposites prepared by intercalation from aqueous medium, *International Journal of Electrochemical Science* **1**, 32-46, 2006.

## *List of Publications*

---

### **A. In refereed International/ National Journals:**

1. M. Deka, A.K. Nath and A. Kumar, "Effect of dedoped (insulating) polyaniline nanofibers on the ionic transport and interfacial stability of poly(vinylidene fluoride-hexafluoropropylene) based composite polymer electrolyte membranes", *J. Membr. Sci.*, **372** (2009) 188-194.
2. M. Deka and A. Kumar, "Ionic transport in P(VdF-HFP)-PEO based novel microporous polymer electrolytes", *Bull. Mater. Sci.*, **32** (2009) 627-632.
3. M. Deka and A. Kumar, "Enhanced ionic conductivity in novel nanocomposite gel polymer electrolyte based on intercalation of PMMA into layered  $\text{LiV}_3\text{O}_8$ ", *J. Solid State Electrochem.*, **14** (2010) 1649-1656.
4. A. Kumar and M. Deka, "PEO/P(VdF-HFP) blend based  $\text{Li}^+$  ion-conducting composite polymer electrolytes dispersed with dedoped (insulating) polyaniline nanofibers", *J. Solid State Electrochem.*, **16** (2012) 35-44.
5. M. Deka, A.K. Nath and A. Kumar, "Ionic conduction and phase separation studies in PEO-P(VdF-HFP)- $\text{LiClO}_4$ -dedoped polyaniline nanofiber composite polymer electrolytes - I", *Indian J. Phys.*, **84** (2010) 1299-1305.
6. A.K. Nath, M. Deka and A. Kumar, "Ionic conduction and phase separation studies in P(VdF-HFP)- $\text{LiClO}_4$ - dedoped polyaniline nanofiber composite polymer electrolytes - II: Effect of incorporation of PC and DEC", *Indian J. Phys.*, **84** (2010) 1307-1313.
7. A. Kumar, M. Deka and S. Banerjee, "Enhanced ionic conductivity in oxygen ion irradiated poly(vinylidene fluoride-hexafluoropropylene) based nanocomposite gel polymer electrolytes", *Solid State Ionics*, **181** (2010) 609-615.
8. M. Deka and A. Kumar, "Enhanced electrical and electrochemical properties of PMMA-clay nanocomposite gel polymer electrolytes", *Electrochim. Acta*, **55** (2010) 1836-1842.
9. M. Deka and A. Kumar, "Electrical and electrochemical studies of poly(vinylidene fluoride)-clay nanocomposite gel polymer electrolytes for Li-ion batteries", *J. Power Sources*, **196** (2011) 1358-1364.



10. M. Deka, A. Kumar, H. Deka and N. Karak, "Ionic transport studies in hyperbranched polyurethane/clay nanocomposite gel polymer electrolytes", *Ionics*, **18** (2012) 181–187.
11. M. Deka and A. Kumar, "Dielectric and conductivity studies on 90 MeV  $O^{7+}$  ion irradiated poly(ethylene oxide)/montmorillonite based single ion conductor", **Communicated to *Nucl. Instrum. Methods Phys. Res. B***.
12. A K Nath, M Deka, S J Hazarika and A Kumar, "A study on electrical properties of intercalated poly(ethylene oxide)-clay polymer electrolytes for lithium ion batteries", **Communicated to *J. Solid State Electrochem***.
13. M. Deka, A. Kumar and P. Chutia, Electrical and electrochemical properties of poly(methyl methacrylate) based nanocomposites gel polymer electrolytes dispersed with dedoped (insulating) polyaniline, **Communicated to *Materials Science and Engineering: B***.

#### **B. In International/ National Conference Proceedings:**

1. M. Deka and A. Kumar, "Photoluminescence studies on PEO-PVdF blend polymer electrolytes", **Proceedings of the XXXIII Optical Society of India (OSI) Symposium-2007**, P.P. Sahu and P. Deb (Eds.), pp. 244-246.
1. A. Kumar and M. Deka, "PVdF-clay nanocomposite gel polymer electrolytes for Li-ion batteries", **Proceedings of the 55<sup>th</sup> DAE Solid State Symposium-2011, AIP Conference Proceedings**, 1349 (2011) 1303-1304.
2. M. Deka, P. Chutia and A. Kumar, "Effect of dedoped polyaniline nanofibers on the electrical and electrochemical properties of PMMA based nanocomposite polymer electrolytes for energy storage applications", **Proceedings of International Congress on Renewable Energy (ICORE)-2011**, S.K. Samdarshi, S. Mahapatra and S. Paul (Eds.), pp. 160-166.

#### **C. Book Chapters:**

1. A. Kumar and M. Deka, "Nanofiber reinforced composite polymer electrolyte membranes", *Nanofibers*, A. Kumar (Ed.), InTech, Ch. 2, 2010, pp. 13-38, ISBN: 978-953-7619-86-2.

2. A. Kumar, S. Banerjee and M. Deka, “ *Electron microscopy for understanding swift heavy ion irradiation effects on electroactive polymers*”, *Microscopy Book Series IV, Vol. 3*, A. Mendez-Vilas and J. Diaz (Eds.), **Formatex Research Center, 2010, pp. 1755-1768, ISBN (13): 978-84-614-6191-2.**
3. M. Deka and A. Kumar, “*Nanocomposite polymer electrolytes for Li-ion batteries*”, *Advances in Energy Research, Vol. 8*, M. J. Acosta (Ed.), **Nova Science Publishers Inc., Ch. 4, 2011, pp. 143-172, ISBN: 978-1-61324-208-7.**
4. A. Kumar and M. Deka, “*Polymer-clay nanocomposite electrolytes for rechargeable lithium batteries*”, *Clay: Types, Properties and Uses*, J.P. Humphrey and D.E. Boyd (Eds.), **Nova Science Publishers Inc., Ch. 8, 2011, pp. 275-300, ISBN: 978-1-61324-449-4.**
5. M. Deka and A. Kumar, “*PMMA-based layered silicate nanocomposite gel polymer electrolytes*”, *Photonics and Quantum Structures*, D. Mahanta and G.A. Ahmed (Eds.). **Narosa Publishing House Pv. Ltd., Ch. 13, 2012, pp. 115-122, ISBN: 978-81-8487-098-5.**

#### **D. Paper/Poster Presented in Conferences:**

1. M. Deka and A. Kumar, *International Seminar on Frontiers in Polymer Science and Technology (POLY-2007)*, Tezpur University, Tezpur, Assam, India, 1-3 November, 2007.
2. M. Deka and A. Kumar, *Condensed Matter Days (CM DAYS-2008)*, Visva-Bharati, Santiniketan, West Bengal, India, 29-31 August, 2008.
3. M. Deka and A. Kumar, *Assam Science Society, 54<sup>th</sup> Annual Technical Session*, Tezpur University, Tezpur, Assam, India, 4 February, 2009.
4. M. Deka, R. Gogoi and A. Kumar, *National Seminar on Photonics and Quantum Structures, (NSPQS-2009)*, Tezpur University, Tezpur, Assam, India, 4-6 November, 2009.
5. M. Deka and A. Kumar, *8<sup>th</sup> National Conference on Solid State Ionics (NCSSI-2009)*, Dr. Hari Sing Gour University, Sagar (M.P.), India, 7-9 December, 2009.

6. M. Deka and A. Kumar, *International Conference on Fundamental and Applications of Nanoscience and Technology (ICFANT-2010)*, Jadavpur University, Kolkata, 9-11 December, 2010.
7. M. Deka and A. Kumar, *National Conference on Condensed Matter Physics, NEHU, Shillong, Meghalaya, India, 22-23 March, 2010.*
8. M. Deka and A. Kumar, *National Conference on Smart Nanostructures (NCSN-2011)*, Tezpur University, Tezpur, Assam, India, 18-20 January, 2011.
9. M. Deka, P. Chutia and A. Kumar, *National Workshop on Nuclear and Atomic Techniques based Pure and Applied Sciences (NATPAS-2011)*, Tezpur University, Tezpur, Assam, India, 1-3 February, 2011.
10. M. Deka and A. Kumar, *Possibilities of Electronics R & D Applications in the North – East: One Day Meet Among the Stakeholders*, Tezpur University, Tezpur, Assam, India, 29 July, 2011.
11. M. Deka and A. Kumar, *Condensed Matter Days (CM DAYS-2011)*, Gauhati University, Assam, India, 24-26 August, 2011.
12. M. Deka, P. Chutia and A. Kumar, *International Conference on Renewable Energy (ICORE-2011)*, Tezpur University, Tezpur, Assam, India, 2-4 November, 2011.